Numerical modelling of the self-sealing of the fractured Callovo-Oxfordian claystone in the context of the deep nuclear waste disposal

Hui Wang

Numerical modelling of the self-sealing of the fractured Callovo-Oxfordian claystone in the context of the deep nuclear waste disposal

By

Hui Wang

A thesis submitted in fulfilment of the requirements for the degree of Doctor of Philosophy in Geotechnical Engineering

Université de Pau et des Pays de l'Adour École Doctorale des Sciences Exactes et de leurs applications

Public defense on 18th December 2020

Members of the Thesis Jury:

Pr. Jianfu Shao	President
Pr. Antonin Fabbri	Reviewer
Pr. Matthieu Briffaut	Reviewer
Pr. Stéphane Morel	Invited member
Dr. Gilles Armand	Invited member
Pr. Christian La Borderie	Supervisor
Pr. Domenico Gallipoli	Supervisor
Dr. Minh-ngoc Vu	Supervisor

Thanksgiving

after all

is a word of action

W.J. Cameron

TABLE OF CONTENTS

LIST OF FIGURES

LIST OF TABLES

ACKNOWLEDGEMENTS

I acknowledge the “Agence nationale pour la gestion des déchets radioactifs (ANDRA)” and the “China Scholarship Council (CSC)” for supporting this project, which was carried out in the laboratory SIAME at the Université de Pau et des, Pays de l’Adour.

I would like to express my gratitude to Pr. Christian La Borderie, Pr. Domenico Gallipoli for supervising this project and offering their passionate and enthusiastic support. Their high standard supervision has been precious for my scientific and personal enrichment.

I would like to thank all the members of SIAME and ISA-BTP, specially Dr. Agostino Walter Bruno, Dr. Hatem Kallel for the useful discussions about my research.

I would like to thank Andra for helping me in providing experimental materials, specially Dr. Minh-Ngoc Vu for helping me too much, no matter in Journal papers’ comments/corrections or in my PhD thesis revision.

Very special thanks to my family. I am deeply grateful to my grandfather SiMin Wang, my father ZhiZhi Wang, my mother ShuXia Jia and my brother Yang Wang for all the sacrifices they have made for me.

Finally, my sincere thanks go to my friends and colleagues with whom I shared the past four years.

Thank you France. Thank you China.

ABSTRACT

The present work explores the numerical modelling of the hydro-mechanical behaviour of the fractured zone in deep nuclear waste disposal schemes. This includes simulation of Callovo-Oxfordian argillite (COx) swelling, cracks estimation of fractured COx, coupled the hydro-mechanical behaviour of COx, self-sealing of fractured COx and the fractured zone by the means of mechanical loading and hydration.

Callovo-Oxfordian argillite is a claystone with the properties of both soils and rocks. Therefore, Van Genuchten model (1980), which usually was used to describe water retention of soils and rocks, is employed to simulate water retention of COx. The relations between tensile strength, fracture energy, Young Modulus and water content of COx are formulated for application in numerical analysis.

The Biot's model conbining to an extra deformation upon to the desaturation/resaturation is proposed to describe the deformation of rock under hydric and mechanical loading. The Von Mises yielding standard, Nadai criterion and the damage model (Fichant et al., 1999) are employed to analyse the plastic damage behaviour of COx. Crack opening/closure of unsaturated fractured COx samples is estimated using a post-processing method based on fracture energy regularization. Based on the crack width estimation, the permeability of fractured material is evaluated using the Cubic Law. Taking into account the permeability resulting from cracks, an classical model of hydraulic diffusion in fractured unsaturated COx has been formulated and executed in the Finite Element code CasT3M.

Uniaxial compression tests under relative humidities of 32%, 44% and 76%, and triaxial compression tests with confining stresses of 0MPa, 2MPa, 6MPa, 12MPa under a relative humidity 90% are simulated and compared with experiments, which prove the reliability of the proposed model for describing the hydro-mechanical behaviour of COx.

One of the most important properties of COx is its swelling potential upon saturation. In this respect, free and restrained swelling during hydration are simulated, and a good agreement between numerical and experimental results are obtained.

The self-sealing potential of fractured COx is evaluated by means of numerical simulations. This analysis is based on laboratory tests and in-situ test CDZ (compression damage zone) performed within the Meuse/Haute-Marne Underground Research Laboratory. Laboratory tests show that the global gas permeability declined from 10-14 m2 to 10-16 m2 following an increase of

confining pressure from 0MPa to 17MPa. Self-sealing of fractured COx was accomplished by injecting water into the samples, which produced an increase of the global water permeability to the levels of the intact COx. For CDZ tests, the global gas and water permeabilities produced by self-sealing of the fractured zone are similar to the laboratory values. Self-sealing of the fractured zone was observed when water flowed into the zone of connected fractures and the zone of diffuse fractures. The numerical simulations of small fractured COx samples show good consistency with experimental results. At the scale of the CDZ tests, the consistency between the numerical and experimental results is worse because it is not easy to obtain the same fracture pattern in numerical simulations and experiments.

In conclusion, a plastic damage model is formulated successfully in this thesis, which behaves correctly in analyzing the hydro-mechanical behaviour of unsaturated COx claystone. The comparison between simulations and experiments shows that the model can predict self-sealing of cracked COx samples at the scales of both small samples and the fractured zone.

KEYWORDS: Callovo-Oxfordian argillite, Biot's model, the fractured zone, swelling, saturation, permeability, fractures, extra deformation, self-sealing, compressive damage zone (CDZ)

RESUMÉ

La thèse a pour but de présenter la modélisation numérique de l'auto-colmatage de l'argilite Callovo-Oxfordien dans le context du stockage profond des déchets radioactifs. Les principaux travaux comprennent la simulation du gonflement de l'argilite Callovo-Oxfordienne (COx), l'estimation des fissures du COx fracturé, le comportement hydromécanique du COx, l'auto-colmatage du COx fracturé et de la zone fracturée par le biais des charges mécaniques et de l'hydratation.

Le comportement de la rétention d'eau de l'argilite COx est décrit par le modèle Van Genuchten (1980). Les relations entre la résistance à la traction, l'énergie de rupture, le module d'Young et la teneur en eau de COx sont formulées dans la modélisation numérique.

Une loi décrite la déformation libre en fonction du dégrée de saturation avec la prise en compte de l'hystérésis désaturation/resaturation est introduit dans la théorie de Biot afin de modéliser la déformation de l'argilite COx sous les chargements hydrique et mécanique. Le critère de plasticité Nadaï et le modèle d'endommagement unilatéral de Fichant sont utilisés pour analyser le comportement mécanique du COx. L'estimation de l'ouverture / fermeture des fissures des échantillons de COx fracturés non-saturé est effectuée à l'aide d'une méthode de post-traitement basée sur la régularisation de l'énergie de rupture. Sur la base de l'estimation de la fissuration et de ses ouvertures, la perméabilité du matériau fracturé est évaluée en utilisant la loi cubique. Les équations de diffusion de l'argilite COx ont été implémentés dans le code des éléments finis Cast3M.

Les tests de compression uniaxiale sous humidités relatives 32%, 44% et 76%, et les tests de compression triaxiale en contrainte de confinement 0MPa, 2MPa, 6MPa, 12MPa sous humidité relative 90% sont effectués en simulation numérique, ce qui prouve la fiabilité du projet modèle pour décrire le comportement mécanique des COx.

Une propriété important du COx non-saturé est le gonflement due à resaturation. Le gonflement libre et sous contrainte sous l'hydratation sont simulés et une bonne accordance entre les résultats numériques et expérimentaux sont obtenus.

L'analyse de l'autocolmatage du COx est faite à traverse la simulation des essais au laboratoire et l'expérimentation in-situ. Le dernier est l'expérimentation CDZ (compression damage zone) qui est réalisé au Laboratoire Souterrain de Meuse/Haute Marne pour le but d'étudier l'auto-colmatage de la zone fracturée induite par le creusement. Les mesures de la perméabilité globale au gaz et de la perméabilité globale à l'eau du COx fracturé ont été effectuées lors d'auto-colmatage sans ou avec contrainte au laboratoire et in-situ. En laboratoire, une pression de confinement a été

imposée sur des échantillons de COx fracturés, et la valeur de la perméabilité aux gaz évolue de $10^{-14}m^2$ à $10^{-16}m^2$ lorsque la pression de confinement augmente de 0MPa à 17MPa. L'auto-colmatage des échantillons de COx fracturés a été réalisée en injectant de l'eau dans les échantillons, la perméabilité globale à l'eau pourrait approximativement retrouver celle de COx intact. Pour les tests CDZ effectués à l'Andra, les résultats en terme de perméabilité globale au gaz et à l'eau pour durant l'auto-colmatage de de la zone fracturée sont similaires à ceux mesurés en laboratoire, et montrent que de la zone fracturée colmater lors du drainage du massif intact vers la paroi de la galerie.

Le modèle proposé est en premier temps appliqué à modéliser les essais au laboratoire afin de monter la validation et sa capacité de modéliser le phénomène d'auto-colmatage de l'argilite.

L'expérimentation CDZ est modélisé dans un deuxième temps. L'observation in-situ est à peu près reproduit mais mois réussite que l'échelle des échantillons car la reproduction de la zone fracturée induite par l'excavation n'est pas une tâche triviale.

En conclusion, le modèle proposé se comporte correctement dans l'analyse du comportement hydromécanique de la zone endommagée par l'excavation, Il est capable de reproduire l'auto-colmatage à l'échelle de l'échantillon de laboratoire ainsi qu'à l'échelle de l'ouvrage.

MOTS-CLÉS : Argilite Callovo-Oxfordien, le modèle de Biot, zone endommagée par l'excavation, gonflement, saturation, perméabilité, fractures, déformation supplémentaire, auto-colmatage, CDZ.

Chapter 1
Introduction

1.1 Nuclear waste disposal schemes

1.1.1 Nuclear waste

Nuclear waste is radioactive and is the by-product of nuclear fission or other applications of nuclear technology. The radioactivity of nuclear waste declines naturally over time, so radioactive waste must be isolated and confined to a suitable disposal facility for a sufficient period time until it no longer poses a threat. The length of time that radioactive waste must be stored depends on the type of waste and radioisotope. Current methods for managing radioactive waste are isolation and storage of short-lived waste, near-surface disposal of low-level and moderate waste, burial in deeper geological reservoirs, and transfer of high-level waste. Radioactive waste is harmful to most forms of life and the environment and its management is regulated by government agencies. The radioactivity of all radioactive waste decreases over time, because radionuclides contained in the waste have a half-life (the time it takes for half an atom to decompose into another nuclide), and therefore eventually all radioactive waste is decomposed into non-radioactive elements, stable nuclides. Since radioactive decay follows the half-life rule, the decay rate is inversely proportional to the decay duration. In other words, the radiation intensity of long-lived isotopes (such as iodine 129) is lower than that of short-lived isotopes (such as iodine 131). The type of energy emitted by radioactive material and the type of ionizing radiation are also important factors in determining its threat to humans. The chemical character of the radioactive element will determine the mobility of the substance and its potential to spread to the environment and pollute humans. In fact, there are many radioactive isotopes do not decay to a stable state immediately, and they decay into radioactive decay products in the decay chain before finally reaching a stable state. The classification of radioactive waste varies from country to country, and the International Atomic Energy Agency (IAEA) provides five main types of nuclear waste classification (Tonhauser and Jankowitsch, 2006):

(1) Mill tailings: Uranium tailings are waste by-products left during the rough processing of uranium-containing cores. They have no significant radioactivity and therefore no significant threats to public safety (US Nuclear Regulatory Commission, 2015).

(2) Low-level waste (LLW): It is produced by hospitals and industry and the nuclear fuel cycle. Low-level waste includes paper, rags, tools, clothes, filters, and other materials that

contain small amounts of very short-lived materials. This kind of nuclear waste is less dangerous in terms of radioactivity comparing with high-level radioactive waste (Yim and Simonson, 2000).

(3) Intermediate-level waste (ILW): Radioactive content is high, usually shielding, but no cooling is required (Janicki, 2013). Among all kinds of nuclear waste destined to disposal, the intermediate-level waste constitutes the majority.

(4) High-level radioactive waste (HLW): This is the waster that originates from nuclear reactors, but HLW definition is different from country to country. When they are removed from the core, after a fuel cycle serving, nuclear fuel rods are considered high-level radioactive waste (Rogner, 2010). Fuel rods, which are produced in the reactor core, contain two parts: fission products and transuranic elements. Spent fuel from the nuclear power plant reactor core is highly radioactive and has a high temperature. High-level radioactive waste contains more than 95% of the total radioactivity originating from nuclear power generation. At present, about 12,000 metric tons of high-level radioactive waste is produced per year. If put together, its volume is almost the same as 100 double-decker buses or a two-story structure occupying the size of a basketball court (Saling, 2018).

For a 1000 MW nuclear power plant, every year the production of spent nuclear fuel is approximately 27 tons. Approximately 250,000 tons high-level nuclear waste were stored before 2010, whereas this did not include the amount that escaped to the environment leading by accident or test. In 2019, America has more than 90,000 tons of high-level radioactive waste (Findlay, 2019). Caesium 137 and strontium 90 are the main components of the radioactive waste produced by spent fuel rods. The half-lives of radioactive elements are different, e.g. it is about 30 years for caesium 137 and strontium 90, however can be as long as 24,000 years for plutonium.

(5) Transuranic waste (TRW): According to USA regulations, transuranic waste (TRW) is waste contaminated by transuranic radionuclides with half-lives greater than 20 years and concentrations greater than 100 nCi/g, excluding high-level radioactive waste. Elements with an atomic number greater than uranium are called transuranium ("outer uranium"). Because TRW has a longer half-life, it is more dangerous than low or medium-level waste (Lyoussi, 2000; National Research Council, 1996). In the United States, it mainly comes from nuclear weapons production and consists of clothing, tools, rags, residues, debris and other items contaminated with small amounts of radioactive elements (mainly plutonium). Under U.S. law, transuranic waste is further divided into "contact treatment" (CH) and "remote processing" (RH) based on the radiation dose rate measured on the surface of the waste container. The surface dose rate of CH does not exceed 200 mrem per hour, while the surface dose rate of RH does exceed 200 mrem or higher. RH does not have the high radioactivity of high-level radioactive waste and does not generate high heat, but RH can have high radioactivity with a surface dose rate of up to 1,000,000

mrem/h. The United States is currently disposing of TRW from military facilities at the Waste Separation Pilot Plant (WIPP) in deep salt formations in New Mexico (Authority, 2014).

1.1.2 Nuclear waste treatment

Radioactivity declines naturally over time, so radioactive waste must be isolated and confined in a suitable disposal facility for a sufficient period time until it no longer poses a threat. The length of time radioactive waste must be stored depends on the type of waste and radioisotope. The fuels burned are reactor-grade plutonium (RGPu), weapon-grade plutonium (WGPu), and mixed oxide fuel (MOX) (Ojovan et al., 2019; Hileman, 1982; Alley, 2012; World Nuclear Association, 2010). For these three types of materials, the relation of total activity and decay time is shown in Figure 1.1.

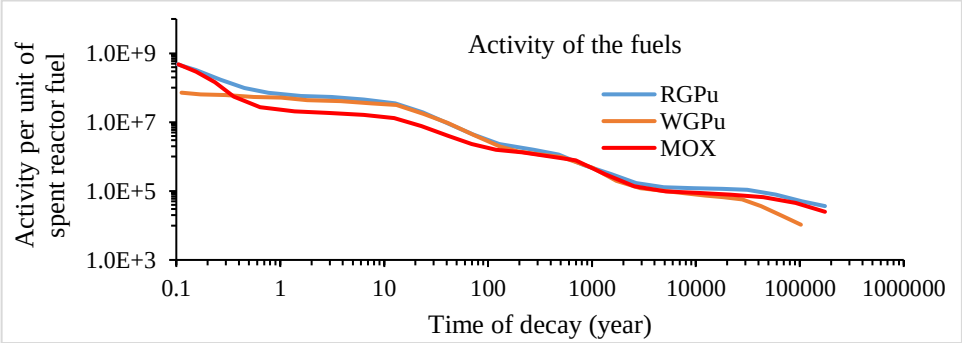

Figure 1.1. Total activity for three fuel types (Sterbentz., 1997)

The ongoing controversy over the disposal of high-level waste is a major constraint on the global expansion of nuclear power. Most scientists agree that the best long-term solution is deep geological burial in mines or deep wells. However, almost sixty years after commercial nuclear power began to be used, no government has successfully established such a repository for civilian high-level nuclear waste. Finland is building such a facility (Onkalo repository), but controversy exists from public and it will need time before becoming fully operational. The same controversies exist in almost every country which are running nuclear power plants and are, therefore, faced with the disposal of nuclear waste. Reprocessing or recycling of nuclear waste is being actively developed worldwide (Walker et al., 1992; Bates et al., 1992; Cooper, 2005) but it still generates waste. It is, therefore, not a total solution to the problem, though it can reduce the amount of waste to be disposed.

Nuclear states have studied several methods of disposing of radioactive waste as follows:

(1) Long-term storage on the ground. There are huge environmental risks, so it is not feasible.

(2) Outer space disposal. Because it is currently too expensive, no disposal of outer space has been performed.

(3) Underground disposal, not implemented yet.

(4) Reuse until attainment of non-radioactivity, unfeasible so far.

(5) Disposal in the subduction zone, not implemented yet.

(6) Marine disposal. In the past, the Soviet Union, the United Kingdom, Switzerland, the United States, Belgium, France, the Netherlands, Japan, Sweden, Russia, Germany, Italy, and South Korea have pursued this option but international agreements no longer allow this.

(7) Subsea disposal, never implemented and not allowed by international agreements.

(8) Placement on the ice sheet, rejected by the Antarctic Treaty as not safe.

(9) Nuclear transmutation by means of lasers to cause beta decay, converting unstable atoms into atoms with shorter half-lives.

Among the above alternatives, the only feasible and realistic option is deep geological storage which remains, at the present, the only responsible way to dispose of nuclear waste.

Some countries are currently selecting suitable repositories for high level waste and spent fuel, but there remain technical challenges and public concerns to be overcome before arriving to the operation of waste storage galleries. The basic concept of nuclear waste underground disposal is to find a large, stable geological formation and use mining technology to construct underground galleries from 500 meters (1,600 feet) to 1,000 meters (3,300 feet) to handle highly radioactive waste. The goal is to permanently isolate nuclear waste from the human environment (Chapman et al., 1987; Shrader-Frechette, 1993; West et al., 1985).

1.2 Nuclear waste underground disposal schemes

1.2.1 U.S. underground nuclear waste repository

The Yucca Mountain Nuclear Waste Repository, designated by the Amendment to the Nuclear Waste Policy Act of 1987, is a deep geological disposal storage facility located in the Yucca Mountain to store U.S. nuclear waste and other highly radioactive materials. The site is located on federal land near the Nevada test site in Nai County, Nevada, approximately 130 kilometres northwest of the Las Vegas Valley (Ressetar, 2003) (Figure 1.2). The 107th Congress of the United States approved the project in 2002, at the request of the Obama administration, the Republican Department of Defense passed federal funding for the site in 2011, and the Annual Continuous Appropriation Act was passed on April 14, 2011. However, the Representative terminated with an amendment and the project encountered many difficulties and was strongly protested by the non-local public, the people of Shoshone, and many politicians. The project also faces strong opposition from states and territories. The Government Accountability Office stated that the shutdown was for political reasons, not technical or security reasons.

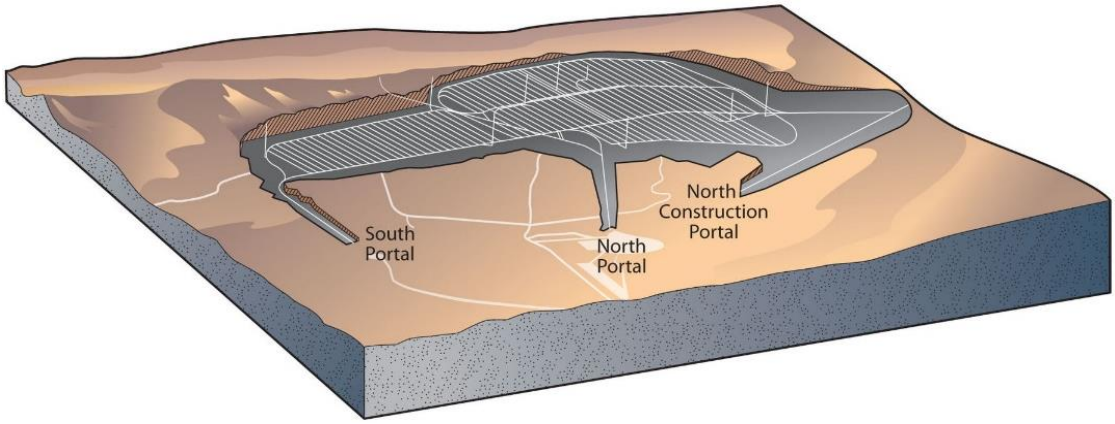

Figure 1.2. Geological map of the Yucca Mountain Nuclear Waste Repository (Ressetar, 2003)

1.2.2 China underground nuclear waste repository

With the rapid development of nuclear power in China, the disposal of high-level radioactive waste has become an important issue for human safety and environmental protection. Deep geological disposal is a feasible and safe method for high-level radioactive waste disposal. Internationally recognized underground research laboratories play an important and multifaceted role in the development of advanced radioactive waste repositories. According to the latest development of this Chinese underground laboratory (URL) site, combined with a comprehensive assessment of the site over the past 33 years, Beishan Xinchang site (Figure 1.3), which is located in the northwestern province of Gansu, China, has been selected as the final site for China's first site for nuclear waste disposal, and the host rock is granite (Guo et al., 2001; Wang et al., 2004; Yang and Guo, 2004).

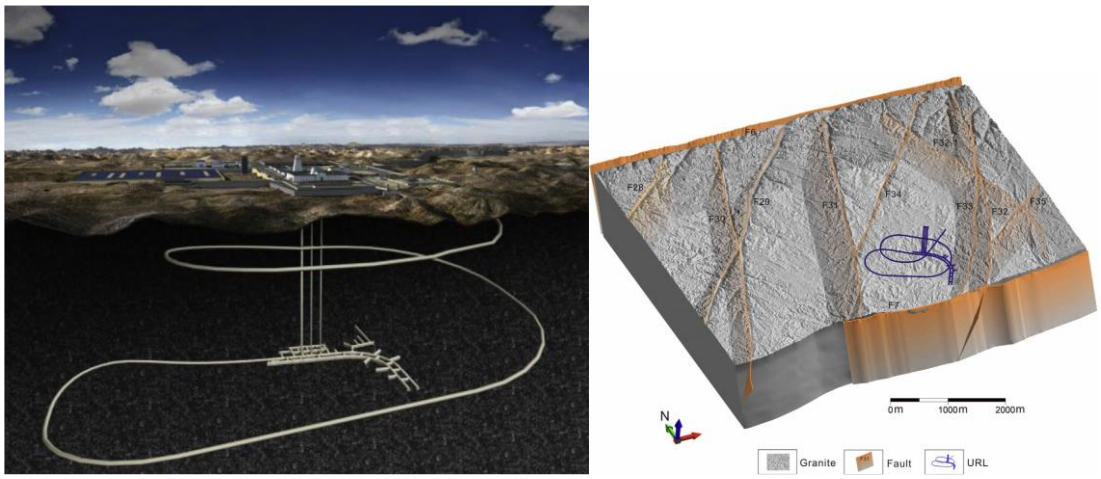

Figure 1.3. Geological map of the Beishan Nuclear Waste Repository (Guo et al., 2010)

In the process of characterizing the Xinchang URL site, a series of surveys have been conducted, including drilling, geological mapping, geophysical surveys, hydraulic tests, and field stress measurements (Wang et al., 2006). The survey results show that the geology, hydrogeology, engineering geology and geochemical conditions of the new site are very suitable for URL

construction. At the same time, to verify and develop the construction technology of Beishan URL, a North Kowloon Exploration Area (BET) has been completed. The tunnel is located 50 meters deep in the Jiujing subdivision and has undergone some field tests, such as drilling. Blast tests were performed in BET, features of the excavation failure zone (Chen et al., 2017), and long-term deformation monitoring of surrounding rocks was carried out. The methods and techniques established in BET will be used for URL construction. Based on the results of URL site characterization, a preliminary design of a URL with a maximum depth of 560 m was proposed, and the necessary field tests were planned in the URL (Zhao et al., 2013).

1.2.3 France underground nuclear waste repository

In France, the National Radioactive Waste Management Agency (Andra) is responsible for investigating and designing sustainable nuclear waste management solutions (Figure 1.4).

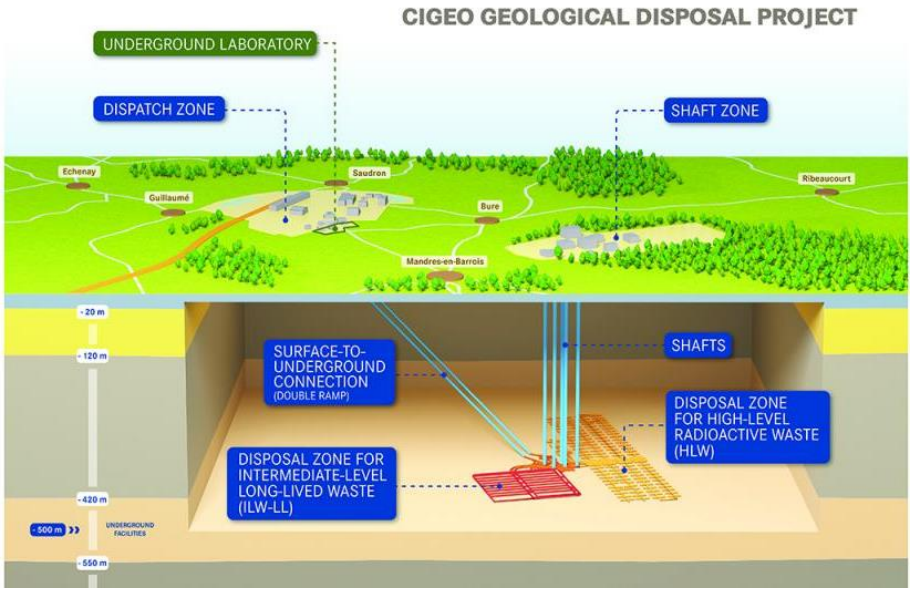

Figure 1.4. Meuse/Haute-Marne Underground Research Laboratory (De La Vaissière et al., 2015)

Because of its extremely low intrinsic permeability ($1 \times 10^{-21} m^2 \sim 5 \times 10^{-20} m^2$), low molecular diffusion and good radioactive waste retention capacity, the Callovo-Oxfordian argillite (COx) deposit was chosen as a potentially suitable geological formation for the construction of nuclear waste repositories. In 2000, Andra started the construction of the Muse Haute-Marne Underground Laboratory by sinking two shafts to COx position at a depth of 420m and 550m below the ground surface (Andra).

1.2.4 Finland underground nuclear waste repository

The Onkalo spent nuclear fuel repository (Figure 1.5) is a deep geological repository for the final disposal of spent nuclear fuel, it is the first of such advanced waste repositories in the world. Posiva is currently constructing the Onkalo nuclear power plant in Eurajoki on the west coast of

Finland, and it is based on the KBS-3 nuclear waste landfill method developed in Sweden by Svensk Kärnbränslehantering AB (SKB) (Johansson et al., 2015; Rempe, 2007). The Finnish Nuclear Energy Act was amended in 1994 to require all nuclear waste generated in Finland to be disposed of in Finland. Onkalo was selected as a long-term underground storage in Finland in 2000. The facility is called "Onkalo" (meaning "small cave" or "cave") and is built in the granite bedrock of the Onkalo site, about 5 kilometres from the power plant. The site was selected during a long process that began in 1983 and screened the entire Finnish territory. From 1993 to 2000, four possible locations were examined: Romuvaara in Kuhmo, Kivetty in Äänekoski, Onkalo in Eurajoki and Hästholmen in Loviisa. In addition to geological and environmental factors, the opinions of local residents was also considered. Eurajoki and Loviisa were selected as the regions with the highest local support. The former site's geographical conditions are more favourable, so in 1999, Posiva proposed to use it. The Pune city government confirmed approval for the site, and the decision was approved by the central government in May 2001. A construction permit was issued on November 12th, 2015. Posiva is expected to begin construction in 2016 and commence operations in 2023 (Siren, 2017).

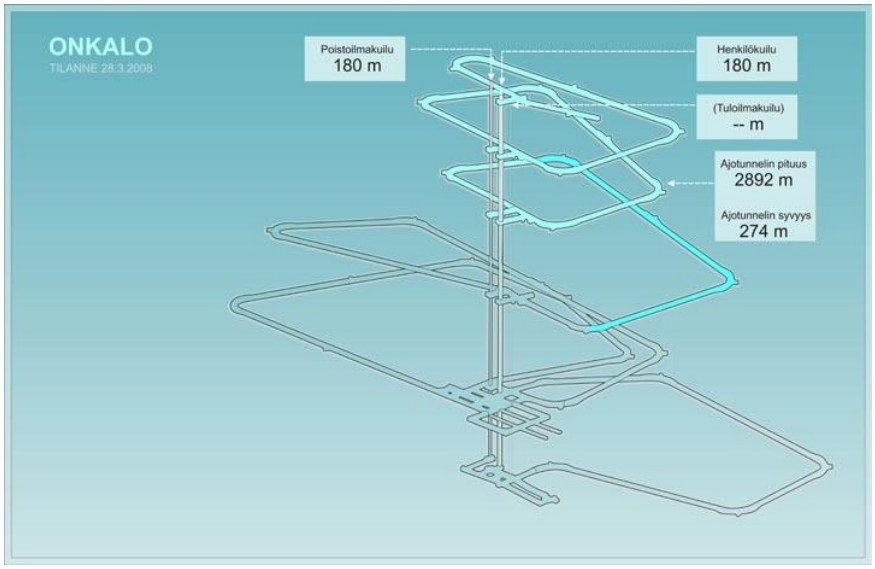

Figure 1.5. Onkalo Nuclear Waste Repository in Finland (Voutilainen et al., 2014)

1.2.5 South Korea underground nuclear waste repository

The Gyeongju Nuclear Waste Treatment Facility (Kim et al., 2011) (Figure 1.6) is designed in the form of silos involving deep processing. It plans to store low and intermediate level waste (LILW). In its first phase, it has a designed storage capacity of 100,000 barrels. After the final stage is completed, a total of 800,000 barrels will be accommodated. South Korea's nuclear program has been fully integrated into the national infrastructure, providing 30% of its electricity and 8.6% of its total energy use. As of May 2012, there were 21 reactors in operation in the country, generating 18.7 GWe. It is estimated that ongoing and planned projects will bring South

Korea's power generation to 32.9 GWe by 2030. Intermediate and low-level radioactive waste is stored on-site at each plant. However, after nearly 30 years of nuclear power production, on-site storage has begun to fill up. The South Korean government estimates that, if there is no separate storage facility, the storage pools of Kori, Ulchin and Yonggwang nuclear power plants will be filled by 2016, 2018 and 2021, respectively. The CANDU facility at Woolson Nuclear Power Plant will be fully operational in 2017. Plans for storage facilities were made as early as 1986, but Gyeongju was not selected until 2005. After obtaining the MKE project license and MEST construction and operation license, construction began in August 2008. By 2010, 1,000 barrels of LILW waste had been processed and shipped to the Gyeongju plant, and Construction was completed in early 2015 (Sung et al., 2017).

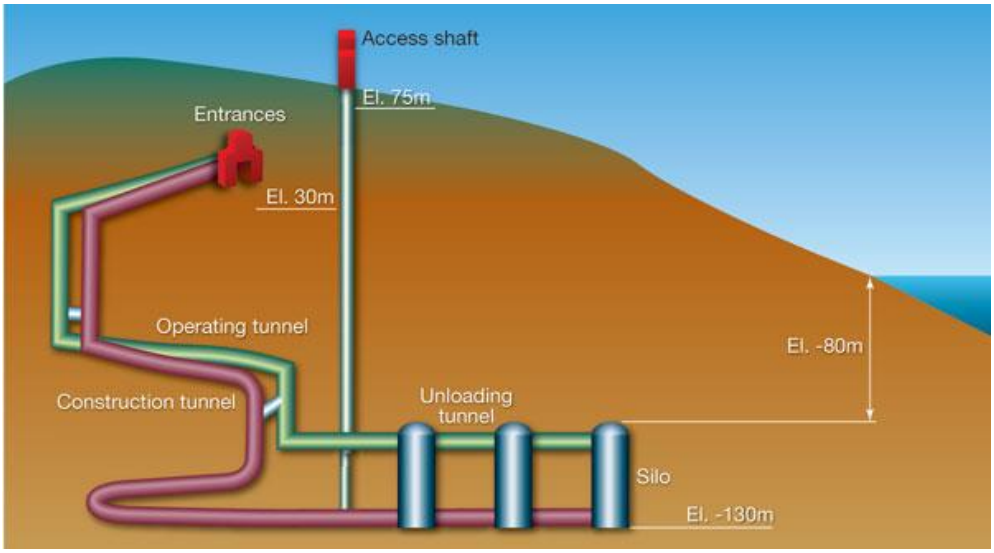

Figure 1.6. Nuclear Waste Repository in South Korea (Peachey, 2014)

1.2.6 Sweden underground nuclear waste repository

Sweden is one of the few countries that provides a final storage solution for highly radioactive waste (Flynn et al., 1992; Martin and Christiansson, 2009). Three nuclear power plants in Sweden can meet about half of the country's electricity needs. Following the disasters that happened in several countries regarding nuclear waste leakage, the plans to establish what could become the Sweden first final storage site for radioactive waste have been met with increasing opposition.

So far, radioactive waste has been kept in temporary storage locations in Sweden, but now the industry has, for the first time, proposed plans to provide a final storage solution for all spent fuel in Swedish nuclear reactors. Nuclear waste is stored in copper capsules and will be buried 500 meters underground. The location (Figure 1.7) is close to Forsmark, a coastal city about 100 kilometres (62 miles) north of Stockholm, (Selroos and Follin, 2014). Local authorities have agreed to the project, and the location is said to be very suitable.

Figure 1.7. Nuclear Waste Repository in Sweden (SKB)

Research on deep geological disposal has spanned decades, including laboratory testing, construction of exploration wellbores, and operation of underground research laboratories undergoing large-scale field testing. The main underground testing facilities are listed in Table 1.1.

Table 1.1. The world main underground repositories for nuclear waste (Gibney, 2015)

Country	Facility name	Location	Geology	Depth
Belgium	HADES Underground Research Facility	Mol	plastic clay	223 m
Canada	AECL Underground Research Laboratory	Pinawa	granite	420 m
Finland	Onkalo	Olkiluoto	granite	400 m
France	Meuse/Haute Marne Underground Research Laboratory	Bure	claystone	500 m
Japan	Horonobe Underground Research Lab	Horonobe	sedimentary rock	500 m
Japan	Mizunami Underground Research Lab	Mizunami	granite	1000 m
Korea	Korea Underground Research Tunnel		granite	80 m
Sweden	Äspö Hard Rock Laboratory	Oskarshamn	granite	450 m
Switzerland	Grimsel Test Site	Grimsel Pass	granite	450 m
Switzerland	Mont Terri Rock Laboratory	Mont Terri	claystone	300 m
United States	Yucca Mountain nuclear waste repository	Nevada	tuff, ignimbrite	50 m

1.3 Mission of Andra

Originally created as a department of the CEA (French Atomic Energy Committee) in 1979, Andra was made an independent entity by the Bataille Act in 1991. Currently Andra, short for French National Agency for Radioactive Waste Management, functions as a state-owned undertaking of industrial and commercial nature, and is in charge of long-term radioactive waste

management on the French territory. Whilst independent from the waste producers, Andra is placed under the supervision of the ministers of Energy, Research and Environment respectively. All Andra's activities have one common goal, to ensure the protection of the present and the future generations and the environment from the effects of ionizing radiation, which translates into several main missions, defined in the Law of June 28, 2006 on the sustainable management of radioactive materials and waste:

- **Design, scientific research and technological development**

To study and develop solutions for sustainable management of those types of radioactive waste that do not yet have a final disposal method: high-level waste, intermediate-level long-lived waste and low-level long-lived waste.

- **Industrial waste management activity**

To accept the waste from the electro-nuclear sector, from industries outside the electro-nuclear sector, from the National Defense, from the research and healthcare sectors;
To operate and monitor radioactive waste disposal facilities so as to ensure safety of the human being and protection of the environment.

- **Public Service and Raising Awareness**

To collect radioactive objects from private and public holders;
To clean up and remediate polluted territories;
Every three years to compile and to publish the National Inventory of Radioactive Waste and Materials in France;
Provide clear and true information on the management of radioactive waste;
To encourage and maintain the dialogue with stakeholders.

- **Outreach on a national scale and abroad**

To develop scientific cooperation on a national, European and international levels;
To promote Andra's know-how and service offers in France and abroad;
To promote scientific and technical culture as broadly as possible.

1.4 Projet Cigéo

Cigeo (Industrial geological disposal center) is the French project for a deep storage center for radioactive waste. It is designed to store the highly radioactive and long-lived waste produced by all current nuclear installations and by the treatment of spent fuels used in nuclear power plants. The objective of the Cigéo deep disposal center project is to protect humans and the environment from the danger of this waste in the very long term. Since 1991, research has been carried out in various ways on the management of the most dangerous radioactive waste. This research led to the choice of deep geological disposal in 2006, the studies of which were entrusted to Andra. To study and design the deep geological repository, Andra has carried out research in various

disciplines ranging from geology to digital simulation, including studies on materials and the environment. To conduct these studies, the hundred scientists from Andra rely on French and international partners recognized in their fields. It also develops and uses tools, including its underground research laboratory in Meuse / Haute-Marne, its long-term environmental and digital observatory. Cigeo will be located in Meuse/Haute-Marne and will be composed of:

- an underground area (where waste will be stored)
- surface installations spread over two areas
- connections between the surface and the underground.

Cigeo will be built gradually to store waste for more than 100 years. It will then be closed to ensure their containment over very long periods of time, without requiring human action. Cigeo's safety is based on the geological layer in which the underground facilities will be located, its design choices and its safety devices. The management of long-lived radioactive waste involves large timescales: the center will operate for more than a century and will protect humans and the environment for hundreds of thousands of years. In order not to transfer the financial burden of this center to future generations, its financing is already provided, through provisions, by the producers of radioactive waste. For more than 20 years, Andra has been present in Meuse / Haute-Marne; alongside local actors and by involving the populations, it is now preparing the integration of Cigéo, so that it becomes an opportunity for the territory.

1.4.1 URL laboratory

The Meuse/Haute-Marne is a laboratory (URL in Figure 1.8) located 500 meters below ground in the east of Paris. This laboratory was employed to study geological formations of the host layer for storing nuclear waste to assess its safety for deep geological repositories of high-level and long-lived medium-level radioactive waste. It is administered by the National Radioactive Waste Management Agency or Andra (French: Agence nationale pour la gestion des déchets radioactifs).

Figure 1.8. Location of underground laboratory (URL) in France (Armand et al., 2014)

Geological conditions

The Meuse/Haute-Marne site belongs to the eastern rim of the Paris Basin, the lowest point of this basin corresponds to the Ile de France region. In the zone studied, the Paris Basin consists of alternating layers of predominantly clay sediment and limestone, these layers were deposited between 250 million and 135 million years ago. Research has led to the definition of a so-called transposition zone, covering an area of some 200 km^2, in which the properties observed on the Meuse/Haute-Marne site seem to be transposed.

The selection of a site for the disposal nuclear waste must also avoid the presence of geological faults. This zone has therefore been located away from faults (Marne fault, Gondrecourt rift, etc.) (Figure 1.9) which may provide transfer pathways for underground water flow, which increases the probability of nuclear waste leakage to the biosphere.

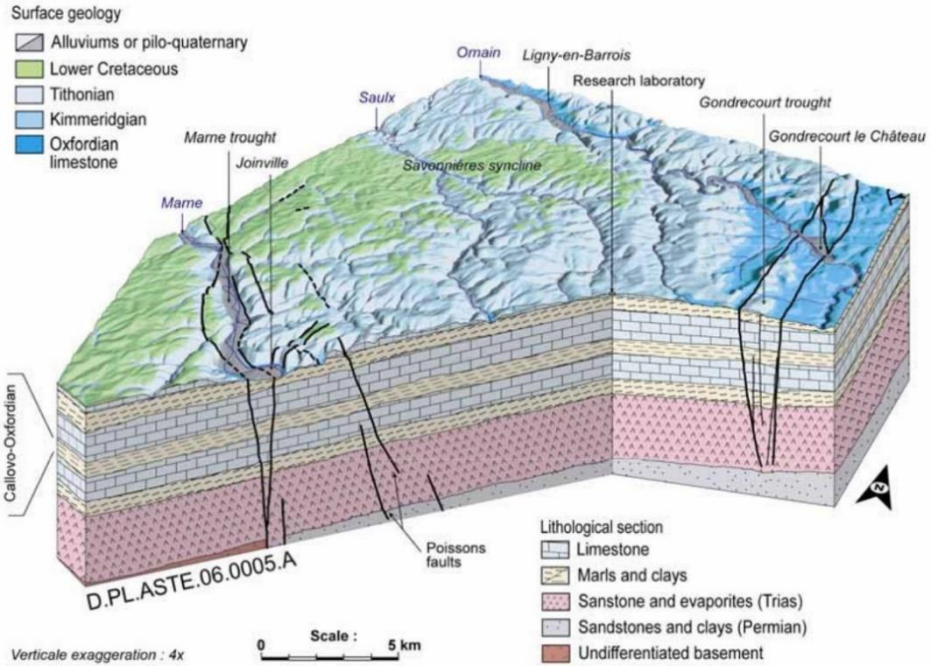

Figure 1.9. Geological structure surrounding Meuse/Haute-Marne site (Andra)

The sedimentary series comprises from the bottom up (and from east to west at the outcrops) (Figure 1.10):

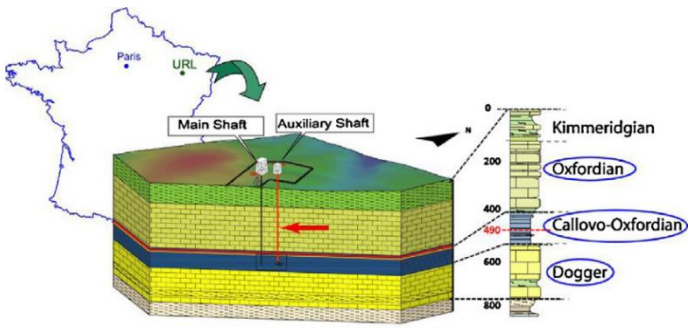

Figure 1.10. Geological layer map of the Nuclear Waste Repository in France (Martin et al., 2010)

- Dogger limestone formation resting on Liassic marls and clays

- Callovo-Oxfordian argillite formation

- Middle to upper Oxfordian limestone formation

- Kimmeridge marls

- Tithonian limestone (known as Calcaire du Barrois) outcrops

- Argilloarenaceous Cretaceous deposits that thinly cover the highest points of the topography. These sedimentary layers have a simple, monoclinal structure with a slight, regular dip of 1 to 1.5 degrees to the northwest.

Host layer for nuclear waste storage

The Callovo-Oxfordian argillite formation has been selected as the host formation for nuclear waste storage within the above sedimentary unit. This formation was carbonated in a relatively calm sea after sedimentation of clay minerals (up to 60% by mass) and fine quartz. The Callovo-Oxfordian argillite is a homogeneous formation of low permeability. The depth from the ground to the top of Callovo-Oxfordian argillite is about 420 meters corresponding to the location of the laboratory site, in the direction of the dip somewhere the thickness becomes over 600 metres (Figure 1.11).

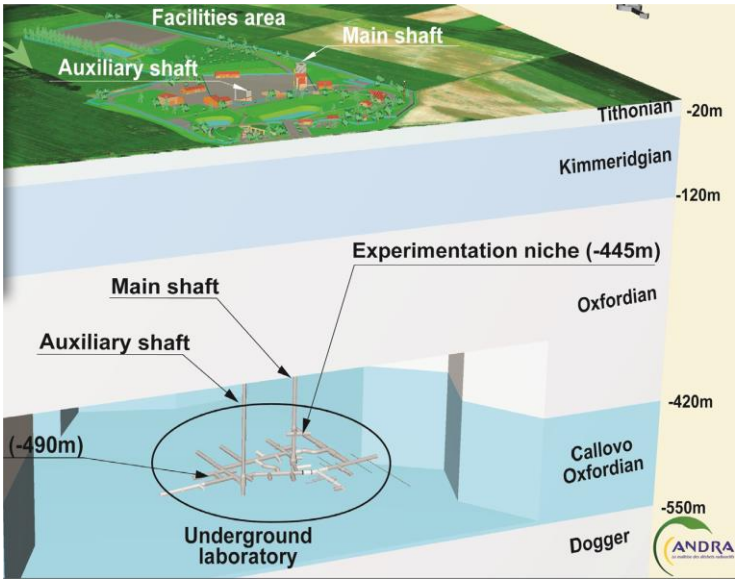

Figure 1.11. Underground laboratory (URL) and its structure (De La Vaissière et al., 2014)

From north to south of the zone, the thickness of the Callovo-Oxfordian argillite formation varies from 160 metres to 130 metres. The Callovo-Oxfordian argillite mineralogical proportions are structured into three sedimentary sequences along the vertical. The upper sequence is characterized by higher carbonate content. The Callovo-Oxfordian argillites were laid down between 158 and 152 million years ago. Under the weight of subsequent deposits, at least 500

metres of sediments were compacted over some fifteen million years, causing water to be expelled. At that time, the Callovo-Oxfordian argillite acquired the properties that are observed today, with a very small permeability to fluid and ions, which is perfect for nuclear waste storage. Subsequent large-scale tectonic events affected the whole of the Paris Basin in the Cretaceous and Tertiary, but they did not cause significant disturbance to the geological medium. The Callovo-Oxfordian is bound by two large limestone formations, i.e. the underlying Dogger formation and the overlying calcareous Oxfordian formation, both containing porous sedimentary horizons where water flows. These horizons have, however, low permeability and are aquifers in the hydrogeological sense.

Galleries excavation and the fractured zone

In France, the earliest geological studies of deep geological reservoirs date back to the 1960s. In the 1980s, the then CEA branch, Andra, investigated the possible locations of underground research laboratories. In 2000, Andra started the construction of the Muse Haute-Marne Underground Laboratory by sinking two shafts to the Callovo-Oxfordian (COx) claystone layer to depths of 420m and 550m below the ground surface and excavating various tunnels and galleries inside the COx layer (Andra, 2005). Disturbance to the surrounding rock cannot be avoided during the construction of the nuclear waste storage galleries (Figure 1.12).

Figure 1.12. Gallery excavation (Armand et al., 2017)

This disturbance leads to rock damage, thus forming pathways for water flow and potential nuclear waste leakage. In the initial periods of storage, the spent nuclear fuel owns continuous reaction capacity. This causes the temperature to go up, which may also undermine the stability of the surrounding rock depending on the thermal-mechanical properties of the material. The main topic of study in this thesis is therefore how to make the fractured zone (Figure 1.13) of the surrounding rock recover to its initial impermeable condition.

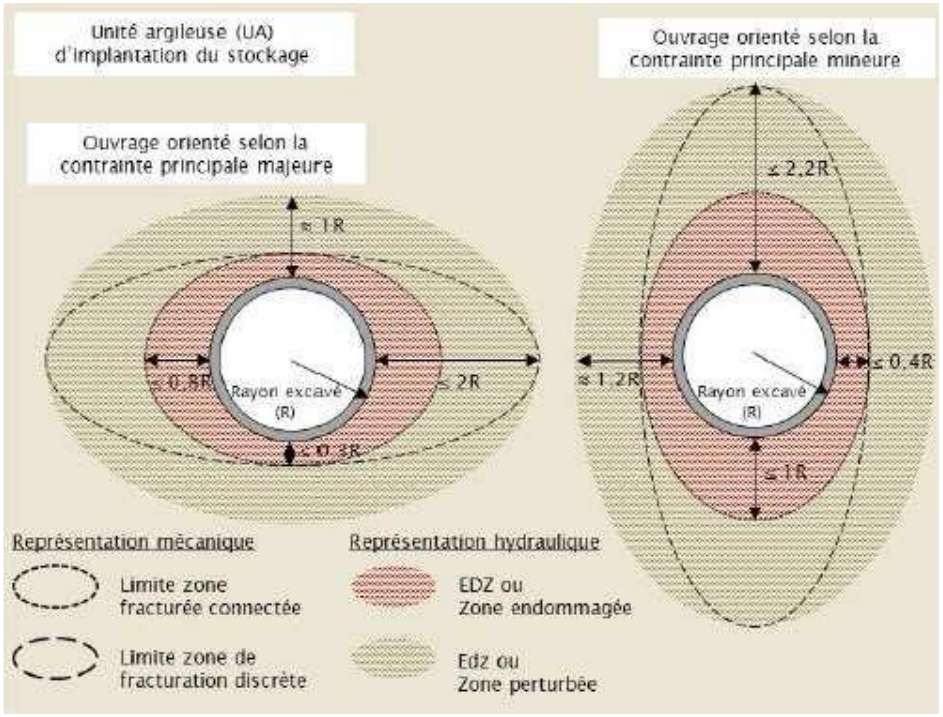

Figure 1.13. A schematic of the fractured zone of circular tunnels (Andra)

1.4.2 Self-sealing behaviour

The fractured zone contains numerous fractures, including tensile fractures and shear fractures, which provide a possible pathway for water flow and nuclear waste leakage. The material is partially unsaturated due to the exchanges with air and will be resaturated after the closing of the tunnels. Resaturation process causes the swelling of COx that can close the pathways and lead to the so-called self-sealing. Figure 1.14 illustrates pictures of a Callovo-Oxfordian argillite sample with a drilled hole before and after a resaturation process.

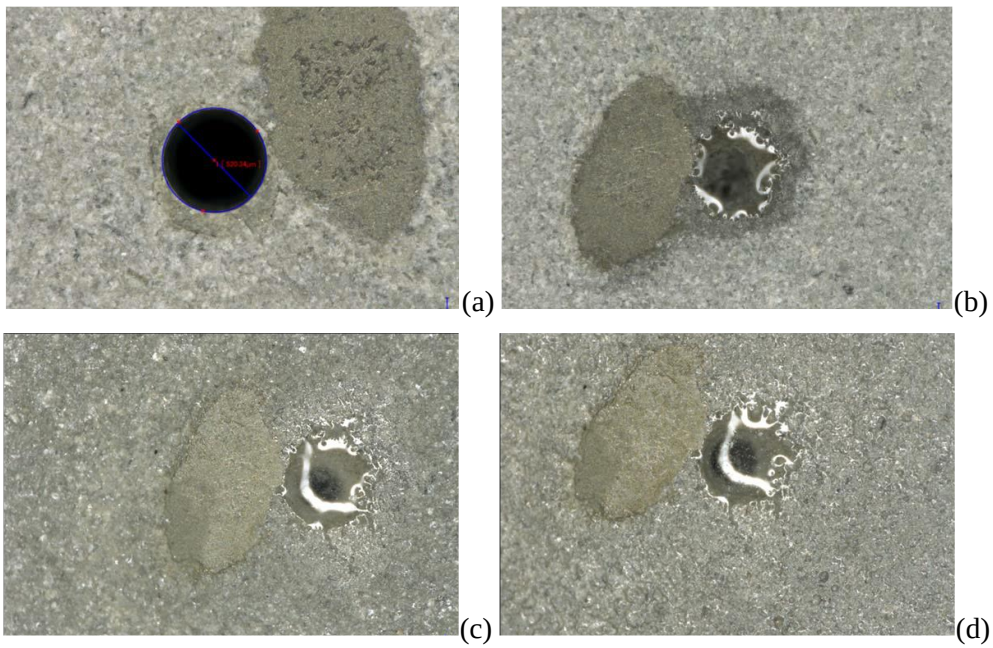

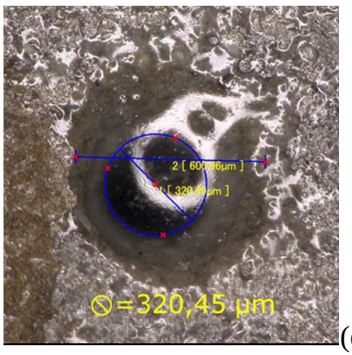

(e)

Figure 1.14. The states of a drilled hole in a Callovo-Oxfordian argillite sample during a resaturation process: (a) before the resaturation process (b) the first moment of wetting (c) wetting 14 hours (d) wetting 48 hours (e) wetting one month (Andra)

The diameter of the drilled hole was 520.34 μm before the resaturation process (Figure 1.14a), and it had a significant decrease when a wetting process started in Figure 1.14b. Figure 1.14c shows the state of the drilled hole in 14 hours wetting, and the value of the diameter reduced to 345.31 μm in 48 hours wetting as shown in Figure 1.14d. With the increment of wetting time, the diameter of the drilled hole tended to be stable gradually, and its value arrived at 320.45 μm as shown in Figure 1.14e.

1.5 Scope of the thesis

The main objective of this thesis is to analyze, by means of numerical simulations, the hydro-mechanical behavior of Callovo-Oxfordian (COx) argillite and its self-sealing capability upon resaturation. A schematic of the research plan is demonstrated in Figure 1.15.

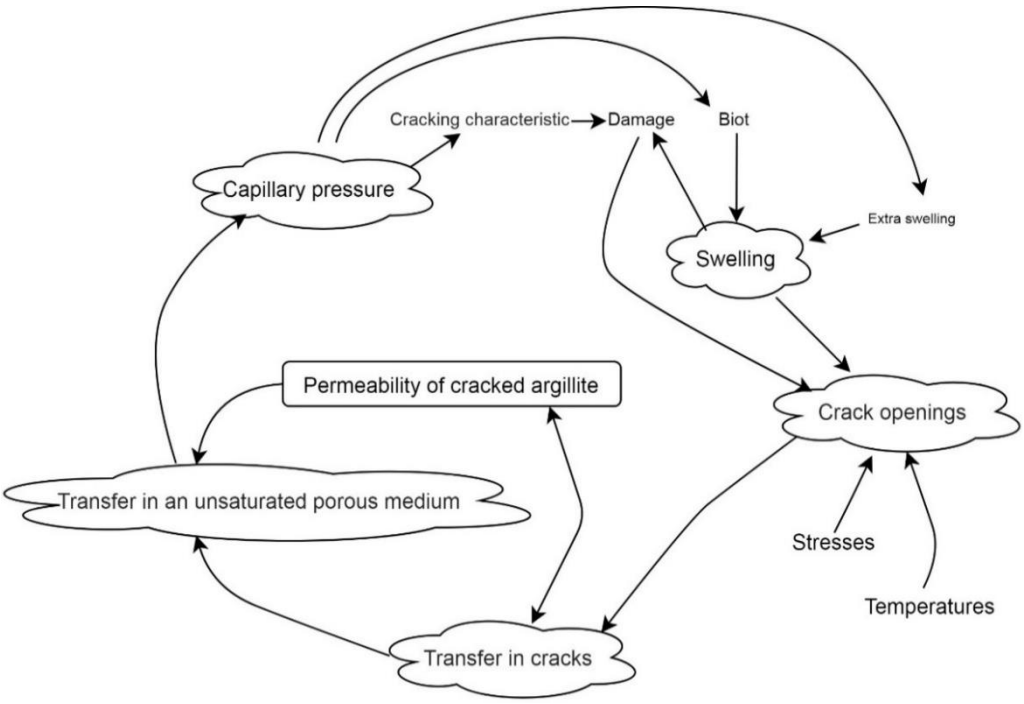

Figure 1.15. A total diagram for the research on thermal-hydro-mechanical behaviour of the fractured zone

According to Figure 1.15, the proposed research must start by considering two important aspects, namely (1) a self-sealing scenario of COx and (2) current bottlenecks in the numerical simulation of self-sealing the fractured zone.

1.5.1 Self-sealing scenario of COx

(1) The fractured zone

The digging of shafts and galleries leads to a change of the geological stresses surrounding the excavation openings. This consists in a gradual process of radial stress decrease and orthoradial stress increase, which may cause local failure under tensile stress and/or shear loading. The extent of the damaged zone is influenced by several factors such as rock properties, local in-situ stresses, shafts and galleries geometry, excavation methods and degree of desaturation due to ventilation. After excavation, fractures and fissures tend to form around the openings, which lead to significant changes in hydraulic pathway and permeability. This fractured region is named the fractured zone and is interested by larger water flow compared to the intact rock. The EDZ (Figure 1.13 red zone) is defined as that region of the host rock whose hydraulic conductivity is greater than $1 \times 10^{-10}\mathrm{m/s}$, namely the fracture connected zone. And next to EDZ is a fracture diffuse zone (conductivity comprised between $1 \times 10^{-12}\mathrm{m/s}$ and $1 \times 10^{-10}\mathrm{m/s}$).

(2) Resaturation of the fractured zone

After excavation, support for the walls of tunnels and galleries is introduced, followed by the installation of underground facilities. The excavation is backfilled by sealing system. Sealing system includes bentonite core, backfill plug and eventually concrete plug. After backfilling, the unsaturated fractured zone region will experience a gradual process of wetting, which is usually termed resaturation. This process also produces a water content growth of the backfill materials, which will swell and produce the development of large stresses against the walls of the repository.

(3) COx swelling

Callovo-Oxfordian (COx) claystone exhibits significant deformations following water content changes. When water content decreases, Callovo-Oxfordian argillite shrinks and, on the contrary, it swells when water content increases. The extent of deformation depends on several factors, including applied stresses, temperature and range of water content changes.

(4) Progressive closure of previously opened cracks

Self-sealing of the fractured Callovo-Oxfordian argillite is the consequence of the resaturation phase that follows backfilling of galleries and shafts. This resaturation process causes the Callovo-Oxfordian argillite to swell while, at the same time, the increase of water content inside the backfill system generates large swelling pressures against the walls of the galleries. Therefore, the cracks inside the fractured zone will progressively close due to the above two concurring

actions. This progressive closure of cracks may lead the fractured zone to recover its original impermeability and, therefore, guarantee the safety of the nuclear waste storage.

1.5.2 Bottlenecks in numerical simulation

(1) Hydro-mechanical coupling of unsaturated cracked porous media

For an intact saturated porous material, the hydro-mechanical behaviour is determined by the interaction between the solid skeleton and the fluid inside the pores. This may also include the effects of the mineralogical composition of the material and the type of porous fluid. For an unsaturated cracked porous material, the impacts of saturation and cracking on the hydro-mechanical behaviour of the material must be also considered. For example, the permeability of the cracked material, the change of relative permeability with saturation and the relation between saturation and suction are important factors that must be taken into account. The numerical analysis of the fractured zone inside underground repositories therefore relies on the correct description of the hydraulic and mechanical properties of unsaturated fractured COx.

(2) Swelling of COx

COx shows significant deformation during changes of the degree of saturation. As many claystones, the swelling of COx during saturation is larger than that of other rocks and differs from that observed in soils. In comparison with soils, COx deformation is reversible to some extent during saturation changes while that of soils is usually irreversible. The standard Biot's model is not enough to describe COx swelling upon saturation and an extra deformation law must be introduced.

(3) Permeability of the fractured zone

The hydraulic conductivity of intact COx depends on the intrinsic permeability and saturation level of the material. On the contrary, the permeability of the fractured zone is mainly controlled by presence of fractures and it evolves as fractures change. During the construction of shafts and galleries, the host rock experiences a progressive opening of fractures due to excavation disturbance, ventilation and desaturation. Instead, during operation of the disposal scheme, the fractures are progressively closed due to the resaturation of the host rock and the swelling pressure exerted by the backfill material. The correct description of the evolving permeability of the fractured zone is therefore essential for the numerical simulation of the repository performance.

1.6 Research objectives

The main deliverable of the thesis is the development of a finite element computer code capable of simulating the hydro-mechanical behaviour of fractured Callovo-Oxfordian argillite around the excavations where nuclear waste is stored. This finite element code will be used to undertake the

following analyses:

(1) Analysis of the COx mechanical behaviour during uniaxial and triaxial compression tests.

(2) Analysis of moisture movement inside COx and consequent deformation under free and restrained conditions.

(3) Analysis of self-sealing during resaturation of fractured COx.

(4) Analysis of self-sealing of the excavated damage zone under changes of hydration level.

(5) Analysis of the hydro-mechanical behaviour of other claystones similar to COx.

1.7 Thesis layout

Chapter 1 introduces the main challenges associated to the disposal of nuclear waste. The chapter describes the modern classification of nuclear waste and reviews possible disposal methods while highlighting the advantages of deep geological storage in terms of feasibility and safety. The different phases of the disposal process are discussed and the hydro-mechanical behaviour of the fractured zone around storage galleries is summarised. The main challenges and objectives of the thesis are also outlined.

Chapter 2 discusses the main hydro-mechanical properties of Callovo-Oxfordian (COx) argillite, including mineralogical compositions, porosity, saturation, water content, density and permeability. The material parameters and models for performing the numerical simulation presented in the thesis are summarised. The characteristics of the fractured zone around galleries parallel to the major and minor horizontal principal stress directions, respectively, are also discussed.

Chapter 3 introduces the finite element software Cast3M together with a discussion of the identification of material parameters for simulating uniaxial/triaxial compression tests.

Chapter 4 presents the numerical simulations of COx swelling/shrinkage during the cyclic variation of degree of saturation by incorporating an extra deformation model to match experimental data.

Chapter 5 analyses the self-sealing of fractured COx, at the scale of both small samples and CDZ, by taking into account the effects of fractures on permeability.

Chapter 6 presents conclusions and perspectives of this project.

Chapter 2

Hydromechanical characteristics of Callovo-Oxfordian argillite

2.1 Properties of Callovo-Oxfordian (COx) argillite

2.1.1 Mineral composition

The Callovo-Oxfordian (COx) argillite is mainly composed of clays, carbonates, quartz and feldspars, with some minor amounts of accessory minerals. The clays content increases while the carbonates content decreases with depth, which is due to changes in the sea level during the deposition of the sedimentary layer. The thickness of the Callovo-Oxfordian deposit is around 130m with a depth from the ground surface between 420m and 550m.

The microscale minerals distribution of a Callovo-Oxfordian claystone sample is shown in Figure 2.1 while the vertical sequence of the entire sedimentary layer is shown in Figure 2.2. The layer is divided into three units, listed in order from bottom to top as UA, UT and USC.

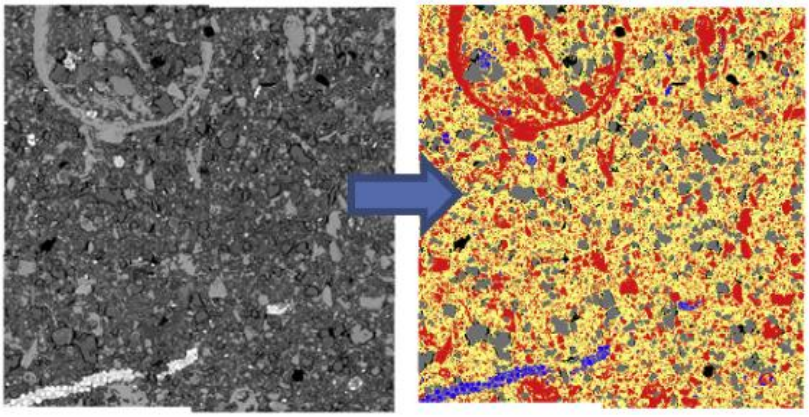

Figure 2.1. Minerals distribution in microscale (yellow represents clay) (Armand et al., 2017)

(1) Clay unit (**UA**): around 90m in thickness, i.e. approximately two-thirds of the entire layer. The mineral content of this unit is relatively stable with a clay content between 40%-60% at the depth of the Muse/Haute Marne underground laboratory (depth 490m). Clay minerals consist of illites, ordered illite/smectite, mixed-layer minerals, kaolinite, iron-rich chlorite and little biotite.

(2) Transition unit (**UT**): 10-20m in thickness. The unit is located at the interface between the silty carbonate-rich unit (USC) and the clay unit (UA). In terms of mineralogy, the

UT has the highest carbonate content, i.e. around 40-90%.

(3) Silty carbonate-rich unit (**USC**): 20-30m in thickness. In this unit, the vertical variation of petrophysical parameters is large due to lithological changes (mudstone and carbonate siltstone). The mineral composition is more diverse and heterogeneous than in other units and progressive carbonate enrichment marks the beginning of the Upper Oxford Carbonate platform.

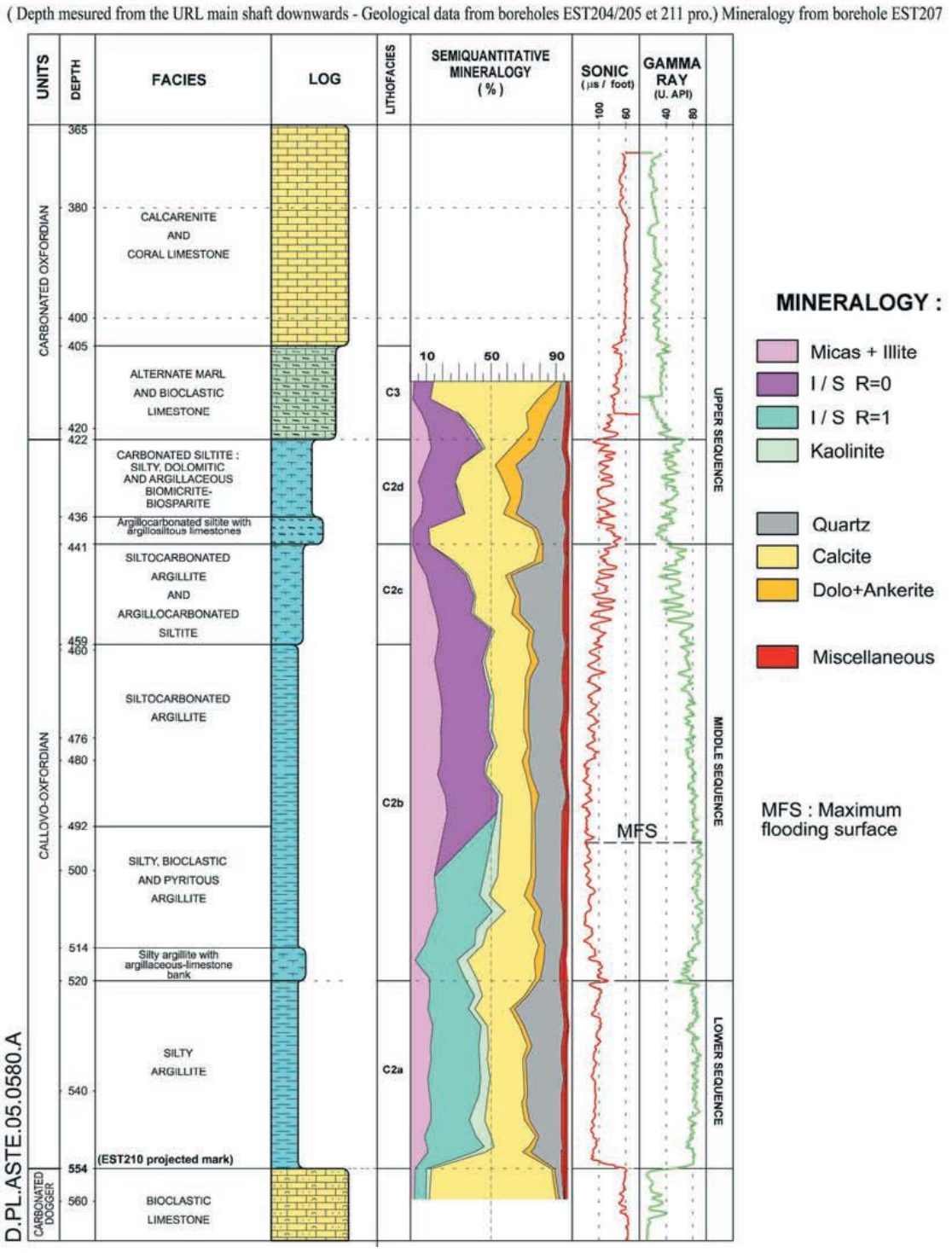

Figure 2.2. Geological units and stratigraphic sequence of the COx formation (Yven et al., 2015)

2.1.2 Porosity φ

Porosity, φ is defined as the ratio between the volume of the voids inside the material, V_v and the total volume of material, V:

$$\varphi = \frac{V_v}{V} \tag{2.1}$$

The porosity of the Callovo-Oxfordian argillite at the position of the Meuse/Haute-Marne underground laboratory is around 18% while the porosity of the entire Callovo-Oxfordian argillite layer is estimated to vary in the range of 14%-20% (Armand et al., 2017). The Callovo-Oxfordian claystone is made of a main matrix, whose clay content ranges from 40% to 60%, with inclusions of carbonate and tectosilicate grains. These inclusions, whose size varies with a range of 0.1-100μm do not have pores and exhibit higher strength in comparison with the clay matrix.

Hellmuth and Siitari (1990) developed the autoradiography technique to study the porosity of heterogeneous granite rocks. This technology provides a spatial distribution of porosity by impregnating the sample with an activated resin doped with carbon 14. The same techniques was subsequently employed to study the porosity of also sedimentary rocks (Sammartino et al., 2002). In particular, the autoradiography of Callovo-Oxfordian claystone samplesd (Figure 2.3) indicates that almost all voids reside within the clay matrix with a strong correlation between clay content and porosity.

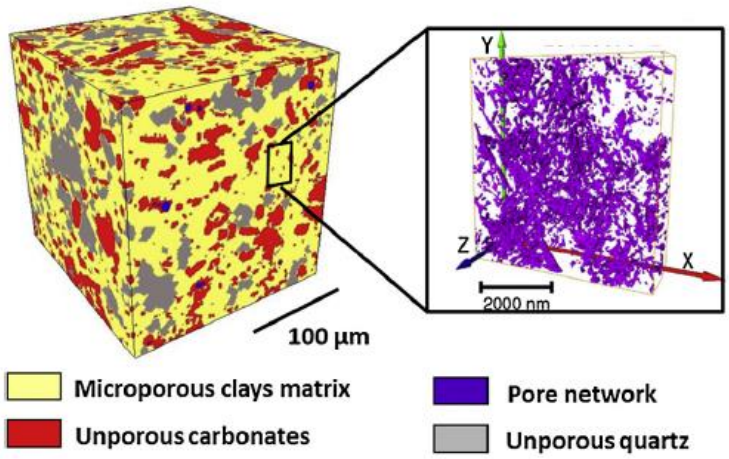

Figure 2.3. Porosity of a Callovo-Oxfordian claystone sample (Armand et al., 2017)

Other imaging techniques, such as electron microscopy (either alone or in combination with a focused ion beam system) and X-ray micro-tomography, have been used to determine the spatial distribution of pores and mineral content of Callovo-Oxfordian claystone. A 3D reconstruction of the pore network shows that if the pore is larger than 40 nm its connectivity is low. This is also consistent with the pore size distribution curve obtained by Mercury Intrusion Porosimetry (MIP), which has shown that the pore network is mainly composed of meso/micro pores with a well-defined peak at about 10-30 nm (Figure 2.4).

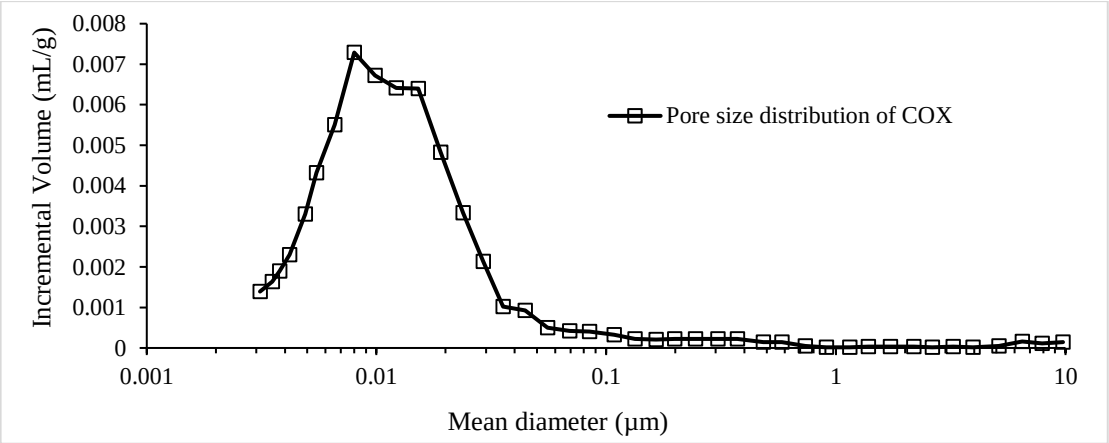

Figure 2.4. Pore size distribution of a Callovo-Oxfordian claystone sample (Armand et al., 2017)

2.1.3 Density

The grain density ρ_s, bulk density ρ_b and dry density ρ_d of Callovo-Oxfordian argillite were measured by Andra (2005). These three quantities are defined as:

$$\rho_s = \frac{M_s}{V_s} \tag{2.2}$$

$$\rho_b = \frac{M}{V} = \frac{M_s + M_w}{V} \tag{2.3}$$

where M_s, V_s, M, V and M_w are the mass of solids, the volume of solids, the bulk mass, the bulk volume and the mass of water, respectively. Characteristic data of samples from the Callovo-Oxfordian argillite at the MHM-URL is listed in Table 2.1.

Table 2.1. Characteristic data of samples from the Callovo-Oxfordian argillite at the MHM-URL Bure (Andra, 2005)

Specimen	*Diameter (mm)*	*Length (mm)*	*Depth (m)*	*Grain density (g/cm^3)*	*Dry density (g/cm^3)*	*Bulk density (g/cm^3)*	*Water content (%)*	*Porosity (%)*
EST05481-01-II	100	200	434.5-434.8	2.70	2.30	2.41	4.99	15.0
EST05547-07-II	40	80	454.3-454.7	2.70	2.22	2.39	7.1	17.8
EST05582-02-II	45	90	463.1-463.4	2.70	2.21	2.40	8.73	18.2
EST05630-02-=	45	90	474.-474-3	2.70	2.18	2.38	8.93	19.2
EST05671-01-II	100	180	484.-487.3	2.70	2.27	2.44	7.38	15.8

2.1.4 Water retention

The natural water content of the Callovo-Oxfordian claystone ranges from 5% to 8% (Figure 2.5). Desaturation and resaturation processes of Callovo-Oxfordian claystone are influenced by a number of factors and, among them, the most important ones are pore size and capillary suction. At the mesoscopic scale, pore water suction will produce an overall confining effect which is related to the microstructure of the rock and can make the claystone shrink or swell during desaturation or resaturation. This is caused by a modification of the distance between clay platelets that also influences the mechanical properties of clay aggregates.

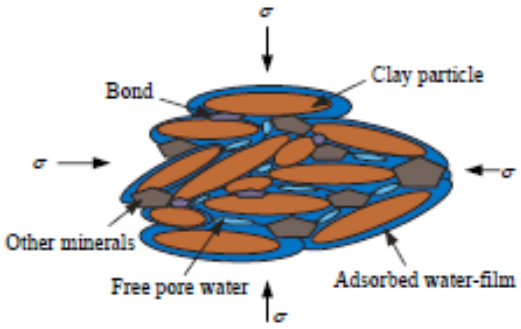

Figure 2.5. A schematic of water distribution inside Callovo-Oxfordian claystone (Zhang, 2007)

Figure 2.6 shows the results of a desaturation and saturation cycle performed on a Callovo-Oxfordian claystone sample taken from the UA unit (Andra, 2005).

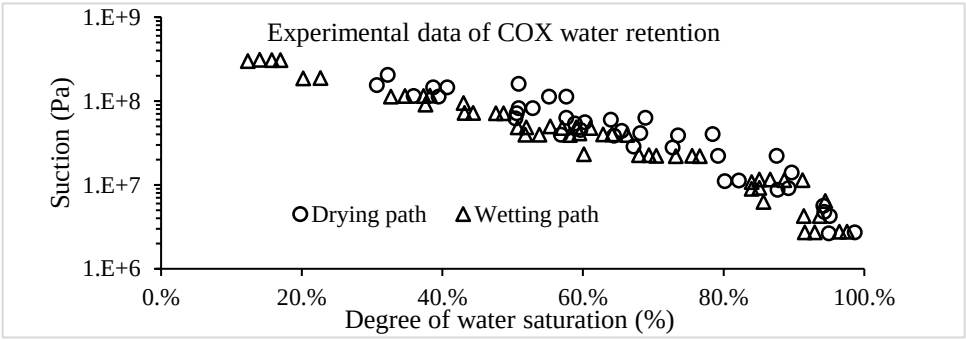

Figure 2.6. Water retention test results on UA sample (Armand et al., 2017)

After examination of experimental data from Zhang *et al.* (2010), Armand *et al.* (2017) and Andra (2005), the Van Ganuchten (1980) model (Figure 2.7) was used to describe the retention behaviour of the COx claystone as:

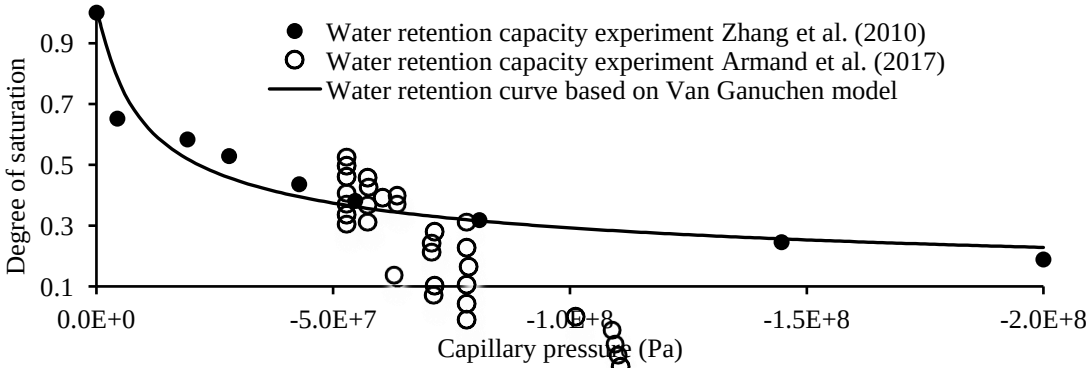

Figure 2.7. Van Ganuchten (1980) water retention curve for COx claystone based on experiments by Zhang et al. (2010) and Armand et al. (2017)

$$S_r = \frac{1}{\left[1+(\alpha P_c)^{\frac{1}{1-m}}\right]^m} \tag{2.4}$$

where S_r and P_c are the saturation degree and capillary pressure (i.e. suction), respectively, while $\alpha = 2.6 \times 10^{-8}$ and $m = 0.45$ (see Table 2.2) are model parameters.

Table 2.2. COx claystone parameters for Van Ganuchten (1980) model

α	m
2.6×10^{-8}	0.45

2.1.5 Young modulus *E*

Mineral composition influences all mechanical parameters of claystone rocks and this certainly also applies to the Callovo-Oxfordian claystone. Therefore, the variation of mineral composition with the depth leads to a corresponding variation of Young Modulus. In the Callovo-Oxfordian argillite layer, the Young modulus decreases following the clay content increase from top to bottom in the USC, UT and UA units.

Consistent with previous investigations, the strains of the COx claystone are linked to the Biot's stress by means of a linear elastic law, with values of the Young modulus that depend on the relative humidity at equilibrium. Following the experimental work of Zhang *et al.* (2013), the ratio between the unsaturated and saturated Young moduli, $\frac{E}{E_{\_saturated}}$ is a function of the relative humidity, RH as shown in Figure 2.8. In particular, interpolation of experimental data in Figure 2.8 suggests the following form of variation:

$$\frac{E}{E_{\_saturated}} = -1.09\, RH + 2.04 \tag{2.5}$$

Furthermore, Kelvin Equation provides a link between capillary pressure and relative humidity at a given temperature, so that the ratio between the unsaturated and saturated Young moduli, $\frac{E}{E_{\_saturated}}$, can also be expressed as a function of capillary pressure (Figure 2.9).

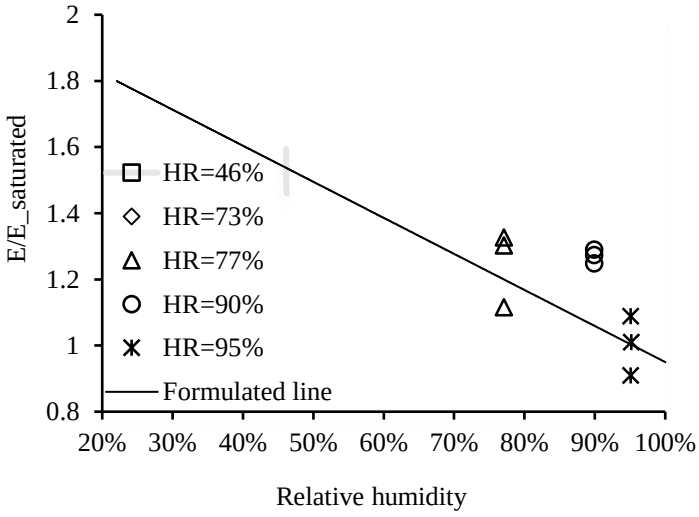

Figure 2.8. Variation of COx Young's modulus with relative humidity (Zhang et al., 2013)

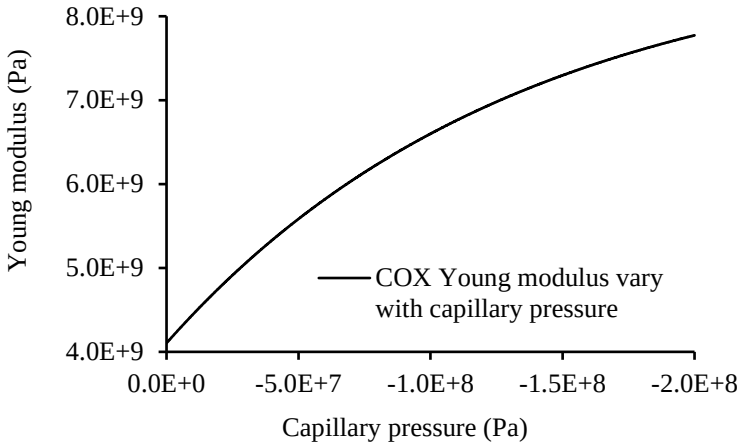

Figure 2.9. Variation of COx Young's modulus with capillary pressure

According to the Kelvin equation and equation (2.5), the relation between the Young modulus of COx and capillary pressure is shown as following, which is used in numerical simulation for describing Young modulus changing with water content of COx.

$$\mathrm{E} = \left(-1.09 \times e^{\frac{W_w P_c}{RT\rho_w}} + 2.04\right) E_{\_saturated} \tag{2.6}$$

where W_w, R, T, ρ_w are Molar mass of water, the universal gas constant, temperature and water density, respectively. Their values are listed in Table 3.1 for the parameters of numerical simulation.

2.1.6 Tensile strength σ_t

Tensile strength, σ_t is an important parameter for predicting the development of damage and plastic strains inside the COx claystone. Figure 2.10 shows the variation of tensile strength with capillary pressure as inferred from experiments (Volckaert et al., 2004; Fouche et al., 2004) that recorded the variation of the material tensile strength with changing water content.

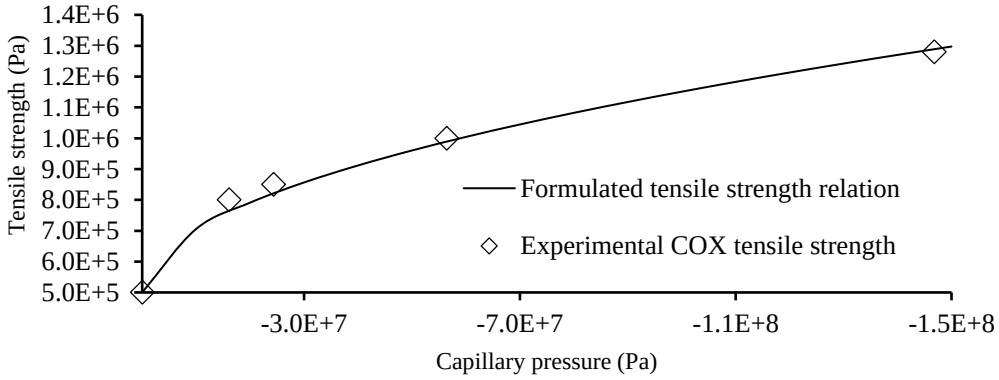

Figure 2.10. Variation of COx tensile strength with capillary pressure (Volckaert et al., 2004; Fouche et al., 2004)

The interpolating line in Figure 2.10 corresponds to the following equation where σ_{t0} is a reference tensile strength equal to $5.\times 10^5 Pa$ while P_t is a reference capillary pressure equal to $-5.9 \times 10^7 Pa$ and their values are listed in Table 3.1 as parameters for numerical simulation:

$$\sigma_t = \sigma_{t0}(1 + \sqrt{\frac{P_c}{P_t}}) \tag{2.7}$$

2.1.7 Fracture energy G_f

The fracture energy G_f is another important parameter that governs the softening of the material . According to the experiment from ANDRA (Abulmajid, 2019), the data has been here used to infer the relationship of Figure 2.11 fracture energy G_f and capillary pressure P_c in the COx claystone, which is described by the following equation:

$$G_f = G_{f0}(1 + \frac{P_c}{P_{gf}}) \tag{2.8}$$

where G_{f0}= 6.4N/m, parameter $P_{gf} = -4.8 \times 10^7 Pa$.

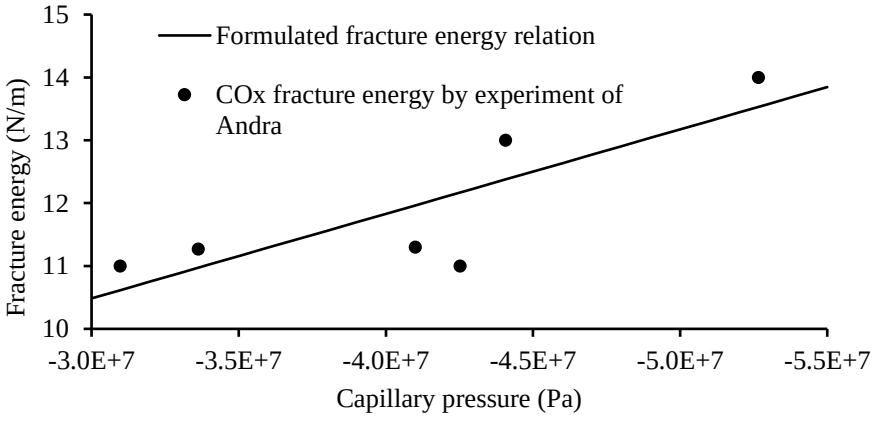

Figure 2.11. Variation of COx fracture energy with capillary pressure

2.1.8 Swelling behavior

The COx swelling capacity guarantees the fractured zone recovering to its impermeability and stop nuclear waste potentially leaking through the fractured zone. Takano et al. (2010) indicated that the COx swelling during a resaturation process is close to an order of 3% in several hours. In unconfined condition, the COx resaturation swelling in volume can reach a maximum of 10%. Zhang (2013) measured the relation between COx saturation (capillary pressure) and normal strain (%) as shown follows:

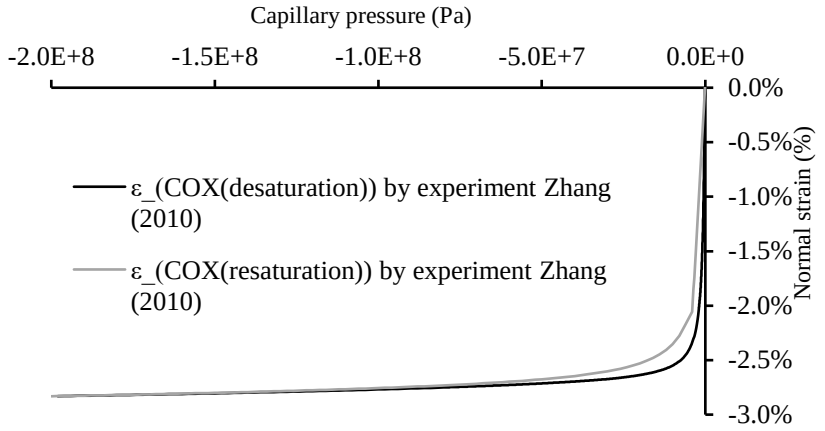

Figure 2.12. Comparison of free swelling/shrinkage deformations measured during experiments

Of course, under geological condition, COx confining stress is still active and impeach the swelling to act as in unconfined conditions. Near opened cracks, the normal stress tends to zero and the swelling is free.

The Biot model can reproduce the stress strain relationship during saturation change and is frequently used for hydro-mechanical analysis of soils. Callovo-Oxfordian argillite is a claystone and its hydro-mechanical properties are similar with that of soil and rock at the same time. The use of the Biot model to analyse the swelling of COx during saturation change produces a deformation curve as follows:

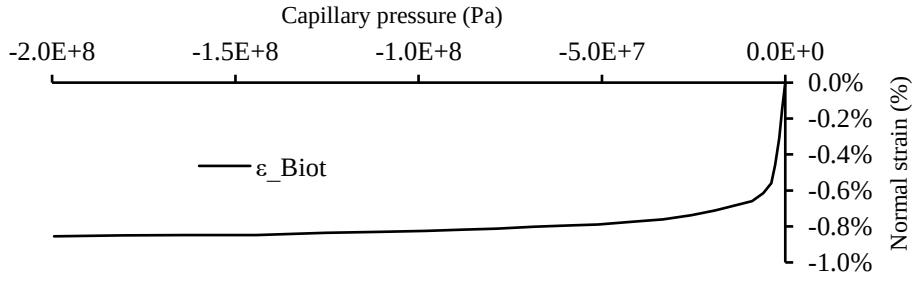

Figure 2.13. Free swelling/shrinkage deformations calculated by the standard Biot model

The maximum value of swelling deformation obtained is below 1% as the experiments which is about 3 times smaller than the test observation. Therefore, the variation of capillary pressure and the elasticity of the skeleton can only reproduce a part of the swelling and other phenomena may be taken into account via an added deformation model that will be introduced in this thesis.

2.2 Underground structure behavior

An extensive program of experimental studies were planned by Andra and their collaborators to characterize the response of the host rock to different shafts and galleries excavation/construction methods. The study of the formation and evolution of the fractured zone around the structures is a main part of the program. In order to have an understanding of the thermal-hydro-mechanical

properties of the surrounding rock of underground galleries, galleries adapting to different research requirements have been constructed. For example, the constructions of galleries which are parallel to major/minor geological stresses, the impacts of the galleries size, the impacts of galleries excavation way, saturation change of surrounding rock, the galleries built were to satisfy the needs of various studies are shown as Figure 2.14.

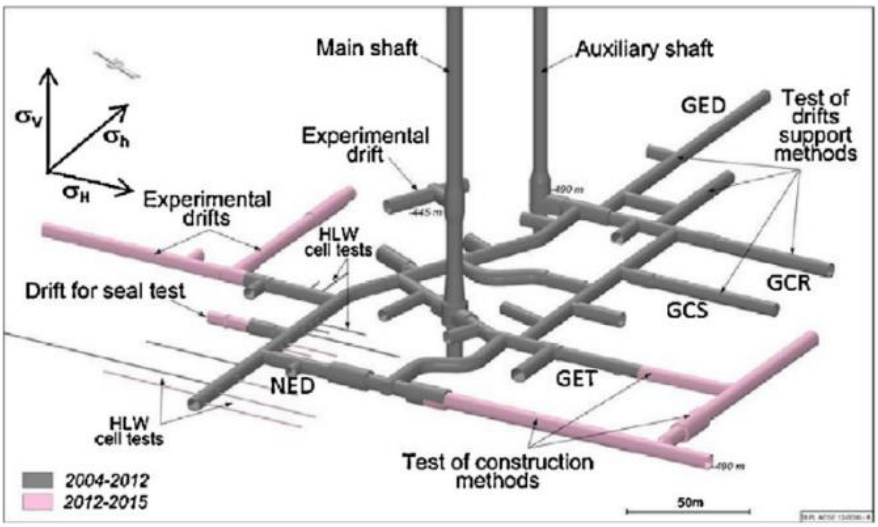

Figure 2.14. Constructing galleries (Armand et al., 2017)

A complete description of the galleries at Muse/Haute Marne underground laboratory can be found in Armand et al., (2014). Geological stress field is the main factor exhibiting significant impacts on Excavation Damage Zone in the vicinity of excavated openings.

Figure 2.15. Excavation and support of galleries (Armand et al., 2013): (a) GCS with compressible concrete wedge, (b) GCR with concrete lining grouted in place, (c) BPE with 0.45 m of shotcrete projected in four layers, (d) GED gallery with classical support, shotcrete and sliding steel arches.

The geological stress field is orthotropic with a vertical stress σ_v which depends on the depth of the host rock layer and two different horizontal stresses (major σ_H and minor σ_h), and their values are σ_v of 12.7MPa, σ_H of 16.1MPa and σ_h of 12.4MPa. A schematic diagram of underground galleries excavation is shown as follow in Figure 2.15, and the following part will introduce three galleries as examples and display fractures and permeability (Armand et al., 2014).

2.2.1 Galleries parallel to σ_H

(1) Gallery GCS

Gallery GCS was excavated in the wall of gallery GLS but keeps a distance of 30m with gallery GAT, and was shown in Figure 2.16.

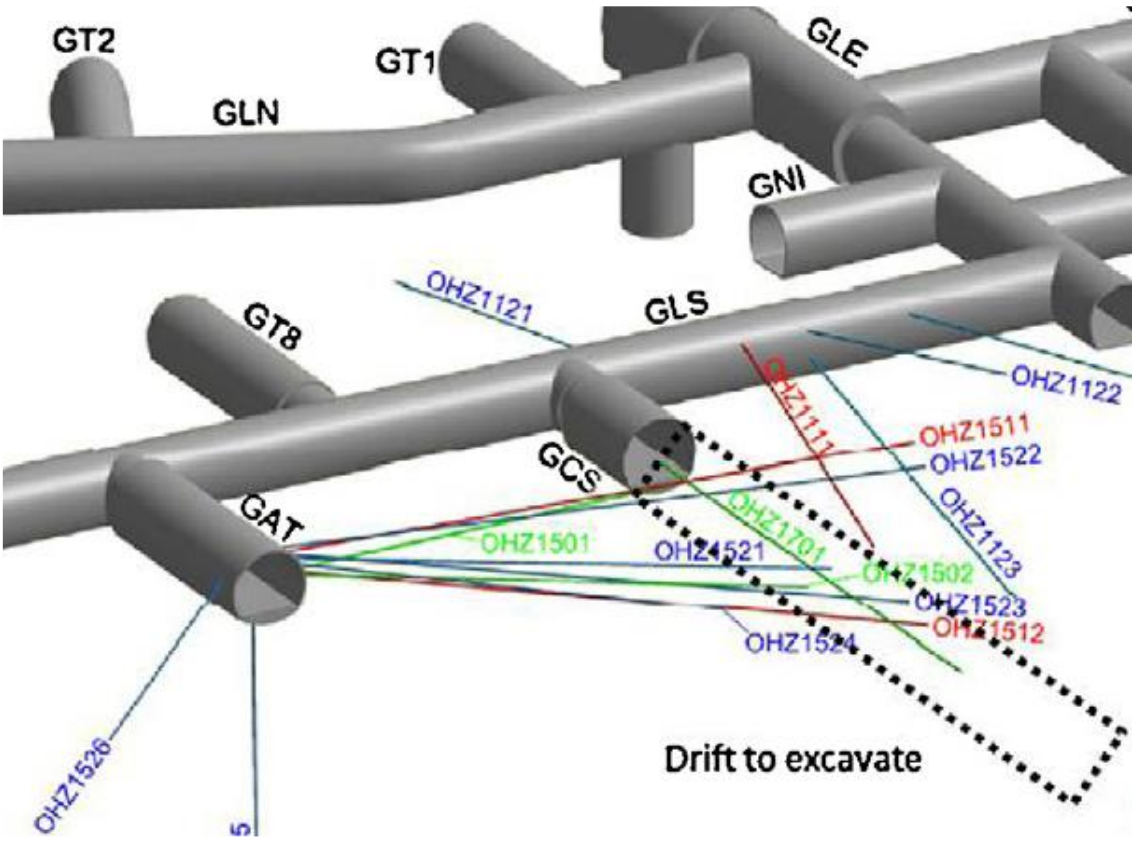

Figure 2.16. Gallery GCS (Armand et al., 2013)

GCS gallery has a circular cross-section with a radius of 2.6 m. Excavation work was performed using a road header, this method can accomplish an average over-excavation is less than 0.1m at the ceiling and sidewalls of gallery, but this value can be more than 0.4m at its floor (Bonnet et al., 2011). 15 instrumented holes with a length of 30-50m were drilled in the surrounding galleries GAT and GLS. The pore pressure were measured in nine holes drilled, from the gallery GCS walls to a depth range up to 50m. Three inclinometers and three extensometers were set up to measure displacements in the vertical direction and axial/radial displacements on the horizontal plane. Some other additional measurements have been carried out during excavation: (1) At every

5 meters, geological survey of gallery sidewalls and of the face were carried out. (2) Special supports have been cast in the shotcrete in order to measure the stresses and deformation in the lining.

The core samples extracted from the boreholes were studied to characterize the fractures of the fractured zone: (1) tracking of resin-filled fractures was performed to localize tensile fractures. (2) S-wave and P-wave velocities' evolution were displayed using microseismic logging method according to the distance from the gallery wall. (3) in view of hydraulic and gas tests, permeability tests were performed in eight boreholes in order to describe the permeability change of the fractured zone with time and saturation of the Callovo-Oxfordian argillite.

(2) Gallery GCR

The GCR gallery (Figure 2.17) has a circular section with a radius of 2.7m, and it is parallel to GCS gallery. The GCR gallery excavation is similar to GCS gallery, but the compressive concrete wedges were cancelled in its the last part.

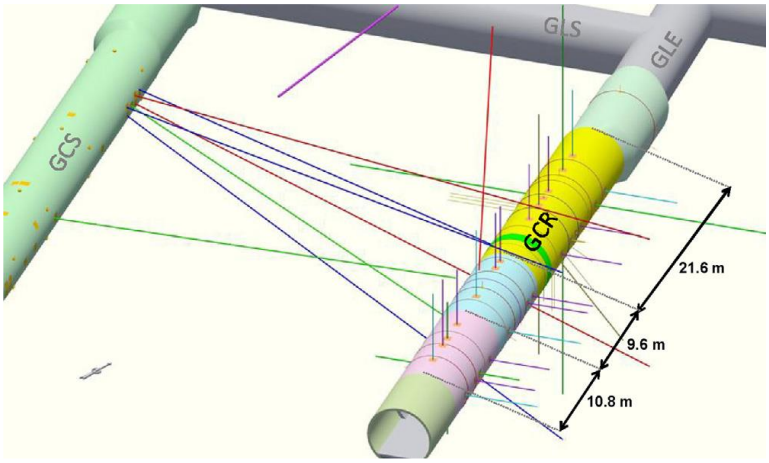

Figure 2.17. Gallery GCR (Armand et al., 2013)

The measurement system install at GCR gallery is like that of GCS. Additional boreholes with length of 40-50m were drilled from the gallery GCS. To characterize the fractured zone, five boreholes were drilled for micro-seismic logging measurement, and multi-packer systems were installed in six boreholes to characterize and follow the fractured zone evolution in time. Strain gages, total pressure cells and flat jacks were installed on the shotcrete and grouted lining, in a way to follow the behaviour of the three different concrete supports. Multi-packer systems were installed in six boreholes characterize and track the evolution of the fractured zone. Strain gauges, total pressure sensors and flat jacks were mounted on sprayed concrete and grout lining to test the performance of the three different concrete supports.

(3) The fractured zone

Resin injection was applied to explore the fractured zone, accordingly to the method developed

by Möri and Bossart (1999).

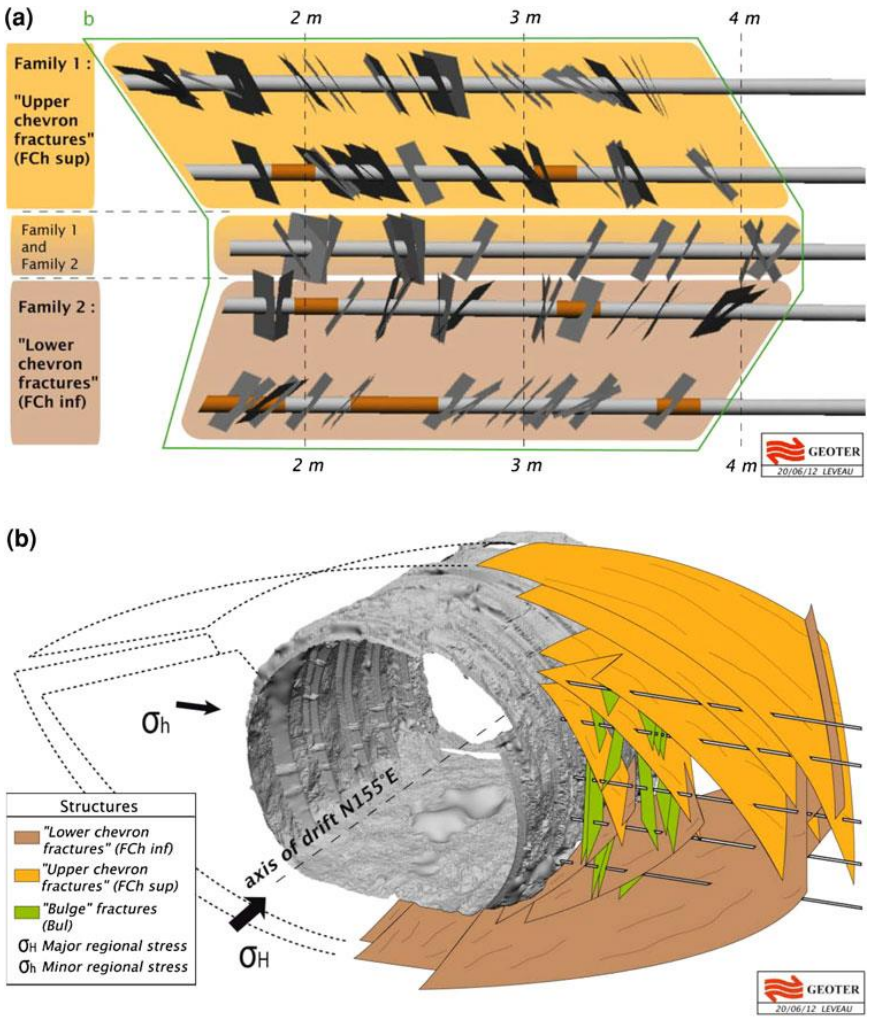

Figure 2.18. The fractured zone of gallery parallel to σ_H (Armand et al., 2014)

Galleries GCS and GCR are parallel to the major horizontal stress σ_H, their the fractured zone is mainly located at the wall direction of galleries, in the ceiling and floor direction the fractured zone is not fully developed, the fractured zone distribution is schematically shown in Figure 2.18. The fractured zone is divided into upper chevron fractures and lower chevron fractures. In upper part, fractures are more developed than the lower part. Therefore, when gallery is parallel to the major horizontal geological stress, the main study of the fractured zone should focus on gallery wall side.

(4) Fracture

According Armand et al., (2014), fractures inside the fractured zone can be categorized as (a) zone and (b) zone, as shown in Figure 2.19. Zone (a) is made up of tensile fractures and shear fractures with heterogeneous orientation while zone (b) is mainly composed of shear fractures with homogeneous orientation.

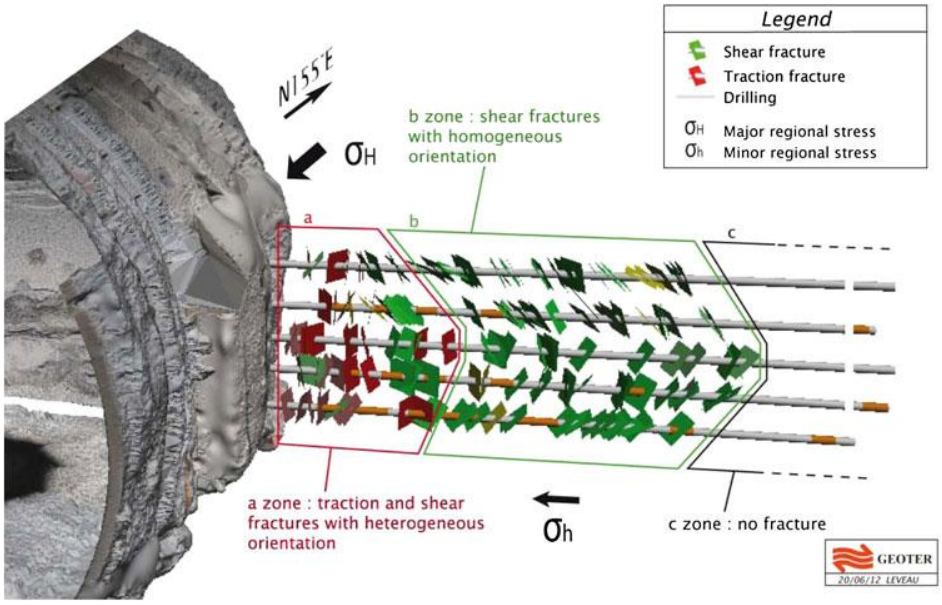

Figure 2.19. Fractures distribution of the fractured zone (Armand et al., 2014)

The average depth of zone (a) from wall surface is 0.57m while the maximum value reaches 1.94m. This area provides the main transfer pathway for water. Zone (b) is next to zone (a) and its average and maximum depth are of 2.5m and 4.3m, respectively.

Figure 2.20 illustrates three kind of fractures density in depth from the wall, including traction fractures density, shear fractures density and all fractures density which is a sum of traction and shear fractures.

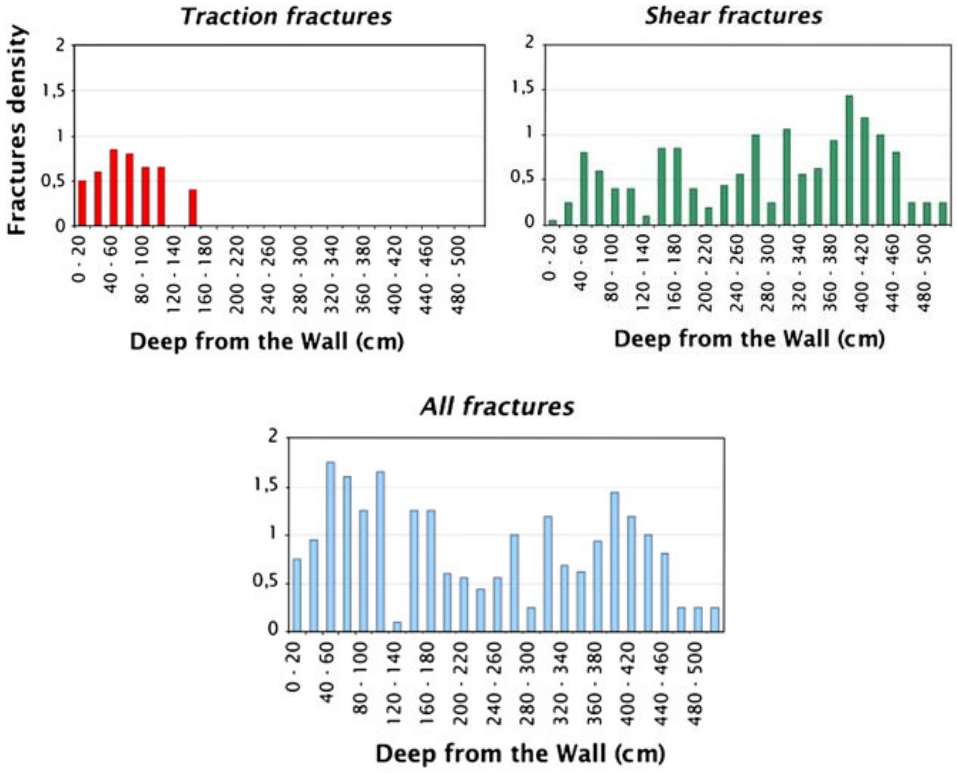

Figure 2.20. Fractures density with the depth of gallery sidewall (Armand et al., 2014)

(5) Permeability

Inside the fractured zone, the main water transfer pathway is led by tensile fractures. The hydraulic definition of the fractured zone is the zone that its hydraulic conductivity is greater than $10^{-10}m/s$. For gallery GCS, which is parallel to the major horizontal stress σ_H, it can be found that the hydraulic conductivity tested from vertical borehole is always lower than $10^{-10}m/s$ at ceiling and floor t. Hydraulic conductivity tested from horizontal boreholes at gallery wall directions is varying from $10^{-8}m/s$ to $10^{-13}m/s$ from the wall surface to a depth of 6m (Figure 2.21), and if the depth is lower than 2m, the hydraulic conductivity is greater than $10^{-10}m/s$.

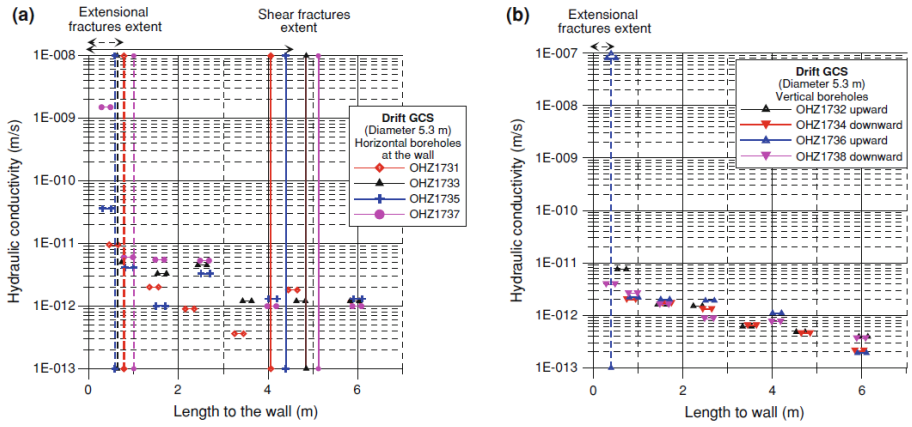

Figure 2.21. Permeability with the depth of gallery GCS sidewall (Armand et al., 2014)

2.2.2 Gallery parallel σ_h

(1) GED

The GED gallery (Figure 2.22) is perpendicular with the galleries GCS and GCR and, parallel to the minor horizontal geological stress σ_h. The stress state at the cross-section of the gallery is anisotropic (around 12MPa in horizontal direction and 16MPa in the vertical direction). The section of the GED gallery is circular with a radius of 2.3m, the supports are bolts, sliding arches and a layer of 10cm of fiber shotcrete.

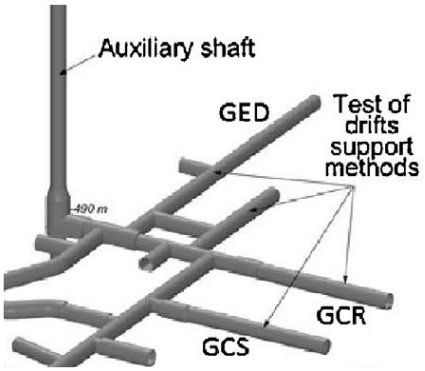

Figure 2.22. Gallery GED and its location with galleries GCS/GCR (Armand et al., 2017)

Convergences of the gallery were measured in six sections, and extensometers were emplaced in 2 sections and, one during excavation and one after excavation. Numerous boreholes were drilled for studying the permeability, the saturation and the fracturation of the fractured zone.

(2) The fractured zone

A schematic view of the fracturation of the fractured zone is displayed in Figure 2.23 for a gallery parallel to the minor stress. the fractured zone located at the wall of gallery is far less than that located at floor and ceiling, its distributions at floor and ceiling are symmetric. the fractured zone at the wall of gallery limits within 0.1 time diameter of gallery, at ceiling and floor the extension of the fractured zone limits within 0.6 time diameter.

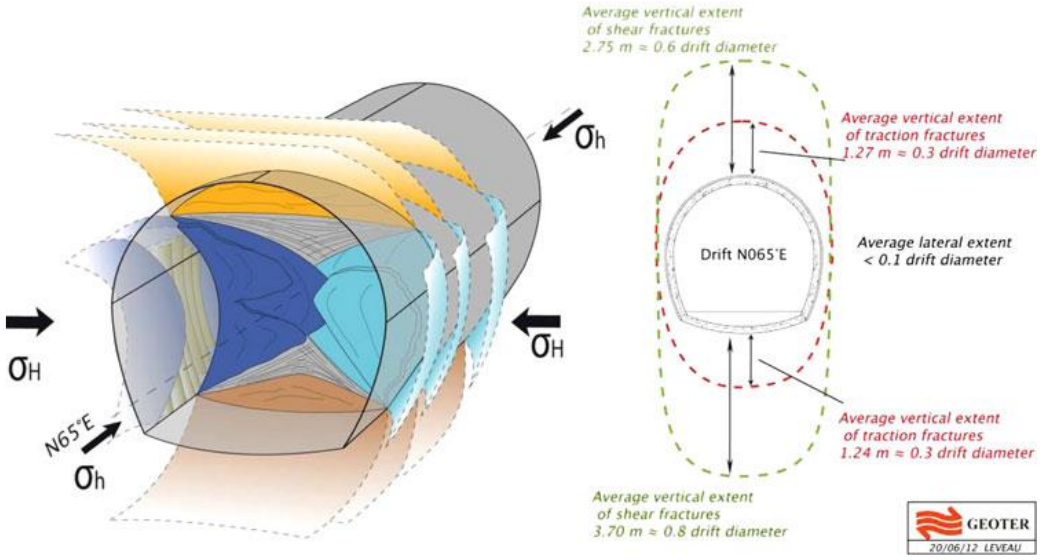

Figure 2.23. Fractures distribution of the fractured zone of gallery GED (Armand et al., 2014)

(3) Fracture

Similarly, for gallery parallel to the minor horizontal stress, fractures of the fractured zone are also a mix of tensile fractures and shear fractures. The average and maximum extension of tensile fractures is 0.1 time diameter of the gallery and 0.3 time diameter of the gallery respectively. Shear fracture area is larger than tensile fracture area, its average extension is about 0.1 time the diameter and the maximum extension reaches 0.8 time the diameter.

(4) Permeability

Similarly, for the fractured zone of the gallery GED, the main water transfer pathway is also led by tensile fractures. Therefore, its permeability evolution is correlated with tensile fractures evolution. Conversely, the main the fractured zone for gallery GED is located at the floor and ceiling, and differs from galleries GCS/GCR.

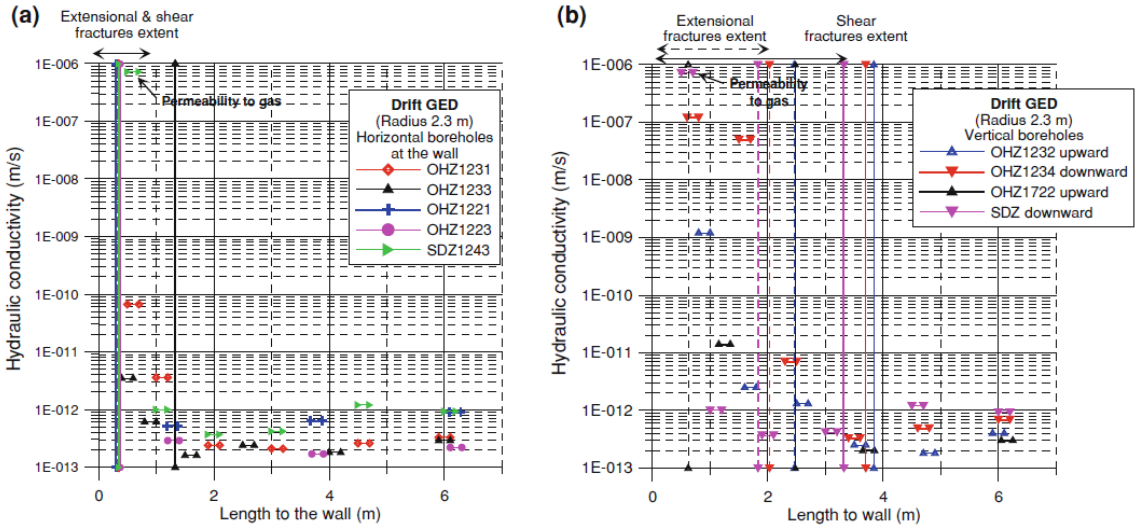

Figure 2.24. Permeability with the depth of gallery GED sidewall (Armand et al., 2014)

According to its hydraulic definition, the fractured zone is the zone where the hydraulic conductivity is greater than $10^{-10}m/s$. For gallery GED parallel to the minor horizontal stress σ_h, it can be found that the hydraulic conductivity is always less than $10^{-10}m/s$ at sidewalk direction which was tested from horizontal boreholes. Hydraulic conductivity tested from vertical boreholes at gallery floor and ceiling directions varying from $10^{-8}m/s$ to $10^{-13}m/s$ from the surface of gallery to a depth of 6m (Figure 2.24), and if the depth is within 2m, its hydraulic conductivity is greater than $10^{-10}m/s$.

2.3 Mechanical constitutive model

Plastic deformation

According to the Biot theory, the equilibrium Equation (2.9) is written in terms of the Biot's stress, $\boldsymbol{\sigma} = \boldsymbol{\sigma_e} + BS_rP_c\boldsymbol{I}$, which is the sum of the skeleton stress $\boldsymbol{\sigma_e}$ and the capillary stress $BS_rP_c\boldsymbol{I}$, where S_r is the saturation degree, P_c is the capillary pressure and B is the Biot coefficient (the Biot coefficient B here is assumed equal to 0.85 according to Armand et al. (2007)).

$$\boldsymbol{div}(\boldsymbol{\sigma}) + \mathbf{f} = \mathbf{0} \tag{2.9}$$

where $\boldsymbol{f}$ represents the body force.

The following flow function $F(\overline{\boldsymbol{\sigma}})$ is introduced to define the plastic surface, where $B1$, $C1$ and $R0$ are three material parameters with $B1$ and $C1$ being determined according to the Nadai plastic criterion, $R0$ being the maximum tensile stress σ_t and $R = MP \cdot \boldsymbol{\varepsilon^p}$ being hardening, the plastic strain slope MP is equal to 0.5 times the Young Modulus E and $\boldsymbol{\varepsilon^p}$ is the plastic strain which is derived from the plastic flow equation with respect to Nadai criterion expressed with the effective stress:

$$F(\bar{\boldsymbol{\sigma}})=\frac{(\bar{\sigma}_v+B1*\mathrm{Tr}\,\bar{\sigma})}{C1}-(R0+R) \tag{2.10}$$

$$\bar{\sigma}_v=\sqrt{\frac{\left(\bar{\sigma}_x-\bar{\sigma}_y\right)^2+(\bar{\sigma}_x-\bar{\sigma}_z)^2+\left(\bar{\sigma}_z-\bar{\sigma}_y\right)^2+6\left(\bar{\sigma}_{xy}^2+\bar{\sigma}_{yz}^2+\bar{\sigma}_{zx}^2\right)}{2}} \tag{2.11}$$

$$\mathrm{Tr}\bar{\sigma}=\bar{\sigma}_x+\bar{\sigma}_y+\bar{\sigma}_z \tag{2.12}$$

Note that $\bar{\sigma}_v$ is the Von Mises equivalent stress while $B1$ and $C1$ depend on the values of $\mathrm{Tr}\,\bar{\sigma}$. In particular, when $\mathrm{Tr}\,\bar{\sigma}>-4\times(R0+R)$, then $B1$=1 and $C1$=2, else $B1$=0.25 and $C1$=3.

The equations of the strain slopes were formulated in equations (2.13) and (2.14), then deformations were obtained by means of equation (2.15):

$$\dot{\varepsilon_x}=-MP-\frac{dF}{d\bar{\sigma}_x}\left(\frac{dF}{d\bar{\sigma}_x}\frac{E}{1+\mu}+Tr\frac{dF(\bar{\boldsymbol{\sigma}})}{d\bar{\boldsymbol{\sigma}}}\frac{E\mu}{(1+\mu)(1+2\mu)}\right) \tag{2.13}$$

$$\dot{\varepsilon_{xy}}=-MP-2\frac{E}{1+\mu}\left(\frac{dF}{d\bar{\sigma}_{xy}}\right)^2 \tag{2.14}$$

$$d\boldsymbol{\varepsilon}=-F(0)/\dot{\varepsilon} \tag{2.15}$$

The expressions of $\frac{dF}{d\,\bar{\sigma}_x}$, $\frac{dF}{d\bar{\sigma}_{xy}}$ and, $Tr\frac{dF(\bar{\boldsymbol{\sigma}})}{d\bar{\boldsymbol{\sigma}}}$ are provided below (the expressions of $\frac{dF}{d\,\bar{\sigma}_y}$, $\frac{dF}{d\,\bar{\sigma}_z}$, $\frac{dF}{d\bar{\sigma}_{yz}}$, $\frac{dF}{d\bar{\sigma}_{zx}}$ would be similar):

$$\frac{dF}{d\,\bar{\sigma}_x}=\frac{2\,\bar{\sigma}_x-\bar{\sigma}_y-\bar{\sigma}_z}{2C\bar{\sigma}_v}+B1/C1 \tag{2.16}$$

$$\frac{dF}{d\bar{\sigma}_{xy}}=3\bar{\sigma}_{xy}/2C1\bar{\sigma}_v \tag{2.17}$$

$$Tr\frac{dF(\bar{\boldsymbol{\sigma}})}{d\bar{\boldsymbol{\sigma}}}=\frac{dF}{d\,\bar{\sigma}_x}+\frac{dF}{d\,\bar{\sigma}_y}+\frac{dF}{d\,\bar{\sigma}_z} \tag{2.18}$$

equations (2.19) and (2.20) display the plastic parts of strains in the normal and shear directions.

$$d\varepsilon_x^p=\,d\varepsilon_x\frac{dF}{d\,\bar{\sigma}_x}\,C1 \tag{2.19}$$

$$d\varepsilon_{xy}^p=\,2*d\varepsilon_{xy}\frac{dF}{d\bar{\sigma}_{xy}}\,C1 \tag{2.20}$$

According to Hooke's law and using $\boldsymbol{\varepsilon^p}$ calculated from plastic flow equation, the effective stress $\bar{\boldsymbol{\sigma}}_{\boldsymbol{ij}}$ after plastic deformation can be expressed as follows:

$$\bar{\boldsymbol{\sigma}}_{\boldsymbol{ij}}=\lambda\left(\boldsymbol{\varepsilon_{kk}}-\boldsymbol{\varepsilon_{kk}^p}\right)\delta_{ij}+2G\left(\boldsymbol{\varepsilon_{ij}}-\boldsymbol{\varepsilon_{ij}^p}\right) \tag{2.21}$$

where $\lambda=\frac{\upsilon E}{(1+\upsilon)(1+2\upsilon)}$ and $\mathrm{G}=\frac{E}{2(1+\upsilon)}$, ε_{kk} and ε_{ij} are total strains, $\boldsymbol{\varepsilon_{kk}^p}$ and $\boldsymbol{\varepsilon_{ij}^p}$ are plastic strains. When i=j, $\delta_{ij}=1$, else $\delta_{ij}=0$. υ is Poisson ratio.

Damage model

The damage model is based on the continuum mechanics framework developed by Fichant *et al.* (1999) where the effective stress in the damaged material is related to the macroscopic stress. Here the damage model is coupled with a plastic model and equation (2.21) is formulated in terms of elastic strains directly as follows:

$$\bar{\boldsymbol{\sigma}}_{\boldsymbol{ij}} = \lambda \boldsymbol{\varepsilon}^{\boldsymbol{e}}_{\boldsymbol{kk}} \delta_{ij} + 2G \boldsymbol{\varepsilon}^{\boldsymbol{e}}_{\boldsymbol{ij}} \tag{2.22}$$

while the effective stress $\boldsymbol{\sigma}^{\mathbf{e}}_{\boldsymbol{ij}}$ of the damage model is expressed as follows:

$$\boldsymbol{\sigma}^{\mathbf{e}}_{\boldsymbol{ij}} = (1-d)\bar{\boldsymbol{\sigma}}^{+}_{\boldsymbol{ij}} + (1-d^{\alpha 1})\bar{\boldsymbol{\sigma}}^{-}_{\boldsymbol{ij}} \tag{2.23}$$

where $\bar{\boldsymbol{\sigma}}^{+}_{\boldsymbol{ij}}$ is the tensile part of $\bar{\boldsymbol{\sigma}}_{\boldsymbol{ij}}$ and $\bar{\boldsymbol{\sigma}}^{-}_{\boldsymbol{ij}}$ is its compressive part. The symbol d indicates the damage variable (note that, in the isotropic version of the model, d is taken as a scalar) while $\alpha 1 = 15$ (It is a parameter that is identified from compression test and its value can be taken 15 for the COx claystone. It couples tension damage to indirect compression damage). The evolution of the scalar damage variable follows the normality rule according to the following expression:

$$d = 1 - \frac{\varepsilon_{d0}}{\tilde{\varepsilon}} \exp(\beta(\varepsilon_{d0} - \tilde{\varepsilon})) \tag{2.24}$$

where ε_{d0} is the damage threshold and its value is equal to σ_t/E while, β is a hardening/softening variable.

The parameter β commands the slope of the softening curve, and its relation with the fracture energy G_f is given below, where h is the size of mesh element:

$$G_f = h\frac{E*\varepsilon_{d0}}{\beta} \tag{2.25}$$

Finally, the equivalent strain $\tilde{\varepsilon}$ is defined as:

$$\tilde{\varepsilon} = \sqrt{\varepsilon_I^{+\,2} + \varepsilon_{II}^{+\,2} + \varepsilon_{III}^{+\,2}} \tag{2.26}$$

where $\varepsilon_I^{+}, \varepsilon_{II}^{+}\ and\ \varepsilon_{III}^{+}$ are the positive parts of the principal elastic strains. The damage model parameters are summarized in Table 2.3.

Table 2.3. COx claystone parameters for damage model

Young's modulus E	Fracture energy G_f	Tensile strength σ_t
Varying with P_c in Figure 2.8	Varying with P_c in Figure 2.10	Varying with P_c in Figure 2.9

2.4 Permeability

There were several numerical models on permeability evolution during concrete cracking (Choinska et al., 2007; Hammood et al., 2016; Ranaivomanana and Benkemoun., 2017; Benkemoun et al., 2018), and they performed very well at simulating gas diffusion in fractured

concrete due to their innovations of describing the relations among cracks, damage and permeability. However, these models are not able to describe fractures closure of concrete due to damage value of fractured concrete keeps constant with increment of confining pressure, whereas the present model in this thesis couples the permeability with the crack width, which will allow us to account for the crack re-closure due to various phenomena like swelling, but also thermal expansion , and modification of the stress distribution.

Crack estimation

Based on a principle of the model which was developed by Matallah and La Borderie (2009), a practical finite element method has been developed to estimate crack width. This method is proposed in the Finite Element code Cast3M (Procedure OUVFISS) and based on the fracture energy regularization. The crack openings evaluation concerns skeleton solid phase, the total strain of the skeleton phase as follows:

$$\boldsymbol{\varepsilon_{kl}} = {C_{ijkl}^{0}}^{-1}\bar{\boldsymbol{\sigma}}_{\boldsymbol{ij}} \tag{2.27}$$

The skeleton effective strain was obtained as follows:

$$\boldsymbol{\varepsilon_{kl}^{e}} = {C_{ijkl}^{0}}^{-1}\boldsymbol{\sigma_{ij}^{e}} \tag{2.28}$$

The total strain $\boldsymbol{\varepsilon_{kl}}$ in the solid skeleton is decomposed into two parts: an elastic part $\boldsymbol{\varepsilon_{kl}^{e}}$ and a cracking part and, it is represented by the Unitary Crack Opening strain tensor $\boldsymbol{\varepsilon_{ij}^{uco}}$:

$$\boldsymbol{\varepsilon_{kl}^{uco}} = \boldsymbol{\varepsilon_{kl}} - \boldsymbol{\varepsilon_{kl}^{e}} \tag{2.29}$$

Multiplying the unitary crack opening strain $\boldsymbol{\varepsilon_{kl}^{uco}}$ by the size of numerical element *h*, the width of a crack of unit normal n is obtained as follows:

$$\boldsymbol{\delta_n} = \boldsymbol{n_i}\boldsymbol{\delta_{kl}}\boldsymbol{n_j} = \boldsymbol{n_i}h\boldsymbol{\varepsilon_{kl}^{uco}}\boldsymbol{n_j} \tag{2.30}$$

The method of crack estimation has been validated under different arbitrary loadings and complex boundary conditions.

Permeability evaluation

Flow through non-fractured porous media occurs at the micro-scale through interstitial pores, and this process is well described by the Darcy law. When cracks occur, the physical-mathematical description of laminar flow through fractures is described by the cubic law that is developed using the Parallel-Plate Concept (Witherspoon, 1980), as shown in Figure 2.25.

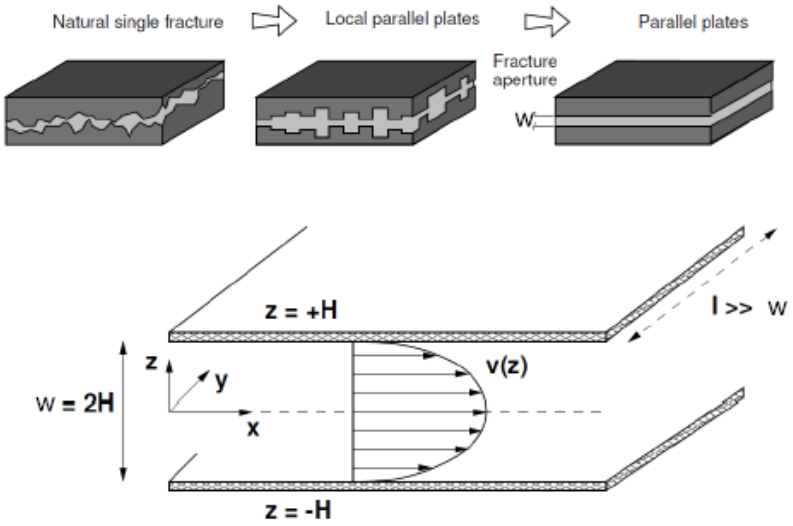

Figure 2.25. Cubic law developed using the Parallel-Plate Concept (Witherspoon, 1980)

In Figure 2.25, making use of cube law and Darcy law, the flow evaluation for cracked material is shown as Equation (2.31) and, for intact material the flow evaluation is shown as Equation (2.32), where k, A, μ and ∇P are intact material intrinsic permeability, the cross-section of flow, water viscosity and pressure gradient, respectively. Equation (2.33) is combined by Equations (2.31) and (2.32), K is global permeability.

$$Q = -(\frac{lw^3}{12\mu})\nabla P \tag{2.31}$$

$$Q = -k\frac{A}{\mu}\nabla P \tag{2.32}$$

$$Q = K\nabla P \tag{2.33}$$

The intrinsic permeability for cracked material is shown as follows:

$$\kappa_c = \frac{w^2}{12} \tag{2.34}$$

Assuming a fractured element with a crack width w in the Z direction as shown in Figure 2.25, the hydraulic behaviour should be described by an anisotropic permeability tensor. The volumetric flow in the Z directions is not modified and is defined by the Darcy law with a permeability of uncracked material. Assuming e_x and e_y is the two orthonormal vectors in the crack plane, and e_z the outward unit is normal to this plane, the fluid-flow governing equation reads:

$$Q * e_z = -\kappa_0 \frac{A_z}{\mu}\nabla P e_z \tag{2.35}$$

where A_z is the cross sectional area in the Z direction. For the X and Y directions, in the uncracked solid matrix, the flow is also described by the Darcy law as follows:

$$Q * e_x = -\kappa_0 \frac{A_x}{\mu} \nabla P e_x \tag{2.36}$$

$$Q * e_y = -\kappa_0 \frac{A_y}{\mu} \nabla P e_y \tag{2.37}$$

A_x and A_y are the cross areas in the directions X and Y. The quantities flowing through the crack are given as follows:

$$Q * e_x = -(\frac{L_y w^3}{12\mu}) \nabla P e_x \tag{2.38}$$

$$Q * e_y = -(\frac{L_x w^3}{12\mu}) \nabla P e_y \tag{2.39}$$

According to Darcy law, and assuming that $A_{cr}^x = L_y w$ and $A_{cr}^y = L_x w$ are the cross-sections of flow. Equations (2.38) and (2.39) can be modified as follows:

$$Q * e_x = -\frac{w^2}{12} \frac{A_{cr}^x}{\mu} \nabla P e_x \tag{2.40}$$

$$Q * e_y = -\frac{w^2}{12} \frac{A_{cr}^y}{\mu} \nabla P e_y \tag{2.41}$$

Therefore, the uncracked and cracked intrinsic permeability governs the fluid flow through material, the one governing the flow through the uncracked material is given as follows:

$$Q_0 * e_x = -\kappa_0 \frac{A_x}{\mu} \nabla P e_x \tag{2.42}$$

$$Q_0 * e_y = -\kappa_0 \frac{A_y}{\mu} \nabla P e_y \tag{2.43}$$

$$Q_0 * e_z = -\kappa_0 \frac{A_z}{\mu} \nabla P e_z \tag{2.44}$$

And driving the flowing through crack is given as follows:

$$Q_F * e_x = -(\frac{L_y w^3}{12\mu}) \nabla P e_x \tag{2.45}$$

$$Q_F * e_y = -(\frac{L_x w^3}{12\mu}) \nabla P e_y \tag{2.46}$$

$$Q_F * e_z = 0 \tag{2.47}$$

Therefore, for the orthotropic plane of the crack (Figure 2.25), the fractured permeability tensor is given as following:

$$\boldsymbol{\kappa} = \begin{bmatrix} \kappa_0 + \frac{w^3}{12L_z} & 0 & 0 \\ 0 & \kappa_0 + \frac{w^3}{12L_z} & 0 \\ 0 & 0 & \kappa_0 \end{bmatrix} \tag{2.48}$$

k_0 is the permeability of the uncracked material. The above permeability tensor has been developed by means of only having one fracture in the Z direction. In general, cracked material is full of fractures in different directions. Therefore, the general form of the permeability tensor for cracked material should be written as follows:

$$\boldsymbol{\kappa} = \begin{bmatrix} \kappa_0 + \frac{w^3}{12L_y} + \frac{w^3}{12L_z} & 0 & 0 \\ 0 & \kappa_0 + \frac{w^3}{12L_x} + \frac{w^3}{12L_z} & 0 \\ 0 & 0 & \kappa_0 + \frac{w^3}{12L_y} + \frac{w^3}{12L_x} \end{bmatrix} \tag{2.49}$$

Diffusion in unsaturated COx

No matter saturated or unsaturated porous materials and the water balance relation can be applied. Namely, the change of water content of porous material is equal to the difference between water flow-in and flow out, as it is showed in Figure 2.26 and expressed in equation (2.50).

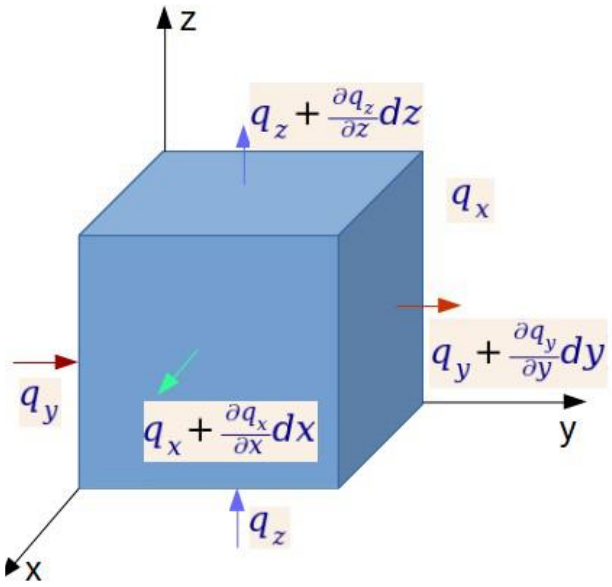

Figure 2.26. A schematic of water dynamic equilibrium

$$-div\ qdxdydz = -(\frac{\partial q_x}{\partial x} + \frac{\partial q_y}{\partial y} + \frac{\partial q_z}{\partial z})dxdydz \tag{2.50}$$

Through introducing Darcy law into the water balance equation, the differential relation can be obtained as following:

$$c\frac{\partial P_c}{\partial t} - \frac{k}{g} div\big(\nabla(P_c - pgz)\big) = 0 \tag{2.51}$$

where c is the mass capacity and P_c is capillary pressure field changing with time. The mass capacity c is written as follows:

$$c = -\rho\frac{\partial \theta}{\partial P_c} \tag{2.52}$$

where ρ and θ are water density and volumetric water content, respectively, and the water mass capacity curve of COx is shown in Figure 2.27.

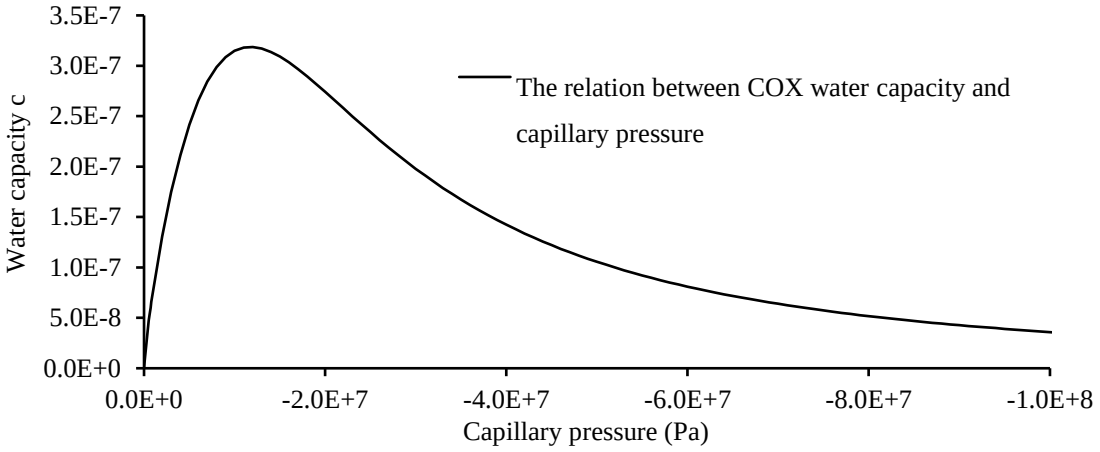

Figure 2.27. Water capacity curve of Callovo-Oxfordian argillite

According to Vogel et al., (2000), they proposed the modified Van Genuchten's retention model and θ is written as follows:

$$\theta = \begin{cases} S_e(\theta_s - \theta_r) + \theta_r & if\ P_c > P_{c(aev)} \\ \theta_s & if\ P_c < P_{c(aev)} \end{cases} \tag{2.53}$$

where S_e, θ_s, θ_r and $P_{c(aev)}$ are effective saturation degree, saturated water content, residual water content and the air-entry value of capillary pressure, respectively. When $S_e = 0$, the water content is θ_r and when $S_e = 1$, the water content is θ_s. According to the modified version of Van Genuchten model (Vogel et al. 2000), the effective saturation S_e is written as follows:

$$S_e = \frac{\theta_m - \theta_r}{\theta_s - \theta_r}\left(1 + \left(\frac{P_c}{a}\right)^{\frac{1}{1-m}}\right)^{-m} \tag{2.54}$$

In particular, θ_m is a parameter, which is equal or greater than the saturated water content θ_s. By imposing the effective saturation S_e=1, we can have the air-entry capillary pressure $P_{c(aev)}$ as follows:

$$P_{c(aev)} = a\left(\left(\frac{\theta_m - \theta_r}{\theta_s - \theta_r}\right)^{1/m} - 1\right)^{1-m} \tag{2.55}$$

However, the hydraulic conductivity k of Darcy law for unsaturated porous material is different from the one for saturated material, it is written as follow (Fachy et al., 2013):

$$k = \begin{cases} \frac{\rho g \kappa}{\mu}\kappa_R & if\ P_c > P_{c(aev)} \\ \frac{\rho g \kappa}{\mu} & if\ P_c < P_{c(aev)} \end{cases} \tag{2.56}$$

where κ_R is written as follows and the relative permeability curve for COx is shown in Figure

2.28:

$$\kappa_R = \sqrt{S_e}\left(\frac{1-\left[1-\left(\frac{\theta_m-\theta_r}{\theta_s-\theta_r}S_e\right)^{1/m}\right]^m}{1-\left[1-\left(\frac{\theta_m-\theta_r}{\theta_s-\theta_r}\right)^{1/m}\right]^m}\right)^2 \quad (2.57)$$

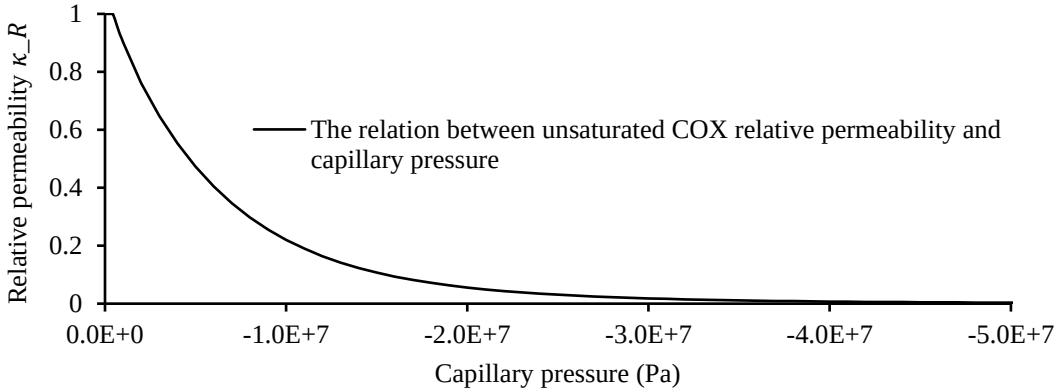

Figure 2.28. Relative permeability curve of unsaturated COx

All the hydraulic parameters of COx for the above equations are listed in Table 2.4 as follows:

Table 2.4. Parameters for COx hydro-mechanical behaviour analysis

θ_s	0.1799
θ_r	0.
θ_m	0.18
$P_{c(ave)}\ [Pa]$	-1×10^{2}
$\mu[t/m*s]$	1×10^{-3}
$\kappa_0\ [m^2]$	1×10^{-20}
m	0.45
$a\ [Pa]$	1.86237×10^{7}

2.5 Conclusions

This chapter presented a literature review on the properties of Callovo-Oxfordian argillite, the fractured zone of galleries parallel to the major horizontal stress σ_H and galleries parallel to the minor horizontal stress σ_h, fractures and permeability of the fractured zone. The hydro-mechanical parameters of COx for numerical simulation are summarized in this chapter, such as the evolutions of Young Modulus, tensile strength and fracture energy with water content change. COx as a kind of unsaturated claystone, the hydraulic parameters for water diffusion in COx are also presented.

In conclusion, through the bibliography in this chapter, we obtained all the parameters and equations those will be applied in the next three chapters for numerical modelling of uniaxial/triaxial compression tests, COx swelling in free condition or under some limitations, self-sealing of macro-cracked samples and compression damage zone (CDZ).

Chapter 3

Cast3M and uniaxial/triaxial compression tests

This chapter presents the finite element software Cast3M and the validation of the previously presented damage model which is now implemented in the frame on unsaturated porous media. Numerical analysis of uniaxial compression tests for Callovo-Oxfordian argillite under different relative humidity's and numerical simulation of COx triaxial compression tests are presented.

3.1 Cast3M

The Mechanics and Technology Department (DMT) of the French Atomic Energy and Alternative Energies Commission (CEA) develops the Multiphysics Finite Element code Cast3M since the 1980s. It is provided free of charge for teaching and research activities. It uses the finite element method to solve different types of scientific problems. Cast3M includes not only preprocessing model build-up but also post-processing for results analysis, it was originally developed for mechanical research domain for analyzing mainly nuclear structures. The sources of Cast3M are distributed and free for research usage. The organization of a calculation is done as follows: Choice of geometry and mesh, definition of points, lines, surface and choice of type of mesh. Definition of the mathematical and physical model, data characterizing the model, material properties, boundary conditions, initial conditions. Solving of the discretized problem, calculation of the stiffness and mass matrices, assembly, application of the loadings, resolution. Analysis and post-processing of results.

The fact that any of the operators can be used at any time in the program allows many facilities such as the display of information at all stages so as to control the data entered and the calculation process, archiving and restoring information in order to be able to interrupt a calculation and continue it later, the ability to iterate through the desired steps. It is to this extent that Cast3M therefore exceeds the adaptability limits offered by conventional calculation codes.

An important feature of CAST3M is the module independence, for example, fluid dynamics, mechanics and thermos-hydraulic, this feature makes users can change them individually. Of course, this feature provides users' possibility to couple these modules, this kind of coupling is vital to multiple interdependent factors analysis. Both of Cast3M standard procedure files and source files can have also been modified for achieving users' intention. After having a formulated model, the hydro-mechanical analysis can be divided into four steps: (1) geometry drawing and mesh choice (2) mechanical model definition and relative parameters input (3) using time step

calculation to find the solution (4) the results post-treatment and analysis. The results from Cast3M calculation can be directly treated in Cast3M and also can be output to some other software to analyze such as EXCEL, while in this work most of the numerical simulations are performed using Cast3M.

3.2 Uniaxial compression tests

In this section, the proposed plastic damage model applied to simulate the uniaxial compression tests performed by Pham (2006) with different hydraulic conditions relative humidity RH 32%, 44% and 76%. In Figure 3.1, the uniaxial compression tests are presented. All the numerical results will be compared with their corresponding experimental results.

Figure 3.1. COx sample and its uniaxial compression test (Pham et al., 2006)

This part presents the details of numerical simulation, including the calculation of capillary pressure P_c, tensile strength σ_t, Young Modulus E and fracture energy G_f. Due to σ_t, E, G_f (They are introduced in Chapter 2) changing with COx water content (It is represented by capillary pressure P_c in numerical simulation), and all the parameters for having their evolutions with capillary pressure P_c in numerical simulation are listed in Table 3.1.

Table 3.1. Parameters for having evolutions of σ_t, E, G_f with changing of water content

Parameters	σ_{t0}	P_t	G_{f0}	P_f	$E_{saturated}$
Values	$5.\times 10^5 Pa$	$-5.9 \times 10^7 Pa$	6.4N/m	$-4.8 \times 10^7 Pa$	4.32×10^9 Pa

A lognormal random field distribution model was adopted to map the Young modulus on the finite element numerical mesh to avoid having homogenous material that can produce special and unwanted failure particularly in compression test, and this method is used to draw the Young modulus of all the numerical analysis in this thesis. An average Young modulus 4.32×10^9 Pa was taken as the expected value of saturated COx in the lognormal random field. A rotating band method introducing a characteristic length as well as a standard deviation. Our experience shows that the result isn't really sensible with the value of these parameter and a standard deviation of 10% is used. For numerical reason, the characteristic length must be larger to one element size and as low as possible to be representative of the real material which owns a very small structure. A characteristic length of two times of the size of the larger element of the mesh is used for the following simulations. The Young modulus distribution of the finite element

mesh for uniaxial compression tests of saturated COx is shown in Figure 3.2. Due to the fact that COx is usually in unsaturated state, the saturated Young's modulus is multiplied by a function of capillary pressure at each Gauss point of the mesh and updated at each time step. It must be stressed out that Young modulus distribution method is used for all the numerical simulation in this thesis, therefore it will not be repeated in other places afterwards.

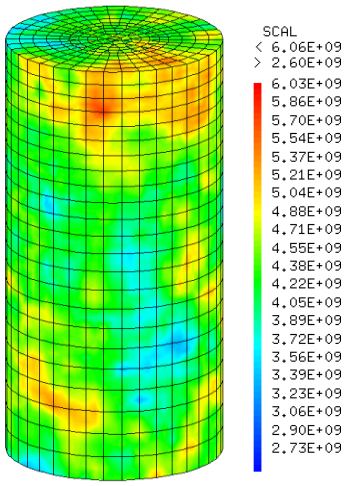

Figure 3.2. A schematic of COx Young modulus lognormal distribution for numerical simulation

According to damage values distribution and lateral displacement of Y direction, the details of numerical results under the above three different relative humidity's are shown afterwards.

3.2.1 Relative humidity of 76%

In the experiment, the sample of Callovo-Oxfordian argillite was kept in humidity chamber under relative humidity 76% until the stabilisation of the sample's mass. The sample is then considered having homogeneous water content. Therefore, the sample's capillary pressure can be calculated by the Kelvin equation as following:

$$P_c = -\frac{RT\rho_w}{W_w} ln\frac{1}{RH} = -\frac{8.314J/(mol*K)\times 298K\times 10^6 g/m^3}{18\text{g/mol}} ln\frac{1}{76\%} = -3.63\times 10^7 Pa \quad (3.1)$$

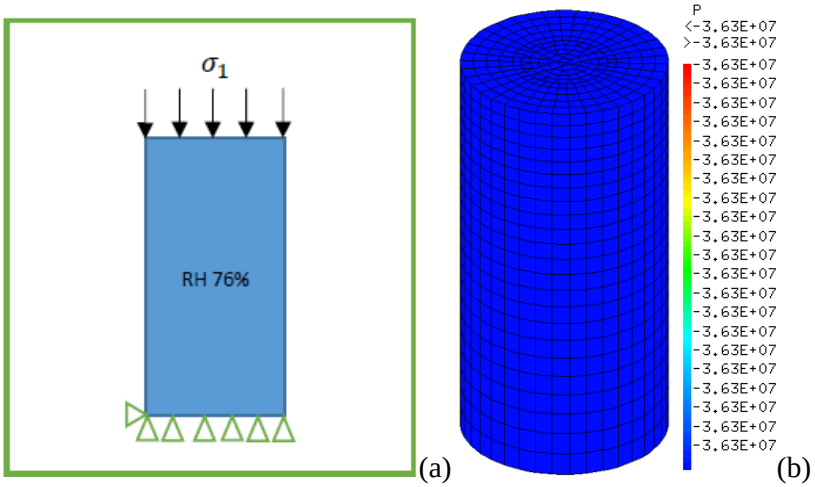

Figure 3.3 Uniaxial compression test of RH 76%: (a) Boundary condition (b) Capillary pressure

Figure 3.3 shows the boundary condition and capillary pressure of cylinder mesh for uniaxial compression test under relative humidity 76% in numerical simulation of CAST3M. According to the evolutions between capillary pressure P_c and Young Modulus E in Figure 2.8, tensile strength σ_t in Figure 2.9 and fracture energy G_f in Figure 2.10, the calculated values of these three parameters are 4.5GPa, 0.9MPa and 11.1N/m under relative humidity of 76% , respectively. The value of Poisson ratio of 0.295 is chosen while the parameter β in equation (2.24) is calculated from equation (2.25) by using the corresponding fracture energy value.

The numerical result of COx uniaxial compression test under RH 76% is shown in Figure 3.12. With vertical compressive load increment, the mesh strain evolves from the initial elastic phase to elastoplastic phase gradually. In the elastic phase, no damage developed inside the mesh, the damage value is zero. Damage occurs when the lateral strain is beyond the material plastic limit, this moment the vertical strain is 0.49%. After the occurring of damage, material goes into a hardening process, the vertical stress goes up continuously. When the vertical stress reaches -38Mpa and the vertical strain is 0.9%, material failed.

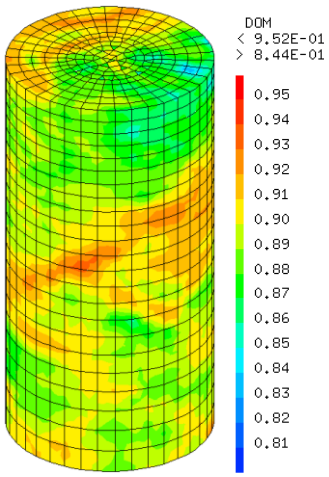

Figure 3.4. Damaged zone and damage value

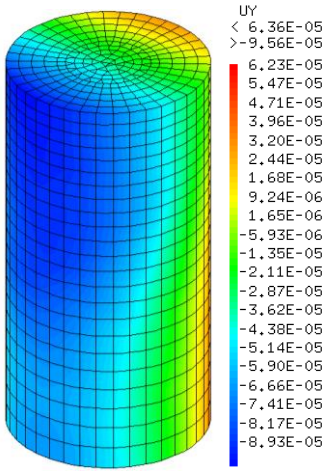

Figure 3.5. Y direction displacement

Figure 3.4 shows mesh damaged zone and their damage values at that moment of material failed, it illustrates that the main damaged zone distributes at the cylinder top surface and its middle part. illustrates that the axial strain-normal stress curve obtained by the simulation shows a good consistency with experiments (Figure 3.12). Figure 3.5 shows the Y direction displacement of the mesh before the moment the material failed. The maximum Y displacement $6.36 \times 10^{-5} m$, and that time the maximum lateral strain is 0.38%. It is obvious that Y displacement values distribution is not homogenous on the mesh. However, inspection of Figure 3.1, the displacement distribution of numerical simulation has a high-level consistency with the failed zone on the experimental sample. In conclusion, the comparison of experimental result with numerical result for RH 76% has a good consistency.

3.2.2 Relative humidity of 44%

The same as the preparation of the experimental sample under RH 76%, the sample of RH 44% also was kept in humidity chamber until the stabilisation of the sample's mass. When relative humidity is 44%, the sample's capillary pressure is calculated by the Kelvin equation as following:

$$P_c = -\frac{RT\rho_w}{W_w} ln\frac{1}{RH} = -\frac{8.314J/(mol*K)\times 298K\times 10^6 g/m^3}{18\text{g/mol}} ln\frac{1}{44\%} = -1.09\times 10^8 Pa \qquad (3.2)$$

Figure 3.6 shows the boundary condition and capillary pressure of the cylinder mesh for uniaxial compression test under relative humidity 44%. When capillary pressure is $-1.09\times 10^8 Pa$, the parameters of Young Modulus E, tensile strength σ_t and fracture energy G_f are 6.5GPa, 1.1MPa and 28N/m, respectively.

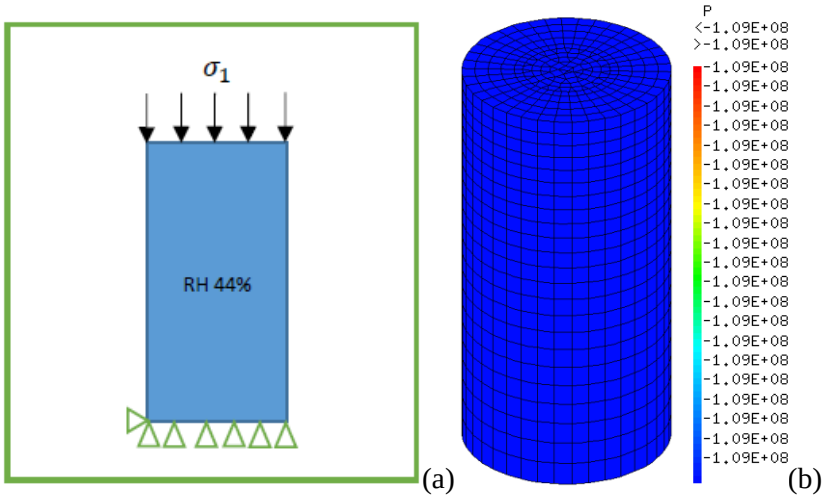

Figure 3.6. Uniaxial compression test of RH 44%: (a) Boundary condition, (b) Capillary pressure

At the beginning of the experiment, the material is linear elastic, when the normal strain reached 0.5%, the relation between strain and stress became nonlinear and plastic deformation occurred. Following the continuous increment of compression load, the strain expanded continuously, when the load arrived at 52MPa the material failed, and the normal strain reached 1%.

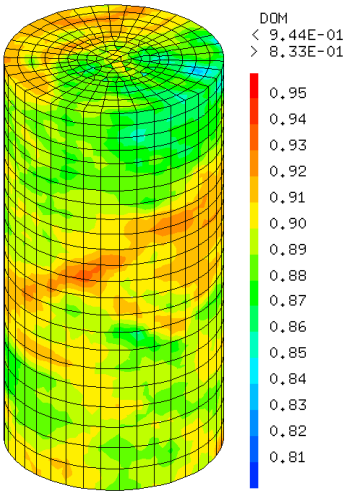

Figure 3.7. Damaged zone and damage value

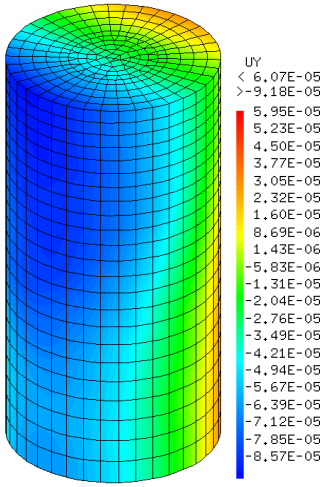

Figure 3.8. Y direction displacement

Figure 3.7 shows the damage values when the failure point reaches. Figure 3.8 shows the Y-direction displacement of the mesh before the moment the material failed. The maximum Y displacement reaches $6.07 \times 10^{-5} m$. This maximum displacement is less than the maximum displacement of RH 76%, and it is consistent with that observed in the experiment, the possible explanation of this phenomena is the increment of capillary pressure limits COx deformation when relative humidity decrease. In Figure 3.12, a good agreement between experimental result and the numerical result has been obtained under relative humidity 44%.

3.2.3 Relative humidity of 32%

When relative humidity is 32%, the sample's capillary pressure is calculated by the Kelvin equation as following:

$$P_c = -\frac{RT\rho_w}{W_w} ln\frac{1}{RH} = -\frac{8.314J/(mol*K)\times 298K\times 10^6 g/m^3}{18\text{g/mol}} ln\frac{1}{32\%} = -1.51\times 10^8 Pa \quad (3.3)$$

Figure 3.9 shows the initial capillary pressure of cylinder mesh for uniaxial compression test under relative humidity 32%. When capillary pressure is $-1.51 \times 10^8 Pa$, the parameters of Young Modulus E, tensile strength σ_t and fracture energy G_f are 7.6GPa, 1.3MPa and 51N/m respectively.

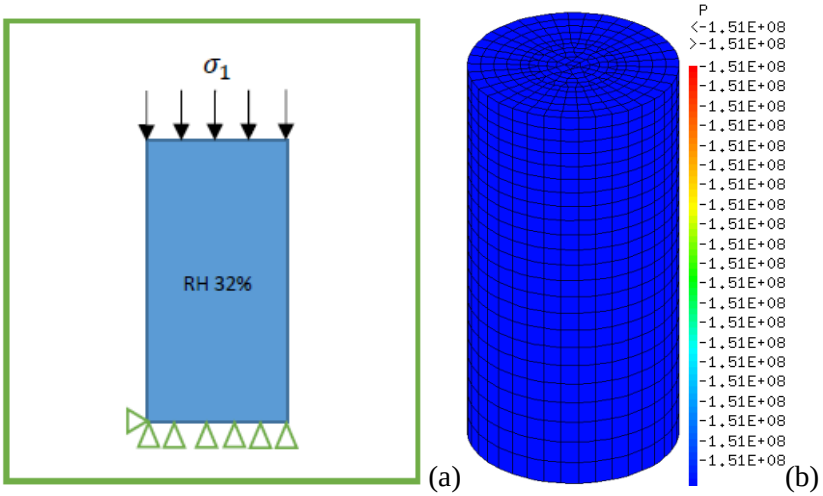

Figure 3.9. Uniaxial compression test of RH 32%: (a) Boundary condition, (b) Capillary pressure

As shown in Figure 3.12, at the beginning of the experiment, the stress strain relation is linear. When the normal strain reached 0.55%, the relation between strain and stress became nonlinear, damage and plastic deformation occurred. Following the continuous increment of compression load, the strain expanded continuously, when the load reached at 58MPa the material failed, this moment the normal strain was 0.9%.

Figure 3.11 shows the Y-direction displacement of the mesh before the moment the material failed. The maximum Y displacement reaches $5.30 \times 10^{-5} m$. This maximum displacement is less than

the maximum displacements of RH 44% and RH 76%, and they are consistent with that observed in experiments, namely COx lateral deformation, reduces with the desaturation process.

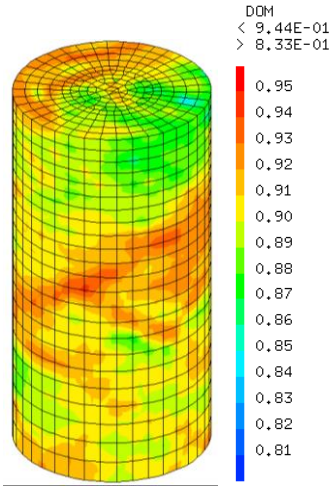

Figure 3.10. Damaged zone and damage value

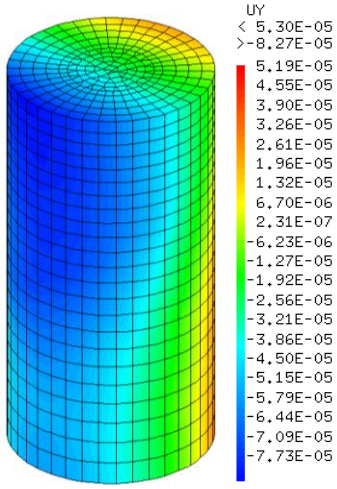

Figure 3.11. Y direction displacement

Figure 3.4, 3.7 and 3.10 indicate that the damage zones at failure points are more developed with the changing of RH 76%, RH 44% and RH 32% in numerical simulation. In experiments, COx was stiffer and more brittle with RH decrease, and the corresponding damage of the material in uniaxial compression tests were more developed. Therefore, the numerical results of damage of the material is consistent with the phenomena observed in experiments.

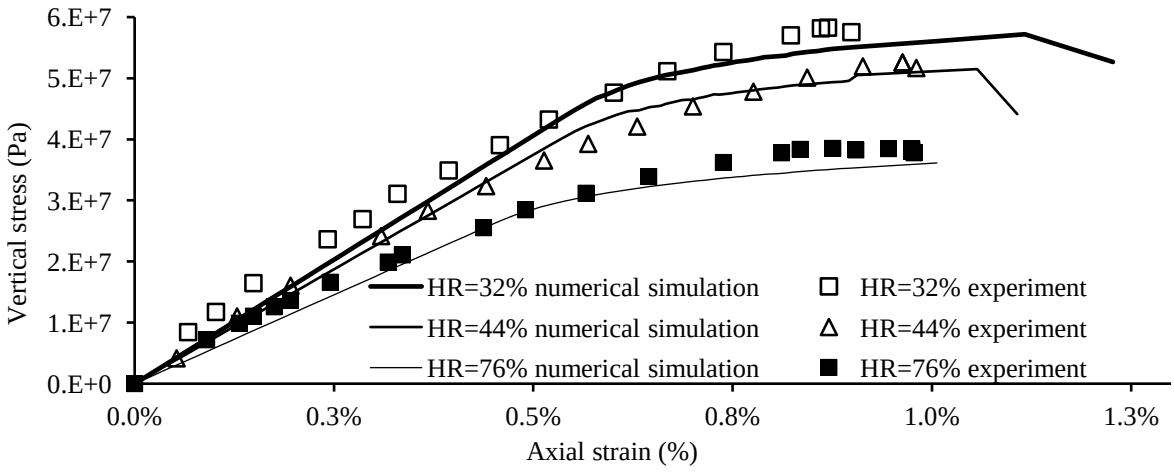

Figure 3.12. Uniaxial compression tests numerical simulation under relative humidities 32%, 44%, 76%

In Figure 3.12, the experimental results of uniaxial compression tests are compared with the numerical simulations, confirming the ability of the proposed model to reproduce the effect of relative humidity on the nonlinear behaviour of the material. The effect of relative humidity is also captured by the proposed model, which correctly predicts an increase in material stiffness as the relative humidity decreases. The experimental value of peak stress is also adequately predicted at all humidity levels. These numerical results prove the good performance of the model in describing the plastic-damage behaviour of the COx claystone.

In conclusion, We observe an apparent decrease in Young's modulus during relative humidity increment, which reflects the damage to the material for each level of humidity. The resistance to uniaxial compression increases with relative humidity decrease. This variation in resistance may be due to the variation of the free surface energy of the clay grains. The humidification of argillite is accompanied by a fixation of water particles on the walls of the pores, and this leads to a decrease in the free surface energy of the COx, and the free energy arrives at its maximum value in the dry state (Ballivy et al. 1992). The decrease in the breaking strength of the argillite in the resaturation phase can also be explained by the decrease in the capillary tension, the increase in pore pressure, the reduction of friction of open micro-cracks.

Suction plays a role analogous to confining pressure. The increase in suction during the desaturation of the clay rock increases the Young's modulus, and the phenomenon is reversed for resaturation. The suction pressure improves the interface between the clay grains by greater adhesion. It, therefore, strengthens the resistance of argillite in the case of low relative humidity and weakens it in the case of high relative humidity.

3.3 COx triaxial compression test

A series of triaxial tests (Figure 3.13) were carried out on COx claystone by Andra (2005) and Armand *et al.* (2017) under the different confining stresses of 0MPa, 2MPa, 6MPa and 12MPa.

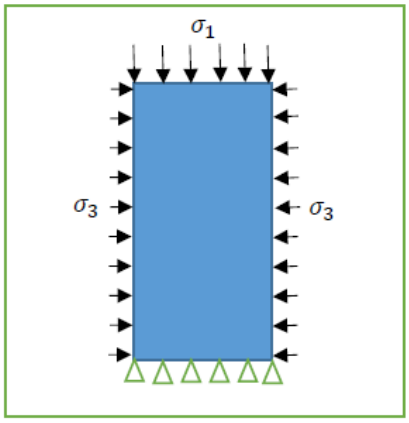

Figure 3.13. A schematic of triaxial test

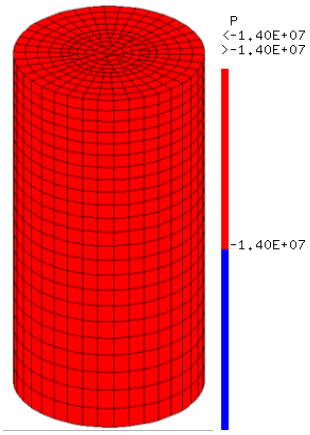

Figure 3.14. Initial capillary pressure of sample

All tested samples were taken from horizontal boreholes in the Muse Haute-Marne underground laboratory located at a depth of -490m underground by ensuring that the coring direction was parallel to the bedding plane of the COx. The samples were carefully protected to avoid exchanges of moisture with the outside environment and, before triaxial testing, they were equalised to a relative humidity of 90%. According to the Kelvin equation $P_c = \frac{RT\rho_w}{W_w} ln \frac{1}{RH}$ and Van Ganuchen water retention model, when relative humidity 90%, the sample capillary pressure is -14 MPa (Figure 3.14), a degree of saturation of 94%, a fracture energy of 10.4N/m and a tensile strength of 1.05 MPa.

The numerical analysis of triaxial tests taken from the experiments are presented in the following part, the comparisons between the experimental results and numerical results are done for deviator stress $\sigma_1 - \sigma_3$, axial strain and lateral strain.

3.3.1 Triaxial simulation under 0 MPa confining stress

Figure 3.15 and 3.16 showed the damage value and displacement of the numerical mesh when the deviator stress reaches its peak value 21.4MPa. The damage was fully developed when failure occurred.

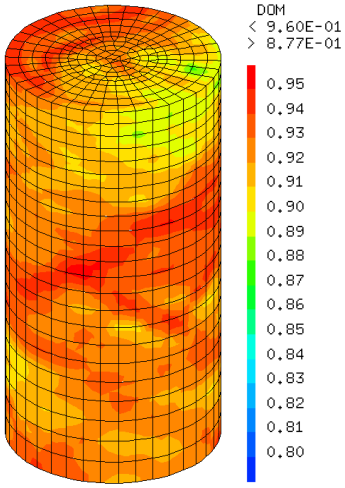

Figure 3.15. Damage at the peak deviator stress

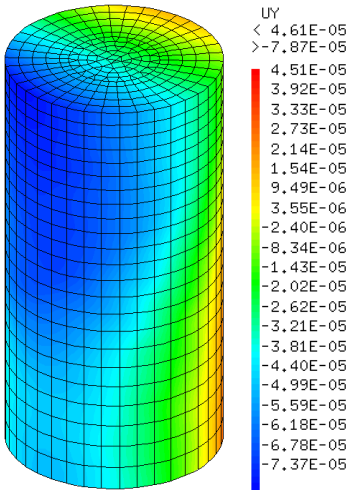

Figure 3.16. Displacement in Y direction

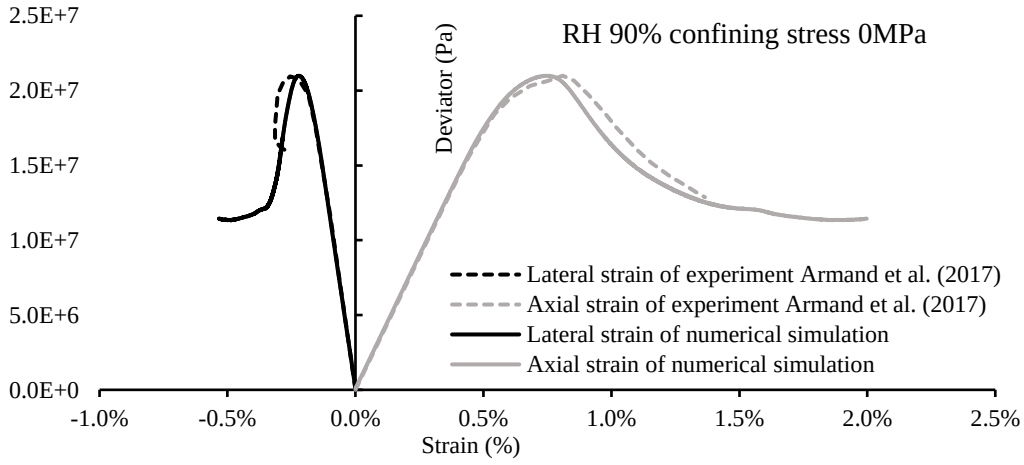

Figure 3.17. Triaxial test under confining stress of 0 MPa at relative humidity of 90%

Figure 3.17 shows deviator stress - strain curve for both axial and lateral strains. It indicates that the model is able to reproduce correctly the behavior of the material including the limit of elasticity, the strength and plasticity.

3.3.2 Triaxial simulation under 2 MPa confining stress

For the 2MPa confining stress of triaxial test, the peak value of deviator increases to 24.1MPa. Figure 3.18 and 3.19 illustrate the damage value and displacement of the numerical mesh when the peak deviator is obtained.

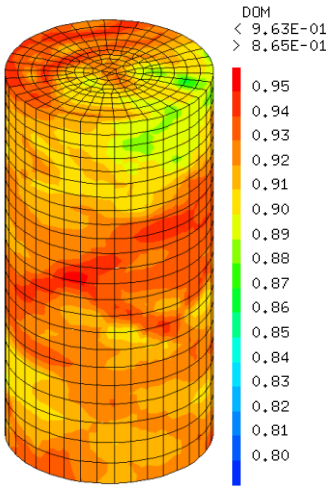

Figure 3.18. Damage at the peak deviator stress

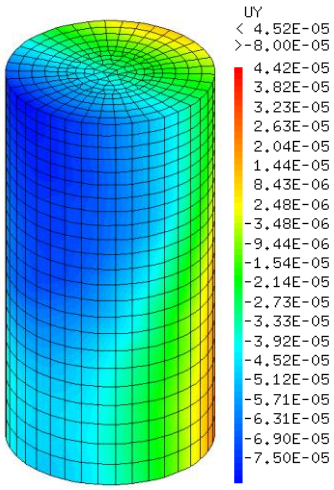

Figure 3.19. Displacement in Y direction

Figure 3.20 compared the numerical results and experimental results in terms of deviator stress with lateral strains and axial strains. In the experiment, when axial strain is less than 0.5%, the relationship between strains and deviator keeps linear. Damage and plasticity occurs at the point of the axial strain reaches 0.5%. In comparison between numerical curves and experimental curves, a good agreement has been accomplished.

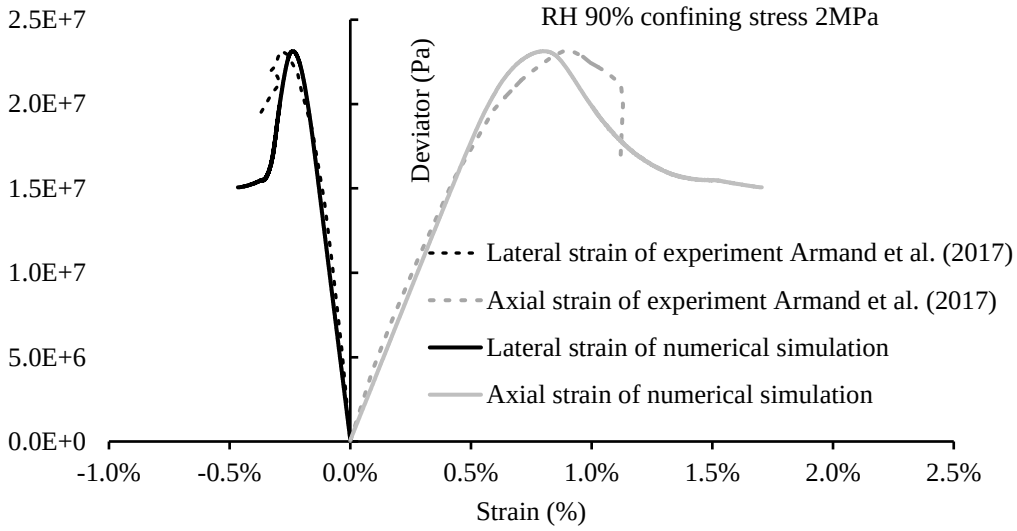

Figure 3.20. Triaxial test under confining stress of 2 MPa at relative humidity of 90%

3.3.3 Triaxial simulation under 6 MPa confining stress

For the 6MPa confining stress of triaxial test, the peak value of deviator increases to 29MPa. Figure 3.21 and 3.22 illustrate the damage value and displacement of the numerical mesh when the peak deviator is obtained.

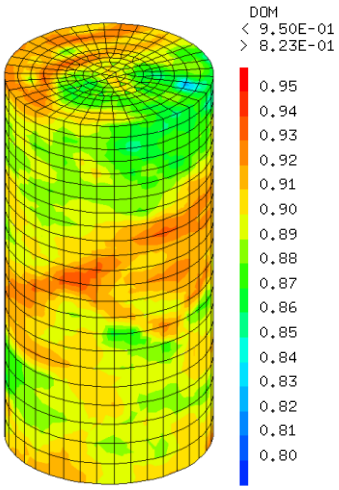

Figure 3.21. Damage at the peak deviator stress

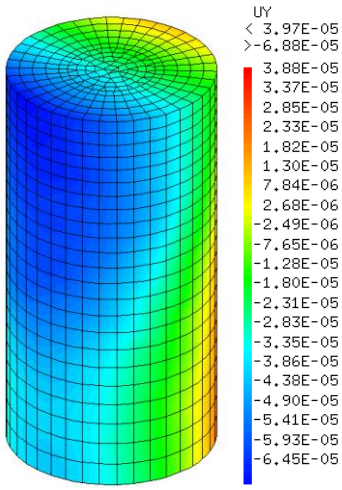

Figure 3.22. Displacement in Y direction

Figure 3.23 compared the numerical results and experimental results in terms of deviator stress with lateral strains and axial strains.

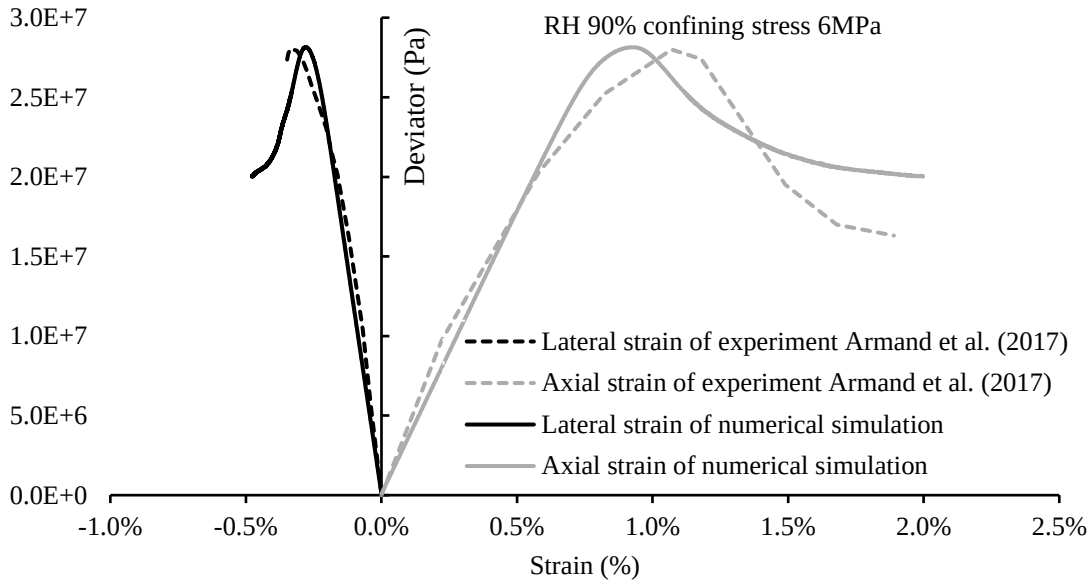

Figure 3.23. Triaxial test under confining stress of 6 MPa at relative humidity of 90%

3.3.4 Triaxial simulation under 12 MPa confining stress

For the 12MPa confining stress of triaxial test, the peak value of deviator reaches to 35.3MPa. Figure 3.24 and 3.25 illustrate the damage value and displacement of the numerical mesh when the peak deviator is obtained.

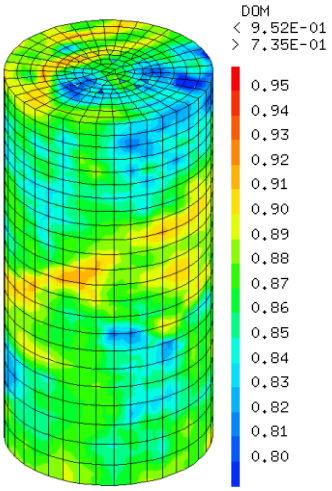

Figure 3.24. Damage at the peak deviator stress

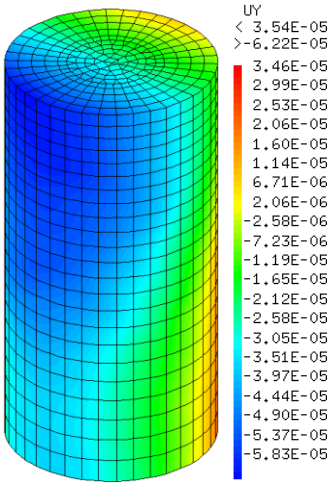

Figure 3.25. Displacement in Y direction

Figure 3.26 compared the numerical results and experimental results in terms of deviator stress with lateral strains and axial strains.

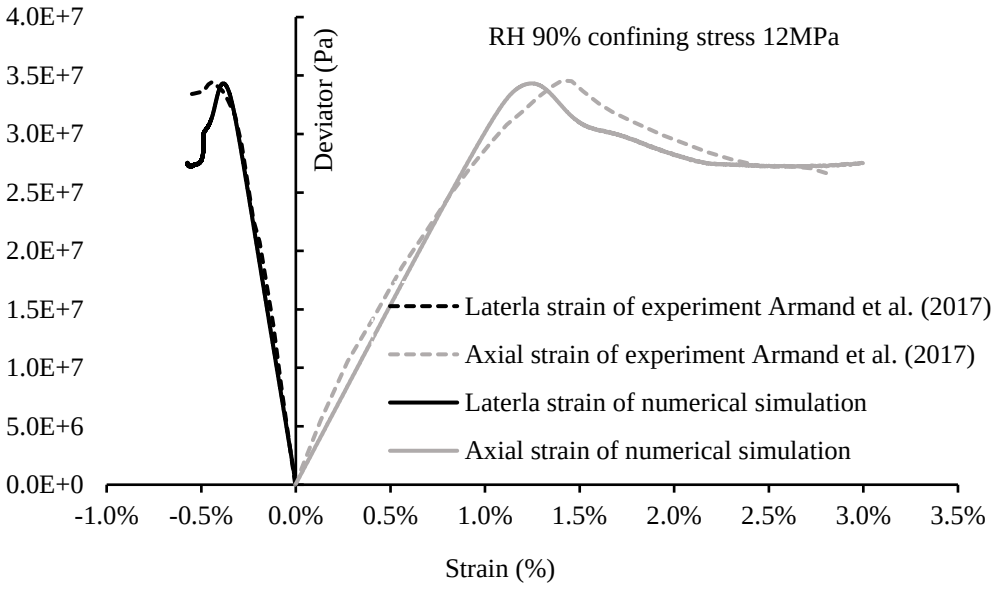

Figure 3.26. Triaxial test under confining stress of 12 MPa at the relative humidity of 90%

Inspection of Figure 3.15, 3.18, 3.21 and 3.24, we can find that the damage values decrease following with the increment of the confining stresses. This phenomenon is consistent with that of experiments, a possible explanation to it is that the confining stresses enhanced the frictions inside COx, which maybe prevent the damage development.

Figure 3.17, 3.20, 3.23 and 3.26 compare the experimental and numerical results in terms of deviator stress, axial strain and lateral strain. The numerical simulation of the test at a confining stress of 0MPa (Figure 3.16) shows that, in the early stages of deviatoric loading, the strain curve exhibits a linear behaviour which is consistent with experimental data. This linear behaviour

continues until the deviator stress reaches a value of about 20MPa, at which point the material response becomes nonlinear, and plastic deformations occur. Moreover, the predicted peak deviator stress of 21.4MPa matches well with the measured value in the experiment. As for the other triaxial tests at confining pressures of 2MPa, 6MPa and 12MPa (Figures 3.19, 3.22 and 3.25), the predicted values of peak deviator stress are 24.1MPa, 29MPa and 35.3MPa, respectively, which match again reasonably well the corresponding measured values. In general, at all four levels of confining pressure, a reasonably good fit is obtained between experimental data and model simulations, though model simulations tend to predict the attainment of the peak deviator stress in correspondence of slightly lower values of axial strain compared to experimental data.

3.4 Conclusions

Good agreements are obtained between numerical simulation and experiment results. It means that no matter from basic mechanical features such as plastic strain, volumetric deformation and softening behaviour, the proposed model is able to describe them correctly. Capillary pressures of these uniaxial/triaxial compression tests are determined by relative humidity, the effects of capillary pressure on the mechanical response are also effectively reproduced. A good concordance between numerical results and experimental results is obtained in terms of mechanical strength changes with the relative humidity variation.

The uniaxial and triaxial compression tests demonstrate the large impacts of relative humidity and confining stress on the mechanical behaviours of COx. The good agreements between numerical results and experimental results validated the proposed model in the numerical analysis of COx mechanical behaviour.

Chapter 4

The swelling of Callovo-Oxfordian argillite

This chapter presents the formulation of the added deformation law to be coupled with a linear elastic Biot stress framework for describing the deformation of Callovo-Oxfordian argillite during the desaturation/resaturation cycles. The resulting constitutive model has been validated against measurements from wetting tests under restrained conditions.

4.1 Biot stress modelling framework

Porous mechanics is the branch of physics that studies the behavior of porous media crossed by multiphase fluid flow. A porous medium is a solid which contains a network of interconnected voids filled with liquid or gas. It is generally assumed that the solid matrix and the pore network are both continuous forming two interpenetrating continua. Many natural substances, such as rocks, soil, biological tissues, and human-made materials, such as foams and ceramics, are classified as porous media.

A porous material in which the solid matrix is elastic and the fluid is viscous is called a porous elastic medium. The engineering behaviour of porous elastic media is characterized by the porosity, permeability and composition of both solid matrix and pore fluid.

The concept of porous media appeared in soil mechanics through the work of Karl von Terzaghi, though the most general treatment of porous elastic media is attributed to Maurice Anthony Biot (1905-1985), a Belgian-American engineer. In a series of papers, published between 1935 and 1957, Biot proposed the dynamic porosity theory, now called the Biot model, which gives a complete and general description of the mechanical behaviour of porous elastic media.

The COx claystone is a porous material that exhibits significant deformation during desaturation/resaturation paths. Unfortunately, the Biot model alone is unable to predict the large shrinkage/swelling caused by drying/wetting and an additional material law must be introduced to simulate the large deformations upon changes of water content. This additional material law is calibrated to match the difference between measured and predicted deformations.

Several researchers have studied the hydro-mechanical behaviour of expansive soils using a modified form of the Biot formulation. For example, Gens and Alonso (1992) proposed a framework to predict the deformation of expansive soil subjected to desaturation and resaturation cycles. In line with previous contributions, the present work proposes a relatively simple model

that enhances the Biot model to predict the swelling/shrinkage of COx claystone produced by changes of water content.

Figure 4.1 compares the shrinkage/swelling of an unconstrained sample of COx claystone produced by a cyclic variation of capillary pressure between zero and -200 MPa (Zhang et al., 2010) with the values predicted by the conventional Biot model. The measured COx deformation is about 3 times larger than that computed by the Biot model, which is therefore uncapable of simulating the deformation of the COx claystone. To overcome this problem, the Biot formulation is enhanced with an additional material law that predicts the extra deformation required to match the experimental data.

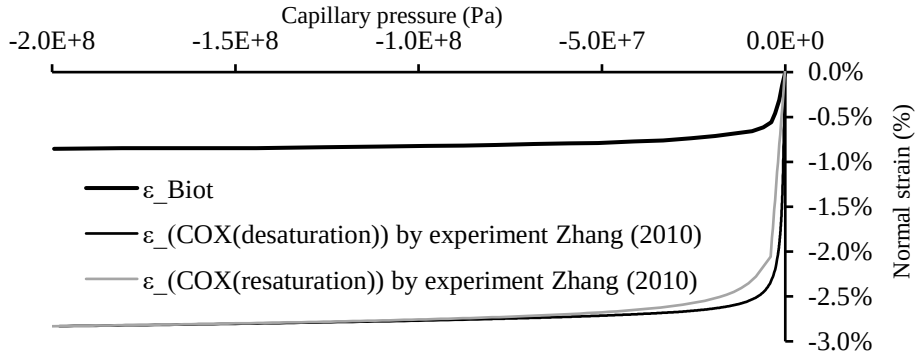

Figure 4.1. Comparison of measured and predicted shrinkage/swelling during unconstrained drying/wetting cycles of COx samples

4.2 Added deformation law

An added deformation law is formulated and calibrated to match the difference between measurements from laboratory experiments and predictions from the standard Biot model. Compared with ordinary soils, which experience large irreversible deformation, the behaviour of the COx claystone is closer to that of a rock, whose swelling during saturation tends to be small and generally reversible.

Figure 4.1 shows the deformation experienced by COx claystone during a change of degree of saturation from 100% ($P_c = 0$ MPa) to 25% ($P_c =$ -200 MPa) and back from 25% ($P_c =$ -200 MPa) to 100% (P_c =0 MPa). Figure 4.1 also shows the desaturation and resaturation curves calculated by the Biot model, which are of course identical as this model is uncapable of predicting material hysteresis.

The added deformation law introduced in the present work consists of two mathematical expressions calculating the difference between the normal strain from the linearly elastic Biot model (ε_{Biot} in Figure 4.1) and the values measured during unconfined desaturation and resaturation paths ($\varepsilon_{COX(desaturation)}$ and $\varepsilon_{COX(resaturation)}$ in Figure 4.1), respectively:

$$\varepsilon_{added(desaturation)} = \varepsilon_{COX(desaturation)} - \varepsilon_{Biot} \tag{4.1}$$

$$\varepsilon_{added(resaturation)} = \varepsilon_{COX(resaturation)} - \varepsilon_{Biot} \tag{4.2}$$

Based on the above experimental differences, the added swelling ε_{sw} and the added shrinkage ε_{sk} equations were formulated as:

$$\varepsilon_{sw} = a_w exp\left(\frac{b_w}{P_c}\right) = \varepsilon_{added(resaturation)} \tag{4.3}$$

$$\varepsilon_{sk} = a_k exp\left(\frac{b_k}{P_c + \Delta P}\right) = \varepsilon_{added(desaturation)} \tag{4.4}$$

where a_w, b_w, a_k, b_k and ΔP are model parameters.

Equations (4.3) and (4.4) are then combined into a single equation (4.5), which can be universally used to calculate the added strain within the region delimited by the $\varepsilon_{added(desaturation)}$ and $\varepsilon_{added(resaturation)}$ curves in Figure 4.3:

$$\varepsilon_{added(i)} = a_i exp(\frac{b_i}{P_{c(i)} + \Delta P_i}) \tag{4.5}$$

where a_i, b_i *and* ΔP_i are three parameters whose calculation from step $(i-1)$ to step (i) is illustrated in the following flow chart:

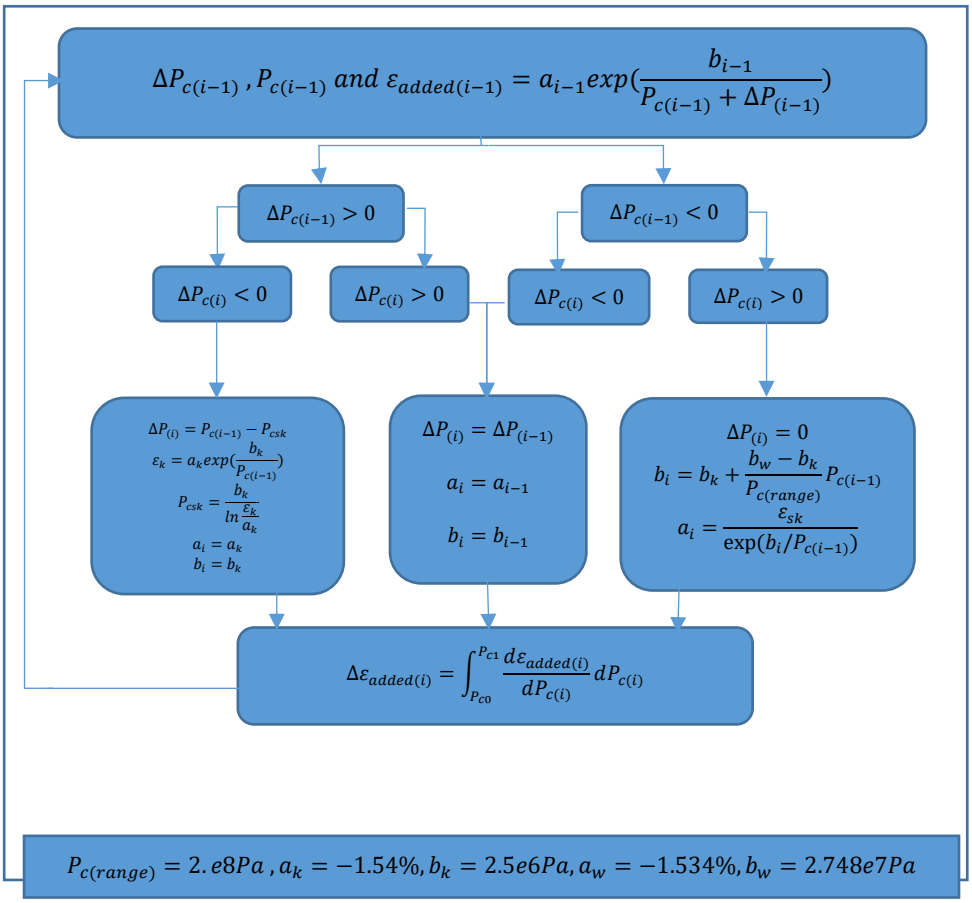

Figure 4.2. Flow chart of numerical algorithm

- Case of ($\Delta P_{c(i-1)} > 0$ and $\Delta P_{c(i)} < 0$):

The inequality $\Delta P_{c(i-1)} > 0$ means that the $(i-1)$ step corresponds to a resaturation path while the inequality $\Delta P_{c(i)} < 0$ means that the i step corresponds to a desaturation path. This indicates a reversal from resaturation (i.e. $\Delta P_{c(i-1)} > 0$) to desaturation (i.e. $\Delta P_{c(i)} < 0$), which requires updating parameters $a_i, b_i \; and \; \Delta P_i$ as shown in Figure 4.2.

- Cases of ($\Delta P_{c(i-1)} > 0$ and $\Delta P_{c(i)} > 0$) and ($\Delta P_{c(i-1)} < 0$ and $\Delta P_{c(i)} < 0$):

In both these cases there is no reversal from resaturation to desaturation, or vice versa, so all parameter values $a_i, b_i \; and \; \Delta P_i$ remain unchanged.

- Case of ($\Delta P_{c(i-1)} < 0$ and $\Delta P_{c(i)} > 0$):

The inequality $\Delta P_{c(i-1)} < 0$ means that the $(i-1)$ step corresponds to a desaturation path while the inequality $\Delta P_{c(i)} > 0$ means that the i step corresponds to a resaturation path. This indicates a reversal from desaturation (i.e. $\Delta P_{c(i-1)} < 0$) to resaturation (i.e. $\Delta P_{c(i)} > 0$), which requires updating parameters $a_i, b_i \; and \; \Delta P_i$ as shown in Figure 4.2.

The added deformation law $\varepsilon_{added(i)}$ defined by equation (4.5) may also be derived with respect to capillary pressure $P_{c(i)}$ to provide the slope $\frac{d\varepsilon_{added(i)}}{dP_{c(i)}}$ of the added deformation law. The added strain differential is then obtained as:

$$d\varepsilon_{added(i)} = \frac{d\varepsilon_{added(i)}}{dP_{c(i)}} dP_{c(i)} = -\frac{a_i b_i exp\left(\frac{b_i}{P_{c(i)}+\Delta P_i}\right)}{\left(P_{c(i)}+\Delta P_i\right)^2} dP_{c(i)} \tag{4.6}$$

and, when the capillary pressure increases from P_{c0} to P_{c1} , the differential can be integrated to obtain the added strain increment as:

$$\Delta\varepsilon_{added} = \int_{P_{c0}}^{P_{c1}} \frac{d\varepsilon_{added(i)}}{dP_{c(i)}} dP_{c(i)} \tag{4.7}$$

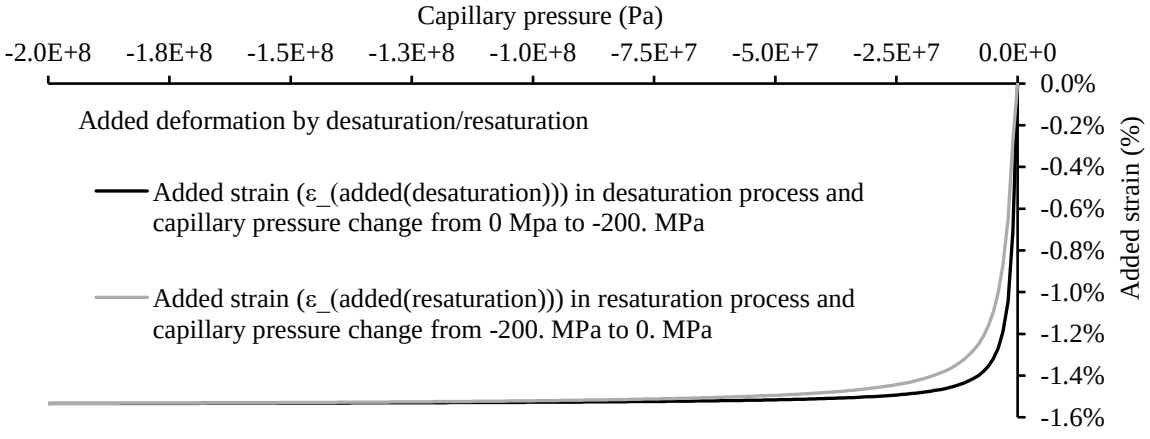

Figure 4.3. Added deformation curves from the proposed model

The stress change $\Delta\boldsymbol{\sigma}$ in the equilibrium equation (2.9) is then written as follows:

$$\Delta\boldsymbol{\sigma} = \Delta\boldsymbol{\sigma_e} + B\Delta(S_r P_c)\mathbf{I} - 3K\Delta\varepsilon_{added}\mathbf{I} \tag{4.8}$$

This model performs very well in predicting the hydro-mechanical behaviour of COx along desaturation and resaturation paths as displayed later in this chapter.

4.3 COx shrinkage/swelling under unconstrained conditions

The proposed model has been employed to simulate the free deformation of COx claystone during desaturation and resaturation experiments carried out by Pham *et al.* (2007) and Zhang *et al.* (2010).

The desaturation/resaturation experiments by Pham *et al.* (2007) are shown in Figure 4.4 together with the results of the numerical simulations.

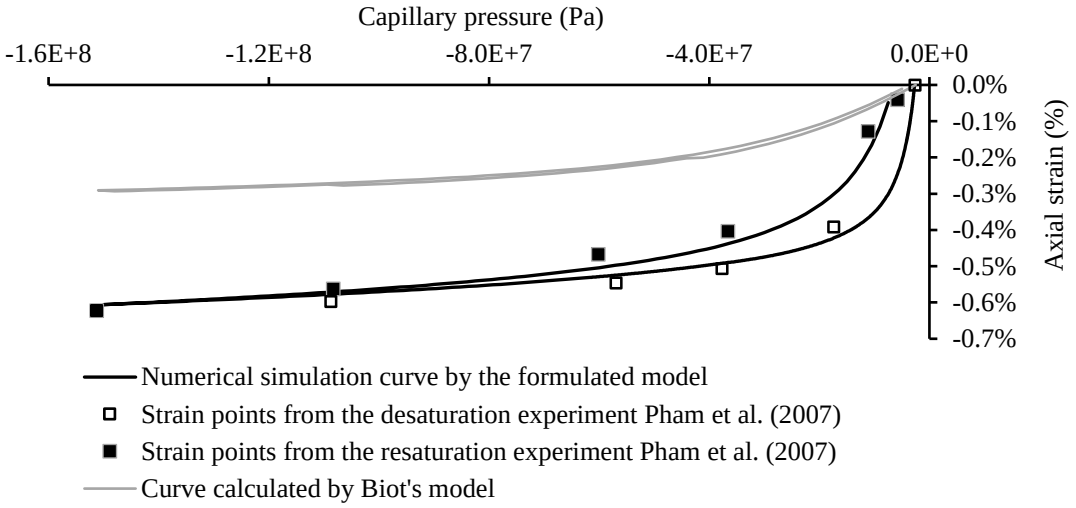

Figure 4.4. Desaturation/resaturation cycle on COx sample (data by Pham, 2007)

Inspection of Figure 4.4 indicates that, when the capillary pressure changes between -60MPa and -150MPa, the deformation is relatively small but it increases considerably when the capillary pressure changes between -2.7MPa and -60MPa. This effect of capillary pressure range on deformation is well captured by the proposed model.

Figure 4.5 shows unconstrained desaturation/resaturation experiments performed by Zhang *et al.* (2010) on COx claystone, which exhibit a similar trend of behaviour. When the COx claystone dries from the initial degree of saturation of around 85% (corresponding to a capillary pressure of -21.5 MPa) to a final degree of saturation of 23% (corresponding to a capillary pressure of -200 MPa), the amount of shrinkage is relatively small.

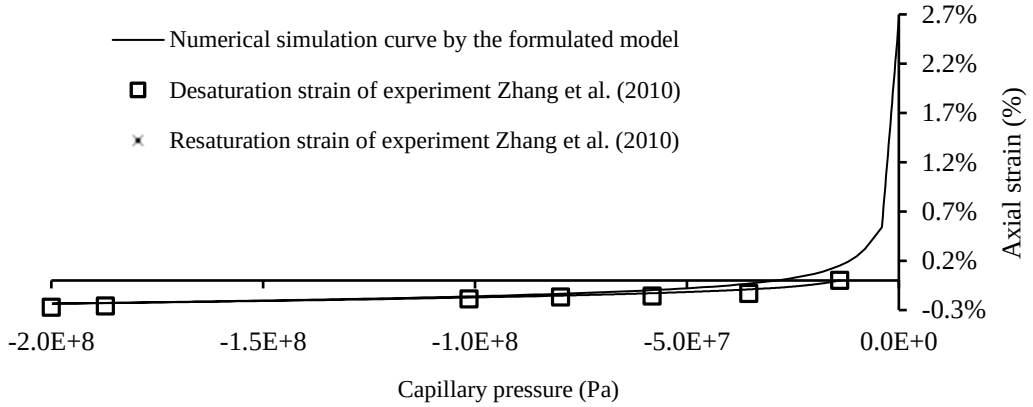

Figure 4.5. Desaturation/resaturation cycle on COx sample (data by Zhang, 2010)

However, as the subsequent wetting brings the material back to full saturation, swelling increases gradually resulting in very high deformations at low levels of capillary pressure. Again this behaviour is faithfully captured by the proposed model.

4.4 COx swelling under constant vertical stresses

Andra (2018) performed a number of wetting tests on COx samples subjected to different levels of constant vertical stress. Three samples drilled from boreholes (Boreholes: EST56054, EST56056 and EST56062) were wetted under a vertical stress of 0.05 MPa, one sample (EST56054) was wetted under a vertical stress of 2 MPa, one sample (EST56054) was wetted under a vertical stress of 12 MPa, one sample (EST56062) was wetted under a vertical stress of 14 MPa. All samples were cylindrical in shape with a height of 10mm and a diameter of 5mm.

By introducing Darcy law into the moisture balance equation, the differential equation (2.51) is employed to simulate water diffusion in the COx claystone with the permeability k defined as:

$$k = \kappa_0 * \kappa_R \tag{4.9}$$

where κ_0 is the intrinsic permeability of the COx claystone equal to $1 \times 10^{-20} m^2$ and $\kappa_R$is the relative permeability under partly saturated conditions. The relative permeability κ_R is defined by equation (2.57) and varies with capillary pressure or degree of saturation.

The numerical simulations followed the same process as in experiments with the initial application of a constant vertical stress (i.e. 14MPa, 12MPa, 2MPa or 0.05MPa) followed by wetting to full saturation via injection of water from the sample surface. The initial degree of saturation of the COx samples was around 85% corresponding to a capillary pressure of $-2.15 \times 10^7 Pa$. Figure 4.6, 4.7, 4.8 and 4.9 show the capillary pressure calculated at different times from the initial unsaturated state to the final saturated state. The entire process of saturation takes around 100 days, which is similar to the time observed during experiments.

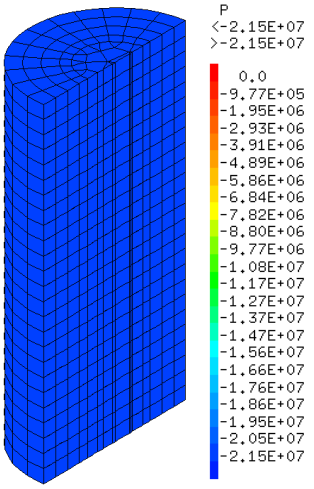

Figure 4.6. P_c after 0 days of wetting

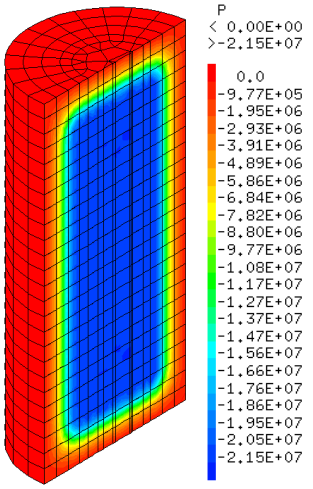

Figure 4.7. P_c after 1 day of wetting

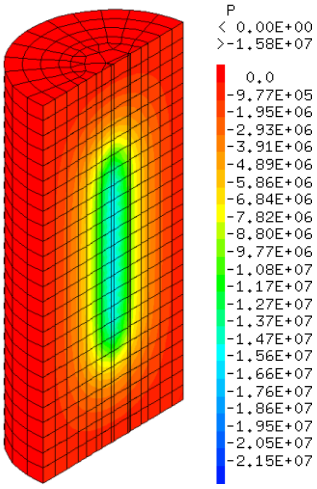

Figure 4.8. P_c after 10 days of wetting

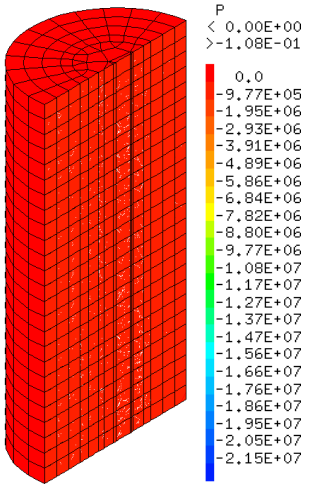

Figure 4.9. P_c after 100 days of wetting

The proposed enhanced form of the Biot model was then employed to simulate the swelling of the COx claystone as discussed in the following.

4.4.1 Case of vertical stress of 14 MPa

Figure 4.10, 4.11 and 4.12 show the computations of constant vertical stress, vertical displacement after 10 days of wetting and damage value after 10 days of wetting, respectively.

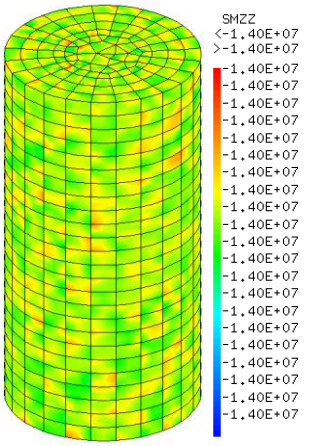

Figure 4.10. Initial vertical stress of 14MPa

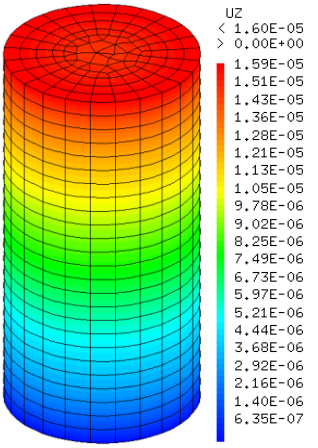

Figure 4.11. Vertical displacement after 10 days of wetting

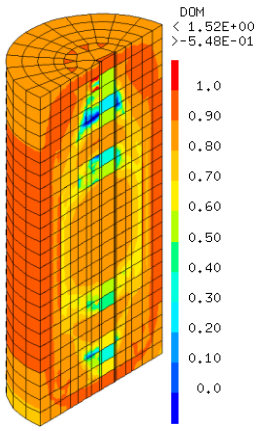

Figure 4.12. Damage value after 10 days of wetting

After 10 days of wetting, the predicted swelling in the axial direction was around 0.15%, which agrees well with the experimental values as shown in Figure 4.13. Comparison between predicted and experimental curves reveals that the proposed model performs very well in simulating the wetting-induced swelling of COx under a vertical load of 14MPa (Figure 4.13).

Given the relatively large vertical stress, the amount of swelling caused by resaturation is relatively small. The peak swelling is equal to 0.24% and occurs after about 0.6 days of wetting. Subsequently, the swelling of the sample reduces and stabilizes around a value of 0.15% after ten days of wetting. Following saturation, the tensile strength of the COx claystone decreases, thus causing the occurrence of material damage. No formation of large cracks was observed in the post-peak phase of the test, which suggests that only micro-fissures, undetected by the naked eye, had formed. This is consistent with Figure 4.12, which shows that after 10 days of wetting the damage value is less than 1 across most of the sample, which explains the absence of large fractures.

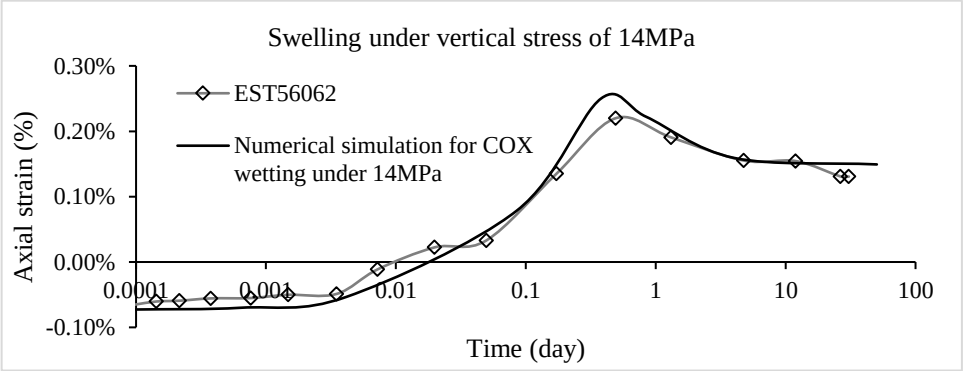

Figure 4.13. Comparison of predicted and experimental swelling

4.4.2 Case of vertical stress of 12 MPa

Figure 4.14, 4.15 and 4.16 show the computations of constant vertical stress, vertical displacement after 10 days of wetting and damage value after 10 days of wetting, respectively.

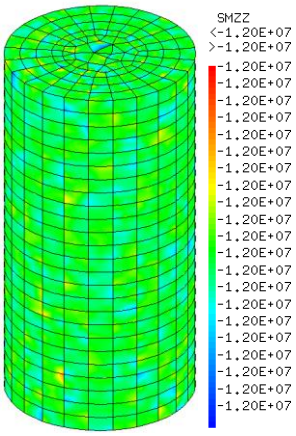

Figure 4.14. Initial vertical stress of 12MPa

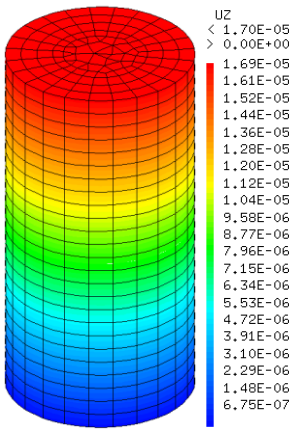

Figure 4.15. Vertical displacement after 10 days of wetting

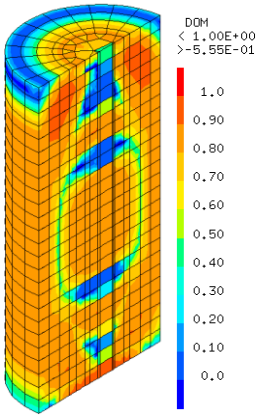

Figure 4.16. Damage value after 10 days of wetting

Also in this case, no formation of large cracks was observed during experiments nor predicted by simulations. Figure 4.16 shows that the predicted damage value after 10 days of wetting was only slightly smaller compared to the previous case when a higher vertical stress of 14 MPa was imposed to the sample.

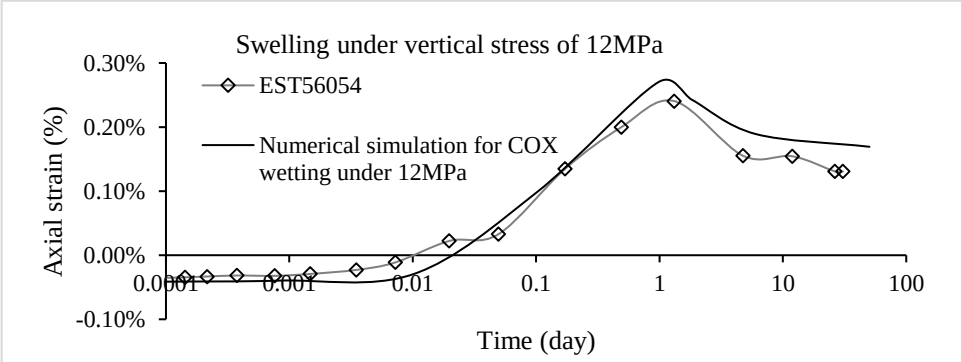

Figure 4.17. Comparison of predicted and experimental swelling

Figure 4.17 shows that after 10 days of wetting the predicted vertical swelling was about 0.17%, which matches relatively well the measured value of 0.14%. Comparison of Figures 4.13 and 4.17 also shows that the amount of swelling is little affected by the variation of the imposed vertical

stress from 12MPa to 14MPa. Nevertheless, the peak value of swelling in Figure 4.17 is slightly delayed compared to Figure 4.13, which suggests an impact of geological stress on swelling rate.

4.4.3 Case of vertical stress of 2 MPa

Figure 4.18, 4.19 and 4.20 show the computations of constant vertical stress, vertical displacement after 10 days of wetting and damage value after 10 days of wetting, respectively.

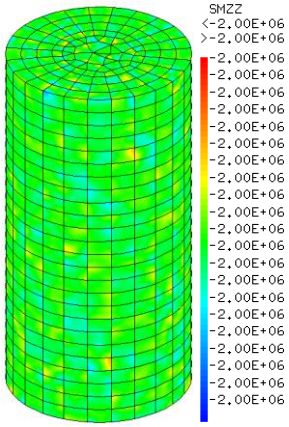

Figure 4.18. Initial vertical stress of 2MPa

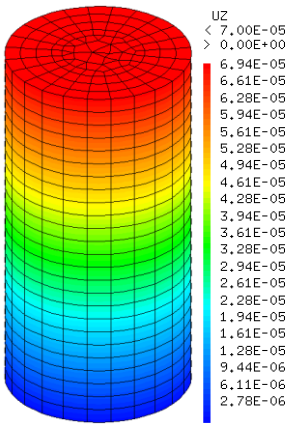

Figure 4.19. Vertical displacement after 10 days of wetting

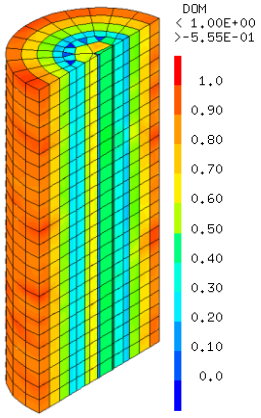

Figure 4.20. Damage value after 10 days of wetting

Comparison of Figure 4.12, 4.16 and 4.20 demonstrates that the distribution of the damage value is significantly influenced by vertical stress. When the vertical stress is 2MPa, the damage value evolves regularly with the radial distance, which is in contradiction with the irregular distribution of damage in the previous two cases when the vertical stresses were 12MPa and 14MPa, respectively. This is also consistent with the swelling curve shown in Figure 4.21, which exhibits a monotonic increase of swelling during wetting, i.e. without the attainment of a peak value as in the previous two cases. The high degree of consistency between predicted and experimental curves in Figure 4.21 confirm once again the predictive capability of the proposed model. Figure 4.21 also shows that after 10 days of wetting the swelling is just above 0.7%, which is about five times the values observed in the previous two cases when the vertical stresses were 12MPa and 14MPa, respectively.

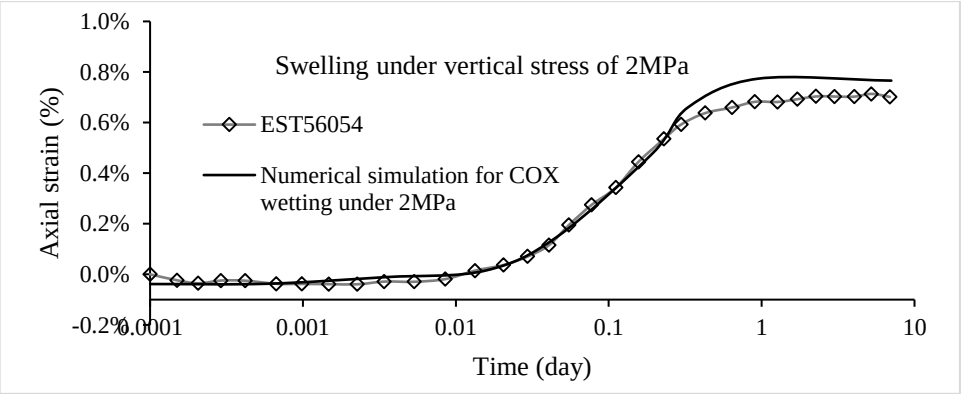

Figure 4.21. Comparison of predicted and experimental swelling

4.4.4 Case of vertical stress of 0.05 MPa

Figure 4.22, 4.23 and 4.24 show the computations of constant vertical stress, vertical displacement after 10 days of wetting and damage value after 10 days of wetting, respectively.

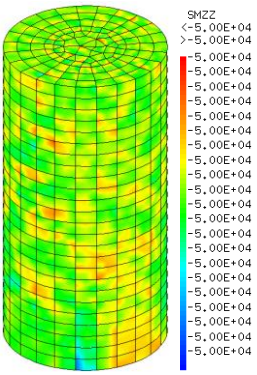

Figure 4.22. Initial vertical stress of 0.05MPa

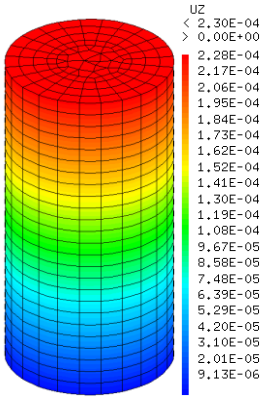

Figure 4.23. Vertical displacement after 10 days of wetting

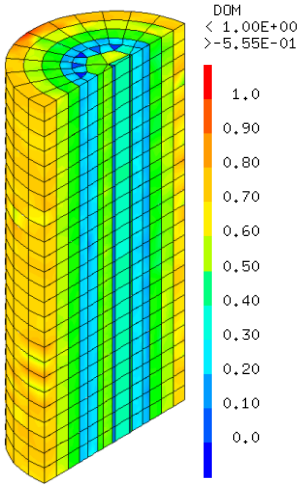

Figure 4.24. Damage value after 10 days of wetting

The maximum axial swelling measured during wetting of the three samples EST56054, EST56056 and EST56062, which were all subjected to a constant vertical stress of 0.05MPa, was 2.29%, 2.62% and 2.82%, respectively. These swelling magnitudes match well the predicted

value of 2.3%, which is attained after about 10 days of wetting (Figure 4.25). Given the small vertical stress, this amount of swelling is also very similar to the case of unrestrained wetting.

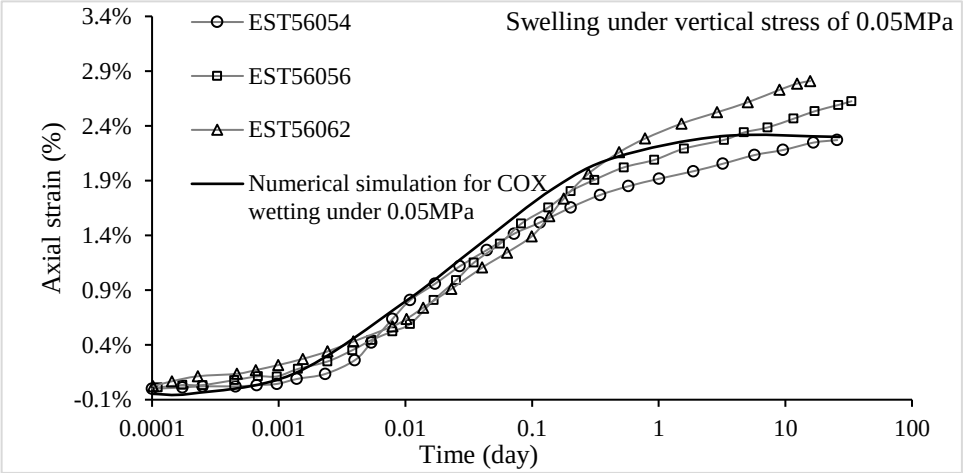

Figure 4.25. Comparison of predicted and experimental swelling

In conclusion, the proposed model can accurately describe the swelling of COx claystone during wetting under different loading conditions. Water diffusion has been coupled to material deformation by means of finite element simulations, which allow to capture the time-dependent evolution of COx swelling during saturation. Finally, the proposed model is capable of successfully describing the development of damage caused by wetting.

4.5 COx swelling pressure evolution under confined conditions

Figure 4.26 shows the experimental setup of Zhang *et al.* (2010) to perform wetting tests on COx claystone samples under axially restrained conditions. This experimental setup was devised to minimize the closure of pores during wetting and to achieve a homogeneous distribution of water inside the sample. During these tests, moist air at a fixed value of relative humidity was circulated along the lateral surface of the sample to facilitate the ingress of water vapour inside the material pores. The consequent increase of degree of saturation and decrease of capillary pressure induce swelling of the sample which is counteracted by the vertical restraint, thus generating an axial pressure that is recorded by the force sensor (Figure 4.26). Figure 4.27 shows the finite element model of the tested sample, whose diameter and height are 40mm and 50mm, respectively. The imposed capillary pressure was computed according to Kelvin's law from the relative humidity of the air circulated along the sample (Figure 4.26).

The numerical simulation of the test was performed in accordance with the following steps:

(1) An initial vertical stress of 2 MPa was applied to the sample together with a uniform capillary pressure of -21.5 MPa. The relative humidity of the surrounding air was subsequently fixed at a value of 77%, which generated desaturation and consequent shrinkage of the sample. This shrinkage caused a reduction of the vertical stress from the initial value of 2 MPa to 0.77 MPa,

which is consistent with the measurements from both tests EST20390-1 and EST20390-2 (Figure 4.28).

(2) Next, the relative humidity of the surrounding air was gradually increased from 77% to 95%, which produced an increase of capillary pressure from -28.5 MPa to -6.7 MPa. This led to a resaturation of the sample and the consequent development of swelling strains which, due to the axially constrained condition, resulted in a marked increase of vertical pressure. Sample failure occurred when the swelling pressure reached a peak value of around 10 MPa. Comparison of numerical and experimental results indicates a good performance of the proposed model from the initial test stages up until sample failure.

(3) Finally, the relative humidity of the surrounding air was left to fluctuate at a value of $95 \pm 3\%$, which caused further damage and plastic deformation of the sample, thus producing a gradual decrease of swelling pressure. Inspection of Figure 4.28 indicates that the proposed model can capture the decreasing trend of swelling pressure during the final stages of the test.

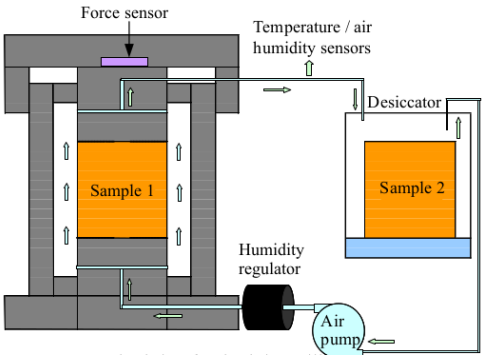

Figure 4.26. Experimental setup for axial swelling pressure test (Zhang et al., 2010)

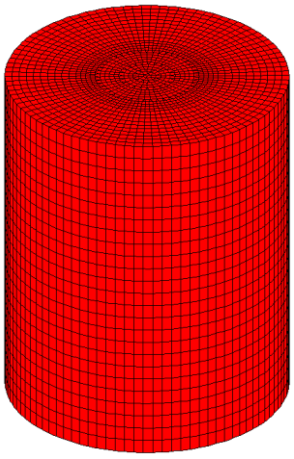

Figure 4.27. Finite element mesh of COx sample

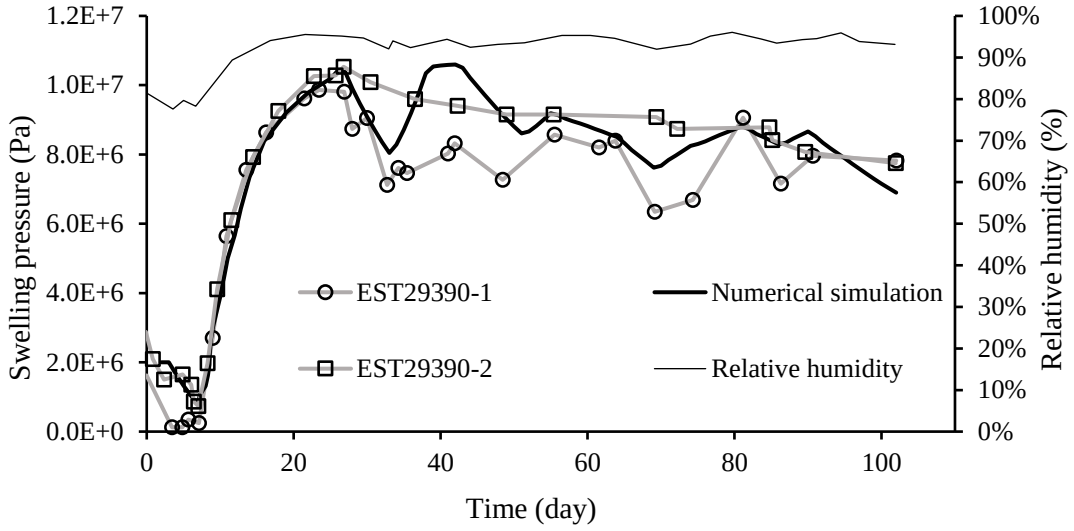

Figure 4.28. Axial swelling pressure test: numerical predictions against experimental measurements by Zhang et al. (2010)

Figure 4.29 illustrates the distribution of the damage value across the sample at the end of the test. In contrast with the damage values in Figure 3.3, which are produced by mechanical loading, in this case the damage is uniformly distributed across the sample. This uniform distribution of damage is also consistent with wetting experiments on COx samples where no evident fracturing was recorded.

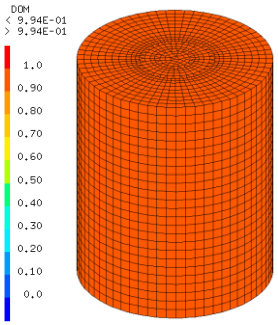

Figure 4.29. Damage value after resaturation under axially restrained conditions

Figure 4.30 shows the swelling cell used by Zhang *et al.* (2010) to perform wetting tests on cylindrical COx claystone samples under volumetric restrained conditions. The constrained sample, having 10 mm height and 50 mm diameter, is wetted from both top and bottom with moist air at controlled humidity or liquid water. The finite element mesh of the tested sample is shown in Figure 4.31, which also indicates that the material is initially subjected to an initial uniform vertical stress of 2MPa. After applying a small vertical stress of 0.5 MPa, a flow of most air at 90% relative humidity is imposed at the top and bottom of the sample. This gas flow is maintained for more than 30 days before imposing circulation of liquid water during more than 100 days.

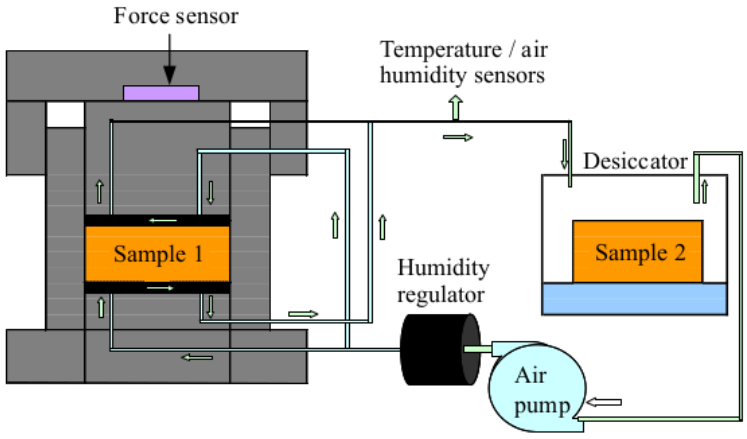

Figure 4.30. Experimental setup for volumetric swelling pressure test (Zhang et al., 2010)

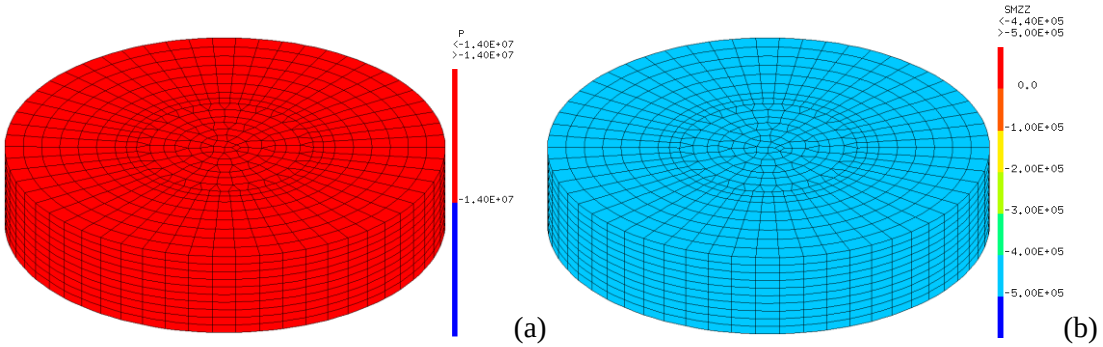

Figure 4.31. Finite element mesh of COx sample and initial stress state: a) Initial capillary pressure of -14MPa and b) Initial vertical compression stress of 0.5 MPa

Figure 4.32 illustrates the variation of the vertical swelling pressure as recorded by the force sensor during the experiment. When liquid water is introduced into the sample, the vertical swelling pressure exhibits a quick rise to 2.5MPa followed by a gradual increase to 3.3 MPa. These values of swelling pressure are far less than those calculated by the standard Biot model. Moreover, if the added deformation law is introduced, the computed pressures are even larger (Figure 4.33) and the mismatch with experimental data becomes greater.

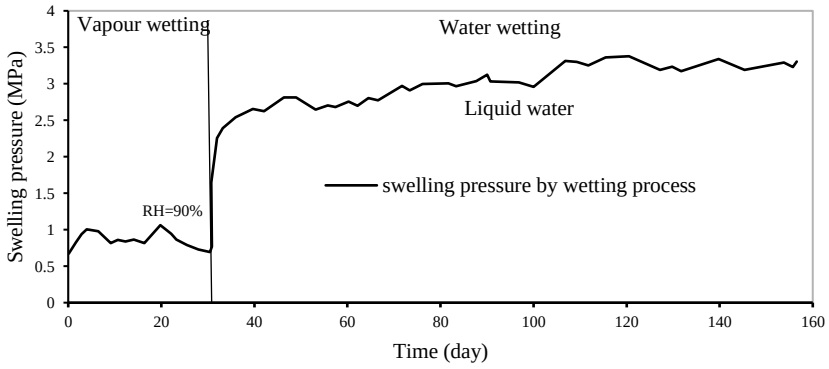

Figure 4.32. Volumetric swelling pressure test: experimental measurements of vertical pressure by Zhang et al. (2010)

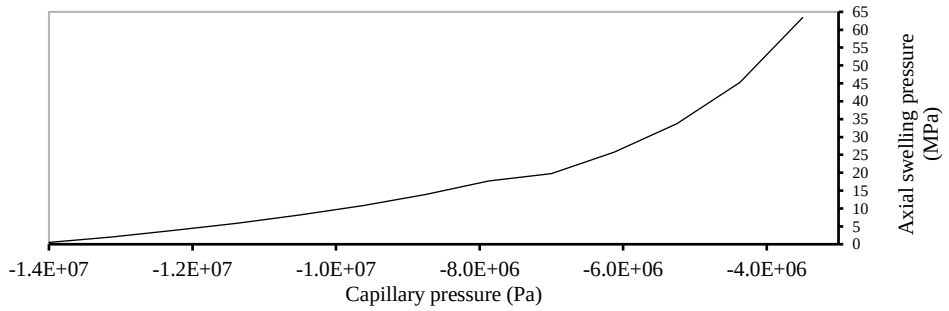

Figure 4.33. Volumetric swelling pressure test: prediction of vertical swelling pressure by proposed model

Simulations of similar volumetric swelling pressure tests were also performed by using other published data on COx claystone (Lebon, 2000; Thury, 1999). In all cases, the numerical simulations tend to overestimate experimental measurements of swelling pressure. There are two possible reasons to explain this difference between numerical and experimental results. The first one relates to the rapid reduction in size of the pores on the sample surface as soon as liquid water comes into contact with the COx claystone, thus resulting in a decrease of the rate of water diffusion. The second reason relates to the particular laboratory setup of the volume-constrained experiment, which does not include a pathway for evacuating air from the material pores, thus resulting in the potential formation of trapped air at the sample core.

The above two mechanisms would prevent water to penetrate the inner region of the sample, thus resulting in an incomplete wetting of the material and a consequently smaller swelling pressure than expected.

4.6 Conclusions

This chapter has presented a hysteretic model that builds upon a standard linear elastic Biot formulation to simulate the large deformation of Callovo-Oxfordian claystone (COx) upon changes of water content. This is the first attempt to enhance a conventional Biot stress formulation to simulate the hydro-mechanical behaviour of COx claystone by introducing an extra deformation law that compensates the inadequacy of the Biot formulation to predict wetting-induced shrinkage/swelling. The numerical simulations of this work generally show a good prediction of the shrinkage/swelling of dried/wetted COx claystone at the scale of laboratory experiments, thus providing a new route for the analysis of the hydro-mechanical behaviour of claystone rocks.

The numerical simulations of this work also provide consistent predictions of damage/plasticity deformations in COx claystone samples subjected to different hydro-mechanical paths. The model therefore provides a basis to predict the evolution of cracks and permeability in geological settings following changes of the material saturation state. In the next chapter, the model will be applied

to simulate the development of permeability inside the fractured zone around the tunnels of underground nuclear waste disposal schemes.

Chapter 5

Self-sealing of fractured Callovo-Oxfordian claystone

This chapter presents the self-sealing of fractured Callovo-Oxfordian argillite samples and the fractured zone. The methods for the self-sealing of COx claystone include hydration and mechanical loads.

5.1 Diffusion of water in fractured COx

5.1.1 Permeability transformation

According to the work of Matallah and La Borderie (2016) and using equation (2.30), cracks estimation has been carried out. The cracks estimated in general coordinate system expresses as follows:

$$\boldsymbol{OUV} = \begin{bmatrix} w_{xx} & w_{xy} & w_{xz} \\ w_{xy} & w_{yy} & w_{yz} \\ w_{xz} & w_{yz} & w_{zz} \end{bmatrix} \tag{5.1}$$

and we assume that the cosine matrix of angle between general coordinate and principal coordinate as follows:

$$\boldsymbol{cs} = \begin{bmatrix} cx1 & cy1 & cz1 \\ cx2 & cy2 & cz2 \\ cx3 & cy3 & cz3 \end{bmatrix} \tag{5.2}$$

Through matrix transformation, the matrix of the principal cracks openings can be expressed as follows:

$$\mathbf{OUV_{123}} = \mathbf{cs}\boldsymbol{OUV}\boldsymbol{cs}^T = \begin{bmatrix} w1 & 0 & 0 \\ 0 & w2 & 0 \\ 0 & 0 & w3 \end{bmatrix} \tag{5.3}$$

In experiment, permeability is tested according to the Darcy's law to calculate how much a fluid flowing through a cross section of materials. However, in the finite element computation, the values of the intrinsic permeability are given at integrations points, which is different from in experiments. Another concern is the assumption of the Parallel-Plate Concept in the cubic law, a constant crack aperture is assumed for the total fracture surface (Figure 2.31), this approach is a very strong hypothesis. Therefore, many authors (Grasberger and Meschke, 2004; Secchi and Schrefler, 2012) make use of an empirical coefficient ξ to correct the standard cubic law:

$$\mathrm{Q} = -\xi\left(\frac{lw^3}{12\mu}\right)\nabla P \tag{5.4}$$

A constant value of ξ was proposed by some authors. However, introduced by Rastiello et al. (2014), this parameter is no longer considered as a constant value and, depends on the following form:

$$\xi = \min(\alpha w^{\gamma}, 1) \tag{5.5}$$

where $\alpha = 5.625 \times 10^{-5} m$ and $\gamma = 1.19$. For the sake of unit homogeneity, Matallah and La Borderie (2016) proposed an equivalent formulation that is not unit dependent:

$$\xi = \left(\frac{w}{w_f}\right)^{\gamma} \quad if\ w < w_f \qquad , \quad \xi = 1 \text{ if w} > \text{wf} \tag{5.6}$$

The parameters $w_f = 278 \mu m$ and $\gamma = 1.45$ are taken form Rastiello experiments performed on mortar specimen. La Borderie and Matallah shown that the transition from diffuse damage to localized crack can explain the meaning of this coefficient, w_f being the crack width value above which cracking can be considered as localized (Matallah and La Borderie, 2016). In the absence of experiments allowing to identify these coefficients on the Cox, the values identified on the mortar will be used.

Using the matrix of principal crack openings $\mathbf{OUV_{123}}$ and the Cubic Law of permeability, the principal permeability, the same as in equation (2.49), expresses as follows:

$$\boldsymbol{\kappa_{123}} = \begin{bmatrix} \kappa_0 + \frac{\xi(w_3)w_3^3}{12L_3} + \frac{\xi(w_2)w_2^3}{12L_2} & 0 & 0 \\ 0 & \kappa_0 + \frac{\xi(w_3)w_3^3}{12L_3} + \frac{\xi(w_1)w_1^3}{12L_1} & 0 \\ 0 & 0 & \kappa_0 + \frac{\xi(w_2)w_2^3}{12L_2} + \frac{\xi(w_1)w_1^3}{12L_1} \end{bmatrix} \tag{5.7}$$

In order to execute diffusion in CAST3M, the permeability has to be transformed into the general coordinate system, the process of transformation is shown as follows:

$$\boldsymbol{\kappa} = \boldsymbol{cs}^T \boldsymbol{\kappa_{123}} \boldsymbol{cs} = \begin{bmatrix} \kappa_{xx} & \kappa_{xy} & \kappa_{xz} \\ \kappa_{xy} & \kappa_{yy} & \kappa_{yz} \\ \kappa_{xz} & \kappa_{yz} & \kappa_{zz} \end{bmatrix} \tag{5.8}$$

5.1.2 Diffusion in unsaturated cracked COx

Fractured COx has excellent self-sealing capability, and this self-sealing succeeded to shut down these fractures, which was proved in small samples' test of laboratory and the large scale of the fractured zone in underground drifts. In laboratory, small samples of COx claystone were fractured by means of splitting tests and, then confined by mechanical loads or resaturated by injecting water or air with controlled relative humidity. The permeability for gas or water were tested during these self-sealing processes.

For testing the self-sealing of the fractured zone, mechanical stress was loaded on the sidewall of underground drift and hydration was carried out inside the boreholes of the fractured zone. In this

chapter, numerical simulation is employed to simulate the hydration processes of samples and the fractured zone.

Therefore, there is a problem of how to describe the diffusion of water in cracked unsaturated porous media. Here, the hydraulic conductivity k of fractured Callovo-Oxfordian argillite is calculated as follows:

$$k = \frac{\rho g(\kappa_0+\kappa_c)}{\mu}\kappa_R \tag{5.9}$$

where κ_0 and κ_c , respectively, are the intrinsic permeability of intact COx and permeability led by fractures. $\kappa_0 = 1 \times 10^{-20} m^2$, κ_c depends on fractures and κ_R is the relative permeability (Figure 2.34).

5.1.3 Calculation of global permeability

Inspection of experiments of Zhang (2013), De La Vaissière et al. (2014) and Davy et al. (2007), we extracted that the gas permeability κ_{gas} and water permeability κ_{water} tested are mean values that were calculated from the following equations:

$$\kappa_{gas} = \frac{2\mu_g L P_{mean} Q_{gas}}{A(P_1^2-P_2^2)} \tag{5.10}$$

$$\kappa_{water} = \frac{\mu_w L Q_{water}}{A(P_1-P_2)} \tag{5.11}$$

The values distribution of the intrinsic permeability in fractured COx samples and the fractured zone are anisotropic due to the anisotropic fractures. Therefore, the tested permeability in experiments usually is a global permeability that is an average permeability between two cross sections (upstream cross-section and downstream cross-section). Figure 5.1 demonstrates a schematic for the calculation of global permeability, S1 and S2 are the upstream cross-section and downstream cross-section, respectively. P1, P2 are the pressures of gas/water.

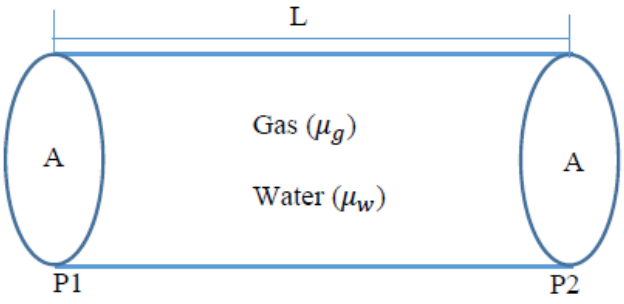

Figure 5.1. A schematic for the calculation of global permeability

We assume gas/water is flowing through the cylinder (Figure 5.1), it is easy to test the flow Q_{gas} or Q_{water} in experiments and, then substitute them into equation (5.10) or (5.11), κ_{gas} and κ_{water} will be obtained. In experiments, the criterion of judging whether fractured COx claystone

accomplished self-sealing during a resaturation process or/and mechanical loads is to check if its final global permeability is less than$1 \times 10^{-17} m^2$. Therefore, the same as in experiments, κ_{gas} and κ_{water} as global gas permeability and water permeability obtained in numerical simulation are also taken to analyse the self-sealing of fractured materials. Comparison between numerical global permeability and experimental global permeability during a resaturation process is the proposed method to validate the proposed model for the hydro-mechanical behaviour of COx claystone.

5.2 Self-sealing of fractured samples

Experiments of Davy et al., (2007) and Zhang (2013) demonstrated the self-sealing capability of fractured COx claystone through mechanical loading or hydration injecting synthetic water and wetting gas at controlled relative humidity. In these experiments, the macro-cracks of Callovo-Oxfordian argillite samples were opened by means of Brazil splitting test (Figure 5.2).

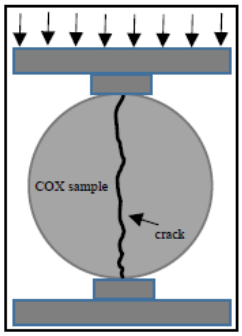

Figure 5.2. Brazil splitting of COx sample

To distinguish the contribution between two methods of mechanical loading and resaturation swelling for the self-sealing of COx, the comparison of the two methods was completed during a period of 6 months (Davy et al., 2007). Tests of steady-state gas flow illustrated that mechanical loading had a significant impact on permeability declination with values by an order of $10^{-14} m^2$ and tests of transient water flow led the permeability varying from $10^{-17} m^2$ to $10^{-20} m^2$ during a resaturation process.

Permeability decrease from mechanical loading mainly induced from a first loading stage when the confining pressure increased from 0MPa to 6MPa. There is a distinct difference observed between the permeability variation of gas injection and permeability variation of water injection tests, that is because the COx claystone swells during hydration, this swelling coupled with mechanical loading extremely improved the self-sealing of COx with several orders' declination of the global permeability. Figure 5.3. shows the setup (LVDT) of gas injection and water injection tests.

Figure 5.3. The setup (LVDT) of gas injection and water injection tests (Davy et al., 2007)

In experiments, macro-cracked samples were installed in LVDT and then it can provide the load of confinement pressure on samples as the requirements of experiments. In the experiments of gas permeability testing (Davy et al., 2007), each macro-cracked sample is placed inside the triaxial confining cell of LVDT with a 0.1-1MPa of hydrostatic pressure loaded initially. Then a gradual increasing of hydrostatic loading was performed and simultaneously at each hydrostatic pressure level the value of crack closure and permeability were recorded. In precise, the confining pressure was loaded from the initial 1MPa to 11MPa in gradual 1MPa steps, from 11MPa to 17MPa in gradual 2MPa. In experiments of water permeability testing, cracked COx samples were wetted 5 days and 24 days, respectively, in order to judge the impacts of wetting time on self-sealing of cracked COx, the details of wetting process will be introduced afterwards.

The flow of gas or water penetrating through the samples can be recorded on the computer, which is brought to calculate the global permeability of the samples. The numerical simulation for the corresponding tests of gas permeability and water permeability will be demonstrated in the following part.

5.2.1 Numerical simulation of gas permeability tests

Figure 5.4 and 5.5 show the preparations of gas permeability test specimens and the method of permeability tests. The size of the three samples are a diameter of 37mm and a length of 40mm.

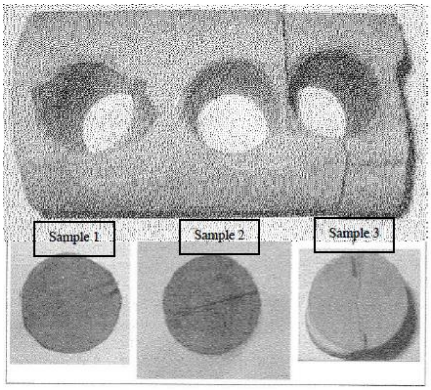

Figure 5.4. Coring of specimens in EST 5600 and macro-cracked samples for gas permeability tests after Brazil splitting (Davy et al., 2007)

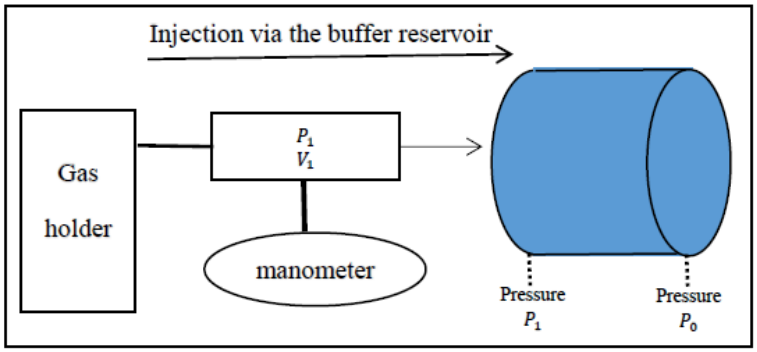

Figure 5.5. The method of gas injection tests

In order to evaluate the effect of the initial cracking on the potentiality of mechanical self sealing, the three different samples were loaded during the splitting tests in order to obtain different states of cracking.

- Sample (1) : localized macrocracking
- Sample (2) : localized macrocracking with higher values
- Sample (3) : diffuse microcracking

(1) Sample 1 EST5600

In the numerical simulation, the size of the numerical mesh is strictly following 1:1 with that in the experiment, a diameter of 37mm and a length of 40mm. the saturation of COx samples *(Davy et al., 2007)* is 0.85, and therefore, their capillary pressure is uniform and a given value of -21.5MPa (Figure 5.6a), and Figure 5.6b shows the Brazil splitting test in numerical simulation where the bottom blue bar is fixed using a boundary in Z direction and, a displacement UZ is loaded on the top blue bar gradually until the numerical global permeability in axial direction of the numerical mesh is approximate to the corresponding initial global permeability of the experiment, and the corresponding displacement UZ is $-2.156 \times 10^{-5} m$. Figure 5.6c shows damage value after the splitting test, and the boundary condition for loading confining pressure for simulating self-sealing of cracked material is shown in Figure 5.6d.

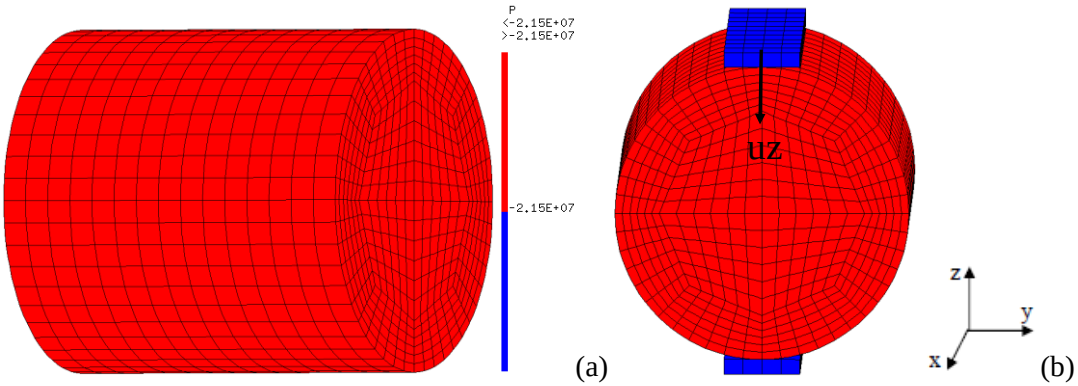

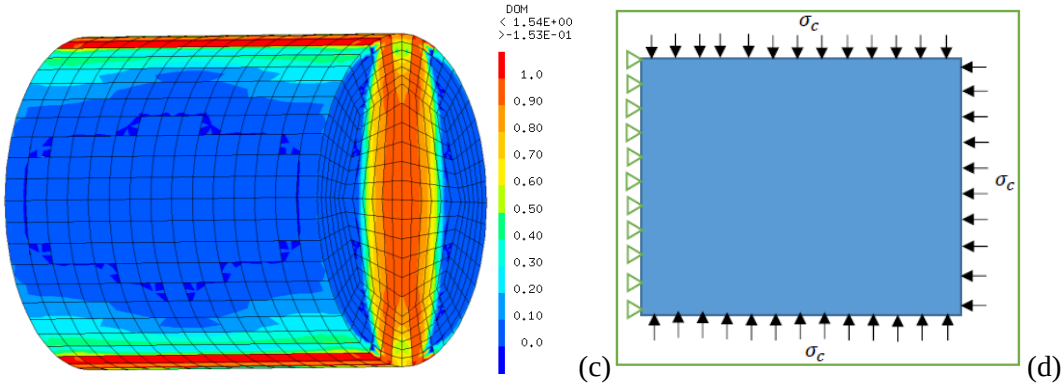

Figure 5.6. numerical simulation of self-sealing of sample 1 EST5600: (a) capillary pressure (b) Brazil splitting test (c) damage value after splitting test (d) boundary condition for simulating self-sealing of COx using confining pressure

The proposed model was used for the analysis of COx uniaxial/triaxial tests and various deformation tests in chapter 3 and 4. It was demonstrated that the model is able to describe the basic hydro-mechanical behaviours of COx. It is important to notice that the coupling between damage and plasticity is important to simulate these experiments (the use of pure damage will drive to null remaining crack with). The quasi unilateral effect is also an important phenomenon to model the crack closure. To explain the effects of confining pressure to the cracks closure of fractured COx, the change of permeability with confining pressure increment is displayed as in the following:

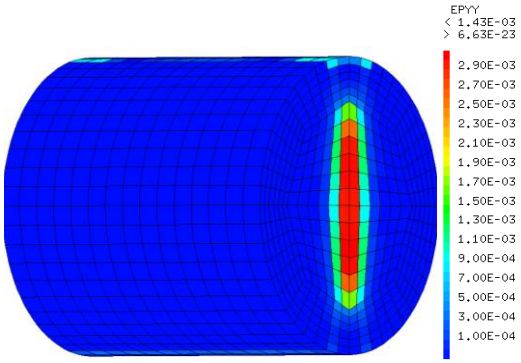

Figure 5.7. Cracks value at confining pressure of 1MPa

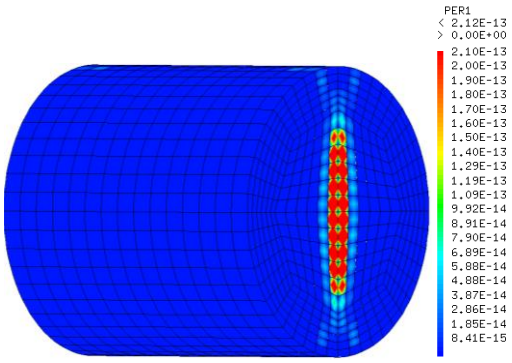

Figure 5.8. Intrinsic permeability at confining pressure of 1MPa

After the Brazil splitting test, and then 1MPa confining pressure was loaded. Figure 5.7 and 5.8 show the cracks value and the intrinsic permeability obtained by the numerical simulation for a confining pressure of 1MPa.

The numerical global permeability (average permeability) for gas in the axial direction of the cylinder calculated from the above intrinsic permeability is approximate to $18 \times 10^{-14} m^2$ which is calibrated from the initial global permeability value of sample1 EST5600 in the experiment *(Davy et al., 2007)*. In experiments, once a sample is broken by splitting test, its cracks value is

obtained, in order to have the correct initial value of cracks opening in numerical simulation, the calibration between numerical and experimental has to be carried out. This calibration is based on a comparison between numerical and experimental global permeability in axial direction of cylinder COx samples so that a cracking state can be found in which the numerical global permeability is approximate to the experimental one, and the cracking state is set as the initial state for simulating self-sealing of cracked COx samples. The cracks value or the intrinsic permeability are presented in the model by a tensor .

For the gas flow along the axial direction of the cylinder, the main factor determining the intrinsic permeability is the cracks EPYY (W_y: a unit strain) in Y direction (the horizontal direction of the cross-section, perpendicular to the axial direction of the cylinder) shown as follows:

$$W_y = Y_i\, W_{ij}\, Y_j = Y_i \begin{bmatrix} w_{xx} & w_{xy} & w_{xz} \\ w_{yx} & w_{yy} & w_{yz} \\ w_{zx} & w_{zy} & w_{zz} \end{bmatrix} Y_j \tag{5.12}$$

Based on the calculated EPYY (W_y) and using the Cubic law, the equation of intrinsic permeability PER1 (K_y) is shown as follows:

$$K_y = Y_i\, K_{ij}\, Y_j = Y_i \begin{bmatrix} \kappa_{xx} & \kappa_{xy} & \kappa_{xz} \\ \kappa_{yx} & \kappa_{yy} & \kappa_{yz} \\ \kappa_{zx} & \kappa_{zy} & \kappa_{zz} \end{bmatrix} Y_j \tag{5.13}$$

Therefore, the subsequent discussion mainly focuses on the variations of the permeability Ky with the increment of confining pressure. Davy et al. (2007) illustrated the initial global permeability for gas of sample 1 EST5600 in axial direction is $17 \times 10^{-14} m^2$ that is less than the maximum of intrinsic permeability $21.2 \times 10^{-14} m^2$ in numerical simulation (Figure 5.8), that is because the distribution of the intrinsic permeability determining by cracks is not uniform. Therefore, it is certain that the maximum value of intrinsic permeability is larger than the global permeability.

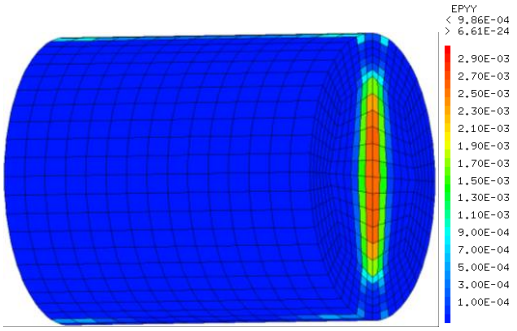

Figure 5.9. Cracks value at confining pressure of 11MPa

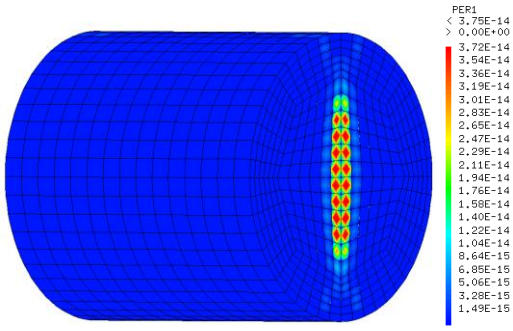

Figure 5.10. Intrinsic permeability at confining pressure of 11MPa

With the increment of confining pressure from 1MPa to 11MPa, either cracks value or intrinsic permeability demonstrated a large scale of declination (Figure 5.9 and 5.10). The maximum value of crack decreases from 1.43mm to 0.986mm at confining pressure of 11MPa; at the same time,

the maximum intrinsic permeability reduces from $21.2 \times 10^{-14} m^2$ to $3.75 \times 10^{-14} m^2$. The declinations of cracks and permeability values are consistent with that occurred in the experiment, which illustrates that the confining pressure has an impact on the self-sealing of fractured COx and proves the capability of the proposed model to describe the mechanism of COx cracks closure during the confining pressure loading process. The confining pressure of 11MPa is slightly lower than the geological stress of Callovo-Oxfordian argillites layer (12MPa-16.5MPa). In order to test what will happen when the confining pressure greater than the geological stress, we have conducted computation for higher values of the confining pressure, the results are shown as following:

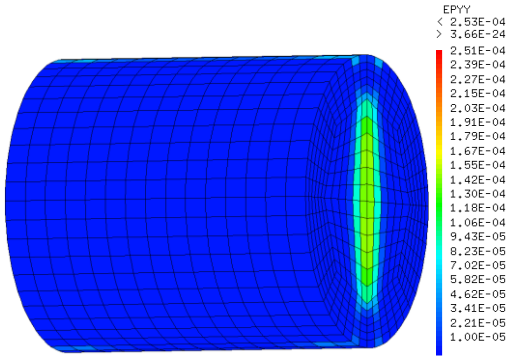

Figure 5.11. Crack value at confining pressure of 17MPa

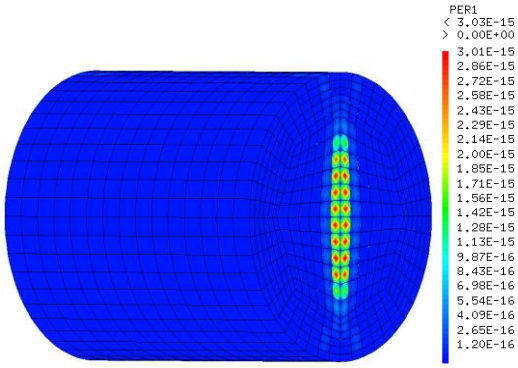

Figure 5.12. Intrinsic permeability at confining pressure of 17MPa

Figure 5.11 and 5.12 demonstrate the crack values and the intrinsic permeability when the confining pressure reaches 17MPa, the maximum crack value declines to 0.254mm, and the maximum intrinsic permeability is $3.03 \times 10^{-15} m^2$. There is a large scale of reduction about 40 times in terms of the intrinsic permeability when the confining pressure increases from 1MPa to 17MPa, the global gas permeability is $4.7 \times 10^{-15} m^2$ in the experiment at confining pressure of 17MPa, and it is approximate to the global gas permeability in numerical analysis at the same confining pressure.

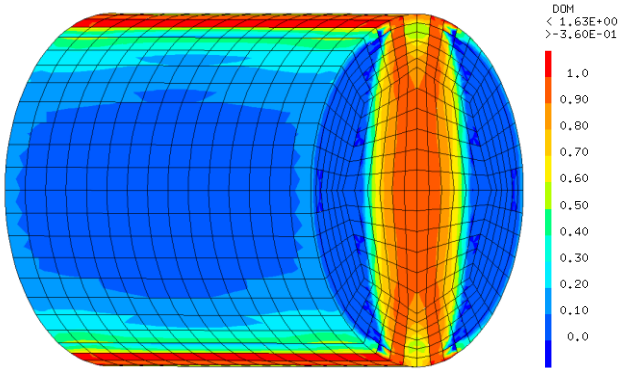

Figure 5.13. Damage at confining pressure of 17MPa

The application of the confinement doesn't create additional damage, Figure 5.13 shows the damage value when the confining pressure reaches 17MPa which can be compared to Figure 5.6c.

Figure 5.8, 5.10 and 5.12 show the cracked permeability when the confining pressures are 1MPa, 11MPa, 17MPa in numerical simulation. To calculate the global gas permeability along the axial direction of the cracked numerical mesh, we assume there is a pure Argon gas flow through the cracked mesh, the flow rate Q_{gas} is calculated using a steady state diffusion model in CAST3M as follow:

$$Q_{gas} = \iint q_{gas} ds \tag{5.14}$$

where q_{gas} are the gas flow crossing through an infinitesimal section ds. κ is calculated in numerical simulation such as in Figure 5.8, 5.10 and 5.12. The other parameters are the same in the experiment of Davy et al. (2007), P_1 is the gas pressure of upstream side (S1 in Figure 5.1) with a value of 1.5MPa and P_2 at the downstream side S2 its value is equal to atmospheric pressure. Q_{gas} is obtained by integration in CAST3M, then the relation between confining pressure and the calculated Q_{gas} is shown as follows:

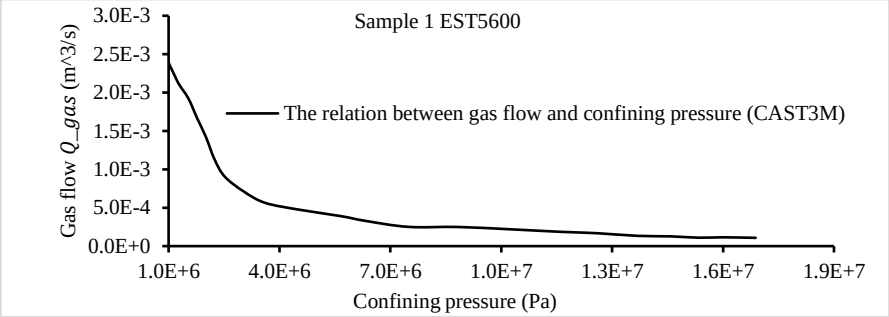

Figure 5.14. Gas flow of fractured COx in numerical simulation

Substituting the values of Q_{gas} into equation (5.10) produces the global gas permeability κ_{gas}:

$$\kappa_{gas} = \frac{2\times(2.2\times10^{-5}Pa*s)\times(1.01\times10^{5}Pa)\times(40\times10^{-3}m)Q_{gas}}{\pi(18.5\times10^{-3}m)^2((1.5\times10^{6}Pa)^2-(1.01\times10^{5}Pa)^2)} \tag{5.15}$$

and then the curve between confining pressure and κ_{gas} from numerical simulation is shown as follows:

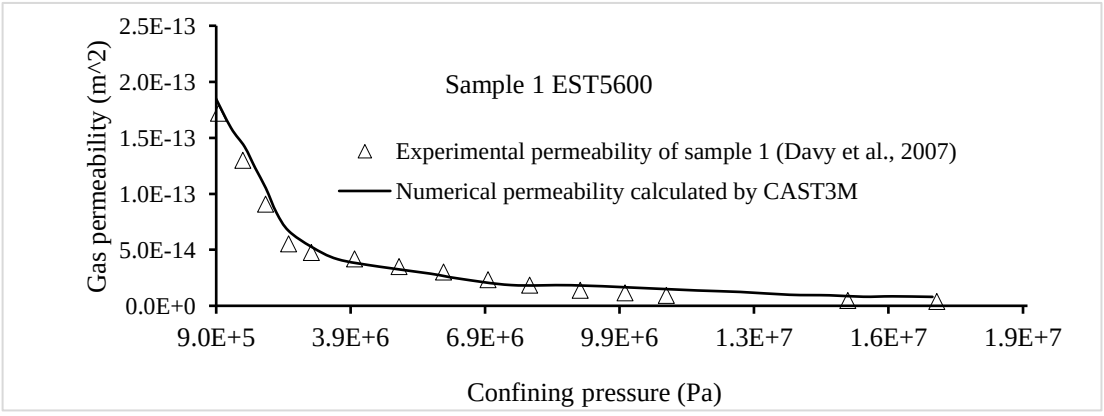

Figure 5.15. Permeability variation with confining pressure

Figure 5.15 illustrates that there is a good agreement between the numerical gas permeability and the experimental gas permeability. Either in the numerical simulation or the experiment, the declination level of the gas permeability is by the order of $10^{-14}m^2$, when the confining pressure reaches 17MPa, the gas permeability of numerical simulation declined to $3.03 \times 10^{-15}m^2$ that is less than the one of the experimental value of $4.7 \times 10^{-15}m^2$. The relation between confining pressure and reduction of permeability expresses that the main self-sealing leading by the confining pressure loading happened before the confining pressure reaches the geological stress, when the confining pressure is equal to or larger than the geological stress, its variation has a little impact on the self-sealing of COx claystone.

(2) Sample 2 EST5600

The initial experimental gas permeability of the cracked sample 2 is $4.4 \times 10^{-13}m^2$, which is almost three times larger than that one of the experiment of sample 1 EST5600. Therefore, the initial cracks value in numerical simulation has an evident increment in comparison with that one of the sample 1 EST5600, and the corresponding displacement UZ for the Brazil splitting test of sample 2 EST5600 is $-2.332 \times 10^{-5}m$. For the sample 2, the increment of confining pressure loading is the same as that for the sample 1, a gradual increment from 1MPa to 17MPa. The variations of the cracks value and the intrinsic permeability during the process are shown as follows:

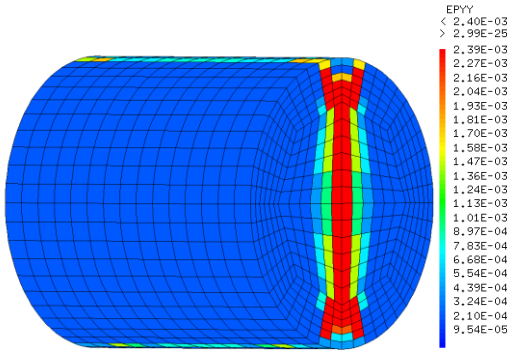

Figure 5.16. Cracks value at confining pressure of 1MPa

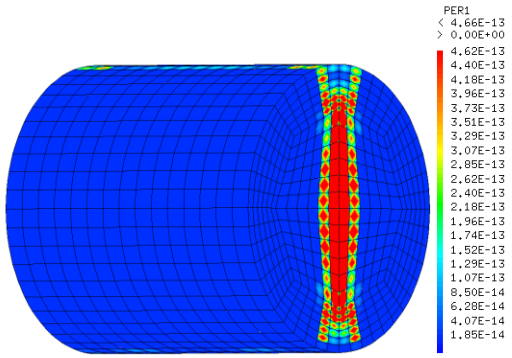

Figure 5.17. Intrinsic permeability at confining pressure of 1MPa

The initial maximum values of the crack width and the intrinsic permeability of sample 2 at confining pressure of 1MPa in numerical simulation are respectively of 2.4mm and $4.66 \times 10^{-13}m^2$, (Figure 5.16 and 5.17). The resulting global permeability is $4.5 \times 10^{-13}m^2$. The larger value of crack opening of sample 2 allows us to check the effect of the initial crack state to the self-sealing of fractured COx during the increment of confining pressure.

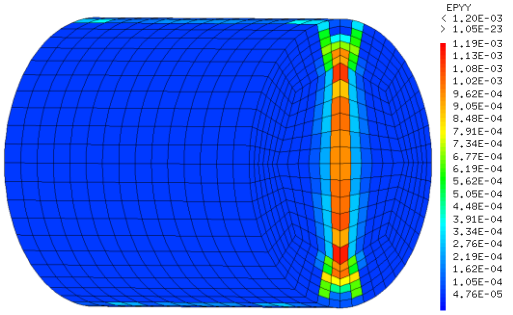

Figure 5.18. Cracks value at confining pressure of 11MPa

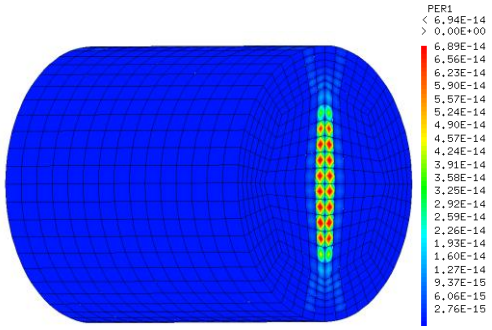

Figure 5.19. Intrinsic permeability at confining pressure of 11MPa

When the confining pressure reaches 11MPa, the maximum values of cracks and the intrinsic permeability reduce to 1.2mm and $6.94 \times 10^{-14} m^2$, respectively. Obviously, the two values are bigger than those ones of the sample 1 when its confining pressure is at the same level, which indicates that the scale of the initial value of cracks pose a negative effect on the self-sealing of COx. The global permeability calculated in numerical analysis is $4.8 \times 10^{-14} m^2$.

Figure 5.20 and 5.21 provide the cracks value and the intrinsic permeability of sample 2 when the confining pressure (17MPa) is over the geological stress of COx claystone layer. The evolution of the calculated global gas flow with the confining pressure shown in Figure 5.22.

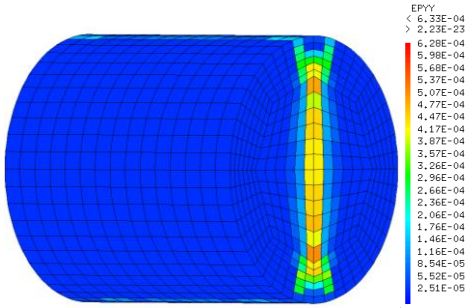

Figure 5.20. Cracks value at confining pressure of 17MPa

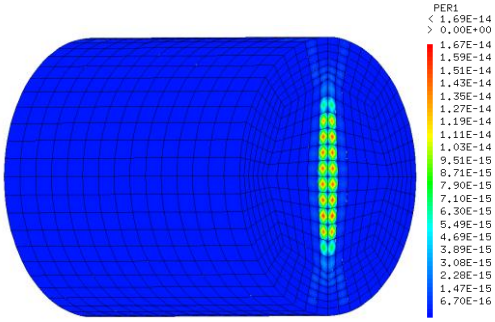

Figure 5.21. Intrinsic permeability at confining pressure of 17MPa

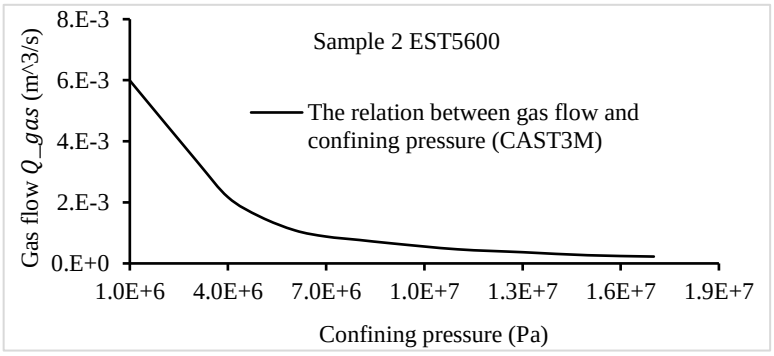

Figure 5.22. Gas flow of fractured COx in numerical simulation

The global gas permeability change of sample 2 with the increment of the confining pressure calculated by numerical simulation is shown and compared to experimental results as following:

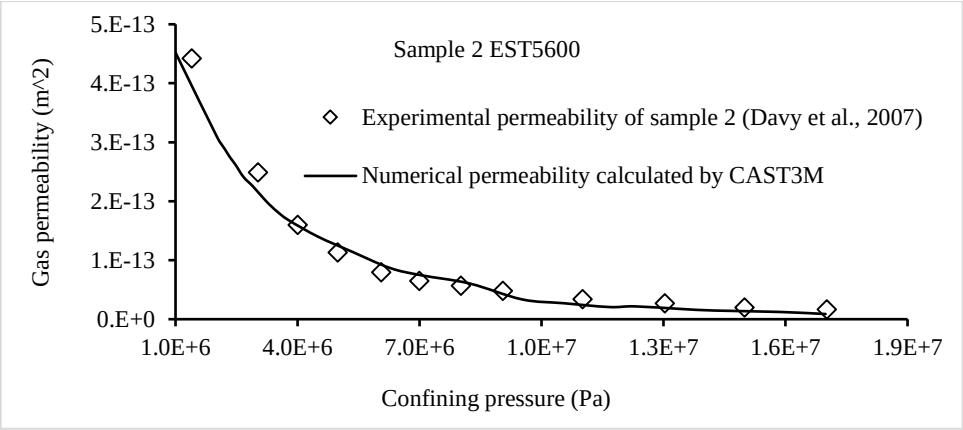

Figure 5.23. Permeability variation with confining pressure

Same as sample 1, the main declination of permeability during the loading process happens before the confining pressure reaches 11MPa. In the numerical simulation, the minimum permeability is $1.69 \times 10^{-14} m^2$ obtained in confining pressure 17MPa, and this value is approximate to the one in the experimental test. Although the big difference of initial permeability between the sample 1 and sample 2 exists, their self-sealing effects are similar either in the numerical simulations or the experiments.

However, experiments were conducted with a smaller initial permeability and the numerical simulation are presented below.

(3) Sample 3 MSE761

This part displays the experimental test of sample 3 MSE761. Comparing with the macro-crack in samples 1 and 2, the sample 3 had a small initial gas permeability of $2.1 \times 10^{-14} m^2$ under 1MPa confining pressure, and this initial maximum value of cracks is lower 8 times and 22 times than that ones of sample 1 and sample 2, respectively. Therefore, the displacement UZ for Brazil splitting test of sample 3 also is smaller than that ones of sample 1 and sample 2, its value is $-1.789 \times 10^{-5} m$. The initial cracks value and the intrinsic permeability in the numerical simulation are shown as following:

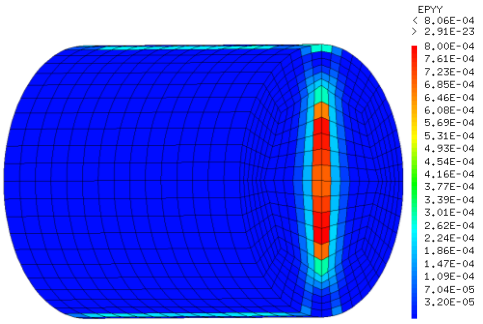

Figure 5.24. Cracks value at confining pressure of 1MPa

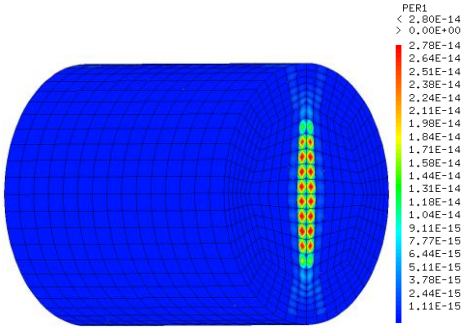

Figure 5.25. Intrinsic permeability at confining pressure of 1MPa

The initial maximum values of the cracks and the intrinsic permeability are 0.806mm and $2.8 \times 10^{-14} m^2$, respectively (Figure 5.24 and 5.25). The calculated global permeability is $2.07 \times 10^{-14} m^2$, which approximates the initial permeability of sample 3 in the experiment. Then the confining pressure increase gradually and its effects on crack closure and the intrinsic permeability are demonstrated as follows:

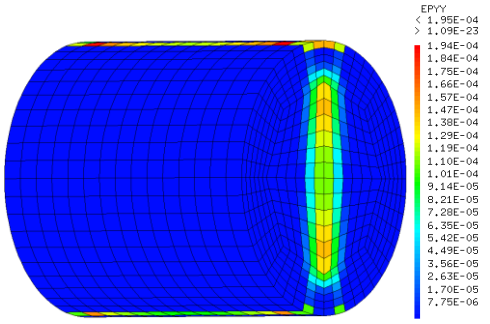

Figure 5.26. Cracks value at confining pressure of 11MPa

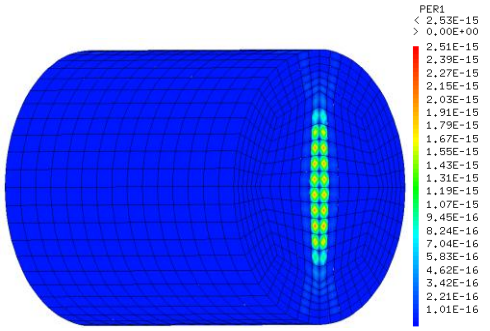

Figure 5.27. Intrinsic permeability at confining pressure of 11MPa

When the confining pressure reaches 11MPa, the maximum value of cracks is 0.195mm, and the corresponding intrinsic permeability is $2.53 \times 10^{-15} m^2$ (Figure 5.26 and 5.27). In comparison with the cracks value and the intrinsic permeability with those of sample 1 and sample 2 at confining pressure 11MPa, these values of sample 3 is lower than almost ten times, the comparison indicates the initial crack performs significant effects on the self-sealing of cracked COx under mechanical loading.

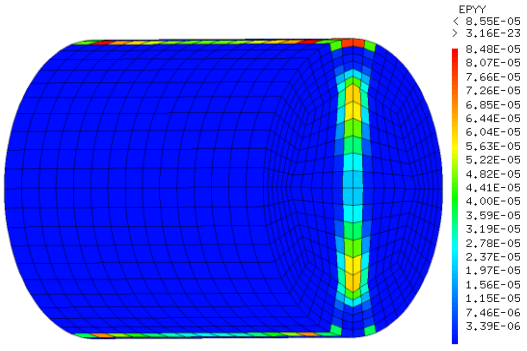

Figure 5.28. Cracks value at confining pressure of 17MPa

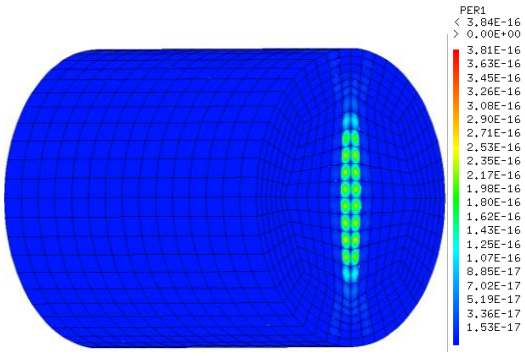

Figure 5.29. Intrinsic permeability at confining pressure of 17MPa

Figure 5.28 and 5.29 show the cracks value and the intrinsic permeability of sample 3 when the confining pressure is over the geological stress of the Callovo-Oxfordian argillite layer (16.5MPa). The maximum intrinsic permeability and its transformation value for the global permeability are $0.0384 \times 10^{-14} m^2$ and $0.019 \times 10^{-14} m^2$, respectively.

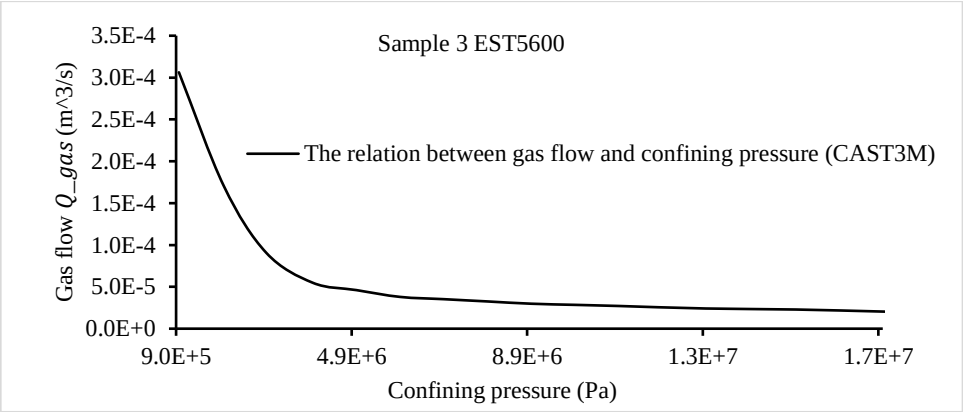

Figure 5.30. Gas flow of fractured COx in numerical simulation

Figure 5.30 illustrates the change of gas flow Q_gas with the confining pressure, and substituting these values into the equation (5.10), the corresponding relation between the gas permeability and the confining pressure is displayed in Figure 5.31.

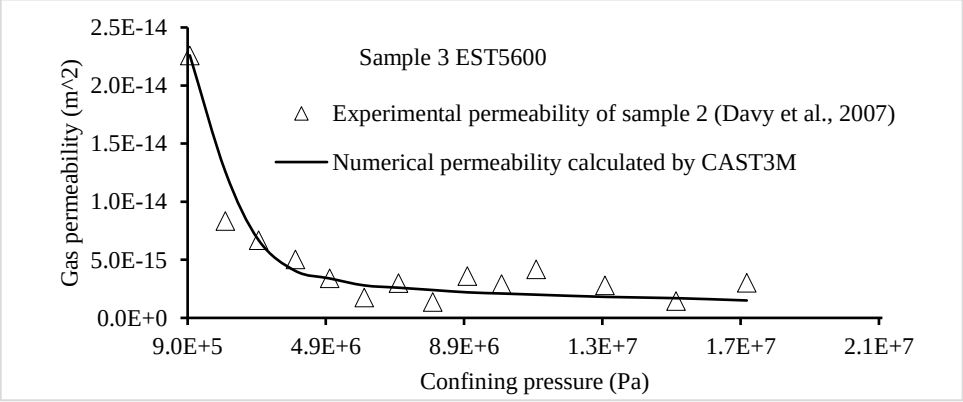

Figure 5.31. Permeability variation with confining pressure

This part simulated the self-sealing performance of sample 1, 2 and 3 using the proposed model, and the good consistencies are obtained between the numerical simulation and the experiments. Macro-cracked samples 1 and 2 illustrate obvious self-sealing during the increment of the confining pressure, the declination of permeability can reach 30 times in comparison with their final values of permeability, and the self-sealing of the micro-cracked sample 3 is also very significant. The results of the above three samples indicate that the confining pressure poses an important impact on the permeability declination no matter the samples have macro-crack or micro-crack in their initial state. In comparison with Zhang (2013) who introduced an empirical relation between the maximum width of cracks and permeability of fractured COx that were validated by experiments, the proposed model can correctly estimate the width of cracks and the subsequent permeability.

In terms of the process of the confining stress loading, the main self-sealing of the fractured COx was obtained by the confining pressure increase from 1MPa to 11MPa. Therefore, when the

confining pressure is approximate to but less than the minimum geological stress, it has big effects on the self-sealing. The self-sealing stabilised relatively when the confining pressure greater than the geological stress.

According to the comparisons between the numerical permeability and the experimental permeability in sample 1, 2 and 3, the numerical results show that our model can describe the self-sealing of fractured COx claystone during the variation of the confining pressure. In terms of the values of the permeability at the confining pressure of 17MPa, all the three samples, their values are larger than $1 \times 10^{-17} m^2$.

The interaction between water and the COx claystone induces significant swelling of the material and is critical to the self-sealing of fractured COx. Therefore, the discussion of COx self-sealing by hydration is necessary, the proposed model will be used to simulate the self-sealing of fractured COx during the resaturation process in the next part.

5.2.2 Hydration by means of relative humidity (Zhang, 2013)

Zhang (2013) carried out an experiment to test the self-sealing capacity of a macro-cracked COx sample during a hydration process by means of flowing wetted air through cracks. The sample was drilled at the Meuse/Haute-Marne underground research laboratory with a size in diameter of 50mm and length of 100mm. After the drilling, it was placed in a special equipment to keep its original hydraulic state (capillary pressure -21.5 MPa), and reduce the impact from the outside environment as much as possible. When the mass of the sample was stabilised, a Brazil splitting test was carried out for opening cracks in the sample, the cracked COx sample is shown as following:

Figure 5.32. Cracked COx sample by Brazil splitting test (Zhang, 2013)

Inspection of Figure 5.32 shows that a main crack was produced by the Brazil splitting test, simultaneously some micro-cracks accompanied along the main crack. After the opening of cracks, a desaturation process and a resaturation process were carried out to explore the cracks expansion during a drying process and cracks closure during a wetting process, respectively. The equipment for the hydraulic tests of the macro-cracked COx claystone sample is shown as following:

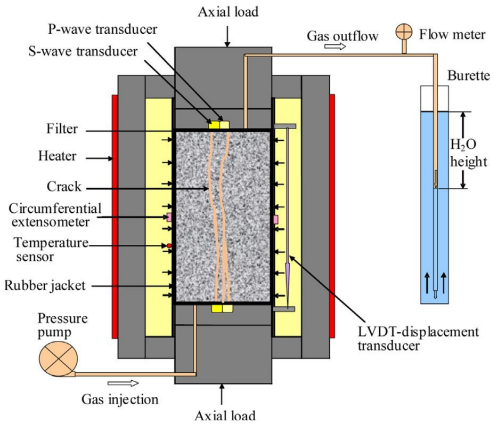

Figure 5.33. Setup for permeability test (Zhang, 2013)

This setup is a triaxial cell with a gas pressure pump and an LVDT-displacement transducer that can be used to pumping gas with controlled relative humidity and testing the displacements normal to the plane of the main cracks, respectively. After placing the cracked sample in the triaxial cell, a confining pressure was loaded on the sample with a value of 1MPa, and this confining pressure kept constant during all the process of hydraulic tests. The sequence of the hydraulic tests is listed as follows:

(1) Loading 1MPa confining pressure and flowing dry gas with a relative humidity of 23% (capillary pressure -200MPa) in between the two ends of the cracked cylinder COx sample for 24 days.

(2) Desaturation 24 days, a re-saturation process lasting 20 days started by flowing wet gas with a relative humidity 75% (capillary pressure -38 MPa).

(3) After the first 24 days resaturation phase with the relative humidity 75%, a second phase with a relative humidity 85% (capillary pressure -21.5 MPa) and a third phase with a relative humidity 100% (capillary pressure 0 MPa) were carried out and lasted 35 days and 26 days, respectively.

According to the procedures of the experiment (Zhang, 2013), the numerical simulation is carried out and is shown in the following part. Figure 5.34 shows the numerical mesh for doing the Brazil splitting test, and the red cylinder and the two blue bars represent the COx sample and the steel bars in the experiment, the initial saturation is 0.85 (capillary pressure -21.5 MPa).

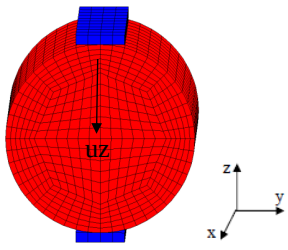

Figure 5.34. Numerical mesh

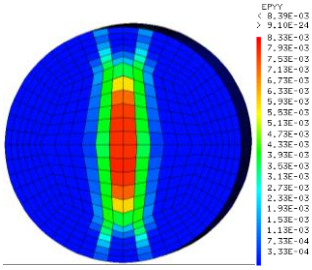

Figure 5.35. Cracks value

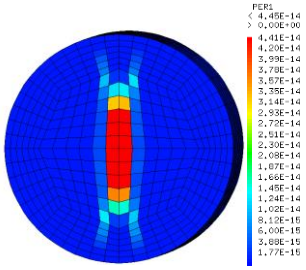

Figure 5.36. Permeability

Figure 5.35 and 5.36 show the cracks value and the intrinsic permeability values and their distribution after the Brazil splitting test. Figure 5.37 shows a schematic diagram for the global permeability computation in numerical simulation.

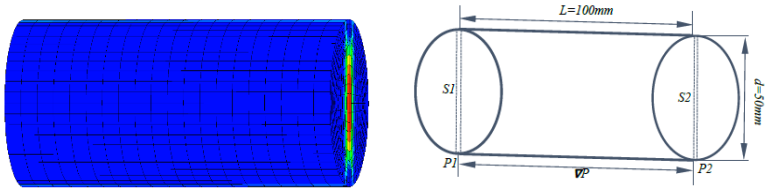

Figure 5.37. Cylinder for showing global permeability computation method

The numerical parameters are the same as in the experiment of Zhang. (2013), P_1 is the gas pressure of the upstream side with a value of 1.5MPa and P_2 is at the downstream side S2, and its value is equal to atmospheric pressure. Q_{gas} is obtained by integration in CAST3M, then the curve between confining pressure and the calculated Q_{gas} is shown as follows:

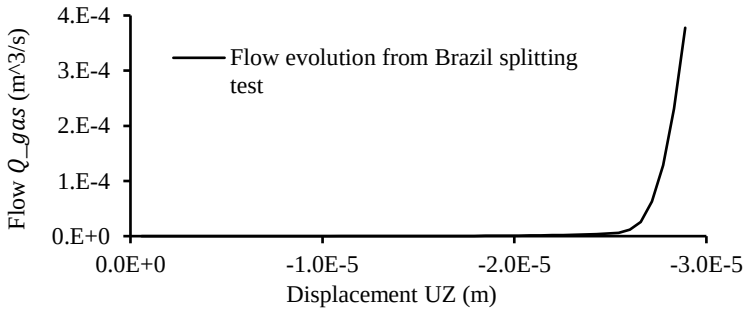

Figure 5.38. Gas flow evolution with the vertical displacement of the upper blue bar in the Brazil splitting test

Substituting the values of Q_{gas} into equation (5.10) produces the global gas permeability κ_{gas}:

$$\kappa_{gas} = \frac{2\times(2.2\times10^{-5}Pa*s)\times(1.01\times10^{5}Pa)\times(100\times10^{-3}m)Q_{gas}}{\pi(25\times10^{-3}m)^2((1.5\times10^{6}Pa)^2-(1.01\times10^{5}Pa)^2)} \quad (5.16)$$

and then the curve between confining pressure and κ_{gas} from numerical simulation is shown as follows:

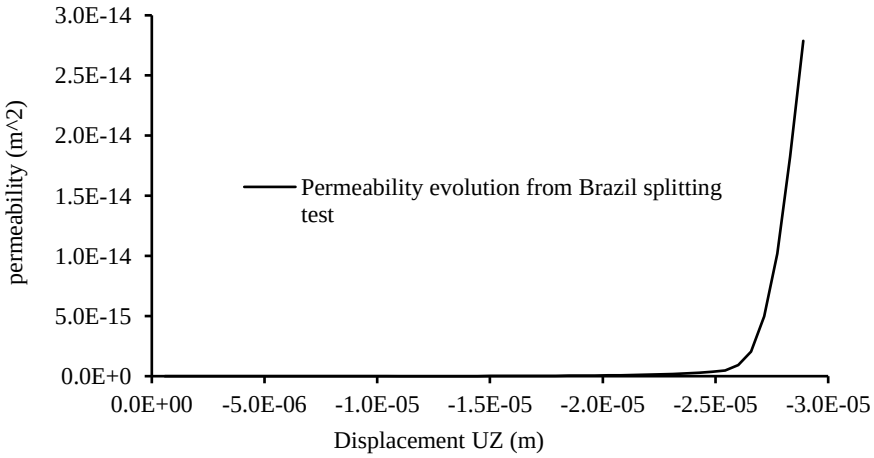

Figure 5.39. Global permeability evolution with the displacement of the upper blue bar in the Brazil splitting test

After the Brazil splitting test, 1 MPa confining stress was loaded, and then a desaturation process was carried out by increasing capillary pressure from -21.5 MPa to -200 MPa. Because the material shrinks during the desaturation process, the cracks of the fractured mesh will expand and the corresponding cracks value, and the intrinsic permeability after the desaturation process are shown in Figure 5.40 and 5.41, respectively.

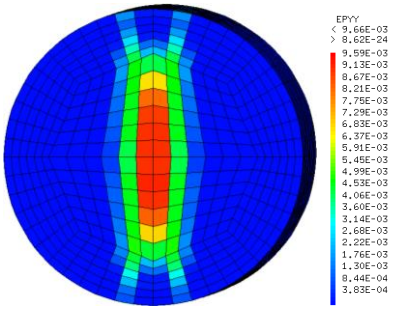

Figure 5.40. Cracks value after desaturation

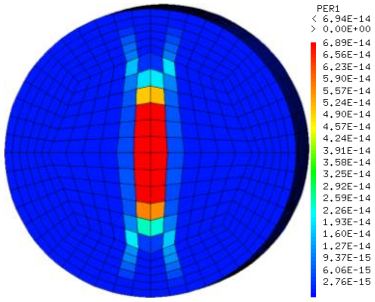

Figure 5.41. Permeability value after desaturation

Inspection of the above two Figures demonstrates that there are not evident increments occurred during the desaturation process no matter in terms of the cracks value or the intrinsic permeability. The reason is that the shrinkage is very small during the desaturation process. Another reason is during the desaturation process, the strength and stiffness of the material goes up, which prevents the development of the cracks.

After the above desaturation process, the numerical simulation of COx cracks self-sealing during a resaturation process is carried out. The resaturation process is implemented by the same procedure as in the experiment Zhang (2013), it is divided into three stages: (1) The fractured COx sample was resaturated from the relative humidity 25% (capillary pressure -200 MPa) to 75% (capillary pressure -37 MPa). (2) Then from the relative humidity 75% (capillary pressure -37 MPa) to 85% (capillary pressure -21.5 MPa). (3) And then increase the relative humidity to 100%.

Figure 5.42 illustrates the cracks value when capillary pressure reaches to 0 MPa, and it has a great declination in comparison with the corresponding value before the resaturation process.

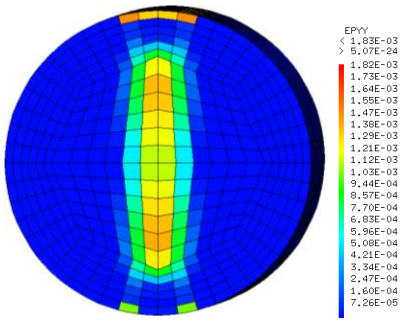

Figure 5.42. Cracks value after resaturation

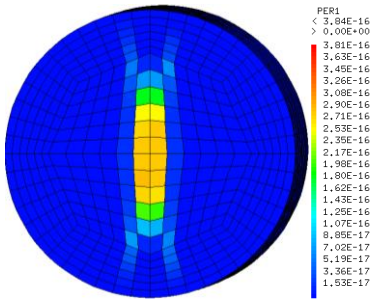

Figure 5.43. Permeability value after resaturation

Figure 5.43 shows the intrinsic permeability during the resaturation process, the maximum value of the intrinsic permeability decreases from $6.94 \times 10^{-14} m^2$ to$3.84 \times 10^{-16} m^2$, the intrinsic permeability of Figure 5.41 and 5.43 are transferred to a global gas permeability in the axial direction of the cylinder sample, the calculated global permeability decreases from $2.996 \times 10^{-14} m^2$ to$4.9 \times 10^{-18} m^2$ during the resaturation process. The declination of the global permeability illustrates that the cracked material accomplished self-sealing. Figure 5.44 and 5.45 show the gas flow and the global permeability with the capillary pressure changes during the re-saturation process, respectively.

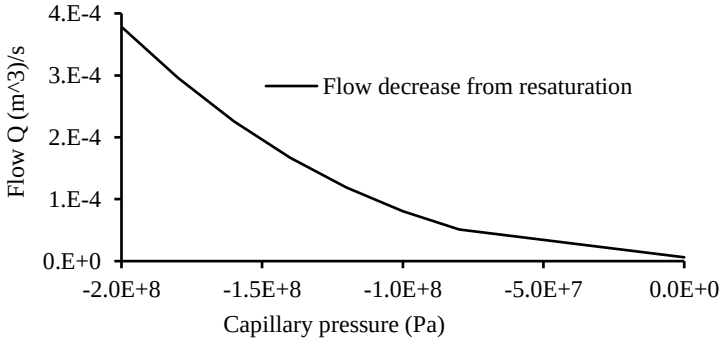

Figure 5.44. Gas flow decreases with the resaturation process

Figure 5.44 illustrates the relation between gas flow and capillary pressure in numerical simulation. Capillary pressure reduction caused crack closure which led to the reduction of conductivity of the cylinder to gas, following the flow reduction, the global permeability numerically decreased from $2.996 \times 10^{-14}\ m^2$ to $4.9 \times 10^{-18}\ m^2$ as shown in Figure 5.45.

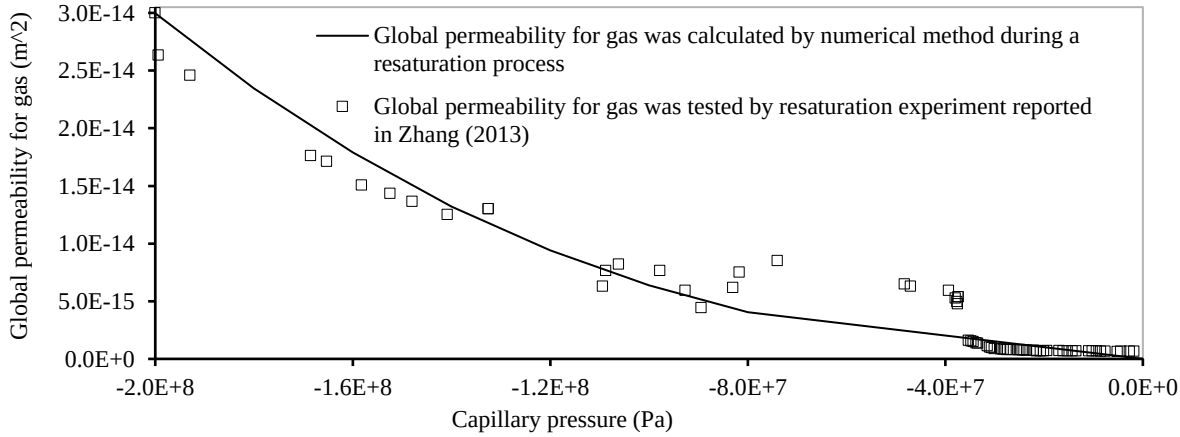

Figure 5.45. Global permeability decrease with the resaturation process

The permeability calculated by numerical simulation decreased from $2.996 \times 10^{-14}\ m^2$ to $2.05 \times 10^{-15}\ m^2$ when capillary pressure decreased from -200 MPa to -21.5 MPa, the corresponding permeability tested in the experiment decreased from $3 \times 10^{-14}\ m^2$ to $1 \times 10^{-15}\ m^2$. The permeability for gas calculated by the numerical simulation decreased from

$2.05 \times 10^{-15}\ m^2$ to $4.9 \times 10^{-18}\ m^2$ when capillary pressure decreased from -21.5MPa to 0MPa. Figure 5.45 illustrates that the numerical gas permeability is consistent with the experimental gas permeability which was tested by the experiment Zhang (2013), and this consistency proves the self-sealing potential of fractured COx and also validated the good performance of this formulated model for the analysis of the COx hydro-mechanical behaviour.

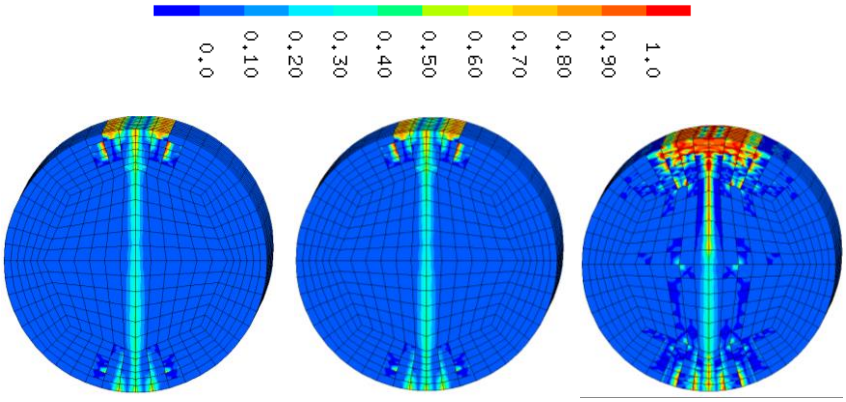

Figure 5.46. Damage after splitting test/desaturation/resaturation

The damage changes with the processes of the splitting test, the desaturation and the resaturation are observed in the numerical simulation. In the experiment, there was not a big difference in terms of damage occurred when the cracked sample desaturated by means of flowing dry gas with a low relative humidity, the explanation is the strength and stiffness of COx went up during the desaturation process which prevents the damage development. However, due to the stiffness and strength of the material went down during the resaturation process, the damage expansion was observed in this period. Figure 5.46 demonstrates that a great consistency on damage development between the numerical results and the experimental observation has been obtained, which indicates the proposed model enables to describe the damage development of fractured COx.

5.2.3 Hydration by liquid water

Davy et al. (2007) carried out self-sealing tests of fractured COx by means of injecting water into cracks of four samples: Sample 2 and 3 (MSE761), Sample 4 and 5 (MSE748). As presented in Andra (2005), in order to have the similar stress condition during plug coring when it was at the depth of 490m underground, a concrete matrix and metallic springs were loaded on the lateral and axial directions of the plug. To avoid the modification of water content of the samples, a watertight envelope was employed until the permeability tests.

Due to the self-sealing property of fractured COx claystone, once the water is flowing through cracks, the intrinsic permeability of cracked sample declines sharply. The material almost recovers its initial impermeability. Therefore, a kind of pulse flow was designed to test the global water permeability during the resaturation process. This designed procedure is detailed as follows: 1) 0.3MPa is loaded as the initial confining pressure, 2) free draining on the downstream side of

cylinder sample in the axial direction, at the same time impose water pressure on the upstream side, 3) when the injecting water flowed through the whole cracked sample and filled the cracks from Brazil splitting, or water flowed out of the downstream side, a gradual increment of confining pressure was carried out from 0.5MPa to 3MPa, 4) both of upstream side and downstream side are imposed by water, 5) a pulse increment of water pressure was put on the upstream side of the sample in order to test the global permeability, 6) in the resaturation process, a gradual increment of confining pressure was carried out by the levels: 3MPa, 5MPa, 11MPa, 13MPa and 17MPa. At each confining pressure level, permeability was measured the moment either after confining pressure loading or after several hours under a given confining pressure.

However, there is evident interaction existing between water and the COx claystone that induces decohesion and swelling of COx . This interaction led to a rapid permeability declination of the fractured COx when water flow through the cracks, the great swelling of COx during the resaturation process makes significant contributions to the declination. The experiment of Davy et al. (2007) provided evidence to the self-sealing of a fractured COx sample during a water injecting process and the crack change of the fractured COx between before water injection and after water injection is shown as follows:

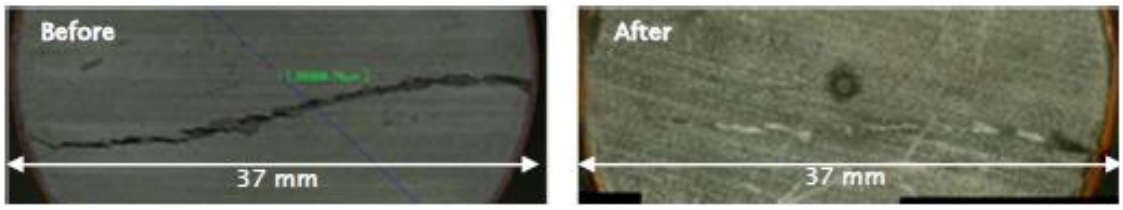

Figure 5.47. The self-sealing causing by water injection

In order to explore the impacts of both of water wetting and wetting time on self-sealing of cracked COx, the two experiments (samples 2 and 5) are selected to carry out the numerical simulation. The wetting process of sample 2 lasted 5 days in the experiment and the corresponding process of sample 5 lasted 24 days, the difference of their wetting time is the reason why they are selected for numerical simulation.

(1) Self-sealing of sample 2 MSE761

The sample 2 MSE761 is a cylinder with a diameter of 37mm, and an axial length of 40mm, its mesh for the numerical simulation and initial capillary pressure are shown in Figure 5.48. Based on the initial capillary pressure, we can obtain the initial values of Young Modulus, fracture energy and tensile strength. During the resaturation process, the capillary pressure changes conforming to the the process of water diffusion. Therefore, the basic parameters that depends on capillary pressure are updated during the process conforming to the method described in chapter 3.

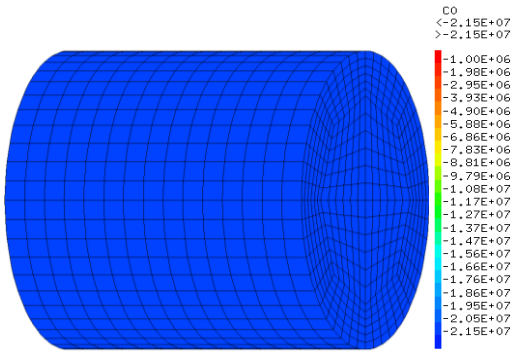

Figure 5.48. The initial capillary pressure

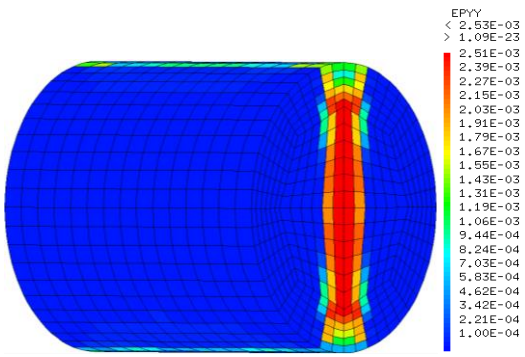

Figure 5.49. The initial cracks EPYY

Figure 5.49 illustrates the cracks value after splitting obtained from the numerical simulation and, the corresponding intrinsic permeability resulting from these cracks are displayed in Figure 5.50. In comparison with the initial values of cracks and intrinsic permeability in previous gas tests, the initial values in Figure 5.49 and 5.50 do not have a significant difference, that is because the properties either in gas tests or in water tests are similar before the water flow imposed. Strictly keeping consistent with the procedures in experiments of Davy et al. (2007), the initial confining pressure 0.3MPa was loaded in numerical simulation as the first step. And then keeping the downstream side draining, the water flow was imposed on the upstream side, this step was numerically achieved by means of loading the capillary pressure 0MPa on the upstream side. Figure 5.51 demonstrated a cutting section of the cylinder along its axial direction when the capillary pressure 0MPa was loaded 0.0001 day, due to the tremendous intrinsic permeability leading from splitting test, a rapid water flow was running along the cracks.

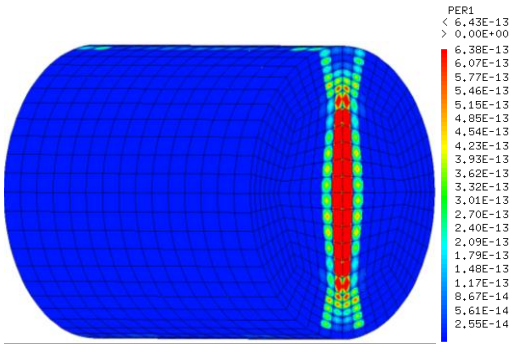

Figure 5.50. The initial intrinsic permeability

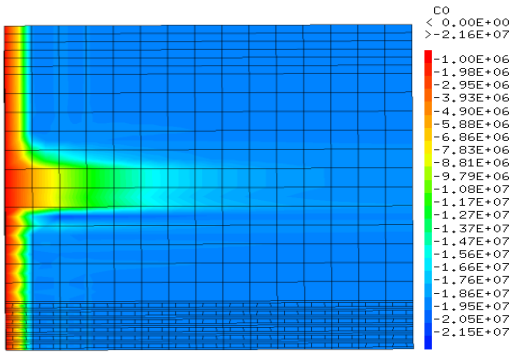

Figure 5.51. The water flow in cutting section

Figure 5.52 displays the state of capillary pressure when the water flow through the macro-crack of the cutting section in 0.001 day. At the same time, a whole state of capillary pressure in the numerical mesh is provided. The distribution of capillary pressure demonstrates the great difference of diffusion rate between the macro-cracked area and the intact area, which implies the large gap of the intrinsic permeability and the increment of the intrinsic permeability accelerate the water flow dramatically. In the experiment, the process of water flow marching through the cracked cylinder was accompanied by a mechanical and a chemical interaction between water and

the COx claystone. It is not clear whether the chemical interaction is good for the declination of the intrinsic permeability and the self-sealing of the fractured COx, but there is distinct evidence showing that the hygro-mechanical interaction produces swelling of COx that is thought to be the main reason of impermeability recovering and self sealing of COx claystone.

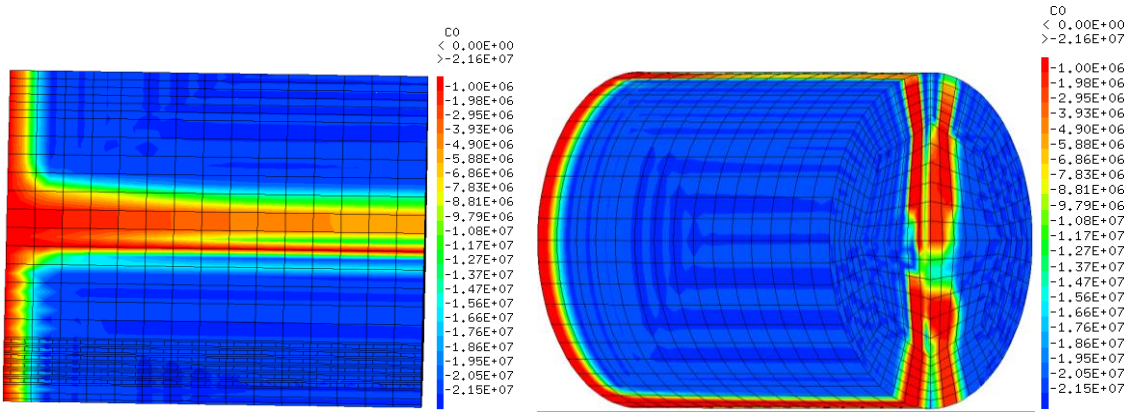

Figure 5.52. Water flow out of the downstream side in cutting section and the capillary pressure of the cracked cylinder

When water flows out of the downstream side of the cylinder, the confining pressure gradually goes up to 3MPa. Then water is imposed on both of the upstream and downstream sides, the state of Uy displacement and of the cracks after this imposition are shown in Figure 5.53 and 5.54. The Uy displacement of the two ends of the cylinder is larger than in the middle part and demonstrates the great impact of the COx swelling during the resaturation process on the deformation of the fractured material. The first moment, water contacts with the two ends of surface of the cylinder, and it takes time for water penetrating into the inner part of the fractured sample, therefore, the swelling both of upstream and downstream sides are larger than that of the cylinder middle part. Figures 5.49 and 5.54 illustrate a distinct declination of cracks width value before and after the resaturation process. The decrease of cracks width value proves that the resaturation is very helpful to cracks closure. Of course, the closure of cracks induces a severe reduction of the intrinsic permeability automatically. The extent of this decrease can be seen through the comparison between Figure 5.50 and 5.55.

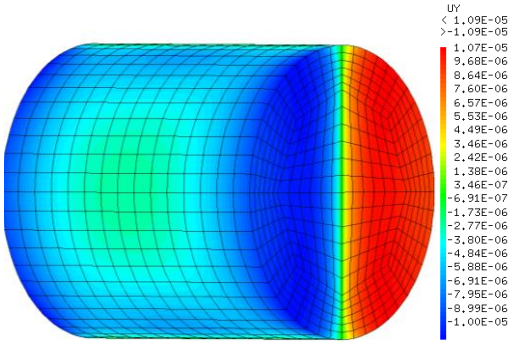

Figure 5.53. Displacement after the initial water flow

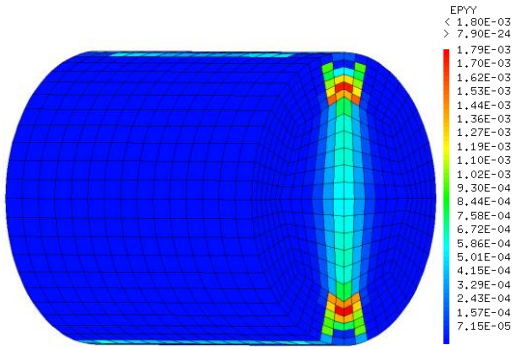

Figure 5.54. The cracks value

The maximum value of the intrinsic permeability after initial water flow is $6.33 \times 10^{-17} m^2$ (Figure 5.55), and the corresponding global/average permeability for water at that time in the axial direction of the cylinder is around $2.\times 10^{-17} m^2$, which is larger than $1.\times 10^{-17} m^2$ which is the standard to judge if the fractured COx accomplishes self-sealing.

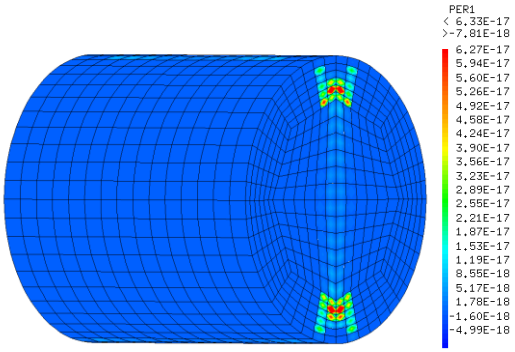

Figure 5.55. Permeability after the initial water flow

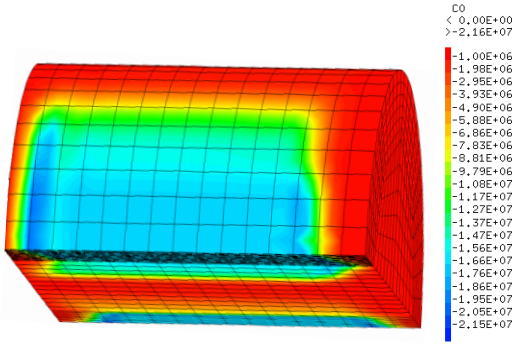

Figure 5.56. Capillary pressure in 5 days diffusion

The confining pressures 5MPa, 11MPa, 13MPa and 17MPa are loaded sequentially in the numerical simulation by a time interval of one day, the interval time is provided for water penetrating into the material. Due to the extremely low permeability of the uncracked material, the penetration is very slow inside the material with the exception of the cracked area. Figure 5.52 and 5.56 demonstrate the capillary pressure of the 0.1day and the 5th-day diffusion, and we can find that the penetration of water spreads along the places of the fractures. Therefore, the water diffusion mainly scattering from the two ends of the cylinder and the central section, whereas there is dry area still remained in 5 days due to the low permeability of uncracked area limiting water diffusion. In fact, following the diffusion process, the swelling of material, the cracks closures and the declining of intrinsic permeability are occurring at the same time. The displacement, cracks value and intrinsic permeability in 5 days are shown in Figure 5.57, 5.58 and 5.59.

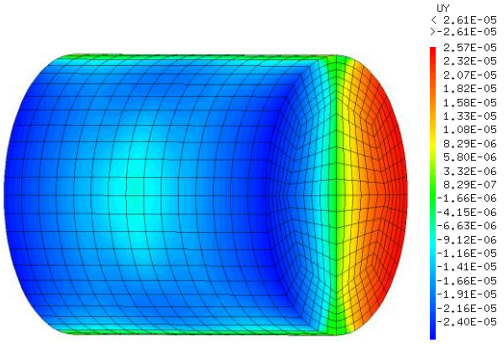

Figure 5.57. The displacement in 5 days

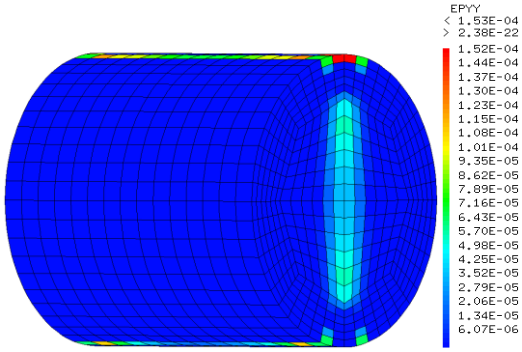

Figure 5.58. The cracks value in 5 days

The confining pressure reaches 17MPa, and it limits the expansion of displacement caused by the swelling during the re-saturation process. Therefore, the displacement values are very small,

whereas the contribution of the swelling to the displacement can be extracted from the comparison between Figure 5.53 and 5.57. Of course, the swelling of the material makes a decisive contribution to the closure of cracks, the maximum value of cracks decreases from the initial state of $2.53 \times 10^{-3} m$ to $1.53 \times 10^{-4} m$.

Within 5 days of re-saturation, the maximum intrinsic permeability reduces from $6.33 \times 10^{-17} m^2$ to $1.15 \times 10^{-19} m^2$, and the global water permeability reduces from $2.\times 10^{-17} m^2$ to $5.67 \times 10^{-20} m^2$, while the initial permeability is of $10^{-20} m^2$ (Figure 5.61). The value of the final global water permeability indicates the cracked material accomplished self-sealing through the re-saturation process.

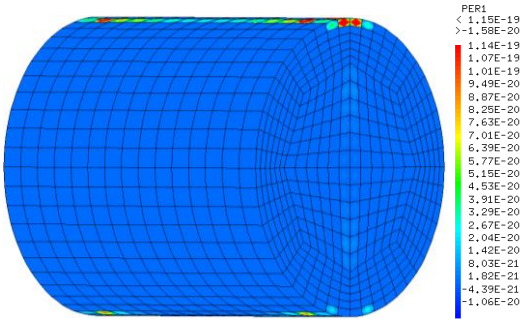

Figure 5.59. The intrinsic permeability in 5 days diffusion

Figure 5.50, 5.55 and 5.59 shows the evolution of the permeability during the five days of resaturation obtained by the numerical simulation. The evolution of the water flow Q_{water} obtained by the numerical simulation is shown as follows:

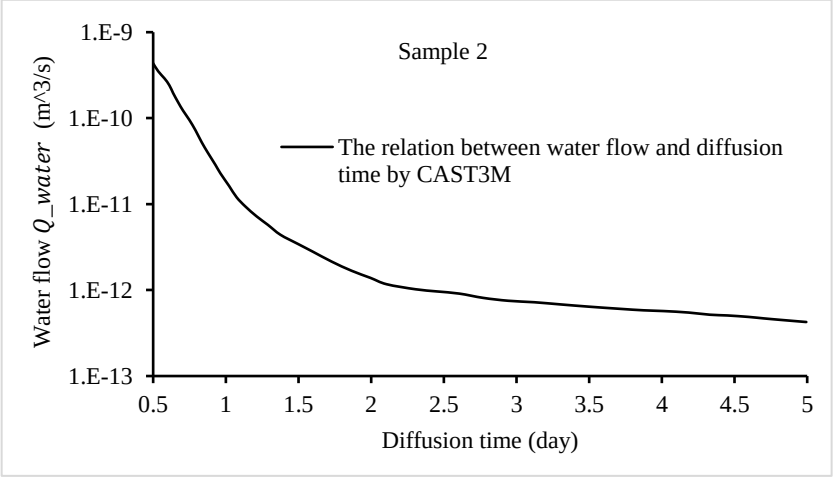

Figure 5.60. The curve of water flow with the diffusion time

The evolution of the global permeability is obtained using the water flow and shown as following:

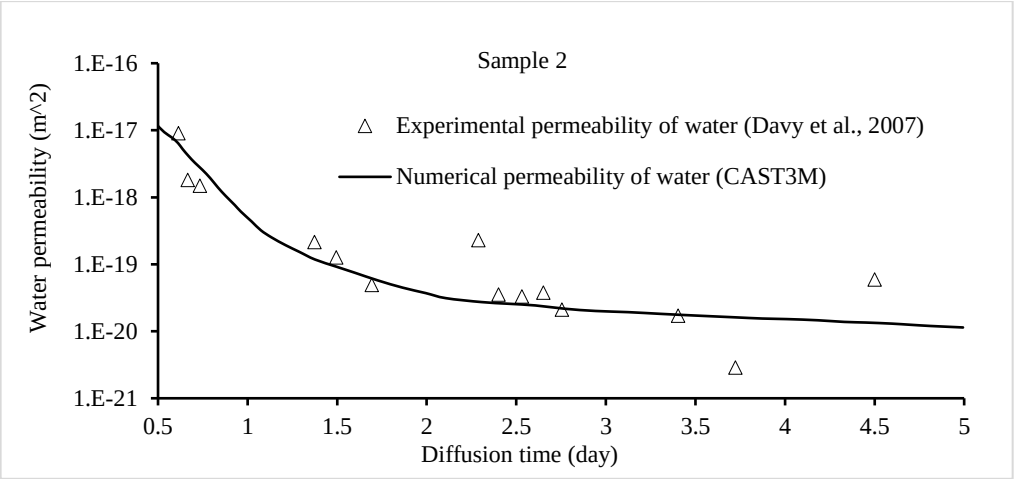

Figure 5.61. Comparison between the numerical permeability and the experimental permeability

Through the comparison between the gas permeability tests and the water permeability tests of the COx claystone, we have a better understanding of the self-sealing of the fractured COx samples. In terms of gas permeability tests, the minimum of the intrinsic permeability can reduce to a level of $10^{-16}m^2$ from $10^{-14}m^2$. During the gradual increment of confining pressure in gas permeability test, the main declination of permeability of cracked sample is obtained when the confining pressure is approximate to the geological stress (12.5MPa-16.5MPa), the reduction in this period occupies 90% the total declination of the permeability. There is no interaction between gas and COx. Therefore, confining pressure makes all the contributions to the self-sealing of the cracked COx sample. For water permeability test, the water permeability of the cracked specimen is ranging between $10^{-16}m^2$ to $10^{-18}m^2$ at the first moment caused by the interaction between water and COx. Confining pressure is loaded during the water permeability test, but its effects on the declination of permeability are not evident, the possible reason is that when permeability is lower than $10^{-16}m^2$, the effects of confining pressure is far less than the impacts of water diffusion. In the five days diffusion of sample 2, the agreement between the numerical and experimental results proves that the proposed model captured the mechanism of self-sealing of fractured COx, both of the results validated that self-sealing of damaged COx can be accomplished successfully even through flowing water inside fractures in a short time.

(2) Self-sealing of sample 5 MSE748

To explore the impact of the diffusion time on the self-sealing of a fractured COx sample, a resaturation process lasting 24 days in sample 5 MSE748 was carried out by Davy et al. (2007). This exploration provided a comparison with the resaturation of sample 2 MSE761, whose resaturation process lasted 5 days. The initial phase of the test is the same as that of the sample 2, an initial confining pressure was loaded on the cracked sample with a value of 0.3MPa, and then water was imposed on the upstream side of the cylinder sample until there was water flow out of the downstream side. Then the confining pressure increased to 3MPa, and the permeability tests

started. Figure 5.62 illustrates the intrinsic permeability when water flows out of the downstream side, transferring the intrinsic permeability to a global permeability in the cylinder's axial direction, the value is $1.84 \times 10^{-17} m^2$. In fact, the global permeability in the axial direction of the Brazil splitting cracked samples is at the level of $10^{-13} m^2 - 10^{-14} m^2$, which was validated by gas permeability of the former experimental and numerical results, that is because no interaction exists between gas and COx or their interactions are tiny and can be neglected.

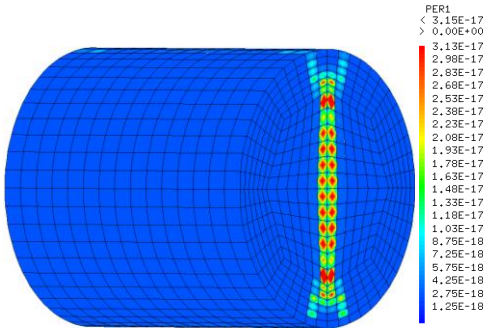

Figure 5.62. Initial permeability

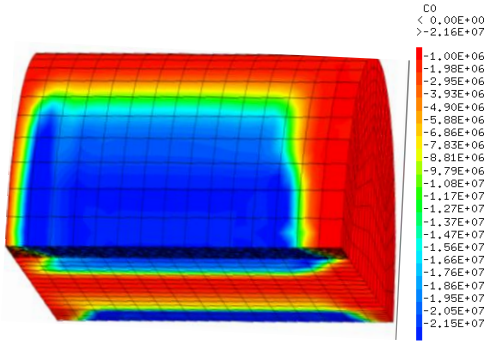

Figure 5.63. Capillary pressure in 4 days diffusion

Figure 5.63 shows the capillary pressure after 4 days of diffusion and the corresponding permeability at that time is displayed in Figure 5.64. The maximum intrinsic permeability is $1.3 \times 10^{-18} m^2$ in the numerical simulation, and the corresponding global permeability is $5.48 \times 10^{-19} m^2$.

Figures 5.63 and 5.65 shows that the capillary pressure increases significantly from the four days diffusion to the eight days diffusion and this spreading mainly along the edge of cracks. The capillary pressure expansion focuses on the cracked area because the permeability of these areas is more significant than that of non-cracked areas of several orders.

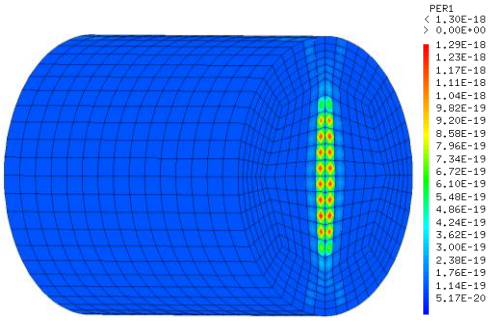

Figure 5.64. Permeability after 4 days of diffusion

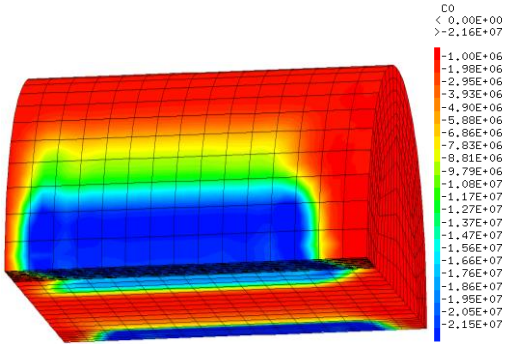

Figure 5.65. Capillary pressure after 8 days of diffusion

Figure 5.66 and 5.67 represent the capillary pressure after 12 and 16 days of diffusion, respectively. It is not difficult to find out that the capillary pressure becomes more well-distributed in comparison with those in 4 days and 8 days diffusion. Another information reading from the comparisons among the above four plots of capillary pressure is that the diffusion rate is slowing

down with the growth of the diffusion time. The explanation of these phenomena is that the cracks close gradually with the increment of the diffusion time resulting in a decreasing of the permeability.

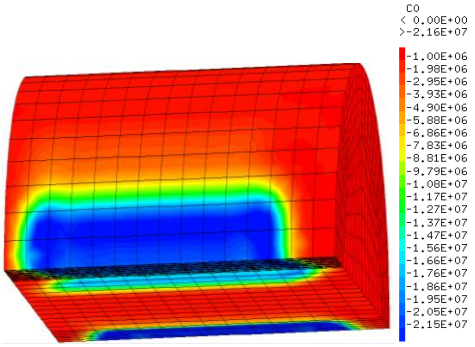

Figure 5.66. Capillary pressure in 12 days diffusion

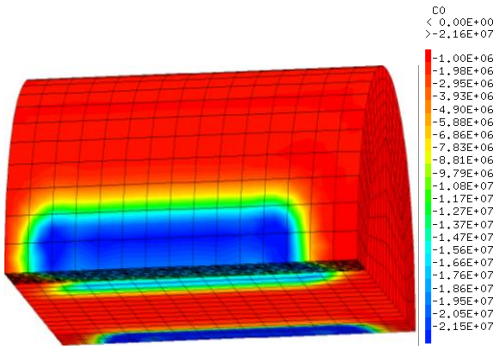

Figure 5.67. Capillary pressure in 16 days diffusion

Figures 5.68 and 5.69 represent capillary pressure after 20 and 24 days of diffusion. We can find that some areas are remaining unsaturated even in 24 days diffusion. The remained unsaturated areas illustrate that there are no new cracks born with the old cracks closure during the resaturation process or the newly produced cracks are very tiny, and they do not pose a valid promotion on permeability.

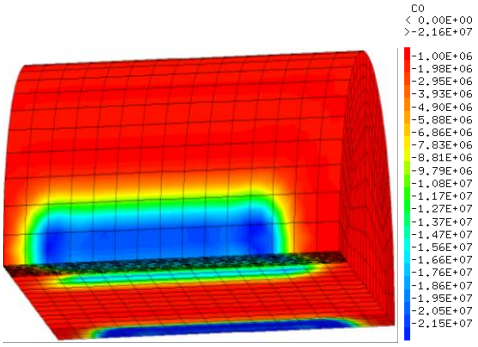

Figure 5.68. Capillary pressure in 20 days diffusion

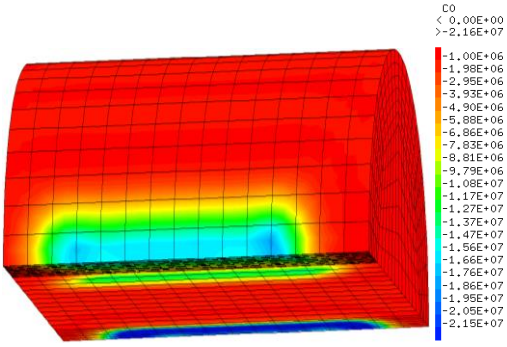

Figure 5.69. Capillary pressure in 24 days diffusion

Figure 5.70 shows the displacement of the sample 5 after 24 days of diffusion. During the resaturation process, confining pressure is loaded by a gradual increment. Therefore, the displacement is a combination between the swelling from the resaturation process and the shrink from the compression of the confining pressure. Inspection of Figure 5.70, the distribution of the displacements in the cracked area is uniform, and the closure of the cracks also focuses on this area due to the swelling of COx during the resaturation process.

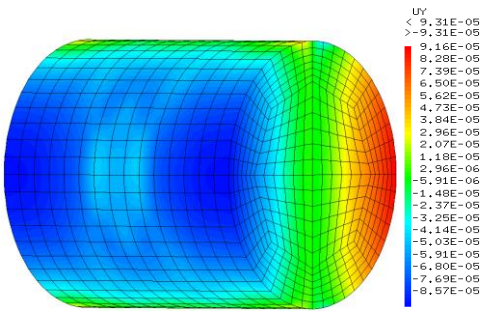

Figure 5.70. The displacement in 24 days

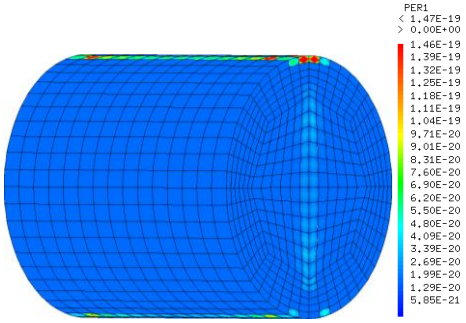

Figure 5.71. Permeability in 24 days diffusion

Figure 5.71 illustrates the permeability of sample 5 MSE768 of the numerical simulation after 24 days of diffusion. The maximum value of the intrinsic permeability is $1.47 \times 10^{-19} m^2$, and the corresponding global permeability calculated in the axial direction is $2.21 \times 10^{-21} m^2$ which is not far from the initial permeability of $10^{-20} m^2$. The evolution of the water flow Q_water obtained by the numerical simulation is shown in Figure 5.72.

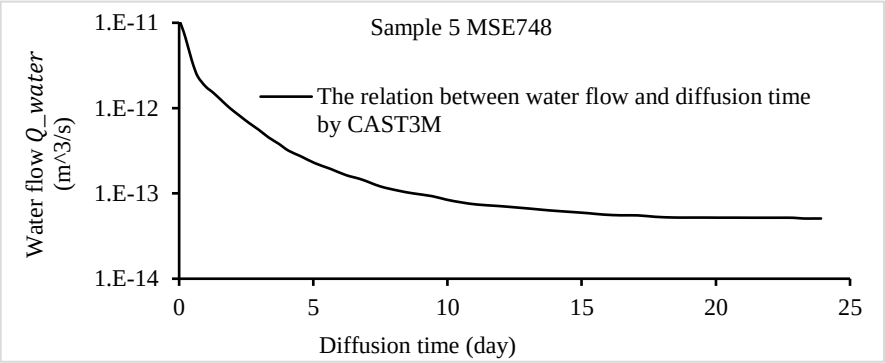

Figure 5.72. The curve of water flow with the diffusion time

Based on the relation between the water flow and the diffusion time in Figure 5.72, the global permeability at the axial direction of the cylinder sample 5 MSE748 is obtained, and the relation between the global permeability and the diffusion time is shown as follows and compared to experiments:

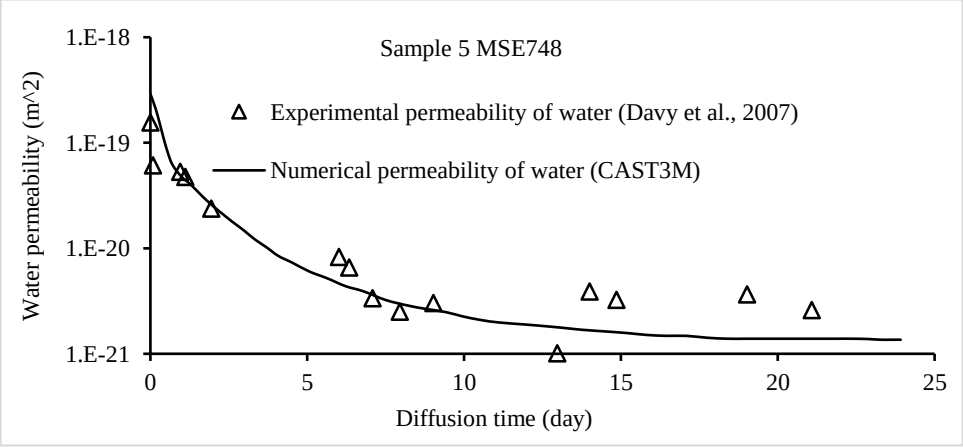

Figure 5.73. Comparison between the numerical permeability and the experimental permeability

We can conclude that the proposed model is able to reproduce correctly the experiments of hydromechanical interaction during re-saturation with water.

Inspection of the experimental self-sealing of sample 2 and sample 5 during their resaturation process illustrates that the global permeability declines to the level of $10^{-17}m^2$ when water flows through cracked samples. The global permeability continues to reduce with the diffusion time. For sample 2, the resaturation time lasted 5 days, and its global water permeability declined to $2.3 \times 10^{-20}m^2$, whereas the resaturation lasted 24 days for sample 5, and the corresponding global water permeability reduces to $2.21 \times 10^{-21}m^2$.

On the basis of the criteria given by Andra (hydraulic conductivity of $1 \times 10^{-10}m/s$ and permeability of $1 \times 10^{-17}m^2$) we can conclude that self-sealing is reached for the two experiments. The numerical simulation is able to reproduce the self-sealing phenomenon and its kinetics at the laboratory scale.

The numerical simulation in small sample scale validated the self-sealing of cracked COx, which builds a basis for the self-sealing of damaged COx in larger-scale analysis. The numerical simulation of the self-sealing in the fractured zone is introduced in the next part of this chapter.

5.3 Self-sealing of the fractured zone

There were many experiments for self-sealing of fractured COx having been carried out in laboratories (Davy et al., 2007; Zhang, 2013). These experiments include gas permeability tests and water permeability tests. By the means of loading confining pressure on cracked COx samples, Gas permeability had a large scale of declination by the order of $10^{-14}m^2$, but their final permeability still were larger than $1 \times 10^{-17}m^2$. In water permeability tests, the global water permeability could reduce to the level of $1 \times 10^{-17}m^2$ rapidly. The self-sealing of the fractured zone has been affected by the geological stresses, the pattern of fractures and saturation, which may be different from the self-sealing tests in laboratories. Therefore, a specific experiment called CDZ (Compression Damage Zone) has been designed and carried out in the underground laboratory of Andra to investigate the self-sealing of the fractured zone. The experiment of CDZ includes two stages:

- loading a compressive pressure against the wall of underground drift, then the gas permeability of the CDZ was teste
- monitoring the water permeability during a resaturation process of CDZ.

This experiment was carried out by de La Vaissière et al. (2015) and implemented in the drift GET (Figure 5.74) in the underground laboratory. This drift is parallel to the major horizontal stress direction $N150^oE$, the σ_H is around 16MPa, the minor horizontal stress σ_h and the vertical stress σ_v are around 12.5MPa (Wileveau et al., 2007). For the underground drifts of Andra, if the

drifts are parallel to the major horizontal stress direction, their excavation damage zone (the fractured zone) mainly placed at the horizontal direction, namely, inside the walls of the drifts. If the drifts are parallel to the minor horizontal stress direction, their fractured zone mainly positioned at the ceilings and floors of the drifts (see chapter 2).

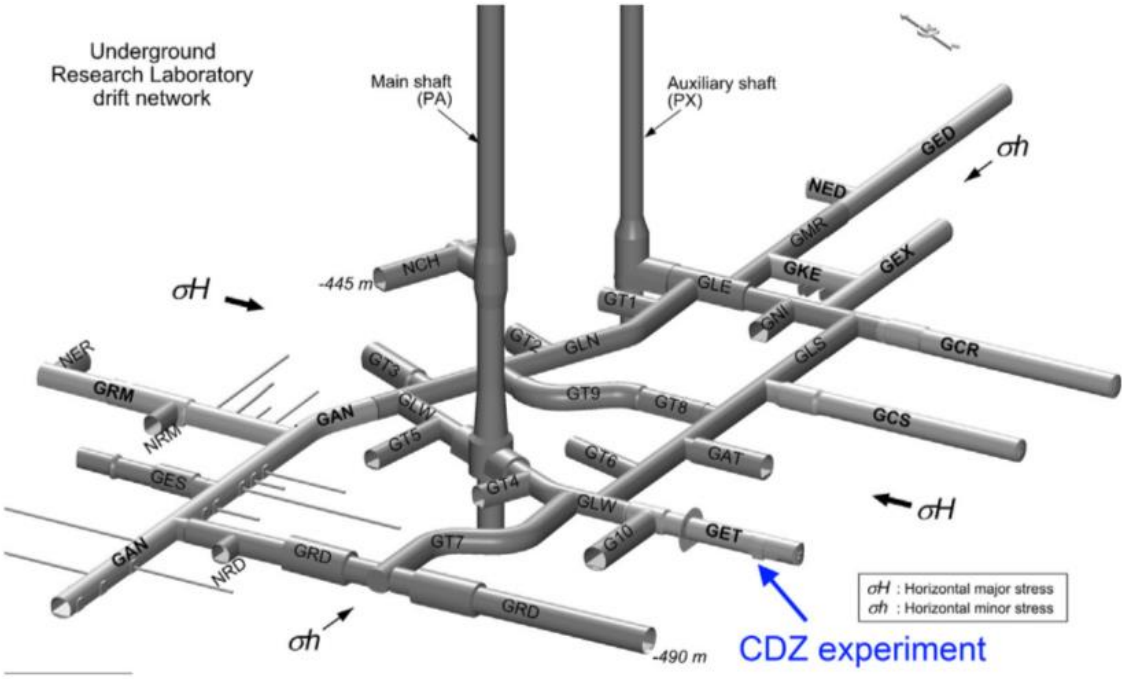

Figure 5.74. Position of the drift GET for the CDZ experiment (de La Vaissière et al., 2015)

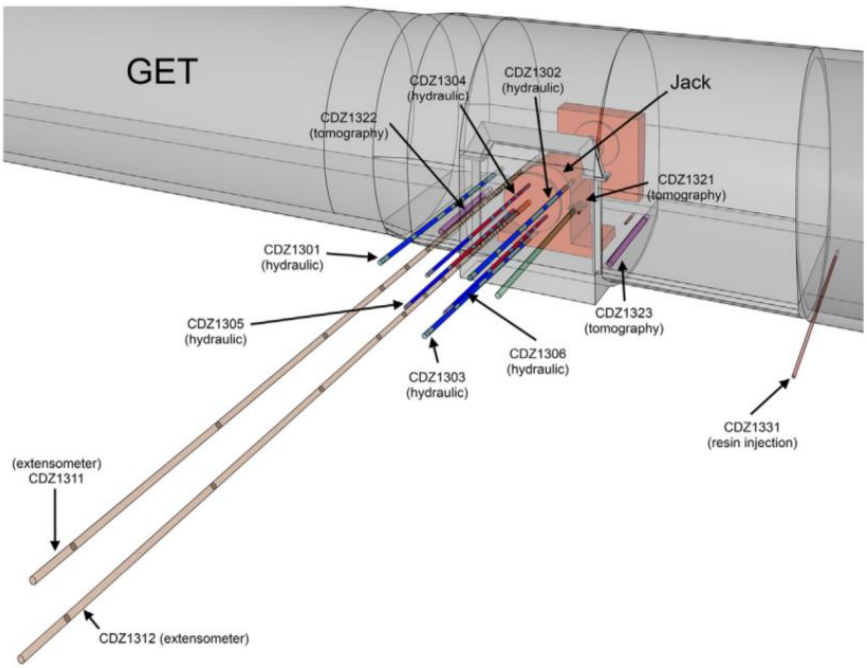

Figure 5.75. Experimental setup for CDZ (de La Vaissière et al., 2015)

Figure 5.75 shows the setup for CDZ experiment. A hydraulic loading device was applied to impose the mechanical compression on the drift wall, this device consists of a $1m^2$ circular steel

plate, and a concrete block was installed between the plate and the wall, the effect of the concrete block is to reinforce the plate. There were six boreholes (CDZ1301 to CDZ1306) were installed multi-packer systems for performance testing and hydraulic measurement. Figure 5.74 shows that three boreholes (CDZ1301 to CDZ1303) were located in the immediate vicinity of the steel plate forming an equilateral triangle with edges of 1.72m, the other three boreholes (CDZ1304 to CDZ1306) located behind the loading plate. The six boreholes hold a total surface area of $1.3m^2$ at the drift wall, and they encompassed a $6.4m^3$ volume of the COx claystone.

Figure 5.76 shows an enlarged view of multi-packer boreholes. Multi-packer systems installed in the boreholes (CDZ1304 to CDZ1306) behind the plate comprise five intervals 20 cm in length with an exception of the last interval at the end of each borehole. Multi-packer systems installed in the rest three boreholes (CDZ1301 to CDZ1303) comprise five intervals of varying lengths. Therefore, there are thirty-three intervals contained in the six boreholes.

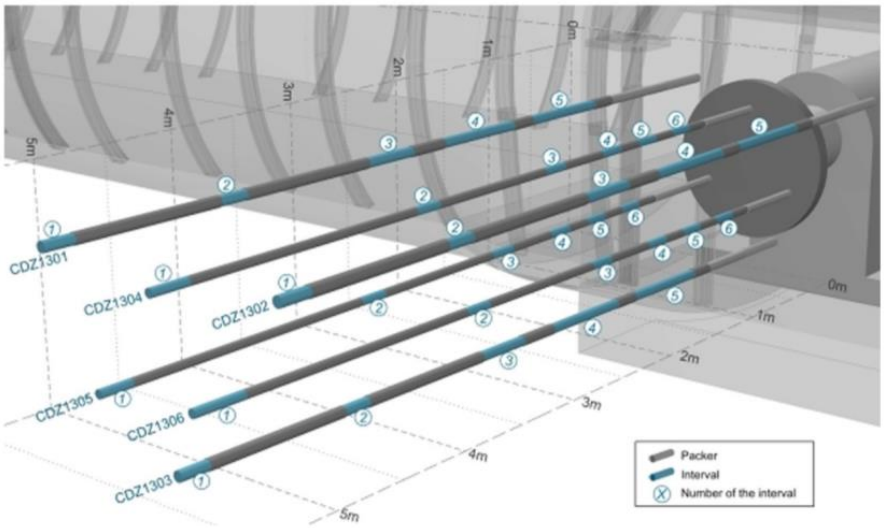

Figure 5.76. Enlarged view of multi-packer boreholes (de La Vaissière et al., 2015)

Between December 2010 and February 2011, all the boreholes were drilled and the installation of jack for the boreholes finished in late February 2011. To avoid the self-sealing effects of the intervals during a resaturation process after the period of installation, only intervals 1 of all the six boreholes and the intervals 2 of the boreholes (CDZ1301 to CDZ1303) were filled with synthetic water, and the rest of the 24 intervals were filled with gas nitrogen at atmospheric pressure.

As mentioned before, the first phase of test is investigating the effects of mechanical compression on the gas permeability of CDZ. This test was carried out by loading compressive pressure on the plate of increasing to 2, 3 and 4MPa and then reduced to 0MPa rapidly. The gas & hydraulic conductivity of all the 33 intervals were recorded during all the compression loading, as shown in the Figure 5.77, 5.78, 5.79 and 5.80.

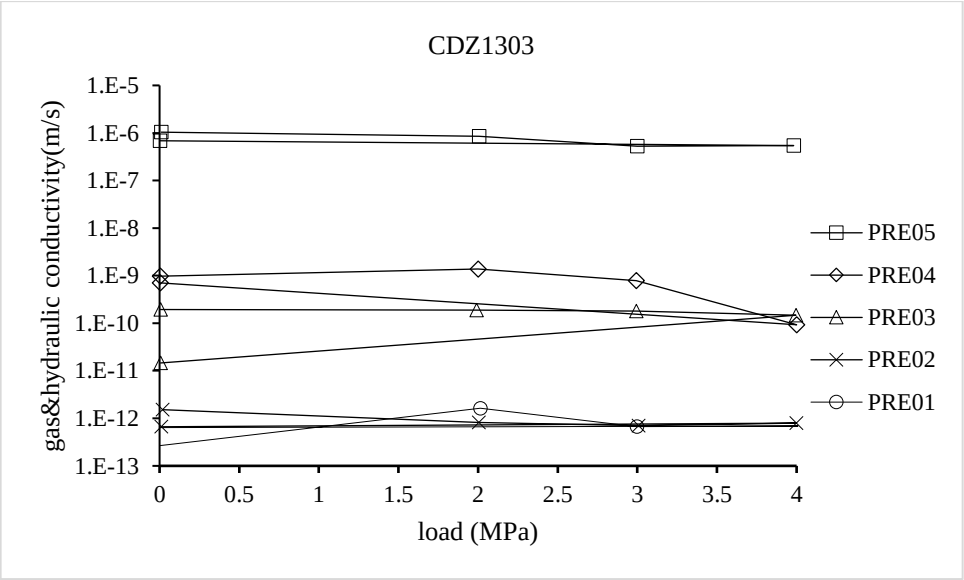

Figure 5.77. Gas & hydraulic conductivity of CDZ1303 (de La Vaissière et al., 2015)

The boreholes (CDZ1301 to CDZ1303) were not in the behind of the steel plate. Therefore, the effect of the mechanical loading on the gas & hydraulic conductivity was limited and the conductivity did not have evident declination with the increment of the loading pressure, which can find from Figure 5.76. Among the five intervals of the borehole CDZ1303, their gas & water hydraulic conductivity were larger than $10^{-10} m/s$ with two exceptions of the interval 1 and interval 2 (PRE01 and PRE02).

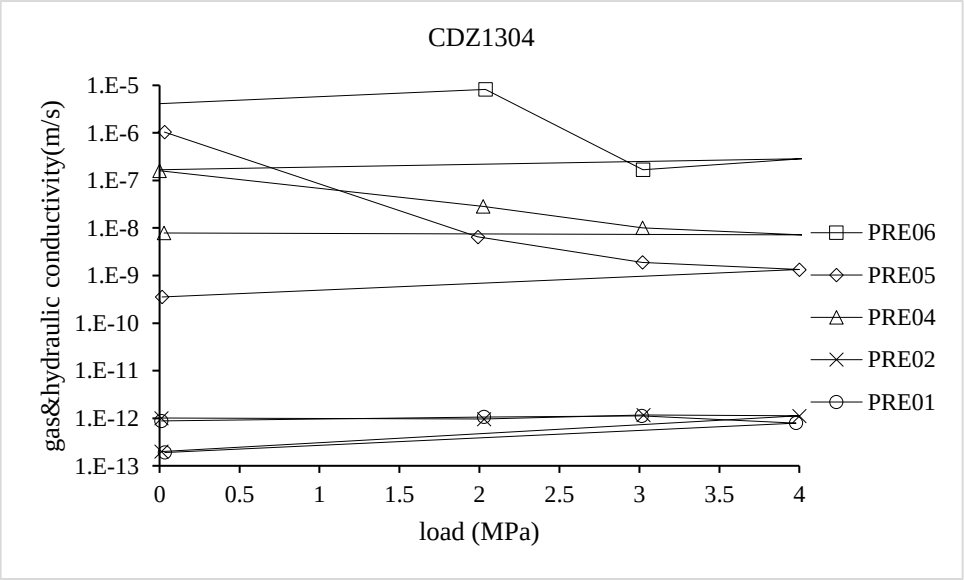

Figure 5.78. Gas & hydraulic conductivity of CDZ1304 (de La Vaissière et al., 2015)

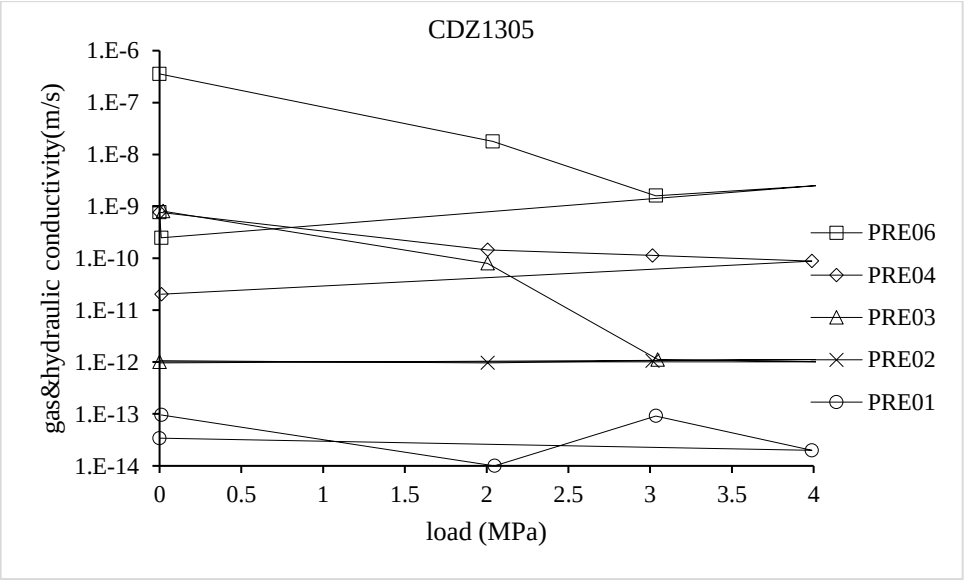

Figure 5.79. Gas & hydraulic conductivity of CDZ1305 (de La Vaissière et al., 2015)

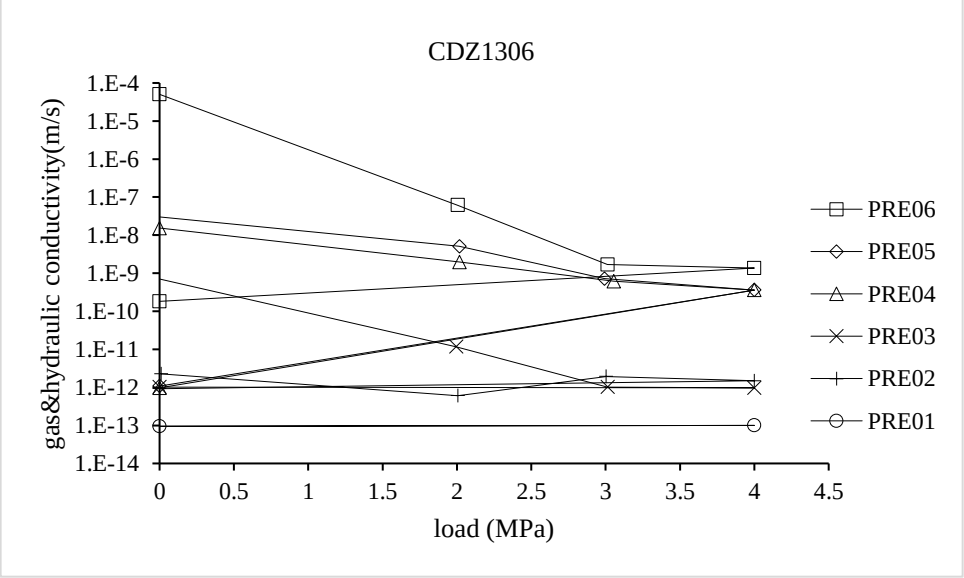

Figure 5.80. Gas & hydraulic conductivity of CDZ1306 (de La Vaissière et al., 2015)

CDZ1304, CDZ1305 and CDZ1306 located behind the loading plate (Figure 5.78, 5.79 and 5.80), the loading pressure was directly imposed on the zone of the three boreholes. The conductivity of the intervals inside this zone reduced with the loading pressure.

For the second phase of investigating hydration effects, the hydration initiated by saturating the gas-filled intervals with synthetic water. The borehole jack placed in contact with the rock without any applying of load. To satisfy the condition of zero-displacement along the wall of boreholes, the displacement of jacks was blocked. The hydration tests lasted one year from September 2011 to September 2012, the hydraulic conductivity of eight intervals was recorded during the hydration process.

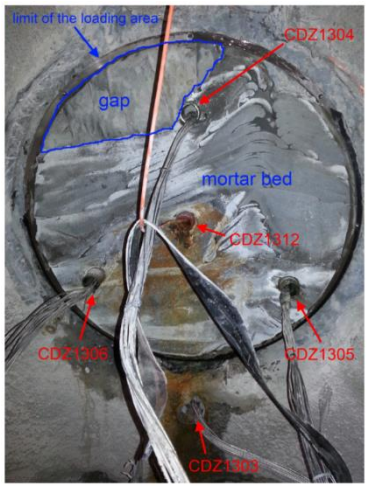

Figure 5.81. Hydration tests of the boreholes CDZ1303, CDZ1304, CZ1305 and CDZ1306 (de La Vaissière et al., 2015)

To study the effects of mechanical compression and hydration on the self-sealing of the fractured zone, numerical simulation by the proposed model is used to analyse the hydro-mechanical behaviour during the above two phases. Figure 5.82 shows cores drilled from boreholes. The fracture pattern is a mixture between tensile and shear fractures, the variation of gas & hydraulic conductivity mainly depends on the tensile fractures.

According to the fracture density of the fractured zone in the wall sides of the drifts, which are parallel to the major horizontal stress (Figure 2.24), the number of fractures is reproduced in the numerical simulations for modelling CDZ experiments.

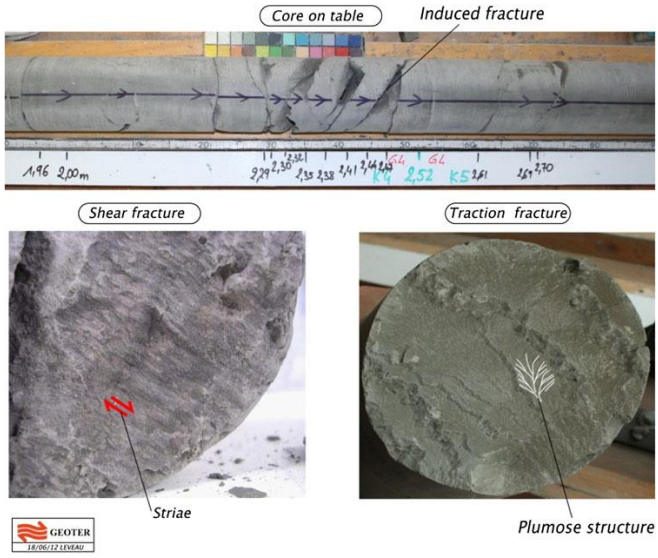

Figure 5.82. Fracture patterns of boreholes (de La Vaissière et al., 2015)

To study the self-sealing of all the area of the fractured zone from the surface of excavated openings to the depth of intact COx, there will be eight intervals of the four boreholes (CDZ1303 to CDZ1306) being reproduced in numerical simulation, and they are interval 5 of CDZ1303,

intervals 4/5/6 of CDZ1304, intervals 3/6 of CDZ1305 and intervals 4/6 of CDZ1306. According to the fracture density obtained in experiments (Figure 2.24), the number of fractures in every interval is set as follows:

- Six fractures in interval 5 of CDZ1303.
- Two fractures in intervals 5/6 of CDZ1304, interval 6 of CDZ1305 and interval 6 of CDZ1306.
- One fracture in interval 4 of CDZ1304, interval 3 of CDZ1305 and interval 4 of CDZ1306.

The details of the number of fractures in the above intervals will be explained in the numerical simulation of CDZ afterwards. Figure 5.83 (a) shows a schematic for calculating the radius direction stress and tangential direction stress in the surrounding claystone of drift GET. In the CDZ experiment, the boreholes (CDZ1301 to CDZ1306) are parallel to the line O_1O_2. Therefore, the tangential stress of the surrounding COx claystone of GET drift in the positions of the boreholes is equal to the tangential stress σ_θ along the line O_1O_2. σ_θ is calculated using the equation (5.18). The evolution between the tangential stress and radius value is shown in Figure 5.84.

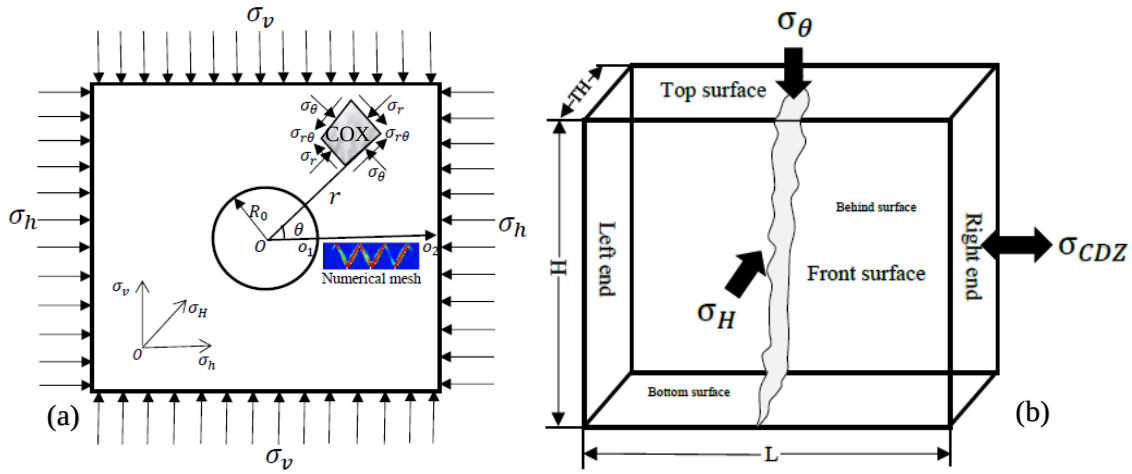

Figure 5.83. (a) Tangential stress calculation for loading the geological stress in numerical simulation (b) A schematic of numerical mesh for crack opening and simulation of the CDZ experiments

Inspection of Figure 5.83 (a) shows the position of the numerical mesh for simulating the intervals of the boreholes in the CDZ experiments, the direction of the length of the numerical mesh is parallel to the intervals' direction. The geological stress of numerical mesh in the direction of the drift GET is equal to the major horizontal stress σ_H.

$$\sigma_\theta = \frac{\sigma_h+\sigma_v}{2}\left(1+\frac{R_0^2}{r^2}\right) - \frac{\sigma_h-\sigma_v}{2}\left(1+\frac{3R_0^4}{r^4}\right)cos2\theta \quad (5.17)$$

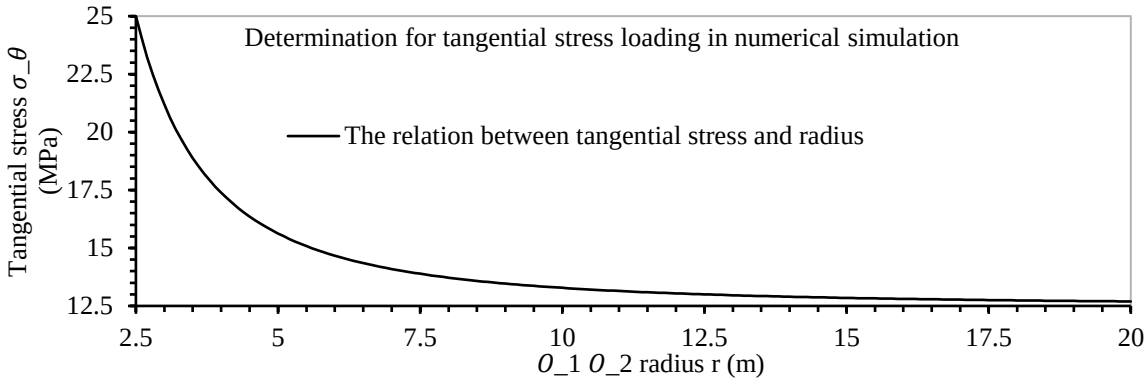

Figure 5.84. Curve between tangential stress and radius value

Figure 5.83 (b) shows a schematic of numerical mesh for simulating the CDZ experiments, and the size of the numerical mesh includes a length of L, a height of H ($0.2m$) and a thickness of TH ($0.1m$), and L is equal to the length of the intervals of the boreholes. There are several steps to achieve the numerical simulation of the self-sealing of the intervals of the boreholes by means of the mechanical loading σ_{CDZ} and hydration as in the CDZ experiments, Figure 5.85 sets the interval 5 of CDZ1303 as an example to introduce the boundary condition and procedures for the numerical simulation. The interval 5 of the borehole CDZ1303 placed at the depth between 0.29m and 0.99m from the surface of the drift wall, which had a length of 70cm. And the mesh for numerical simulation is designed as a cuboid with a length of 70cm (the length of interval 5 is 70cm), a height of 20cm and a thickness of 10cm (Figure 5.86). The surfaces of the cuboid are named the same as the corresponding surfaces in Figure 5.83(b). The diameter of the borehole is very small in comparison with the fractured zone, it is assumed that the main fractures of the interval drilled from the borehole are the same as the main fractures of the zone surrounding the interval. Based on this assumption, it is thought that the intrinsic permeability surrounding the interval is similar to the corresponding intrinsic permeability of the interval. Therefore, the gas permeability test and water permeability tests in the experiment are numerically transferred into the corresponding tests within the cracked cuboid, namely testing the global gas/water permeability between the thickness 10cm from the behind surface to the front surface. In order to have six fractures as it is in interval 5 of CDZ1303, there are seven notches designed in the numerical mesh, three at the bottom surface of the mesh and four on the top surface.

Figure 5.85 is a picture drawn in order to introduce a detailed process of simulating self-sealing of CDZ1303PRE05 using mechanical loading and hydration, and the procedures are listed as following:

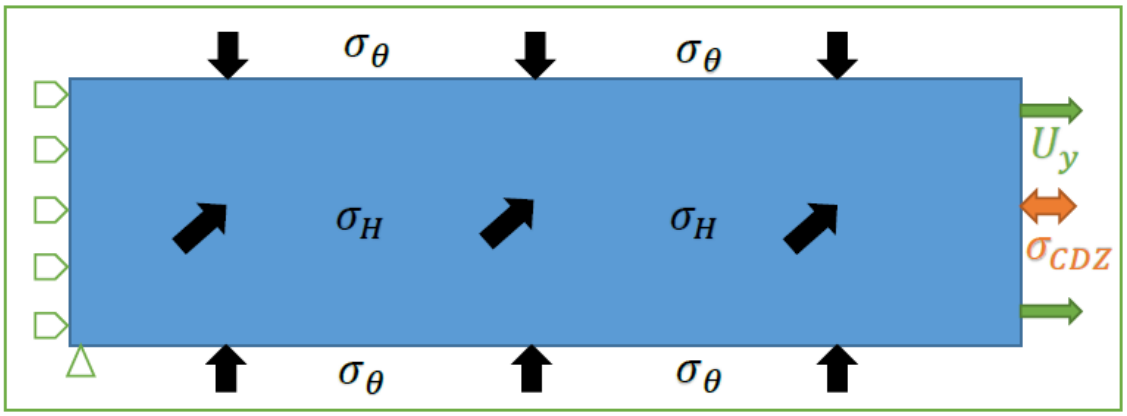

Figure 5.85. A 2D schematic picture for boundary condition and mechanical loadings for the numerical simulation of CDZ1303PRE05

The steps for the numerical simulation of CDZ1303PRE05 are listed as follows:

(1) The numerical mesh is blocked on its left end.

(2) A displacement U_{y1} is loaded on the right end of the numerical mesh, and the numerical mesh is cracked from this loading. For the numerical mesh of CDZ1303PRE05, U_{y1} is $2.35 \times 10^{-4} m$.

(3) σ_θ (21.2MPa) and σ_H (16MPa) are imposed on the numerical mesh after the displacement loading. There is an displacement increasing process of the right end (ΔU_y) during the loading of σ_θ and σ_H, therefore, a displacement U_{y2} loaded on the right end whose value keeps consistent with ΔU_y so that the stress on the right end is close to 0 MPa after the two stresses loaded. $U_{y2} = \Delta U_y = 9.8 \times 10^{-4} m$.

(4) A global permeability produced by the above three steps a, b, c in numerical simulation is $1.1 \times 10^{-13} m^2$ which is approximate to the initial global permeability of $1.04 \times 10^{-13} m^2$ in CDZ experiment of CDZ1303PRE05. Therefore, the total displacement (U_y) of the right end for cracking the numerical mesh is a sum of U_{y1} and U_{y2}. $U_y = U_{y1} + U_{y2} = 1.215 \times 10^{-3} m$.

(5) Based on the above four steps, self-sealing of CDZ1303PRE05 is carried out by loading σ_{CDZ}. The method for this loading is to give a displacement U_{y3} on the right end at the opposite direction of U_{y1} and U_{y2}. When the stress on the right end reaches to 4 MPa (the maximum mechanical loading in CDZ experiments), $U_{y3} = -3.78 \times 10^{-4} m$.

(6) This step is to unload σ_{CDZ}. The method for this unloading is loading a displacement U_{y4} based on U_{y3}. When the stress on the right end comes back to 0 MPa, $U_{y4} = 2.41 \times 10^{-4} m$.

(7) After the gas permeability test, keeping σ_H, σ_θ constant, fixing the displacement of the right end, and then a hydration process is carried out by means of imposing water on the behind surface, and water flows out of the front surface through the cracks rapidly. This

diffusion process lasts 100 days, and a water flow between the behind and front surface is calculated. And then a relation of a global water permeability with the diffusion time is obtained.

Due to an existed difficulty to find out a displacement U_{y1} to guarantee a obtained global permeability in numerical mesh is approximate to the initial permeability of CDZ1303PRE05 in CDZ experiment, a process of trying many times is inevitable so that an appropriate U_{y1} can be picked out. The method for finding out U_{y1} for the rest of other seven intervals is the same, therefore, and their processes will not be repeated here but the data of them for numerical simulation is listed in Table 5.1.

Table 5.1. The data for simulating self-sealing of the eight intervals in numerical simulation

	CDZ1303PRE05	CDZ1304PRE05	CDZ1304PRE06	CDZ1305PRE06	CDZ1306PRE06	CDZ1304PRE04	CDZ1305PRE03	CDZ1306PRE04
Dpt	0.29m-0.99m	0.88m-1.08m	0.48m-0.68m	0.53m-0.73m	0.38m-0.58m	1.28m-1.48m	1.93m-2.13m	1.18m-1.38m
Fn	6	2	2	2	2	1	1	1
Pex	$1.04\times10^{-13}m^2$	$1.95\times10^{-14}m^2$	$4.12\times10^{-13}m^2$	$3.56\times10^{-14}m^2$	$4.95\times10^{-12}m^2$	$9.76\times10^{-16}m^2$	$9.08\times10^{-17}m^2$	$3.07\times10^{-15}m^2$
σ_θ	21.2MPa	19.5MPa	21MPa	20.8MPa	22MPa	18MPa	16.5MPa	18.5MPa
σ_H	16MPa	16MPa	16MPa	16MPa	16MPa	16MPa	16MPa	16MPa
S_r	0.85	0.85	0.85	0.85	0.85	0.85	0.85	0.85
U_{y1}	$2.35\times10^{-4}m$	$2.78\times10^{-5}m$	$9.14\times10^{-5}m$	$5.25\times10^{-5}m$	$1.87\times10^{-4}m$	$1.27\times10^{-5}m$	$1.04\times10^{-5}m$	$1.33\times10^{-5}m$
U_{y2}	$9.8\times10^{-4}m$	$2.8\times10^{-4}m$	$2.8\times10^{-4}m$	$2.8\times10^{-4}m$	$2.8\times10^{-4}m$	$2.8\times10^{-4}m$	$2.8\times10^{-4}m$	$2.8\times10^{-4}m$
Pnu	$1.1\times10^{-13}m^2$	$2.04\times10^{-14}m^2$	$4.3\times10^{-13}m^2$	$4.93\times10^{-14}m^2$	$5.15\times10^{-12}m^2$	$9.89\times10^{-16}m^2$	$1.03\times10^{-16}m^2$	$3.33\times10^{-15}m^2$
U_{y3}	$-2.48\times10^{-4}m$	$-2.48\times10^{-4}m$	$-2.48\times10^{-4}m$	$-2.48\times10^{-4}m$	$-2.48\times10^{-4}m$	$-2.48\times10^{-4}m$	$-2.48\times10^{-4}m$	$-2.48\times10^{-4}m$
U_{y4}	$2.11\times10^{-4}m$	$2.11\times10^{-4}m$	$2.11\times10^{-4}m$	$2.11\times10^{-4}m$	$2.11\times10^{-4}m$	$2.11\times10^{-4}m$	$2.11\times10^{-4}m$	$2.11\times10^{-4}m$

Note: Dpt, Fn, Pex and Pnu are depth of intervals from gallery wall surface, fracture number, initial experimental permeability and initial numerical permeability, respectively.

Strictly follow the above seven steps, the numerical analysis of the self-sealing of eight intervals from the four boreholes is carried out, and the discussion and comparison between numerical and experimental results will be demonstrated in the next part.

5.3.1 Interval having six main fractures (CDZ1303PRE05)

The initial saturation of 0.85 observed in the experiments is imposed in the numerical simulations, the corresponding capillary pressure at this saturation is $-2.15\times10^7 Pa$. σ_θ and σ_H are -21.2MPa and -16MPa, respectively. The two stresses are loaded on the top surface and the front surface of the numerical mesh, respectively.

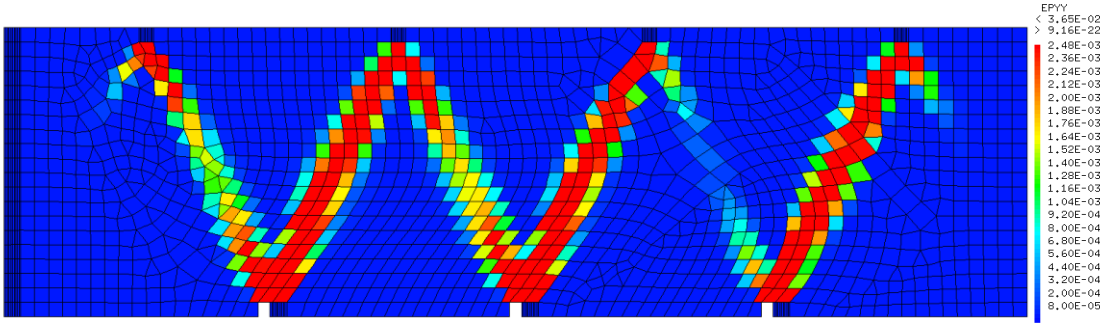

Figure 5.86. Cracks value of 1303PRE05 in numerical simulation

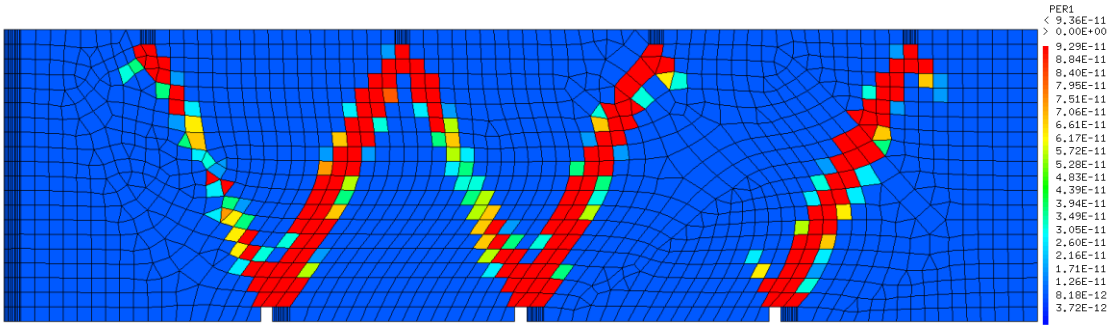

Figure 5.87. Permeability value of 1303PRE05 in numerical simulation

Figure 5.86 and 5.87 demonstrate the cracks value and the intrinsic permeability when the global gas permeability is $1.1 \times 10^{-13} m^2$, and the global gas permeability is calculated from a gas flow which is evaluated using Fick's law by CAST3M based on the intrinsic permeability in Figure 5.87. A gas pressure of p1 is imposed on the front surface and another gas pressure p2 on the behind surface, this gap of gas pressure (p1-p2) provides a gas flow between the two surfaces, the equation for flow calculation is shown as follow:

$$Q_{gas} = \iint q_{gas} ds \tag{5.18}$$

Based on the gas flow Q_{gas}, the global gas permeability is calculated as follow:

$$\kappa_{gas} = \frac{2\times(2.2\times10^{-5}Pa*s)\times(1.01\times10^{5}Pa)\times(1\times10^{-1}m)Q_{gas}}{(0.7m*0.2m)((1.5\times10^{6}Pa)^2-(1.01\times10^{5}Pa)^2)} \tag{5.19}$$

Although there was no loading pressure σ_{CDZ} directly imposed on the interval 5 of CDZ1303 in the experiment, a try to load it is carried out in the numerical simulation. The boundary condition is fixing the left end side of the numerical mesh (Figure 5.86), the compression pressure σ_{CDZ} is loaded on its right end side with a gradual increment from 0MPa to 4MPa. With the growth of the compression pressure, the cracks close and the intrinsic permeability decreases. Therefore, the gas flow Q_{gas} which is calculated from CAST3M decreases at the same time, and the corresponding global gas permeability κ_{gas} decreases also, the results are displayed in the following Figure:

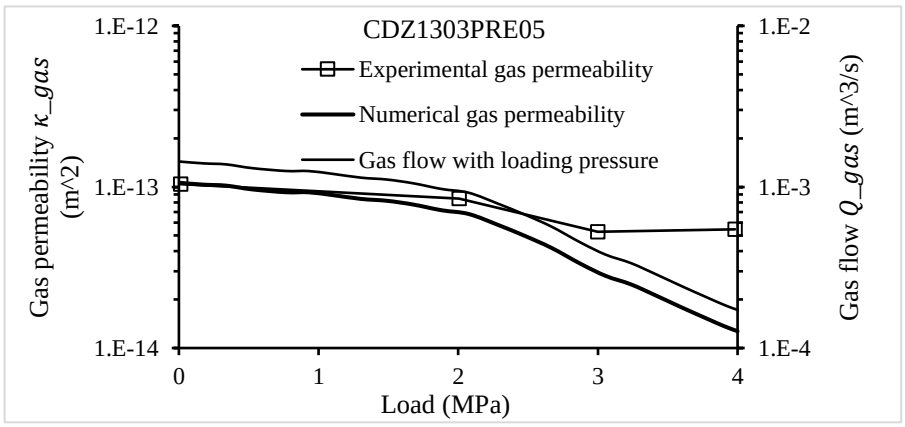

Figure 5.88. Permeability change with loading pressure

Figure 5.88 shows that the gas permeability decreases from $1.04 \times 10^{-13} m^2$ to $1.2 \times 10^{-14} m^2$ with the loading pressure increases from 0MPa to 4MPa in the numerical simulation. The difference between the experimental and numerical results is partly due to the fact that in the experiments, the pressure didn't apply directly on the core (which wasn't in front of the loading plate) and the resulting stress was probably lower than the applied pressure. In the numerical simulations, the pressure is directly applied to the specimen.

For the hydration process of CDZ1303PRE05, no mechanical load σ_{CDZ} is imposed in the numerical simulation so that it keeps consistent with self-sealing of CDZ1303PRE05 in experiment where the interval 5 of CDZ1303 placed at outside of the steel plate for mechanical loads. Therefore, the initial global permeability for hydration is numerically beginning from $1.1 \times 10^{-13} m^2$. The hydro-mechanical behaviours occurred in the hydration process both of the experimental and numerical processes include:

(1) Water was injected in the gas-filled interval CDZ1303PRE05 in the experiment. In the numerical simulation, capillary pressure of the behind surface of the numerical mesh is decreased from $-2.15 \times 10^7 Pa$ to $0\ Pa$, and a diffusion process begins.

(2) In the experiment, interval 5 of CDZ1303 was filled with water and water diffusion occurring in the surrounding area of the interval. This diffusion included water penetrating in intact COx claystone and water flowing through fractures. In the numerical simulation, capillary pressure starts to vary due to the capillary pressure gap between the behind surface of the cuboid and its other parts, the variation rate is determined by the intrinsic permeability which is summed up by the original permeability of intact COx and the permeability from cracks.

(3) In the experiment, the interaction between water and COx made swelling occurring, and the cracks closure during the resaturation process. This swelling closed water pathway, and it slowed down the rate of water diffusion. In the numerical simulation, the variation of capillary pressure produces deformation and swelling, which decreases the width of cracks (Figure 5.86) and permeability (5.87).

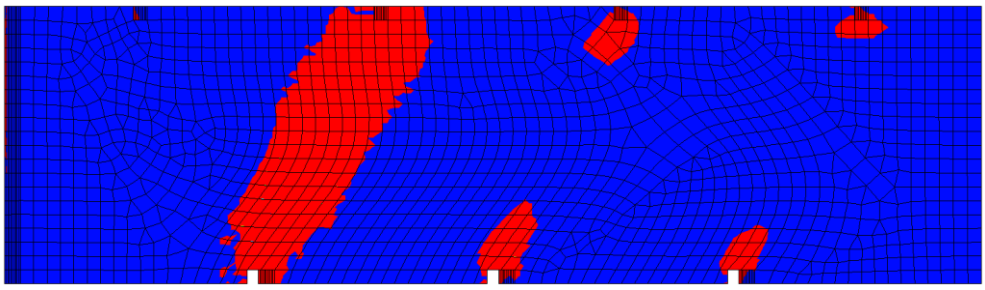

Figure 5.89. Saturated zone in 0.1-day diffusion

Figure 5.89 shows the saturated and unsaturated parts in 0.1-day water diffusion obtained by the numerical simualtion. If the six main cracks in Figure 5.86 are numbered 1- 6 from the left to the

right side, we can find that water flows through the second crack at the first moment due to its high permeability, that is why the place of the second crack has the largest saturated zone (the red area). In the experiment, the thickness of the cracked COx for water diffusion could be regarded as infinite, and the corresponding one in numerical simulation is 0.1m. Therefore, water will completely flow out of all the six cracks by turns and, and finally, all the material will be saturated.

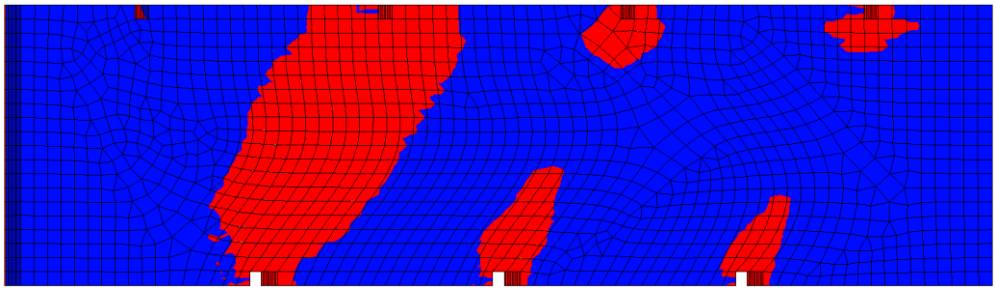

Figure 5.90. Saturated zone in 1 day diffusion

Figure 5.90 illustrates the saturated zone in one-day diffusion. In comparison with the one in 0.1-day diffusion, there is a significant expansion of the red zone, and the expansion in the second crack zone is more evident due to the well-developed micro-cracks around the second main crack.

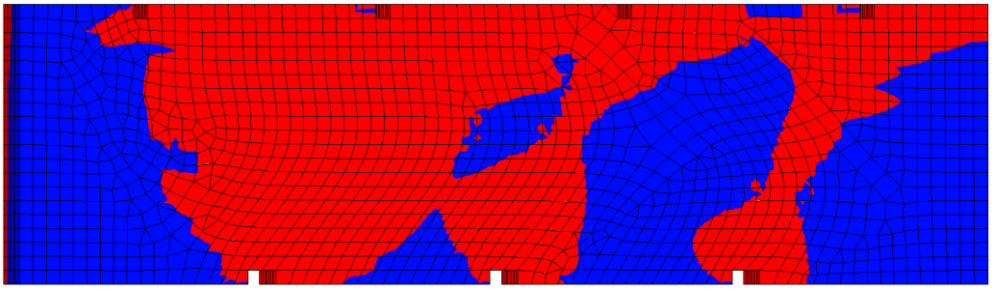

Figure 5.91. Saturated zone in 10 days diffusion

Figure 5.91 displays the distribution of the saturated and unsaturated zone in 10 days diffusion. It is clear that water flows out of all the main cracks with the exception of the fifth main crack.

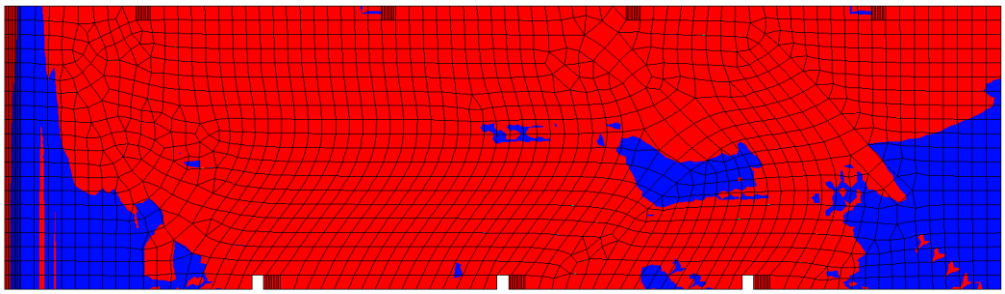

Figure 5.92. Saturated zone in 100 days diffusion

Figure 5.92 shows the proportion between the saturated zone and unsaturated zone in 100 days diffusion, and there are around 70% of the mesh saturated. Due to the extremely low permeability of the intact COx, there are about 30% area unsaturated remained.

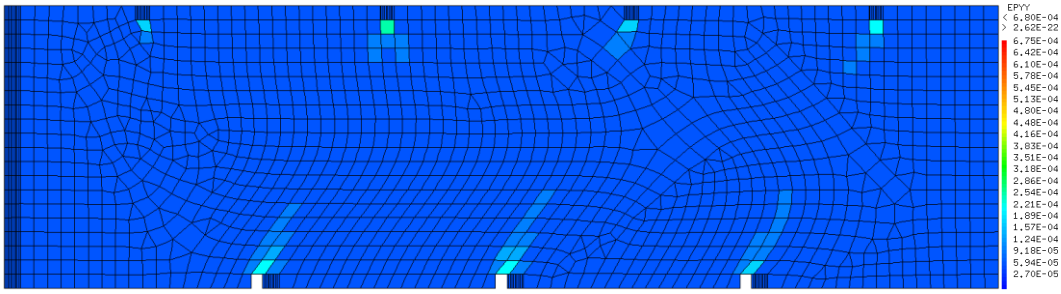

Figure 5.93. Cracks value of 1303PRE05 in 100 days diffusion

In comparison with the cracks value before the resaturation process, there is a significant declination of this value after 100 days resaturation. This declination proves the self-sealing capacity of cracked COx during the resaturation process.

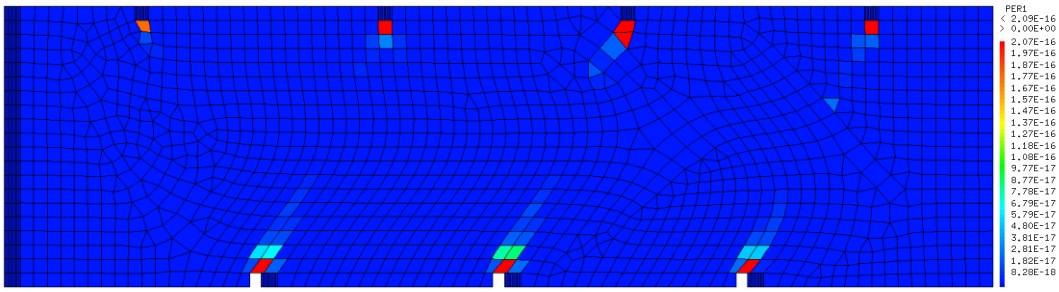

Figure 5.94. Permeability value of 1303PRE05 in 100 days diffusion

The maximum intrinsic permeability is $9.36 \times 10^{-11} m^2$ before the resaturation process, whereas it declines to $2.09 \times 10^{-16} m^2$ in 100 days resaturation. Moreover, the maximum intrinsic permeability mainly placed at the positions of notches. Therefore, there would be a great decrease when the intrinsic permeability is transferred into the global water permeability. Through this calculation, the global water permeability of the cracked material between the behind and the front surface is shown as following:

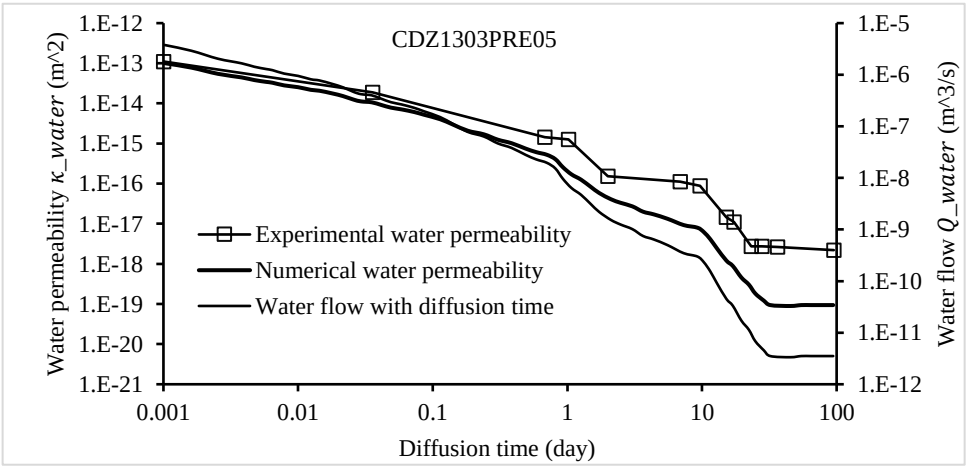

Figure 5.95. Permeability change with diffusion time

Figure 5.95 shows the evolutions of the experimental water permeability, numerical water permeability and water flow with the diffusion time. This Figure illustrates that the minimum values both of the numerical and experimental water permeability are less than $1 \times 10^{-17} m^2$, this information proves that the cracked zone of CDZ1303PRE05 accomplished self-sealing without an extra compression pressure was loaded on the wall of a drift. The initial global water permeability is $1.04 \times 10^{-13} m^2$ in the experiment, and the corresponding value is $1.1 \times 10^{-13} m^2$ in the numerical simulation. This value decreased to $2.28 \times 10^{-18} m^2$ in 100 days diffusion in the experiments while the numerical simulation gives a value of $1.13 \times 10^{-19} m^2$.

The most significant decrease of the water permeability was obtained the first day of diffusion due to the swelling of COx claystone during the hydration process. And the proposed model captured this behaviour with the declination of the water permeability to $2.1 \times 10^{-16} m^2$ after one-day diffusion. This decrease of permeability slows down the water diffusion in the later period, and it contributes significant effects on the self-sealing of the fractured material.

5.3.2 Intervals having two main fractures

The hydro-mechanical behaviour of four intervals during mechanical loading and hydration process is simulated. These four intervals are intervals 5/6 of CDZ1304, interval 6 of CDZ1305 and interval 6 of CDZ1306.

(1) CDZ1304PRE06

According to the fracture number of intervals introduced in Table 5.1, two tensile fractures are produced by setting three notches in the numerical mesh for simulating self-sealing of CDZ1304PRE06. The numerical mesh has a length and a height of 20cm and a thickness of 10cm as following:

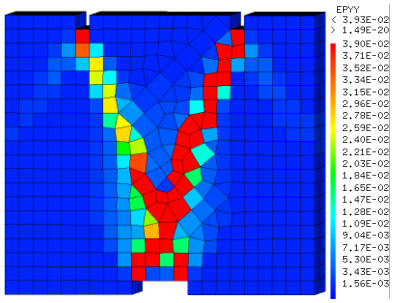

Figure 5.96. Cracks at loading pressure 0MPa

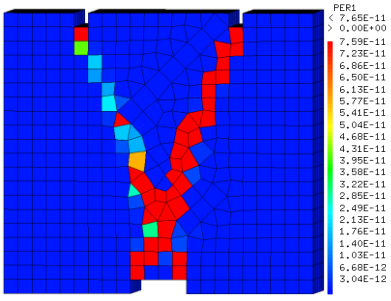

Figure 5.97. Permeability at loading pressure 0MPa

Figure 5.96 and 5.97 show the cracks value and the corresponding intrinsic permeability when the loading pressure σ_{CDZ} is zero. The initial global gas permeability is $4.13 \times 10^{-13} m^2$ in the experiment, and the corresponding gas permeability is $4.30 \times 10^{-13} m^2$ in the numerical simulation.

Figure 5.98 shows that the experimental gas permeability does not decrease with the increment of the loading pressure. The reason is perhaps that there are new cracks produced which led a growth of permeability when the loading pressure increased from 0MPa to 2MPa, whereas there was rapid cracks closure when the loading grow from 2MPa to 3MPa. Therefore, the maximum and minimum gas permeability were $8.21 \times 10^{-13} m^2$ and $1.68 \times 10^{-14} m^2$ which were obtained at the points of loading pressure 2MPa and 3MPa, respectively.

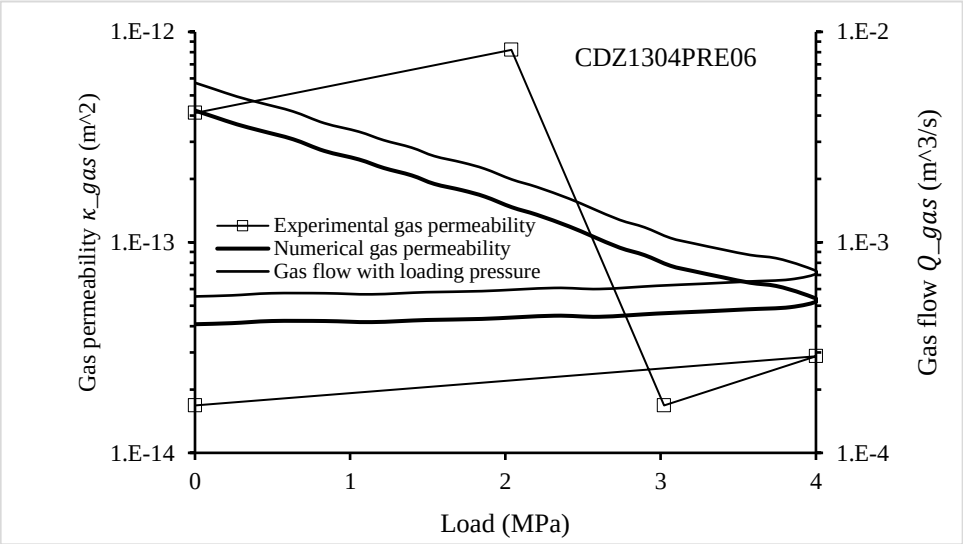

Figure 5.98. Permeability change with loading pressure

In the numerical simulation, the intrinsic permeability decreases with the increment of the loading pressure σ_{CDZ} which is imposed on the right end of the mesh, and the left end of the mesh is fixed by boundary condition. During the loading process, the gas flow is calculated by CAST3M using the intrinsic permeability (Figure 5.97 and 5.100).

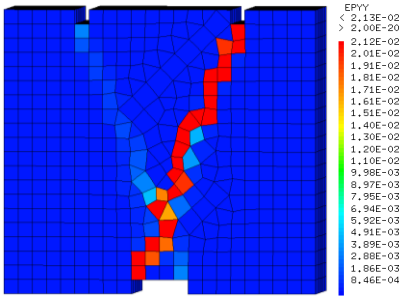

Figure 5.99. Cracks at loading 4MPa

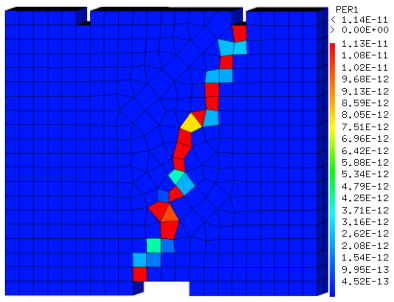

Figure 5.100. Permeability at loading pressure 4MPa

Comparison of the cracks value at loading 0MPa and that at loading 4MPa indicates that one of the two main cracks almost disappears in the later state. Of course, the intrinsic permeability at the two loading levels has a similar change with the loading variation. The changes of cracks and permeability demonstrate that the mechanical loading change is helpful to self-sealing of excavated damage zone, the numerical gas permeability is $4.99 \times 10^{-14} m^2$ at the loading pressure 4MPa, and the corresponding experimental gas permeability is $2.28 \times 10^{-14} m^2$.

Inspection of Figure 5.98 shows that the significant declination of gas permeability happened with the growth of the loading pressure in both of the numerical and experimental ones. However, the final intrinsic permeability is still significant in terms of the safety of nuclear waste storage Mechanical loading is not sufficient to achieve self-sealing of the excavated damage zone.

After the mechanical loading, the hydration process was carried out, as for CDZ1303PRE05. In the experiment, water was injected into the gas-filled interval of CDZ1304PRE06 and, capillary pressure of the behind surface of the numerical mesh was reduced to 0MPa in the numerical simulation.

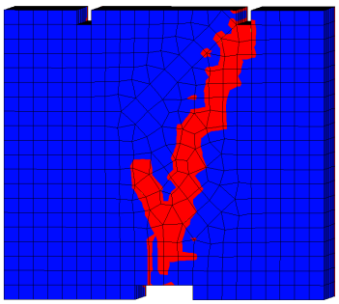

Figure 5.101. Saturated zone in 0.1 day diffusion

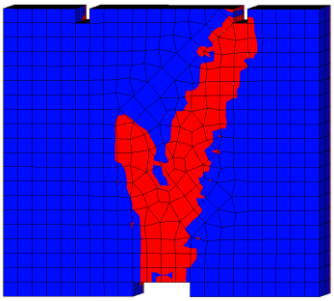

Figure 5.102. Saturated zone in 1 day diffusion

Figure 5.101, 5.102, 5.103 and 5.104 show the saturated zone (red area) when water flows through cracks in 0.1 day, 1 day, 10 days and 100 days, respectively.

Figure 5.101 shows that water flows through the cracked zone rapidly due to the high permeability of this zone. Between the main cracks, one of the two cracks is entirely saturated and for the other crack, only half of it is saturated that means the flow rate slows down due to the mechanical loading. This rapid water flowing inside crack validates that the self-sealing of the fractured zone cannot be accomplished only by mechanical loading. The saturated zone grows with the diffusion time increasing from 0.1 days to 1 day, of course, this resaturation process is accompanied by the swelling of the material either in the experiment or in the numerical simulation.

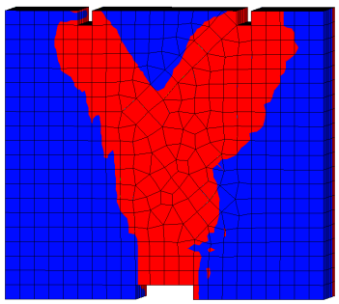

Figure 5.103. Saturated zone in 10 days diffusion

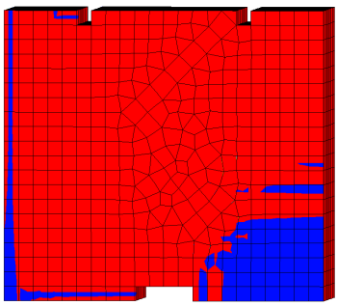

Figure 5.104. Saturated zone in 100 days diffusion

In 10 days diffusion, the saturated zone mainly concentrated at the areas of the cracks, and one-third of the total front surface is saturated. Almost all the numerical mesh is saturated in 100 days diffusion and the corresponding cracks value and permeability at this time are shown as following:

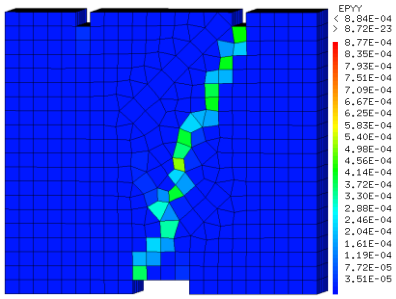

Figure 5.105. Cracks in 100 days diffusion

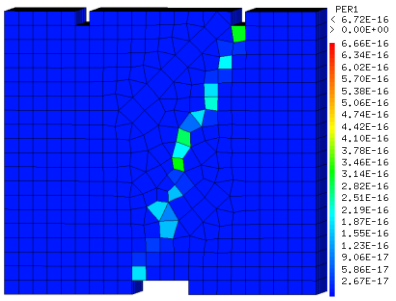

Figure 5.106. Permeability in 100 days diffusion

Figure 5.105 and 5.106 show that both of the cracks and permeability have a large scale of declination. The maximum intrinsic permeability decreases from $1.14 \times 10^{-11} m^2$ to $6.72 \times 10^{-16} m^2$ after 100 days resaturation in the numerical simulation, and the intrinsic permeability is transferred into the global water permeability in the direction normal to the front surface of the numerical mesh The evolution of the global water permeability during the diffusion time obtained by the numerical simualtion is shown as following:

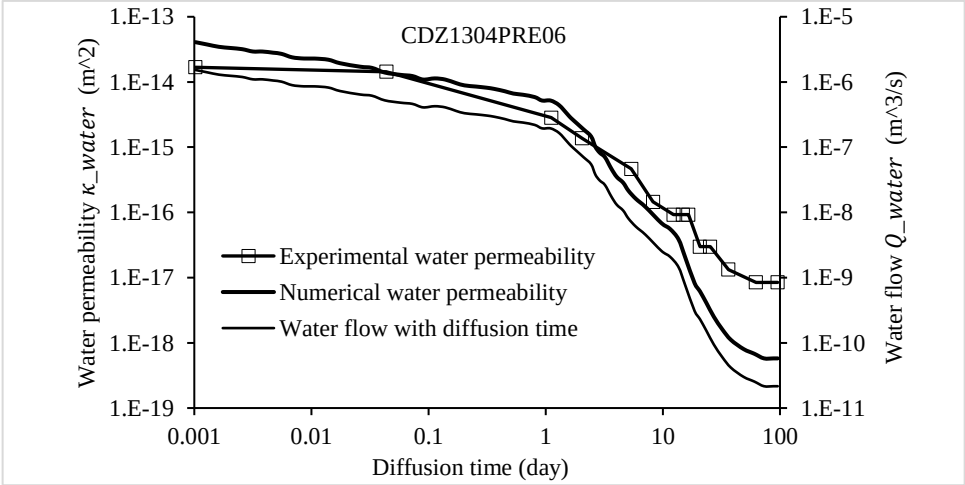

Figure 5.107. Permeability change with diffusion time

Figure 5.107 shows the changes of the experimental water permeability, the numerical water permeability and the water flow with the increment of the diffusion time. This figure illustrates that the minimum values, and both the numerical and experimental water permeability are less than$1 \times 10^{-17} m^2$, which proves that the cracked zone of CDZ1304PRE06 accomplished self-sealing during the hydration process. The initial global water permeability is $1.68 \times 10^{-14} m^2$ in the experiment, and the corresponding value is $4.1 \times 10^{-14} m^2$ in numerical simulation, this value decreased to $8.48 \times 10^{-18} m^2$ in 100 days diffusion in the experiments while the numerical simulation gives a value of $5.\times 10^{-19} m^2$.

(2) CDZ1304PRE05

The interval 1304PRE05 located in depth between 0.88m and 1.08m to the surface of the drift wall, and the analysis of the interval self-sealing includes two phases: a mechanical loading phase and a hydration process that are shown in Figure 5.108 and 5.109, respectively.

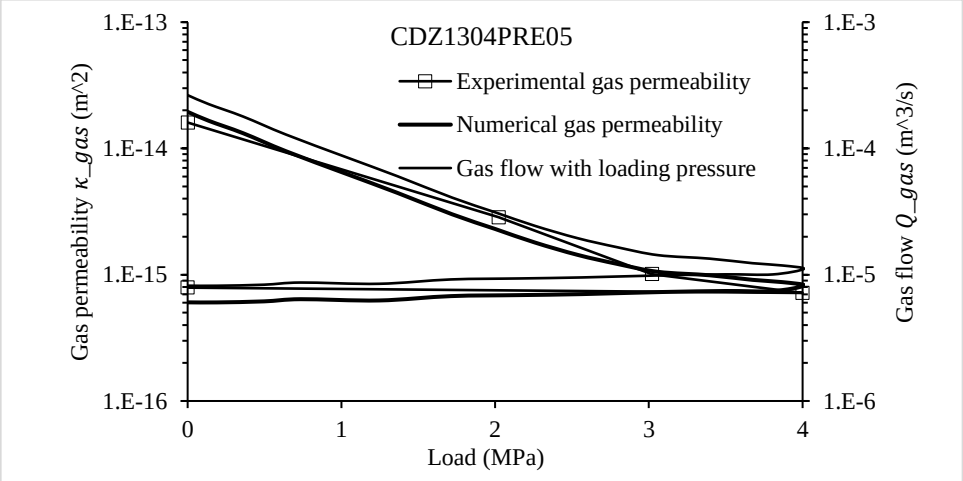

Figure 5.108. Permeability change with loading pressure

Figure 5.108 illustrates that the gas permeability decreased with the increment of the loading pressure in both of the experiment and the numerical simulation, and the numerical gas permeability is calculated from the gas flow Q_gas whose evaluation way is the same as the gas flow estimation for the intervals CDZ1303PRE05 and CDZ1304PRE06. Gas flow decreases with the increment of the loading pressure demonstrates that the loading pressure reduces the gas conductivity of the fractured material. This is the reason why the numerical gas permeability decreases with the loading pressure growth. In this test, the initial gas permeability of the numerical and experimental are $2 \times 10^{-14} m^2$ and $1.6 \times 10^{-14} m^2$, respectively, when the loading pressure is 0MPa. They declined to $8 \times 10^{-16} m^2$ and $7.17 \times 10^{-16} m^2$, respectively, at loading pressure of 4MPa. A perfect agreement between the numerical gas permeability and experimental gas permeability has been obtained, and this is different from the relation of gas permeability between the numerical and experimental obtained in CDZ1304PRE06. The different change pattern of experimental gas permeability between CDZ1304PRE06 and CDZ1304PRE05 indicates that the permeability decrease is irregular during the mechanical loading.

After the mechanical loading, the hydration process was carried out, and the relation between water permeability and the diffusion time is shown in Figure 5.109.

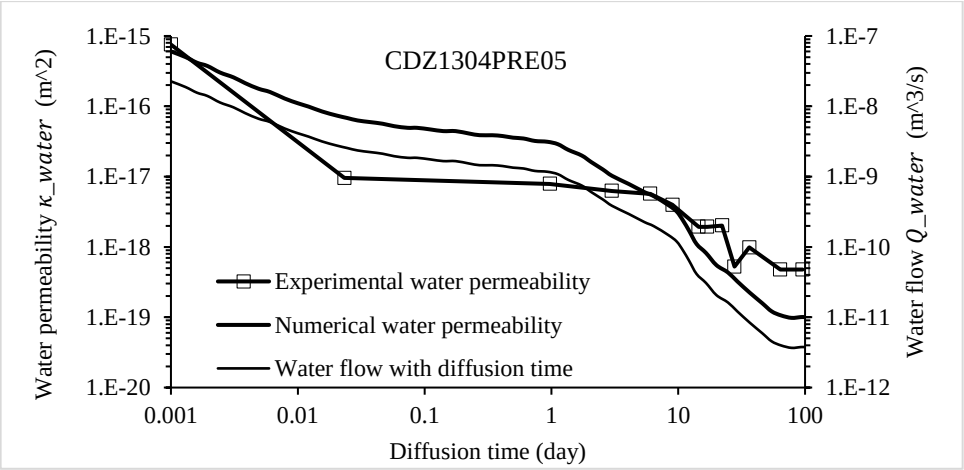

Figure 5.109. Permeability change with diffusion time

Figure 5.109 shows the changes of the experimental water permeability, the numerical water permeability and the water flow with the increment of diffusion time. Inspection of this Figure illustrates that the minimum value of the global water permeability is less than$1 \times 10^{-17} m^2$, and this information indicates that the cracked zone of CDZ1304PRE05 accomplished self-sealing under the former mechanical loading and the later hydration process. In the beginning of the hydration process, the initial global water permeability is $7.55 \times 10^{-16} m^2$ in the experiment, and the corresponding value is $6.1 \times 10^{-16} m^2$ in the numerical simulation. This value of the experiment is $4.77 \times 10^{-19} m^2$ in 100 days diffusion, and the corresponding value of the numerical simulation is $1 \times 10^{-19} m^2$.

(3) CDZ1305PRE06

The interval 1305PRE06 located in depth between 0.53m and 0.73m to the surface of the drift wall and the saturation of this zone is 0.85. The geological stresses σ_θ and σ_H are 20.8MPa and 16MPa, respectively. The analysis of the interval self-sealing includes two phases: a mechanical loading phase and a hydration process that are shown in Figure 5.110 and 5.111, respectively.

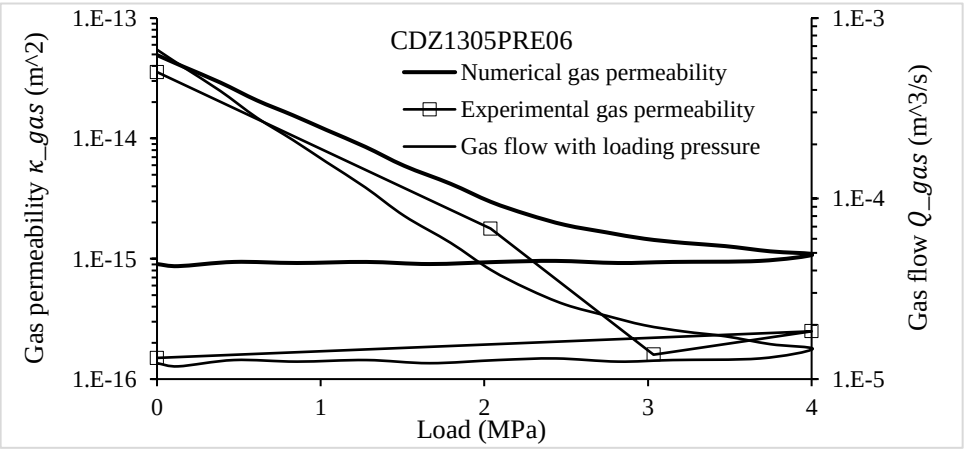

Figure 5.110. Permeability change with loading pressure

Inspection of Figure 5.110 illustrates that the gas permeability experimentally decreased with the increment of the loading pressure from 0MPa to 3MPa, whereas gas permeability irregularly increased when the loading pressure increased from 3MPa to 4MPa. The explanation to the experimental result is that the cracks of the interval CDZ1305PRE06 closed gradually, and the gas permeability decreased when the loading pressure varied from 0 MPa to 3MPa. Whereas there was some new cracks produced or the original cracks expanded when the loading pressure increased from 3MPa to 4MPa, and the corresponding gas permeability went up in this phase. Therefore, the minimum value of gas permeability was $1.6 \times 10^{-16} m^2$ which was obtained at the point of loading pressure 3MPa.

In terms of the numerical simulation, the gas permeability decreased with the increment of the loading pressure, and the numerical gas permeability is calculated from the gas flow Q_gas whose evaluation way is the same as the gas flow estimation for intervals CDZ1303PRE05 and CDZ1304PRE06. The gas flow decreases with the increment of the loading pressure demonstrates that the loading pressure reduced the intrinsic permeability of the fractured material, that is the reason why the numerical gas permeability decreases with the loading pressure growth. In this test, the initial gas permeability of numerical is $5.0 \times 10^{-14} m^2$ when the loading pressure is 0MPa, it declined to $1.1 \times 10^{-15} m^2$ at loading pressure of 4MPa.

A perfect agreement between the numerical gas permeability and experimental gas permeability has been obtained when the loading pressure was less than 2MPa whereas the changes of the numerical and experimental gas permeability were different when the loading pressure went up from 2MPa to 4MPa. The different change patterns between the numerical and experimental gas permeability indicates that the permeability decrease is irregular in the experiment during the mechanical loading, and the numerical method cannot capture this kind of irregular change.

After the mechanical loading, the hydration process was carried out, and the relation between water permeability and the diffusion time is shown in Figure 5.111.

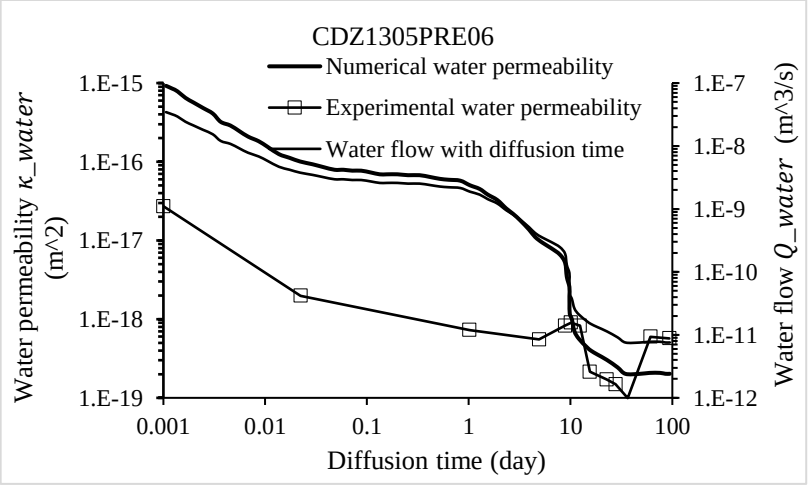

Figure 5.111. Permeability change with diffusion time

Figure 5.111 shows the changes of the experimental water permeability, numerical water permeability and the water flow with the increment of diffusion time. Inspection of this Figure illustrates that the minimum values of the global water permeability of numerical and experimental are less than$1 \times 10^{-17} m^2$ that proves that the cracked zone of CDZ1305PRE06 accomplished self-sealing in 10 days diffusion. The initial global water permeability is $2.72 \times 10^{-17} m^2$ in the experiment, and the corresponding value is $1.1 \times 10^{-15} m^2$ in the numerical simulation. This value of the experiment is $5.7 \times 10^{-19} m^2$ in 100 days diffusion, and the corresponding value of the numerical simulation is$1.2 \times 10^{-19} m^2$.

(4) CDZ1306PRE06

The interval 1306PRE06 located in the depth between 0.38m and 0.58m from the surface of the drift wall and the saturation of this zone is 0.85. The geological stresses σ_θ and σ_H are 22MPa and 16MPa, respectively. The analysis of the interval self-sealing includes two phases: a mechanical loading phase and a hydration process that are shown in Figure 5.112 and 5.113, respectively.

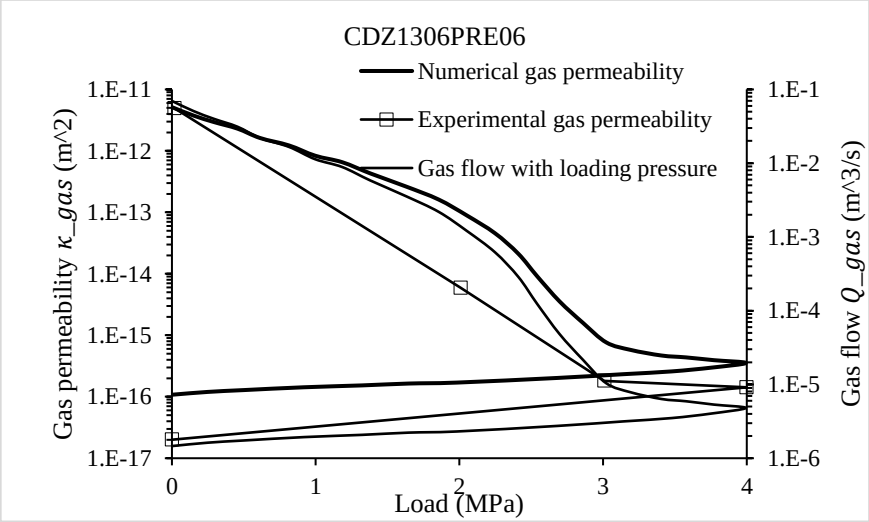

Figure 5.112. Permeability change with loading pressure

Figure 5.112 illustrates that the experimental gas permeability decreased with the increment of the loading pressure. The maximum and minimum gas permeability were $4.95 \times 10^{-12} m^2$ and $1.42 \times 10^{-16} m^2$ which were obtained at the points of loading pressure 0MPa and 4MPa, respectively, whereas the main declination of the experimental gas permeability happened during the increment of loading pressure from 0MPa to 3MPa.

The numerical gas permeability declination during the increment of the loading pressure has a good consistency with the reduction of the experimental one. The main declination of gas permeability occurred during the increment of the loading pressure from 0MPa to 3MPa is captured in the numerical simulation, the minimum value of numerical gas permeability is

$1.13 \times 10^{-16} m^2$ at the loading pressure 4MPa that is approximate to the corresponding minimum value of the experimental one.

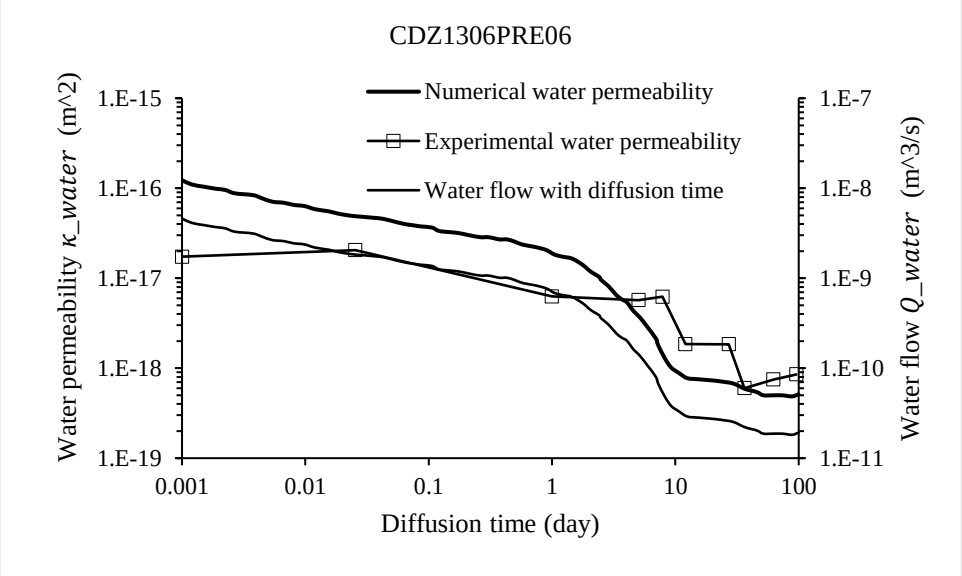

Figure 5.113. Permeability change with diffusion time

After the gas permeability test in the first phase of the mechanical loading, the water permeability test during the hydration process was carried out in the second phase. Figure 5.113 shows the changes of the experimental permeability, numerical permeability and the water flow with the increment of the diffusion time. The initial global water permeability is $1.73 \times 10^{-17} m^2$ in the experiment, and the corresponding value is $3 \times 10^{-16} m^2$ in the numerical simulation. This value of the experiment is $8.55 \times 10^{-19} m^2$ in 100 days diffusion, and the corresponding value of numerical simulation is $5 \times 10^{-19} m^2$.

There are four intervals of CDZ1304PRE06, CDZ1304PRE05, CDZ1305PRE06, and CDZ1306PRE06 whose self-sealing by means of the mechanical loading and hydration have been analysed in the experiment and numerical simulation. In terms of the self-sealing leading by mechanical loading, the gas permeability decreased with the increment of loading pressure, which was obtained either in the experiment or numerical simulation. The great declination of gas permeability has been accomplished, but their final permeability at the end of the mechanical loading was still larger than $1 \times 10^{-17} m^2$, therefore, it is evident that only the mechanical loading is not enough for the self-sealing of fractured zones that are close to the surface of the drift wall. No matter how much the gas permeability of experimental and numerical after mechanical loading, but all the fractured intervals sealed in the hydration process. The declination of water permeability occurred rapidly when water flows through the fractured intervals. The numerical water permeability declined to the level of $10^{-19} m^2$ in the diffusion time between 10 and 20 days.

This part validated the self-sealing of the tensile fractures by comparing the experimental and the numerical results during the resaturation process. In the deeper place of the drift wall, the fracture patterns gradually transferred into a mixture of tensile and shear fractures or only shear fractures, and it is necessary to analyse the self-sealing of the shear fractures zone. The study to the self-sealing of this zone will be displayed in the following part by means of analysing the self-sealing of several intervals having one fracture.

5.3.3 Intervals having one main fracture

This part will demonstrate the hydro-mechanical behaviours of three intervals during a mechanical loading and a hydration process, and the three intervals are interval 4 of CDZ1304, interval 4 of CDZ1306 and interval 3 of CDZ1305. Comparisons between numerical and experimental results of them will be introduced in the following part.

(1) CDZ1304PRE04

The interval 4 of borehole CDZ 1304 placed in depth between 1.28m to 1.48m to the drift wall surface which occupied a length of 20cm. The mesh for numerical simulation is designed as a cuboid with a length of 20cm (the length of the interval 4), a height of 20cm and a thickness of 10cm (Figure 5.114). Therefore, the gas permeability test and water permeability tests in the experiment are numerically transferred into the corresponding tests within the cracked cuboid, namely calculating the global gas/water permeability between the thickness 10cm from the front surface and the behind surface. To have one main fracture in the numerical mesh, there are two notches designed, one at the bottom surface of the mesh, and another on the top surface. The saturation of this zone of the interval is 0.85, and the geological stresses σ_θ and σ_H are 18MPa and 16MPa, respectively.

Because the borehole CDZ1304 is located behind of the steel plate in CDZ experiment, the loading pressure from the steel plate had significant effects on the gas permeability, and that can be observed in Figure 5.116. The global gas permeability of the interval CDZ1304PRE04 was $9.76 \times 10^{-16} m^2$ when the loading pressure was 0MPa, and it was $1.6 \times 10^{-16} m^2$ with the loading pressure increased to 4MPa. We can see that the level of experimental gas permeability is very low in comparison with that of the intervals CDZ1304PRE05/CDZ1304PRE06, the reason is that the extent of damage reduced with the depth growth between the interval and the drift wall. Following the reduction of damage degree, the number of fractures also decrease, and this is why there is only one main crack produced in the numerical mesh of the interval CDZ1304PRE04 (Figure 5.114).

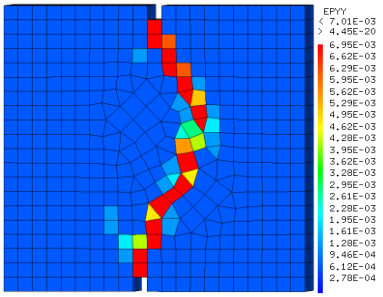

Figure 5.114. Cracks at loading pressure 0MPa

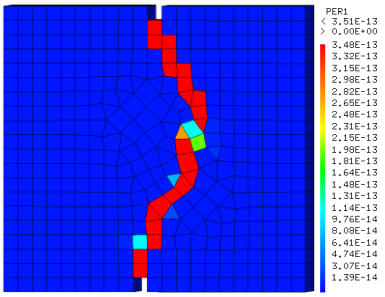

Figure 5.115. Permeability at loading pressure 0MPa

Figure 5.114 and 5.115 show the cracks value and the corresponding intrinsic permeability when the loading pressure is zero. Transferring the intrinsic permeability into global gas permeability, the initial numerical gas permeability is $1.01 \times 10^{-15} m^2$ at the loading pressure of 0MPa. There was loading pressure was imposed on the interval 4 of CDZ1304 in the experiment, and it was also carried out in numerical simulation. The boundary condition is fixing the left end side of the numerical mesh (Figure 5.114), and the compression pressure is loaded on its right end side with a gradual increment from 0MPa to 4MPa. With the growth of the compression pressure, the cracks close and the intrinsic permeability decreases. With the decreasing of the intrinsic permeability, the corresponding global gas permeability κ_{gas} decrease also. And the relation between the global gas permeability and the mechanical loading is displayed in Figure 5.116:

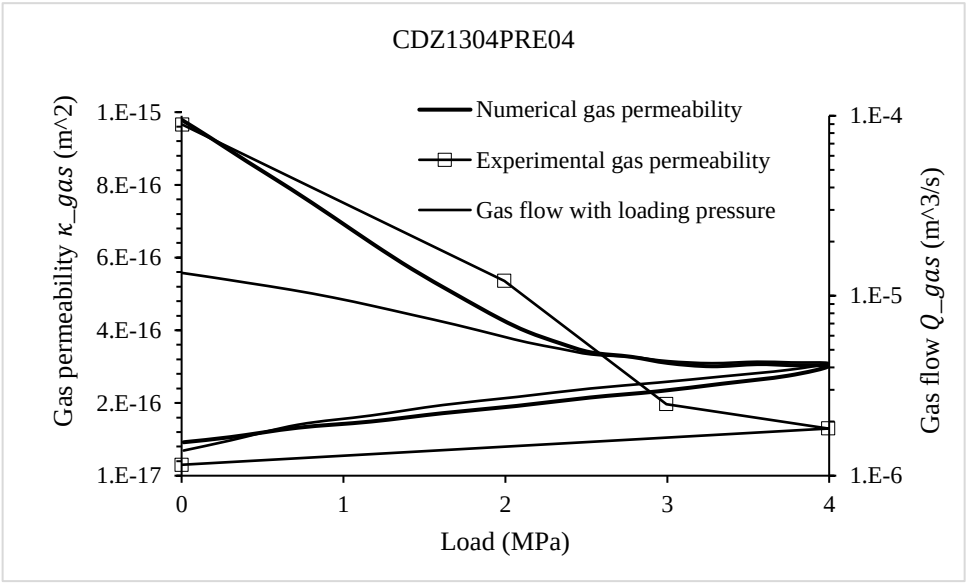

Figure 5.116. Permeability change with loading pressure

Figure 5.116 illustrates that the gas permeability decreased with the increment of the loading pressure. In the loading process, the experimental gas permeability reduced from $9.76 \times 10^{-16} m^2$ to $1.4 \times 10^{-16} m^2$, and the corresponding numerical gas permeability decreases from $1.\times 10^{-15} m^2$ to $3 \times 10^{-16} m^2$. A good agreement between the numerical and the experimental curves has been obtained which indicates that the proposed model correctly described the

permeability changes during the mechanical loading when the initial gas permeability is low in comparison with those high initial gas permeability of the intervals CDZ1304PRE06/CDZ1305PRE06.

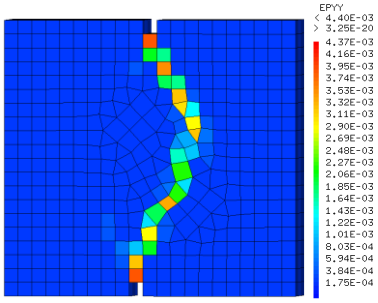

Figure 5.117. Cracks at loading 4MPa

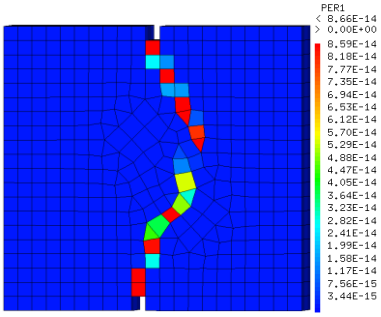

Figure 5. 118. Permeability at loading pressure 4MPa

Figure 5.117 and 5.118 show the cracks value and the intrinsic permeability in the numerical simulation when the loading pressure goes up to 4MPa. Comparing them with the corresponding initial values at the loading pressure 0MPa illustrates that there is an evident declination has been obtained due to the increment of the loading pressure. Inspection of the above two plots demonstrates that the main crack seals too much and the intrinsic permeability changes a lot too.

For the hydration process of CDZ1304PRE04, the initial global permeability for hydration is beginning from $1.4 \times 10^{-16} m^2$ in the experiment, and the corresponding value is $3 \times 10^{-16} m^2$ in numerical simulation. The procedures of the hydration process in both of the experiment and numerical simulation include:

(1) Water was injected in the gas-filled interval CDZ1304PRE04 in the experiment. In the numerical simulation, capillary pressure of the behind surface in the cracked numerical mesh is decreased from $-2.15 \times 10^{7} Pa$ to $0\ Pa$ and a diffusion process begins.

(2) In the experiment, the interval 4 of CDZ1304 was filled with water and water diffusion occurring in the surrounding area of the interval. This diffusion included water penetrating in intact COx claystone and water flowing through fractures. In the numerical simulation, capillary pressure starts to vary due to the capillary pressure gap between the cuboid behind surface and its rest part, and the variation rate is determined the intrinsic permeability which is summed up by the original permeability of intact COx and the permeability from cracks.

(3) In the experiment, the interaction between water and COx made swelling occurring and cracks closure during the resaturation process, and this swelling closed water pathway and slowed down water diffusion. In the numerical simulation, the variation of capillary pressure produces deformation, which decreases the width of cracks (Figure 5.123) and the intrinsic permeability (5.123).

Figure 5.119, 5.120, 5.121 and 5.122 show the saturated zones (red area) when water flows through cracks in 0.1 day, 1 day, 10 days and 100 days, respectively.

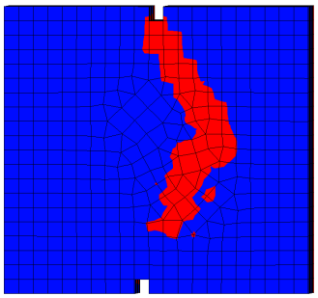

Figure 5.119. Capillary pressure in 0.1-day diffusion

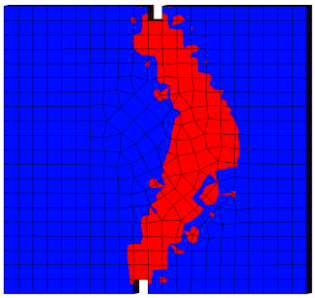

Figure 5.120. Capillary pressure in 1-day diffusion

Figure 5.119 numerically demonstrates the saturated and unsaturated part in 0.1-day water diffusion. We can see that water flows through the main crack at the first moment due to its high permeability, and that is why the place of the main crack has the largest saturated zone (red area). This rapid water flow inside crack shows that the self-sealing of the fractured zone can not accomplish by mechanical loading, but still there is some part of the main crack zone unsaturated which represents that the flow rate slows down due to the mechanical loading. In the experiment, the thickness of cracked COx for water diffusion could be regarded as an infinitive, and the corresponding one in numerical simulation is 0.1m. Following the increment of the diffusion time , the red saturated zone will expand in the numerical mesh.

The saturated zone grows with the diffusion time increasing from 0.1 days to 1 day. Of course, this resaturation process is accompanied by swelling of material either in the experiment or in the numerical simulation. Figure 5.120 illustrates the saturated zone in one-day diffusion, in comparison with the one in 0.1-day diffusion, there is a significant expansion of the red zone, and the expansion along the zone of the main crack is evident due to the well-developed micro-cracks in this part.

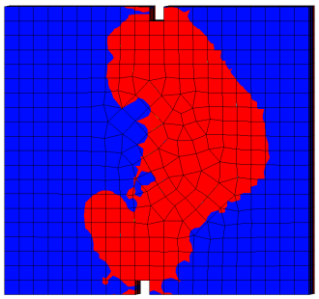

Figure 5.121. Capillary pressure in 10 days diffusion

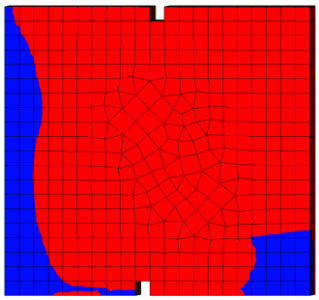

Figure 5.122. Capillary pressure in 100 days diffusion

Figure 5.121 displays the distribution of saturated zone and unsaturated zone in 10 days diffusion, the saturated zone main concentrated at the area of cracks and less than one-third of the total front surface is saturated. It is clear that the saturated zone expands at least two times in comparison

with that in 1-day diffusion, and the irregular expansion of the saturated zone illustrates the existence of micro-cracks along the main crack zone.

Figure 5.122 shows the proportion between the saturated and unsaturated zone in 100 days diffusion, and there are 80% of the mesh saturated. Due to the extremely low permeability of the intact COx, there are 20% area unsaturated remained. Of course, the resaturation process produced a swelling of the cracked material which leads to the sealing of the main cracks and micro-cracks, and the corresponding cracks value and intrinsic permeability at this time are shown as following:

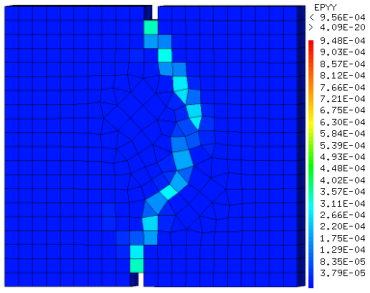

Figure 5.123. Cracks in 100 days diffusion

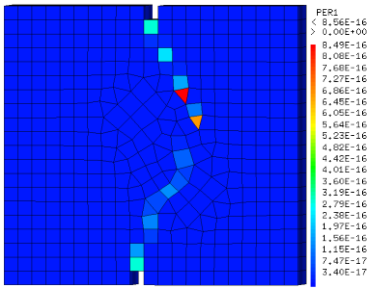

Figure 5.124. Permeability in 100 days diffusion

Examination of Figure 5.123 and 5.124 indicate that both of the cracks and intrinsic permeability have a large scale of declination. The maximum intrinsic permeability decreases from $8.66 \times 10^{-14} m^2$ to $8.56 \times 10^{-16} m^2$ after 100 days resaturation in the numerical simulation, and these intrinsic permeability is transferred into the global water permeability, and the global water permeability during the diffusion time is shown in Figure 5.125.

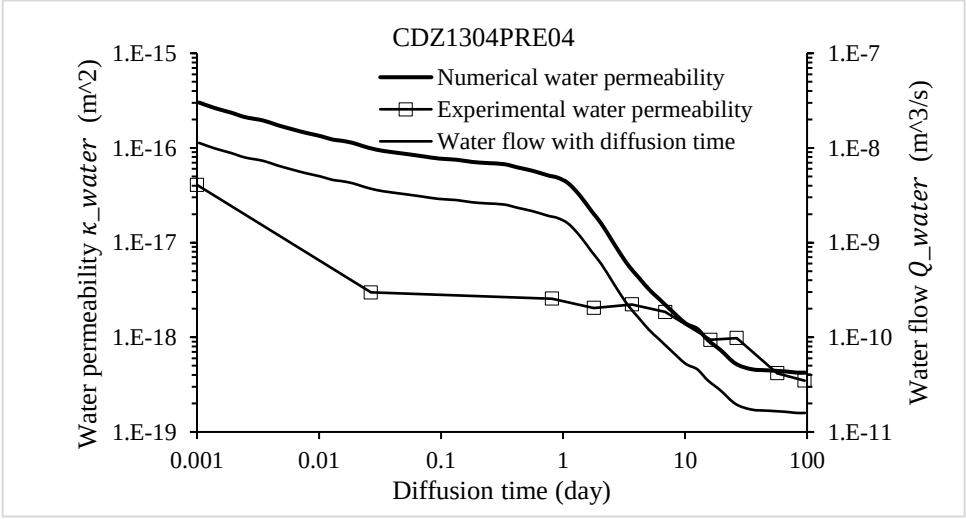

Figure 5.125. Permeability change with diffusion time

Figure 5.125 shows the changes of the experimental water permeability, the numerical water permeability and the water flow with the increment of the diffusion time. For experimental water permeability, the main declination from $4.07 \times 10^{-17} m^2$ to $2.97 \times 10^{-18} m^2$ obtained when the diffusion time went up from 0.001 days to 0.1 days, this rapid decrease illustrates that the fractured

interval can accomplish an immediate self-sealing during the hydration process if its initial cracks are very small. Whereas the experimental water permeability kept constant during the diffusion time is from 0.1 days to 10 days, a possible explanation is that the interval CDZ1304PRE04 can reach extremely low permeability once water was injected which slowed the diffusion process down to a great extent. The experimental water permeability went down during the diffusion time from 10 days to 100 days and then kept stable.

In the numerical simulation, the declination of gas permeability slows down due to the low initial intrinsic permeability. The numerical gas permeability decreases from $3 \times 10^{-16} m^2$ to $5 \times 10^{-17} m^2$ in one-day diffusion. And the self-sealing by the hydration continues from one day to 100 days, and the numerical gas permeability reaches to the level of $10^{-19} m^2$. Therefore, no matter in the numerical simulation or the experimental test, the interval CDZ1304PRE04 accomplished self-sealing. The accomplishment of the self-sealing of CDZ1304PRE04 proves that the deeper zone of the fractured zone from the drift wall can recover to its impermeability.

(2) CDZ1306PRE04

The interval 1306PRE04 located in depth between 1.18m and 1.38m from the surface of the drift wall, and the geological stresses σ_θ and σ_H are 18.5MPa and 16MPa, respectively. The analysis of the interval self-sealing is shown in Figure 5.126 and 5.127, respectively.

Figure 5.126 shows the changes of the experimental gas permeability, numerical gas permeability and the gas flow with the increment of the loading pressure. With the increment of the loading pressure from 0MPa to 4MPa, the experimental gas permeability declined from $3.07 \times 10^{-15} m^2$ to $3.62 \times 10^{-17} m^2$ which indicates that the loading pressure had significant effects on the sealing of the interval CDZ1306PRE04 even it distanced 1.18m from the loading plate. However, a significant declination of the experimental gas permeability was observed when the mechanical loading decreased from 4MPa to 0MPa, the possible explanation is that the fractures of the zone of this interval are micro-cracks, which are very easy to be sealed during a variation of stresses state among σ_θ, σ_H and σ_{CDZ}.

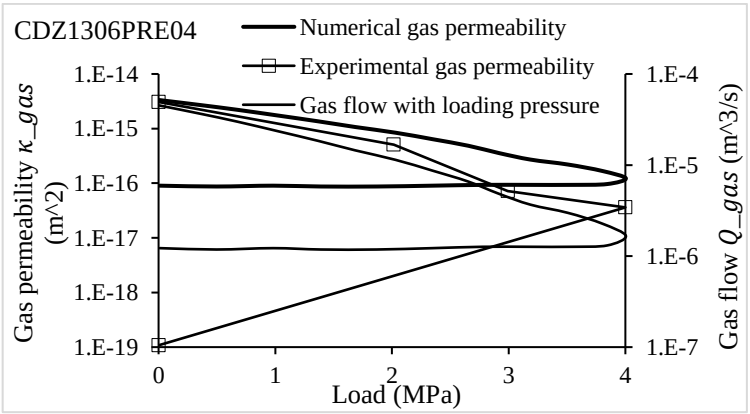

Figure 5.126. Permeability change with loading pressure

In the numerical simulation, the gas permeability also reduces with the loading pressure going up, and the initial gas permeability is $3.2 \times 10^{-15} m^2$ at the loading pressure 0MPa, the corresponding value decreases to $1.1 \times 10^{-16} m^2$ at the loading pressure 4MPa.

After the sealing process by means of the mechanical pressure loading on the steel plate, the hydration process was carried out, and the relation between the gas permeability and the diffusion time during the hydration process is shown as follows:

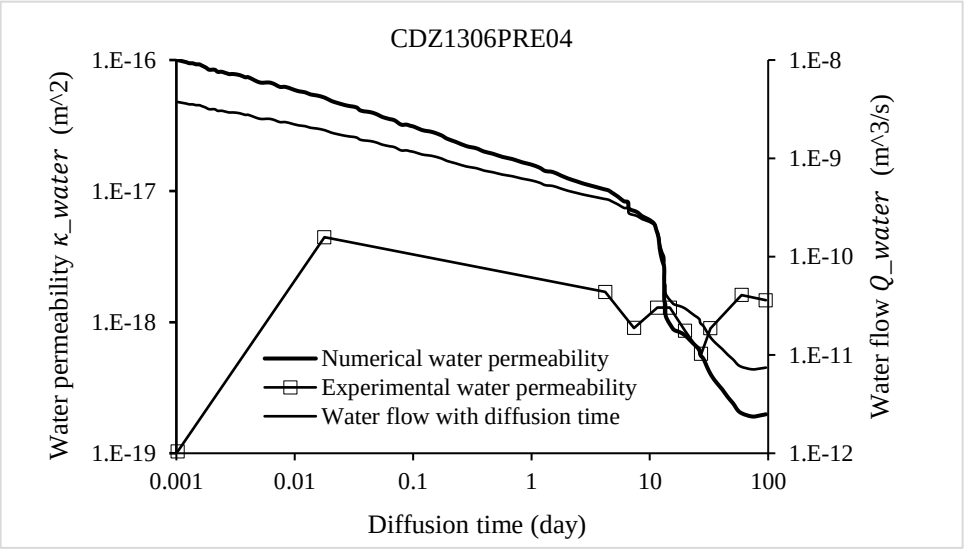

Figure 5.127. Permeability change with diffusion time

Figure 5.127 shows the changes of the experimental water permeability, numerical water permeability and water flow with the increment of the diffusion time. It can be seen that the initial water permeability in the experiment is $1.03 \times 10^{-19} m^2$ that is extremely approximate to the permeability of intact COx claystone and, the experimental water permeability went up to $4.45 \times 10^{-18} m^2$ in 0.01 day diffusion, and the water permeability reduced from $4.45 \times 10^{-18} m^2$ to $5.47 \times 10^{-19} m^2$ with the diffusion time growing from 0.01 day to 30 days, and then the values of the permeability stabilised. Therefore, the global water permeability irregularly varies when its value is at the level between $10^{-18} m^2$ and $10^{-19} m^2$, and keeps being sealed.

The initial water permeability after mechanical loading is $1.01 \times 10^{-16} m^2$ in the numerical simulation, it reduces with the diffusion time, and the value reaches to $2 \times 10^{-19} m^2$ in 10 days diffusion. However, inspection of Figure 5.127 shows that there is no good agreement between the numerical water permeability and experimental water permeability, the explanation for this inconsistency is that the possible self-sealing of shear fractures in the experiment is not easy to be captured in the numerical simulation. Although the experimental and numerical water permeability is not consistent, both of them are less than $1 \times 10^{-17} m^2$. Therefore, the interval CDZ1306PRE04 accomplished self-sealing in terms of the quantity of water permeability.

(3) CDZ1305PRE03

The interval 1305PRE03 located in depth between 1.93m and 2.13m from the surface of the drift wall, and the geological stresses σ_θ and σ_H are 16.5MPa and 16MPa, respectively.

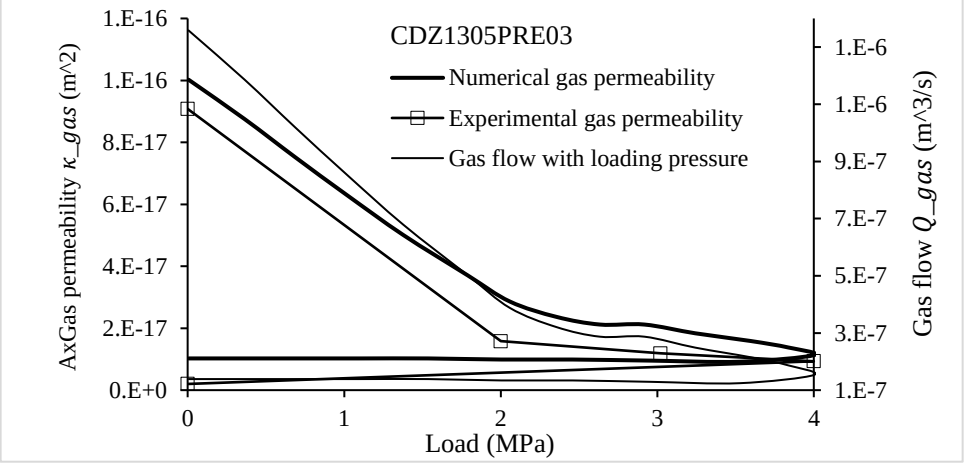

Figure 5.128. Permeability change with loading pressure

Figure 5.128 shows the changes of experimental gas permeability, numerical gas permeability and gas flow with the increase of the loading pressure. With the increment of the loading pressure from 0MPa to 4MPa, the experimental gas permeability declined from $9.08 \times 10^{-17} m^2$ to $9.37 \times 10^{-18} m^2$ which indicates that the loading pressure had significant effects on the sealing of the interval CDZ1305PRE03 even it distanced 1.93m from the loading plate.

In the numerical simulation, the gas permeability also reduces with the loading pressure going up, the initial gas permeability is $1.03 \times 10^{-16} m^2$ at the loading pressure 0MPa, and the corresponding value decreases to $1.1 \times 10^{-17} m^2$ at the loading pressure 4MPa. Inspection of the Figure 5.128 shows that a good agreement between the numerical curve and experimental curve of gas permeability has been obtained, which illustrates that the geological stress recovery will also be helpful to seal the deep part of the excavated damage zone.

Figure 5.129 shows the changes of the experimental water permeability, numerical water permeability and water flow with the increment of the diffusion time. It can be seen that the initial water permeability in the experiment is $2.28 \times 10^{-18} m^2$, it is extremely approximate to the permeability of intact COx claystone and, the experimental water permeability went down to $1.05 \times 10^{-18} m^2$ in 0.01-day diffusion. In 10 days diffusion, the experimental water permeability had a jump from $2.94 \times 10^{-19} m^2$ to $4.97 \times 10^{-18} m^2$. After this jump, the permeability went down to around $2.2 \times 10^{-19} m^2$ and kept stabilised gradually. The initial water permeability after mechanical loading is $1.12 \times 10^{-17} m^2$ in the numerical simulation, and it reduces with the diffusion time, the value reaches to $4 \times 10^{-19} m^2$ in 10 days diffusion. Inspection of Figure 5.129 shows that there is no good agreement between the numerical water permeability and

experimental water permeability, which is the same as that occurred in the interval CDZ1306PRE04. Although the experimental and numerical water permeability is not consistent, the interval CDZ1305PRE03 accomplished self-sealing in terms of the quantity of water permeability.

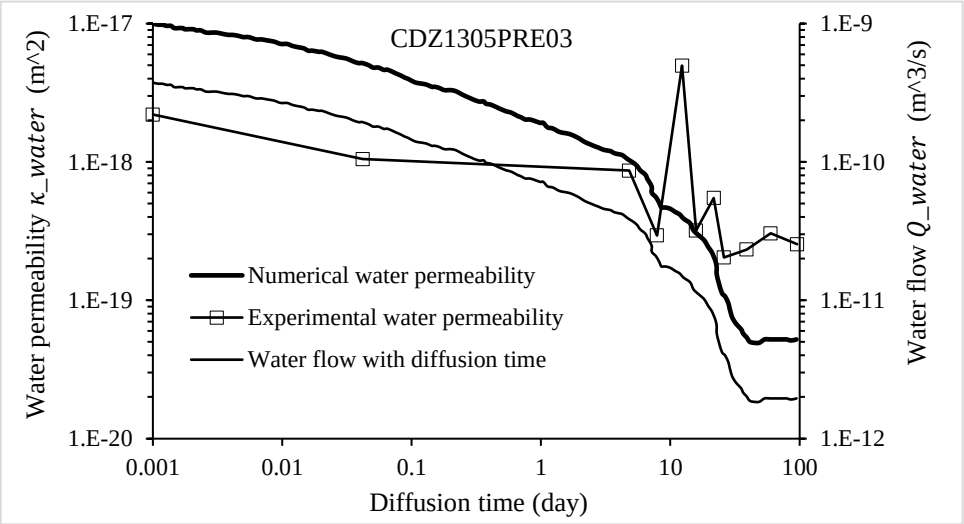

Figure 5.129. Permeability change with diffusion time

5.3.4 Discussions of CDZ tests

This part presented the analysis of self-sealing of eight intervals in four boreholes by means of numerical simulation. The eight intervals cover the whole range of the fractured zone. Therefore, the self-sealing of these intervals can demonstrate if the fractured zone is able to recover its impermeability. In numerical simulation, mechanical pressure was loaded on the seven of the above eight intervals, and permeability changes were calculated using gas flow. Following the increment of the mechanical loading, the corresponding decrease of the gas flow was captured in all the seven intervals, which indicated that self-sealing was occurring during the loading process. The maximum gas permeability of the seven intervals could reach the level of $10^{-12}m^2$ and the minimum one was around the level of $10^{-17}m^2$ before the mechanical loading, and the maximum gas permeability of the seven intervals reduced to the level of $10^{-14}m^2$, the minimum one reduced the level of $10^{-19}m^2$. Therefore, a large declination of permeability could be accomplished by means of mechanical loading. The following five plots shows the impacts of the mechanical loading on decreasing the gas conductivity among the six boreholes in CDZ experiment, and a comparison between numerical results and experimental reaction during mechanical loading is analysed.

Figure 5.130 illustrates that there are intensive interferences among every interval. Because the most damaged part of the fractured zone placed within 1.5m distancing from the surface of the drift wall, good interference among intervals could be observed at low gas pressure.

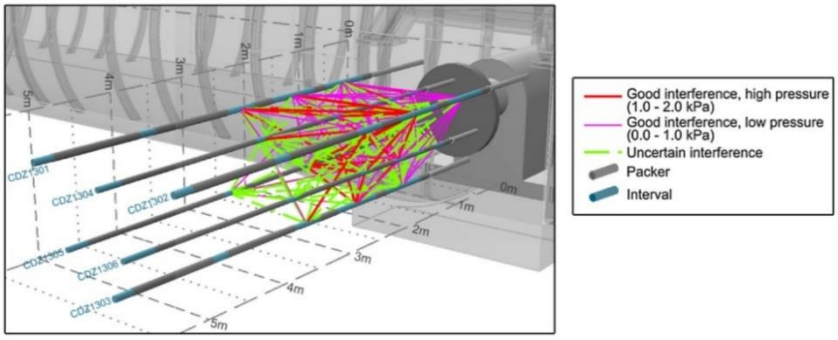

Figure 5.130. The interferences at mechanical loading 0MPa (de La Vaissière et al., 2015)

With the depth increment from the drift wall, the fracture patterns gradually transferred from tensile fractures to shear fractures that led the connection among the intervals going down. Therefore, good interference could be tested in deeper places only at high gas pressure. In numerical simulation, the initial permeability of numerical mesh was produced according to the initial experimental permeability of intervals in CDZ experiments. The fracture numbers using designed notches in numerical mesh and adjusting a displacement for cracking successfully reproduced the permeability varying inside the fractured zone, and the intervals placed in fracture connected zone are given large cracks in numerical mesh, small cracks are produced for the intervals placed in fracture diffuse zone.

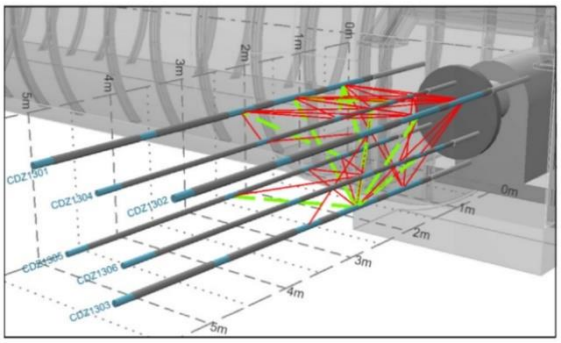

Figure 5.131. The interferences at mechanical loading 2MPa (de La Vaissière et al., 2015)

When the mechanical loading went up to 2MPa in numerical simulation, there was an obvious decrease of gas flow calculated, which links with plenty of fractures closed due to the mechanical loading. This decrease of gas flow in numerical simulation is validated in experiment as observed weak interference when a low pressure was imposed.

Comparison of Figure 5.131 and 5.132 shows that the numbers of the interference had an evident reduction among the intervals that were located out of the loading plate, and there was no interference observed among the intervals that were located behind the loading plate. In numerical simulation, the permeability of all the eight intervals evidently decreases during the mechanical loading increasing from 2 MPa to 3 MPa, and good agreements between numerical and

experimental results also validated the changing of interference observed when the mechanical loading grow from 2 MPa to 3 MPa.

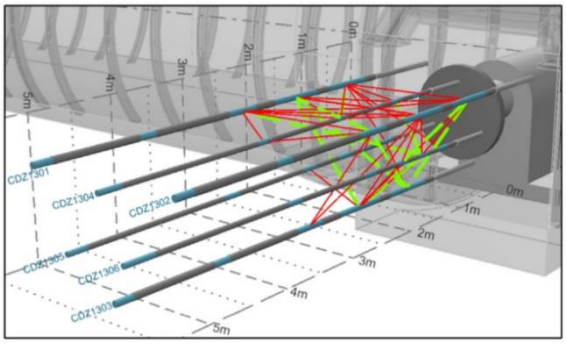

Figure 5.132. The interferences at mechanical loading 3MPa (de La Vaissière et al., 2015)

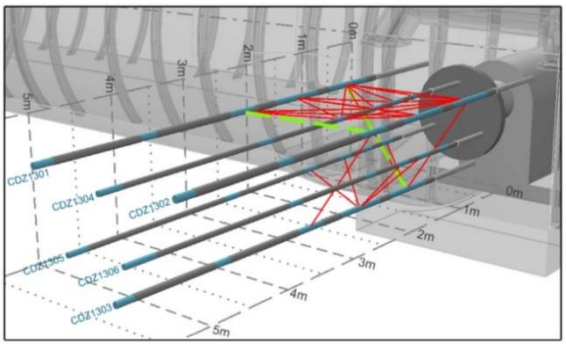

Figure 5.133. The interferences at mechanical loading 4MPa (de La Vaissière et al., 2015)

In both of numerical and experimental results, the permeability among the intervals at the mechanical loading of 4MPa (Figure 5.133) had a reduction again in comparison with that at the mechanical loading of 3MPa. However, the permeability among the intervals went down lightly no matter in experiments and numerical simulation when the mechanical loading rapidly reduced to 0MPa (Figure 5.134) which was an exceptional phenomenon, and the possible explanation is that the geological stresses has significant effects on sealing the fractures when the mechanical loading was unloaded rapidly.

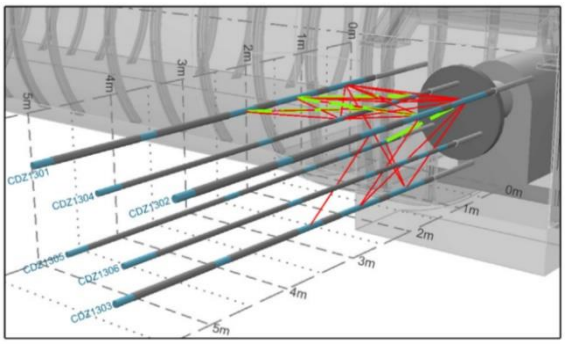

Figure 5.134. The interferences at mechanical loading 0MPa (de La Vaissière et al., 2015)

In the numerical simulation of all the eight intervals, the decrease of intervals' gas permeability

with the increment of the mechanical loading has good agreements with the corresponding results of the experimental ones with an exception of the interval CDZ1303PRE05 that was located out of the loading plate. Therefore, the proposed model is able to describe the change of mechanical behaviour of fractured COx claystone in large dimension when there is mechanical loading imposed. In terms of the level of the intrinsic permeability after mechanical loading, they are still larger than the level of $10^{-17}m^2$.

During the hydration tests, all the damaged intervals accomplished self-sealing rapidly when water was injected inside the intervals due to the swelling of COx during the resaturation process and maybe exist chemical interaction between water and COx claystone. The experimental water permeability of all the intervals reduced to the level between $10^{-18}m^2$ and $10^{-20}m^2$ in one hundred days diffusion, and then the water permeability stabilized gradually. In numerical simulation, good agreements has been accomplished between the numerical and experimental water permeability with the increment of the diffusion time. The coupling of water diffusion in fractured material and the cracks closure due to COx resaturation swelling enable us to describe the self-sealing process, no matter the self-sealing of CDZ1303PRE05 without mechanical loading during the hydration process or the self-sealing of the rest seven intervals, their final water permeability can reduce to the level between $10^{-18}m^2$ and $10^{-20}m^2$ in 100 days diffusion. Concluded from the above discussions, the fractured zone can accomplish self-sealing validated by means of the experimental tests and numerical simulation.

Chapter 6

Conclusions and perspectives

This chapter presents conclusions and perspectives of this project, including numerical model formulation and validation, self-sealing of the fractured zone and recommendations for future work.

6.1 Nuclear waste disposal

This dissertation summarized the classifications of nuclear waste and the corresponding disposal methods according to historical bibliographies and new researches. In terms of safety and feasibility for nuclear waste storage in long-term, deep disposal in underground galleries is a considerable way in current. Of course, following the scientific progress, it is worthy to look forwards to have a significant breakthrough in technology which can deteriorate the radioactive waste into non-radioactive. The literature review of the construction and their characteristics of underground facilities, including underground drifts excavation, desaturation/resaturation of galleries excavation openings, and evolution of fractured zone, are displayed in this thesis.

6.2 Numerical model formulation and validation

To model hydro-mechanical behaviour of Callovo-Oxfordian argillite claystone, an elastoplastic damage model coupled with the Biot's model and an extra swelling component is proposed in the present thesis. The model accounts for the variation of Young's modulus, tensile strength and fracture energy with capillary pressure change and is able to represent the mechanical behaviour of claystone under different saturation and stress conditions. Because the standard Biot's model is not able to exhibit the significant shrinkage/swelling deformation of Callovo-Oxfordian argillite due to the variation of water content, an hysteretic model that accounts for this "extra deformation" is proposed. There were many uniaxial compression tests at different saturation of COx claystone and triaxial compression tests under different confining pressures carried out, and good agreements between the numerical and experimental results were obtained. this means that the proposed model is able to describe correctly the basic features of material behaviour at different humidity levels and confining pressures, including the evolution of stiffness, plastic straining, volumetric deformation and softening. The effect of relative humidity is also captured by the proposed model, which correctly predicts an increase in material stiffness as the relative humidity decreases. The experimental value of peak stress is also adequately predicted at all humidity levels. These numerical results prove the good performance of the model in describing the plastic-damage behaviour of the COx claystone.

The model of Vogel et al. (2000) coupled with the Darcy law for describing moisture movement inside porous material is employed to simulate water diffusion inside the COx claystone, and the corresponding hydraulic parameters of COx, including maximum volumetric water content, volumetric water content of saturated COx, residual volumetric water content and critical capillary pressure of air-entry, are summarized. Introducing the model for moisture movement into the hydro-mechanical model formulated from the combination of plastic damage model with extra deformation model, the numerical simulation of COx deformation during a resaturation process performed correctly. For COx swelling during a resaturation process under free condition, a good consistency between numerical and experimental result is obtained, and the volumetric swelling rate can reach the level of 7%-8%. For COx swelling during a resaturation process under constant normal stresses, the swelling rate varies with the scale of normal stress. When the normal stresses are 0.05MPa and 2MPa, the corresponding normal swelling rates are 2.3% and 0.75%, respectively. When it reaches the geological stress levels of 12MPa and 14MPa, the swelling rates are negligible, and the good fitting between numerical and experimental results illustrates that the proposed model is able to analyse the COx deformation of the fractured zone under geological stress condition. The proposed model captured the macro-damage phenomena in uniaxial/triaxial compression tests, and it also captured the micro-damage phenomena of the COx claystone during a resaturation process. These results imply that the proposed model can correctly describe the time-dependent swelling of COx during a resaturation process.

Callovo-Oxfordian argillite (COx), as a kind of claystone, its properties are similar to many other kinds of claystone or mudstone due to the variation of clay content inside the materials. Therefore, this formulated model can be modified and used to analyse the hydro-mechanical behaviours of other claystone in future.

6.3 Researches on the self-sealing of the fractured zone

Due to the necessity of describing connected fractures and diffuse fractures of the fractured zone, cracks width estimation is carried out by a method based on fracture energy regularization, and then permeability evaluation is carried out by introducing the estimated cracks value into the Cubic law. In this thesis, the self-sealing of fractured COx samples and the self-sealing of CDZ experiments are analysed using numerical method in terms of the evolution of cracks and permeability. For the self-sealing of fractured COx samples, water permeability can easily decline to less than $1 \times 10^{-17} m^2$ when water flows through cracks of COx, and an evident crack-closure process was observed in numerical simulations as in experiments due to the induced swelling of COx. The declination of permeability obtained in numerical simulation were compared to experimental results, and good agreements between the numerical and experimental results were obtained including the self-sealing of fractured COx. Of course, the time for water diffusion in fractured COx samples has a significant impacts on permeability reduction, therefore, the self-

sealing of fractured COx samples which experienced a long time of water diffusion has a better performance in comparison with those with a shorter diffusion time.

The mechanical compression promoting the self-sealing of the fractured zone in CDZ experiments provides a proof that the swelling pressure from sealing system against walls of drifts is able to improve the self-sealing of the fractured zone. In the CDZ experiments, the maximum value of the provided mechanical compression loaded on the steel plate is 4MPa, whereas it is certain this value can recover to the original geological stress (12.5MPa-16.5MPa) in long term. Therefore, the extent of self-sealing of the fractured zone will be enlarged in comparison with that in CDZ experiments. In terms of permeability, the value in the fractured zone can decline from the level of $10^{-12}m^2$ to the level of $10^{-19}m^2$ during a hydration process, and the value in the diffuse fractures zone of excavation disturbance zone can reduce from the level of $10^{-15}m^2$ to the level of $10^{-20}m^2$.

In numerical simulation, the method of setting the number of fracture in numerical meshes according to empirical fracture density obtained from experiments was used. Based on this hypothesis, the proposed model performed correctly in describing the self-sealing of CDZ experiments, including cracks opening and closure evolution, permeability evolution, water flow inside cracks. Of course, it is impossible to obtain cracks and permeability distributions in numerical meshes identical to CDZ experiments, however, the evolutions of the permeability with hydration time obtained numerically for different conditions of stress and fracturing are comparable to experiment results.

In conclusion, a new model for the COx claystone which can describe the hydro-mechanical behaviours of excavated damage zone in French nuclear waste deep disposal scheme, including stiffness, fracture energy, tensile strength, damage, crack estimation, permeability evaluation, moisture movement and deformation, is formulated successfully based on the great works of previous researchers in this dissertation. Of course, the application of the new model can expand to analyse the hydro-mechanical behaviours of other claystone which are similar to COx. In fact, when the underground drifts and galleries are backfilled, the re-saturation process will begin automatically. The re-saturation of COx will bring a significant swelling which will lead to the self-sealing of the fractured zone, at the same time, bentonite has great swelling capacity during hydration which will provide a large swelling pressure against the drift wall.

6.4 Recommendations for future work

Some potential developments of the present work are summarised as follows:

- Further work could be conducted to numerically explore the thermal-hydro-mechanical behaviours of the COx claystone based on the study of the hydro-mechanical behaviours in this project. Taking the heating from high-level nuclear waste into account and the

great effects of high temperature on the mechanical behaviour of COx observed from many experiments, the self-sealing of the fractured zone under thermal-hydro-mechanical conditions should be analysed, including cracks development, permeability evolution and so on (see Figure 1.15).

- Further work could be performed to introduce the creep behaviour of the COx claystone in the numerical model. Due to the time range for nuclear waste decay could reach the level of 100,000 years and many experiments in short-term indicated that the creep behaviour of COx is significant, the impacts of COx creep on the self-sealing of the fractured zone in long-term should be predicted.
- Further investigation should be conducted to study the porosity evolution under mechanical loadings or changing of water content due to there are significant effects of porosity to the hydro-mechanical behaviours of COx.
- Further researches on the hydraulic behaviours of unsaturated fractured materials has to be conducted due to the difference of moisture movement in pores and cracks.

REFERENCES

Armand, G., Conil, N., Talandier, J., Seyedi, D. M. (2017). Fundamental aspects of the hydromechanical behaviour of Callovo-Oxfordian claystone: from experimental studies to model calibration and validation. *Computers and Geotechnics, 85:* 277-286.

Armand, G., Leveau, F., Nussbaum, C., de La Vaissiere, R., Noiret, A., Jaeggi, D., Righini, C. (2014). Geometry and properties of the excavation-induced fractures at the Meuse/Haute-Marne URL drifts. *Rock Mechanics and Rock Engineering, 47(1):* 21-41.

Andra. (2005). Dossier 2005 Argile: tome architecture and management of a geological repository.

Authority, N. D. (2014). *Progress on approaches to the management of separated plutonium. Position Paper*, January.

Alley, W. M., Alley, R. (2012). Too hot to touch: the problem of high-level nuclear waste. *Cambridge University Press.*

Bates, J. K., Bradley, J. P., Teetsov, A., Bradley, C. R., Ten Brink, M. B. (1992). Colloid formation during waste form reaction: implications for nuclear waste disposal. *Science, 256(5057):* 649-651.

Bradshaw, K., Gribble, N. R., Hughes, D. O., Riley, A. D. (2007). UK Full-Scale Non-Active vitrification development and implementation of research findings onto the waste vitrification plant. *In Proceedings of Waste Management 2007 Conference, Tucson AZ, paper* (Vol. 7197).

Baechler, S., Lavanchy, J. M., Armand, G., Cruchaudet, M. (2011). Characterisation of the hydraulic properties within the EDZ around drifts at level− 490 m of the Meuse/Haute-Marne URL: a methodology for consistent interpretation of hydraulic tests. *Physics and Chemistry of the Earth, Parts A/B/C, 36(17-18):* 1922-1931.

Cooper, M. B. (2005). Naturally occurring radioactive materials (NORM) in Australian industries-Review of current inventories and future generation. *Report ERS-006 (EnviroRad Services Pty. Ltd.) to the Radiation health and Safety Advisory Council.*

Chapman, N. A., McKinley, I. G., Hill, M. D. (1987). The geological disposal of nuclear waste.

Chen, S., Yang, C., Wang, G. (2017). Evolution of thermal damage and permeability of Beishan granite. *Applied Thermal Engineering, 110:* 1533-1542.

De La Vaissière, R., Morel, J., Noiret, A., Côte, P., Helmlinger, B., Sohrabi, R., Nussbaum, C. (2014). Excavation-induced fractures network surrounding tunnel: properties and evolution under loading. *Geological Society, London, Special Publications, 400(1):* 279-291.

Dunnett, B. F., Gribble, N. R., Short, R., Turner, E., Steele, C. J., Riley, A. D. (2012). Vitrification of high molybdenum waste. *Glass Technology-European Journal of Glass Science and Technology Part A, 53(4):* 166-171.

Davy, C. A., Skoczylas, F., Barnichon, J. D., Lebon, P. (2007). Permeability of macro-cracked argillite under confinement: gas and water testing. *Physics and Chemistry of the Earth, Parts A/B/C, 32(8-14):* 667-680.

De La Vaissière, R., Armand, G., Talandier, J. (2015). Gas and water flow in an excavation-induced fracture network around an underground drift: a case study for a radioactive waste repository in clay rock. *Journal of Hydrology, 521:*141-156.

Flynn, J., Kasperson, R., Kunreuther, H., Slovic, P. (1992). Time to rethink nuclear waste storage. *Issues in Science and Technology, 8(4):* 42-48.

Fouché, O., Wright, H., Le Cléac'h, J. M., Pellenard, P. (2004). Fabric control on strain and rupture of heterogeneous shale samples by using a non-conventional mechanical test. *Applied Clay Science, 26(1-4):* 367-387.

Fouché, O., Wright, H., Le Cléac'h, J. M., Pellenard, P. (2004). Fabric control on strain and rupture of heterogeneous shale samples by using a non-conventional mechanical test. *Applied Clay Science, 26(1-4) :* 367-387.

Findlay, T. (2010). Nuclear Energy to 2030 and its Implications for Safety, Security and Nonproliferation: Overview. Tech. rep., *Canadian Center for Treaty Compliance.*

Fichant, S., La Borderie, C., Pijaudier-Cabot, G. (1999). Isotropic and anisotropic descriptions of damage in concrete structures. *Mechanics of Cohesive-frictional Materials: An International Journal on Experiments, Modelling and Computation of Materials and Structures, 4(4) :* 339-359.

Gens, A., Alonso, E. E. (1992). A framework for the behaviour of unsaturated expansive clays. *Canadian Geotechnical Journal, 29(6) :* 1013-1032.

Garitte, B., Bond, A., Millard, A., Zhang, C., Mcdermott, C., Nakama, S., Gens, A. (2013). Analysis of hydro-mechanical processes in a ventilated tunnel in an argillaceous rock on the basis of different modelling approaches. *Journal of Rock Mechanics and Geotechnical Engineering, 5(1):*1-17.

Gibney, E. (2015). Why Finland now leads the world in nuclear waste storage. Nature News.

Grasberger, S., Meschke, G. (2004). Thermo-hygro-mechanical degradation of concrete: From coupled 3D material modelling to durability-oriented multifield structural analyses. *Materials and Structures, 37(4) :* 244-256.

Guo, Y., Li, Y., Wang, H., Liu, S., Su, R., Zong, Z. (2010). Study on regional hydrogeochemical characteristics of Beishan area-the preselected area for China's high level radioactive waste repository. *In Proceedings of the 3rd academic seminar on waste underground disposal.*

Guo, Y., Yang, T., Liu, S. (2001). Hydrogeological characteristics of Beishan preselected area, Gansu province for China's high-level radioactive waste repository. *Uranium Geology, 17(3):* 184-189.

Gin, S., Abdelouas, A., Criscenti, L. J., Ebert, W. L., Ferrand, K., Geisler, T., Marra, J. C. (2013). An international initiative on long-term behavior of high-level nuclear waste glass. *Materials Today, 16(6):* 243-248.

Grassl, P., Fahy, C., Gallipoli, D., Wheeler, S. J. (2015). On a 2D hydro-mechanical lattice approach for modelling hydraulic fracture. *Journal of the Mechanics and Physics of Solids, 75 :* 104-118.

Guéguen, Y., Sarout, J., Fortin, J., Schubnel, A. (2009). Cracks in porous rocks Tiny defects, strong effects. *The Leading Edge, 28(1):* 40-47.

Hileman, B. (1982). Nuclear waste disposal. *Environmental science and technology, 16(5):* 271A-275A.

Hellmuth, K. H., Siitari-Kauppi, M. (1990). Investigation of the porosity of rocks. Impregnation with 14C-polymethylmethacrylate (PMMA), a new technique. *Rapport Finnish Centre for Radiation and Nuclear Safety.*

Harrison, M. T. (2014). Vitrification of high level waste in the UK. *Procedia Materials Science, 7(44):*10-15.

Johansson, E., Siren, T., Kemppainen, K. (2015). ONKALO–Underground Rock Characterization Facility for In-situ Testing for Nuclear Waste Disposal. *In 13th ISRM International Congress of Rock Mechanics. International Society for Rock Mechanics and Rock Engineering.*

Janicki, M. (2013). Iron boxes for ILW transport and storage. *NUCLEAR ENGINEERING INTERNATIONAL, 58(711):* 47-48.

Kallel, H., Carré, H., Laborderie, C., Masson, B., Tran, N. C. (2018). Evolution of mechanical properties of concrete with temperature and humidity at high temperatures. *Cement and Concrete Composites, 91:* 59-66.

Kim, J. S., Kwon, S. K., Sanchez, M., Cho, G. C. (2011). Geological storage of high level nuclear waste. *KSCE Journal of Civil Engineering, 15(4):* 721-737.

Larkin, M. J. (1986). Development of highly active waste conditioning at Sellafield. *Atom (London),* 25-27.

Lebon, P., Ghoreychi, M. (2000). French underground research laboratory of Meuse, Haute-Marne THM aspects of argillite formation. *In Proceedings of Eurock 2000 Symposium,* March, 27-31.

Lee, J., Lopez, M. M. (2014). An experimental study on fracture energy of plain concrete. *International Journal of Concrete Structures and Materials, 8(2):*129-139.

Li, W., Jin, Z., Cusatis, G. (2017). Characterization of marcellus shale fracture properties through size effect tests and computations. *arXiv preprint arXiv:1710.07366.*

Lyoussi, A., Romeyer-Dherbey, J., Jallu, F., Payan, E., Buisson, A., Nurdin, G., Allano, J. (2000). Transuranic waste detection by photon interrogation and on-line delayed neutron counting. *Nuclear Instruments and Methods in Physics Research Section B: Beam Interactions with Materials and Atoms, 160(2):* 280-289.

Martin, C. D., Christiansson, R. (2009). Estimating the potential for spalling around a deep nuclear waste repository in crystalline rock. *International Journal of Rock Mechanics and Mining Sciences, 46(2):* 219-228.

Martin, F., Laviguerie, R., Armand, G. (2010). Geotechnical feedback of the new galleries excavation at the ANDRA underground research laboratory-Bure (France). *In ISRM International Symposium-EUROCK 2010. International Society for Rock Mechanics and Rock Engineering.*

Martín, L. B., Hadj-Hassen, F., Tijani, M., Armand, G. (2011). New numerical modelling of the mechanical long-term behaviour of the GMR gallery in ANDRA's Underground Research Laboratory. *Physics and Chemistry of the Earth, Parts A/B/C, 36(17-18):* 1872-1877.

Matallah M, La Borderie C. (2016). 3D numerical modelling of the crack-permeability interaction in fractured concrete. *In Proceedings of 9th International Conference on Fracture Mechanics of Concrete and Concrete Structures, FraMCoS-9, Berkeley, USA*. DOI 10.21012/FC9.245 .

Möri, A., Bossart, P. (1999). Results of the Hydrogeological, Geochemical and Geotechnical Experiments *(performed in 1996 and 1997).*

National Research Council. (1996). The Waste Isolation Pilot Plant: A Potential Solution for the Disposal of Transuranic Waste. *National Academies Press.*

Ojovan, M. I., Lee, W. E., Kalmykov, S. N. (2019). An introduction to nuclear waste immobilisation. *Elsevier.*

Peachey, C. (2014). Korean repository realised. *Nuclear Engineering International, 59(720):* 16-17.

Pham, Q. T. (2006). Effets de la désaturation et de la resaturation sur l'argilite dans les ouvrages souterrains *(Doctoral dissertation).*

Pham, Q. T., Vales, F., Malinsky, L., Minh, D. N., Gharbi, H. (2007). Effects of desaturation–resaturation on mudstone. *Physics and Chemistry of the Earth, Parts A/B/C, 32(8-14):* 646-655.

Rogner, H. H. (2010). Nuclear power and sustainable development. *Journal of International Affairs*, 137-163.

Riley, A., Walker, S., Gribble, N. R. (2009). Composition changes and future challenges for the Sellafield waste vitrification plant. *MRS Online Proceedings Library Archive*, 1193.

Rastiello, G., Boulay, C., Dal Pont, S., Tailhan, J. L., Rossi, P. (2014). Real-time water permeability evolution of a localized crack in concrete under loading. *Cement and Concrete Research*, *56*: 20-28.

Roth, G., Weisenburger, S., Fleisch, J., Weishaupt, M. (2005). Process technique and safety features of the German VEK vitrification plant currently under commissioning. *In Proc. GLOBAL*.

Rempe, N. T. (2007). Permanent underground repositories for radioactive waste. *Progress in nuclear energy, 49(5):* 365-374.

Ressetar, R. (2003). The Yucca Mountain Nuclear Waste Repository from a Federalism Perspective. J. *Land Resources and Envtl. L., 23:* 219.

Shrader-Frechette, K. S. (1993). Burying uncertainty: Risk and the case against geological disposal of nuclear waste. *Univ of California Press.*

Sung, K. Y., Yun, S. T., Park, M. E., Koh, Y. K., Choi, B. Y., Hutcheon, I., Kim, K. H. (2012). Reaction path modeling of hydrogeochemical evolution of groundwater in granitic bedrocks, South Korea. *Journal of Geochemical Exploration, 118:* 90-97.

Saling, J. (2018). Radioactive waste management. Routledge.

Selroos, J. O., Follin, S. (2014). Overview of hydrogeological site-descriptive modeling conducted for the proposed high-level nuclear waste repository site at Forsmark, Sweden. *Hydrogeology Journal, 22(2):* 295-298.

Sterbentz, J. W. (1997). Radionuclide mass inventory, activity, decay heat, and dose rate parametric data for TRIGA spent nuclear fuels (No. INEL--96/0482). *Idaho National Engineering Lab.*

Sammartino, S., Siitari-Kauppi, M., Meunier, A., Sardini, P., Bouchet, A., Tevissen, E. (2002). An imaging method for the porosity of sedimentary rocks: adjustment of the PMMA method-example of a characterization of a calcareous shale. *Journal of Sedimentary Research, 72(6):* 937-943.

Secchi, S., Schrefler, B. A. (2012). A method for 3-D hydraulic fracturing simulation. *International journal of fracture, 178(1-2) :* 245-258.

Smith, W. (1985). Vitrification of Sellafield wastes. *Atom (London):*3-7.

Siren, T. (2017). Overview of Finnish Spent Nuclear Fuel Disposal Programme. *J. Korean Soc. Miner. Energy Resour. Eng*, *54*: 367-376.

Tonhauser, W., Jankowitsch-Prevor, O. (2006). The Joint convention on the safety of spent fuel management and on the safety of radioactive waste management. *International nuclear law in the post-Chernobyl period*, *OECD-NEA,* Paris, 201-214.

US Nuclear Regulatory Commission. (2015). Backgrounder on Radioactive Waste.

Van Genuchten, M. T. (1980). A closed-form equation for predicting the hydraulic conductivity of unsaturated soils 1. *Soil science society of America journal, 44(5):* 892-898.

Volckaert, G., Bernier, F., Sillen, X., Van Geet, M., Mayor, J. C., Göbel, I. (2004). Similarities and differences in the behaviour of plastic and indurated clays. *Proceedings of Euradwaste, 4.*

Voutilainen, M., Poteri, A., Helariutta, K., Siitari-Kauppi, M., Nilsson, K., Andersson, P., Lindberg, A. (2014). In-situ experiments for investigating the retention properties of rock matrix in ONKALO, Olkiluoto, Finland–14258. *In Conference proceedings WM2014 Conference, Phoenix,* AZ(pp. 2-6).

Wang, J., Su, R., Xue, W., Zheng, H. (2004). Preliminary site characterization at Beishan northwest China-A potential site for China's high-level radioactive waste repository. *In The progress report of geological disposal of high level radioactive waste in China in the past ten years.*

Wang, J., Chen, W., Su, R., Guo, Y., Jin, Y. (2006). Geological disposal of high-level radioactive waste and its key scientific issues. *Chinese Journal of Rock Mechanics and Engineering, 25(4) :* 801-812.

World Nuclear Association. (2010). Storage and Disposal Options. *Radioactive Waste Management Appendix, 2.*

Walker, S., Hyde, R. A., Piper, R. B., Roy, M. W. (1992). An overview of in situ waste treatment technologies (No. EGG-M-92342; CONF-920851-57). EG and G Idaho, Inc., Idaho Falls, ID (United States).

Weisenburger, S., Roth, G. (1984). Status and plans for high-level liquid waste vitrification in the Federal Republic of Germany. *In Fuel reprocessing and waste management.* Volume 1.

West, J. M., Christofi, N., McKinley, I. G. (1985). An overview of recent microbiological research relevant to the geological disposal of nuclear waste. *Radioact. Waste Manage. Nucl. Fuel Cycle, 6(1):*79-95.

Witherspoon, P. A., Bodvarsson, G. S. (2001). Geological challenges in radioactive waste isolation: Third worldwide review. *Geological Challenges in Radioactive Waste Isolation.*

Wileveau, Y., Cornet, F. H., Desroches, J., Blumling, P. (2007). Complete in situ stress determination in an argillite sedimentary formation. *Physics and Chemistry of the Earth, Parts A/B/C, 32(8-14):* 866-878.

Yven, Béatrice, Michel Garcia, and Aliouka Chabiron. "Geometry and physical rock properties modelling of the Callovo-Oxfordian claystone formation from a 3D high resolution seismic cube."

Yim, M. S., Simonson, S. A. (2000). Performance assessment models for low level radioactive waste disposal facilities: a review. *Progress in Nuclear Energy, 36(1):* 1-38.

Yang, T., Guo, Y. (2004). The ground water chemical characteristics of Beishan area-the China's potential high level radioactive waste repository. *In The progress report of geological disposal of high level radioactive waste in China in the past ten years.*

Zhang, C. L., Rothfuchs, T., Jockwer, N., Kröhn, K. P., Miehe, R., Moog, H. (2004). Results of laboratory investigations on clays. *In Proceedings of the International Conference on Radioactive Waste Disposal—DisTec*, April 26-28, Berlin, Germany, (Vol. 2004).

Zhang, C. L., Rothfuchs, T. (2007). Moisture effects on argillaceous rocks. *In Experimental Unsaturated Soil Mechanics* (pp. 319-326). Springer, Berlin, Heidelberg.

Zhang, C. L., Wieczorek, K., Xie, M. L. (2010). Swelling experiments on mudstones. *Journal of Rock Mechanics and Geotechnical Engineering, 2(1):* 44-51.

Zhang, C. L. (2013). Sealing of fractures in claystone. *Journal of Rock Mechanics and Geotechnical Engineering, 5(3) :* 214-220.

Zhang, F., Jia, Y., Bian, H. B., Duveau, G. (2013). Modeling the influence of water content on the mechanical behavior of Callovo–Oxfordian argillite. *Physics and Chemistry of the Earth, Parts A/B/C, 65 :* 79-89.

Zhao, X. G., Wang, J., Cai, M., Ma, L. K., Zong, Z. H., Wang, X. Y., An, Q. M. (2013). In-situ stress measurements and regional stress field assessment of the Beishan area, China. *Engineering geology, 163 :* 26-40.